Single-Nanocrystal Photon Correlation: A Versatile Tool for Elucidating Basic Physics and Characterizing Applications-Relevant Properties

by

Andrew Paul Beyler

B.A. Chemical Physics
Hamilton College, 2010

Submitted to the Department of Chemistry
in partial fulfillment of the requirements for the degree of

Doctor of Philosophy

at the

MASSACHUSETTS INSTITUTE OF TECHNOLOGY

September 2015

Author .....
Department of Chemistry
July 28, 2015

Certified by .....
Moungi G. Bawendi
Lester Wolfe Professor of Chemistry
Thesis Supervisor

Accepted by .....
Robert W. Field
Haslam and Dewey Professor of Chemistry
Chairman, Department Committee on Graduate Students

This doctoral thesis has been examined by a committee of the Department of Chemistry as follows:

.....

Professor Keith A. Nelson
Thesis Committee Chairman

.....

Professor Moungi G. Bawendi
Thesis Advisor

.....

Professor Mei Hong
Thesis Committee Member

Single-Nanocrystal Photon Correlation: A Versatile Tool for Elucidating Basic Physics and Characterizing Applications-Relevant Properties

by

Andrew Paul Beyler

Submitted to the Department of Chemistry
on July 28, 2015, in partial fulfillment of the
requirements for the degree of
Doctor of Philosophy

Abstract

Single-molecule spectroscopy has been a critical tool for the development and understanding of semiconductor nanocrystals because of their inherent heterogeneity size-dependent properties. In the past two decades, researchers have developed a diverse toolbox of single-nanocrystal techniques and analyses that is capable of elucidating the complex physics of nanocrystal fluorescence and characterizing many of the subtle but important optical properties of nanocrystal samples. This effort has been enabled by the flexible and modular structure of the single-molecule microscope, which offers a multitude of opportunities for shaping the information gained from single-nanocrystal experiments and provides a convenient and powerful framework for creativity in experimental design.

In this thesis, we present two investigations that illustrate the full range and versatility of single-nanocrystal spectroscopy and, in particular, of photon correlation analysis. In Part I, we use single-nanocrystal spectroscopy as a tool for elucidating basic physics by investigating the rapid spectral diffusion of individual nanocrystals at low temperature. We develop a technique capable of measuring spectral dynamics over eight orders of magnitude in time ranging form microseconds to hundreds of seconds, and show that we can extract previously unavailable information about the spectral diffusion mechanism. In Part II, we use single-nanocrystal spectroscopy as a tool for characterizing optical properties by devising an experiment to measure the average biexciton quantum yield of nanocrystal samples. This experiment allows us to measure the biexcitonic properties of underdeveloped materials and can serve as a quick and reliable characterization technique to aid in synthetic optimization. Finally, in Part III, we look to the future by highlighting several modifications of existing experiments that could reveal new and exciting insight into nanocrystals.

Thesis Supervisor: Moungi G. Bawendi
Title: Lester Wolfe Professor of Chemistry

Acknowledgments

I have been putting off writing this section for so long because it feels like such a daunting task to try to adequately thank all of the people who have helped me get to the point of writing this thesis. But, it is the night before print day and I guess I am finally out of time! There are so many people to thank; so many people who have either helped shape the research I have written about here, helped shape me as a scientist and as a person, or helped me make it from one day to the next. Insofar as this is a thesis worth reading, they deserve as much of the credit for this work as I do, and I cannot even begin to express my gratitude for knowing and learning from all of them. Let's give it a shot anyway.

I, of course, should start by thanking my Mom, my Dad, my brother Matthew, and the rest of my family. They have always been such an important and positive force in my life. I could not have asked for a better childhood, better role models, or a better support system. I am so proud to be a part of our family and to have grown up in (and hopefully contributed to) our family's unique and truly special culture. You guys mean the world to me.

I would like to thank my advisor, Moungi Bawendi. I sort of stumbled into the Bawendi Lab by accident my first year and now I cannot even imagine having made any other decision. Moungi is the best scientific role model I could possibly have asked for: his intelligence, attention to detail, grasp of the bigger picture, commitment to scientific rigor, and kind personality. It has been a true joy to work with him and learn from him for the past five years. Everyone should have a graduate advisor as awesome as Moungi, but unfortunately, he is one in a trillion.

Much of the work presented in this thesis has been produced in collaboration with or with the support of "Team PCFS": Jian Cui, Xavier Brockmann, Lisa Marshall, and more recently Justin Caram, Hendrik Utzat, and Leigh Heathcote. As it turns out, photon-correlation Fourier spectroscopy is a pretty hard experiment to do and an even harder experiment to understand. I count myself extraordinarily lucky that my various partners in crime over the years have been so brilliant, friendly, helpful, and just plain fun to work with, whether it was Xavier's willingness to bang out or read derivations over his lunchbreak at his real job, Lisa's commitment to show me the ropes over her last couple of months when she could have had one foot out of the door, the years of strong and productive collaboration between Jian and I, or the more recent fun times helping Hendrik get up to speed (like he needs my help!). I am so happy that I had the opportunity to be a part of that.

In fact, the spectroscopy subgroup of the Bawendi Lab has, in general, been one of the most kind, supportive, and genuinely helpful communities I have ever had the honor to be a part of. In addition to Team PCFS, this has included Thomas Bischof, Mark Wilson, Igor Coropceanu, Russ Jensen, and Katie Shulenberger. I am so proud of the way that we managed to build such a friendly environment where everyone could be so open and available to each other to talk to each other about our science and to help each other out. Not only did it make my experience in gruduate school that much more enjoyable, but I think it helped us all produce better science than any of

us could have produced individually. Nowhere was this more keenly manifested than in the review paper several of us wrote a couple years ago. That paper is probably the biggest achievement that I was a part of in graduate school, and one of the few things I can truly say I am proud of doing.

I would also like to thank all of the Bawendi Lab as a whole. The structure of the research group is pretty unique, the way that we are all bound by the singular vision of improving and using semiconductor nanocrystals, but heavily diversified by smaller, intermediate goals. We have a synthesis subgroup for improving their synthesis, we have a spectroscopy subgroup for understanding their properties, we have a devices subgroup for working on their device applications, and we have a biological subgroup for working on their bio-imaging applications. We all work on nanocrystals, but sometimes it feels like our research has nothing in common. And, that is awesome because it gives us the capabilities and resources to do pretty much any kind of research that we need to do to get the job done. However, this can only work effectively if we are all willing to help each other out. Luckily, we really has been. I found the Bawendi Lab to be an incredibly friendly and helpful place to work, and as a non-synthesis person, I strongly benefitted from the synthetic capabilities of the lab. Special thanks to Igor Coropceanu, Ou Chen, and Dan Harris for making samples for me.

Finally, to wrap up the graduate school portion of my acknowledgements, I would like to thank all of the support staff that make our research possible. Li Miao, our administrative assistant, is simply the best. Thank you for helping us all navigate the bureaucracy, for being so cool with all of our horrible spending mistakes, and for being such a fun person to hang out with while we wait for meetings with Moungi to begin. I would also like to thank the Chem Ed office for being so friendly and helpful, Gang Liu for helping save our electronics, and Dennis Nagle in the chemistry machine shop.

I would also like to thank all of the people who were part of my education before graduate school. I was honestly not the best or most dedicated student in the world during elementary and middle school. However, my teachers at Guilford Elementary School and Hammond Middle School saw talent and ability in me that I either did not or did not care about. They believed in me, pushed me, and ultimate got me on track. You hear a lot in the news about how American public schools are failing and so forth, but they didn't fail for me. I also want to thank my teachers at Hammond High School for constantly challenging me and engaging my curiosity. I enjoyed my classes in high school and grew as a person because of them, to the point that when I was graduating from high school, I didn't know if I wanted to be a Chemistry major, a Physics major, a Math major, a History major, a Philosophy major, or what. It was all great and it was all fun.

There are also a tremendous number of people I would like to thank surrounding my undergraduate education at Hamilton College. Deciding to attend Hamilton was one of the best decisions I have ever made. Not only did I have a fantastic time and meet so many great people, but the teaching there was top notch and highly prioritized by professors. I learned so much during those four years, and I would like to thank all of my professors, especially the Physics department, for their commit-

ment to teaching and dedication to their students' well-being. I would like to thank my Hamilton friends and problem set companions, including but not limited to Phill Milner, Kathryn Arpino, David Foster, James Greisler, Glenn Smith, Val Hanson, Will Bauder, Tom Morrell, Tom Nevers, Kye Lippold, Emily Anderer, Jessie Brown, Jennifer Strater, Marisa Warner, Juancho Hurtado, Colin Wheeler, Alex Hinton, Jessica Carroll, Pete Weitzmann, Kate Zavin, Chandra Thompson, Michael DiPasquale, Nick Kolesar, Dan Campbell, Xiyue Li, and Josh Meah. And, I would like to thank my various undergraduate research advisors, including George Shields, Gordon Jones, Brian Collett, Marc Baldo (from MIT), JudithAnn Hartman (from the USNA), and Ann Silversmith. You guys showed me how much fun research can be, and I certainly never would have gone to (or gotten into) graduate school without you.

There are a number of people I would like to thank who helped me get through the day to day slog of graduate school. I would like to thank my roommates: Thomas Bischof, Phill Milner, Sam Teitelbaum, Matthew Beyler, and Stephanie Chapman. Because we both worked together and lived together, I saw Tom for practically twelve hours a day over the last five years. Not only was he a great and valuable friend, but he was also a top-notch labmate and collaborator. So much of the work in this thesis is heavily influenced by conversations we had over the years, and Tom is the sort of guy you can always turn to for advice, troubleshooting help, or technical knowledge. He is an incredible person and I am so glad to have had the opportunity to know him. Phill has been one of my best friends since college. We first met our pre-freshman summer when we were in the same summer research program, and we have been living together ever since. I cannot believe we are about to part ways, and I am going to miss hanging out, our sense of camaraderie, and our late night conversations on the porch. I also would like to thank my gaming crew that helped me avoid flopping down on the couch for the whole weekend. Besides my roommates, this includes David Grimes, Miller Li, and Mik Minier. I am going to miss our borderline-psychopathic DnD adventures.

Finally, I would like to thank MIT Mental Health and Counseling, and specifically my therapist Audra Bartz. It is truly an unfortunate coincidence that graduate school happens to fall in your mid-20's, when many mental health problems begin to manifest themselves. As it turns out, they are not two great tastes that taste great together. I am so thankful that MIT offers free mental health services to students, I highly recommend them to everyone, and I feel so lucky to have been randomly assigned to Audra. She was so great, and I think we did a lot of really good work together. I am pretty sure I would not have been able to produce this thesis without her.

Contents

1 Introduction **23**

1.1 What Is So Great About the Nanoscale? 23

1.2 Semiconductor Nanocrystals are One of the Major Model Systems of Nanoscience. 27

1.3 The Simplicity and Flexibility of Nanocrystals Also Make Them Desirable Fluorophores for Optoelectronic Applications. 34

1.3.1 The Modern Nanocrystal Architecture 34

1.3.2 Select Applications of Semiconductor Nanocrystals 41

1.4 Single-Molecule Spectroscopy Has Been a Central Tool Characterizing the Fluorescence Properties of Nanocrystals and for Investigating their Fundamental Photophysics. 44

1.5 Summary of the Properties of NCs and the Physical Effects at Play . 58

1.5.1 Basic Fluorescence Properties 58

1.5.2 Inter-Nanocrystal and Device-Relevant Properties 64

1.5.3 Biologically-Relevant Properties 68

1.6 Thesis Overview 71

I Investigating the Local Environment of Semiconductor Nanocrystals **75**

2 Background on Spectral Diffusion in Nanocrystals at Low Temperature **77**

2.1 What We Know about Spectral Diffusion in Semiconductor Nanocrystals 80
2.2 The Problem 84
2.3 Improving Temporal Resolution Using Photon Correlation 86
2.4 Overview of Photon-Correlation Fourier Spectroscopy 91
2.5 How We Use the Spectral Correlation 97
2.6 The Mission 103

3 Theory Behind Photon-Correlation Fourier Spectroscopy 105
3.1 Derivation of Photon-Correlation Fourier Spectroscopy 105
3.1.1 Notation 106
3.1.2 Assumptions 108
3.1.3 Derivation 111
3.2 Chosing a Dither Waveform 122
3.2.1 Several Dither Examples 123
3.2.2 Properties of the Ideal Dither 128
3.3 Artifacts and Instrument Functions in PCFS 131
3.4 A Correction for Detector Dark Counts 140
3.5 What if the Emitter has Correlated Spectral and Intensity Fluctuations? 141
3.6 Interpreting the Spectral Correlation 143
3.6.1 The Wiener Model 145
3.6.2 The Poisson Model 146
3.6.3 Extracting Spectral Jump Kinetics 148
3.7 Interpreting the Spectral Autocorrelation 151

4 Combining PCFS with Conventional Spectroscopy 157
4.1 Temporal Limitations of PCFS 157
4.2 Deeper Problems Measuring Multi-Timescale Dynamics 159
4.3 A Compound Experiment Can Reveal the Entire Range of Rapid Spectral Dynamics. 160
4.4 Determining the Spectral Correlation from a Time Series of Integrated Spectra 161

4.4.1 Approximating the Spectral Correlation From the Average Correlation of Integrated Spectral Frames 163
4.4.2 Approximating the Spectral Correlation From the Histogram of Energy Shifts Between Frames 166

5 Investigation of Rapid Spectral Diffusion in Semiconductor Nanocrystals 169

5.1 Experimental Setup and Data Analysis 170
5.1.1 Optical Setup 170
5.1.2 The Sample 172
5.1.3 Experimental Parameters and Data Collection 174
5.1.4 Data Analysis 176
5.2 Results and Discussion 178
5.2.1 Rapid Spectral Dynamics Are a Discrete Process. 180
5.2.2 The Discrete Spectral Jumps Exhibit Correlated Effects Over Several Orders of Magnitude in Time. 181
5.2.3 Salient Features of Rapid Spectral Diffusion Revealed by the Spectral Correlation 183
5.2.4 The Intricate Interplay Between Spectral Diffusion Mechanisms 189
5.3 Summary of the Properties of Rapid Spectral Dynamics and Implications for its Physical Interpretation 194
5.3.1 What to Do with the Magnitude of Discrete Spectral Jumps . 198
5.4 Future Directions 203

II Investigating the Biexciton Quantum Yield of Semiconductor Nanocrystals at the Ensemble Level 207

6 Background on the Biexciton Quantum Yield of Semiconductor Nanocrystals 209

6.1 What Do We Know About Auger-Like Processes? 211
6.2 How Do We Measure Multiexciton Fluorescence? 213

6.3 The Plan 216
6.4 Conceptual Summary of the Solution-Phase $g^{(2)}$ Measurement 217

7 Theory Behind the Solution-Phase $g^{(2)}$ Experiment 227
7.1 Derivation of the Solution-Phase $g^{(2)}$ Experiment 227
7.1.1 Notation 227
7.1.2 Assumptions and Requirements 229
7.1.3 Derivation 232
7.2 Calculating the Uncertainty in the Measured Quantum Yield Ratio . 246
7.3 Balancing Average Occupation and Signal Intensity 249
7.4 Long Measurements and How to Make Them 250
7.5 Coping with Long Radiative Lifetimes 253

8 Measuring the Sample-Averaged Biexciton/Exciton Quantum Yield Ratio Using the Solution-Phase $g^{(2)}$ Experiment 255
8.1 Experimental Setup and Data Analysis 256
8.1.1 Optical Setup and Data Collection 256
8.1.2 Sample Preparation 257
8.1.3 Data Analysis 258
8.2 Results and Discussion 260
8.2.1 Experimental Verification of the Technique 260
8.2.2 Measuring the Quantum Yield Ratio of Several Synthetically-Underdeveloped Materials 262
8.2.3 Evaluating the Biexcitonic Properties Produced by a CdSe/CdS Shell Growth Procedure 265
8.3 Summary and Future Directions 267

III Developing Advanced Photon Correlation Experiments 269

9 Three Photon-Correlation Fourier Spectroscopy-Based Techniques 271

9.1 Raster-Scanned Photon-Correlation Fourier Spectroscopy 272
9.1.1 Motivation and Background 272
9.1.2 Experimental 273
9.1.3 Theory 274
9.1.4 Outlook 280
9.2 Pulsed-Excitation Photon-Correlation Fourier Spectroscopy 282
9.2.1 Motivation and Background 282
9.2.2 Experimental 283
9.2.3 Theory 283
9.2.4 Outlook 287
9.3 Heterodyne-Detection Photon-Correlation Fourier Spectroscopy . . . 288
9.3.1 Motivation and Background 288
9.3.2 Experimental 289
9.3.3 Theory 291
9.3.4 Outlook 298

List of Figures

1-1 The densities of states for nD confined semiconductors. 28

1-2 Fluorescence spectrum of a core-only CdSe nanocrystal at room temperature. 31

1-3 Schematic of the modern nanocrystal architecture. 35

1-4 Experimental setup of a standard blinking experiment. 46

1-5 Widefield image of CdSe/CdS nanocrystals in a dilute film. 48

1-6 Three ways of analyzing the single-nanocrystal fluorescence from pulsed excitation. 53

1-7 Three ways of analyzing the fluorescence from a solution-phase focal volume. 56

2-1 Time series of integrated spectra illustrating the different types of spectral dynamics. 84

2-2 Schematic of a conventional single-nanocrystal spectroscopy setup. . . 85

2-3 The inherent tradeoff of conventional single-nanocrystal spectroscopy. 86

2-4 Dual monochromator setup used by Sallen et al. 88

2-5 A single-point PCFS experiment can measure whether spectral dynamics have occured. 90

2-6 Interferometer output intensity given a Poissonian, monochromatic signal. 93

2-7 Intensity interferogram and spectral correlation of a Gaussian spectrum. 94

2-8 Evaluating the cross-correlation of the interferometer outputs with and without a dither. 95

2-9 Connection between the mathematical and conceptual representations of the spectral correlation. 98
2-10 The spectral correlation of three possible spectral diffusion mechanisms. 101

3-1 Instrument functions and bandwidth in PCFS 136
3-2 Shape of the detector afterpulsing feature 137
3-3 The effect of afterpulsing on the spectral correlation 138
3-4 Shape of the cross-detector afterpulsing feature 139
3-5 Interpretation of the amplitude of the non-diffused distribution in the spectral correlation 148
3-6 Simulations of the amplitude of the non-diffused distribution of the spectral correlation 150
3-7 The intrinsic spectrum cannot be recovered from the PCFS interferogram 154

4-1 Raw data from a compound PCFS/Camera experiment. 162

5-1 Schematic of the low temperature PCFS setup. 170
5-2 The Wiener and Poisson diffusion models. 179
5-3 A spectral correlation exhibiting discrete spectral diffusion. 180
5-4 Time series of integrated spectra collected during PCFS. 182
5-5 Data from a compound PCFS/Camera experiment. 184
5-6 Magnified image of rapid spectral dynamics in a time series of integrated spectra. 185
5-7 Extracting spectral diffusion kinetics from the spectral correlation. . . 186
5-8 Several low temperature nanocrystal spectral diffusion kinetics traces. 187
5-9 Three integrated spectra from the same nanocrystal. 190
5-10 Compound experiment data for two fluorescence positions of the same nanocrystal 191
5-11 Theoretical spectral shifts caused by charge trapping. 200
5-12 Theoretical spectral jump magnitudes for a charge trapping model. . 201
5-13 Theoretical spectral jump magnitudes for a ligand perturbation model. 202

6-1 Fluorescence saturation of nanocrystals at high excitation flux. 210
6-2 Number of pathways for detecting two photons from two single-photon emitters. 219
6-3 Number of pathways for detecting two photons from one two-photon emitter. 220
6-4 Number of pathways for detecting two photons from two two-photon emitters. 222
6-5 Annotated nanocrystal fluorescence correlation spectroscopy trace. . . 224

7-1 Correlation offset caused by drift during a long correlation measurement. 251
7-2 Time series of solution-phase correlation measurements. 252
7-3 Determining the side-peak value using FCS and phenomenological fits. 254

8-1 Experimental implementation of the solution-phase $g^{(2)}$ experiment. . 261
8-2 Concentration series validating the solution-phase $g^{(2)}$ theory. 263
8-3 Quantum yield ratios of three under-developed materials. 264
8-4 Quantum yield ratios of CdSe nanocrystals undergoing our recent CdS shell growth. 267

9-1 Theoretical proof-of-concept for the pulsed-PCFS experiment. 286
9-2 Schematic of the heterodyne-PCFS experimental setup. 290

List of Tables

1.1 Summary of the optical, electronic, and phyical properties of nanocrystals and the relevant parameters and phenomena that define them. . . 71

Chapter 1

Introduction

1.1 What Is So Great About the Nanoscale?

In the past 35 years, the field of nanoscience has been transformed from an obscure field of physics into one of the major areas of scientific publication. The website Stat-Nano.com reports that approximately 9% of the total number of scientific articles published in 2014 and indexed by the Web of Science database were nano-related. [1] This staggering wave of publication and cross-citation, and the proliferations of articles on the synthesis of whimsical materials such as organic nanofruit, [2] titanium dioxide sea-anenome nano-assemblies, [3] and hybrid organic/iron oxide nanodisco balls, [4] could lead the remaining 91% to label 'nano' a cynical buzzword used to glorify otherwise insignificant science. However, nanoscale materials have several general properties that make them unique compared to either their bulk or molecular analogues, including their high surface-to-area ratios; subtle, predictable, and controllable tunability; and greater functional specificity and structural complexity. These features have opened the door for tremendous scientific creativity and technological problem solving, and make them worthy of such extensive investigation.

Higher surface-to-volume ratio. Many applications of bulk metals and semiconductors rely on activity on the surface of the crystal. For instance, heterogeneous catalysts are often metallic crystals that promote reactions on specific surface atom or

crystal face, and optoelectronic devices rely on the migration of carriers to and from device interfaces. In both of these cases, decreasing the domain size or introducing porosity can increase performance by either increasing the density of active sites per unit catalyst [5] or decreasing the average diffusion length to the interface. [6, 7] The nanoscale represents the smallest crystal size that can maintain the beneficial structural properties of the bulk crystal.

The remarkably high surface-to-volume ratio of nanostructures can also give rise to conceptually interesting new physics. The theoretical framework of solid state physics is predicated on the idea that crystal lattices can be treated as infinitely large. [8] Surface states in bulk semiconductors can be explained using the effective mass theorem to confine the extent of the lattice, but they are not usually considered to be a major contributor to the overall behavior of the crystal. Although conventional tools such as the effective mass theorem or classical electromagnetic theory can be used to rationalize the simple optical physics of nanostructures like the core states of semiconductor nanocrystals [9] or the plasmon resonances of metallic nanoparticles, [10] poorly understood surface effects become essential for capturing their optical and electronic behavior as the size of crystals decrease. As we will discuss later, many of the nanoscale phenomena of active interest to researchers today appear to be strongly influenced by surface effects not captured by traditional theoretical paradigms.

Predictable, and controllable tunability. The nanoscale also offers an appealing compromise between the macroscopic and molecular regimes in terms of the degree of functional tunability. On one hand, the functional properties of molecular species can be hugely affected by relatively minor structural changes. One of the major causes of the widespread sucess and general applicability of Organic chemistry is that minor functionalization can spell the difference between the toxic and the tonic in small organic molecules. An additional methyl group can transform methanol from a blinding poison into a popular and relatively safe recreational drug, and the addition of a few fluorine groups to a prospective pharmaceutical compound can turn a biologically inert failure into a blockbuster. [11] This feature of small molecules

can unfortunately also make rational design extremely difficult. On the other hand, altering the size and shape of bulk materials hardly has any effect on their functional properties at all.

Nanostructures offer a compromise between these regimes by maintaining most of the properties of their bulk analogues and introducing the opportunity for subtle size and shape-dependent perturbation. In catalysis, the shape of catalytic nanoparticles has become an additional degree of freedom for further increasing the surface-to-area ratio of catalyst or by improving the accessiblity of various crystal faces. [12] The aforementioned titanium dioxide sea-anenome nano-assemblies, [3] for example, were shown to have higher catalytic activity of methylene blue degradation than more traditional, commercially available titanium dioxide nanocrystals. Moreover, in optical and electronic applications, the size and shape of nanostructures have been used to introduce controllable tunability in the energies and wavefunctions of their electronic states. Major electronic properties, such as the semiconductor band gap and metallic plasmon resonanance, can be affected by particle size and morphology on the nanoscale. [13, 14]

Greater functional specificity and structural complexity. Finally, scientists have often admired the elegant biochemical processes found in nature. Life as we know it is only possible if the chemical components of living cells have sufficient specificity that many different processes can occur simultaneously and independently within the cell. Nature accomplishes this using complicated nanoscale organic species (i.e. proteins, lipid membranes, carbohydrate structures, and nucleic acid polymers) capable of adopting highly specific conformations and often capable of multiple functional roles depending on their environment. Nanoscience can present the opportunity for humans to straight-forwardly and affordably design structures with similar complexity and specificity. For example, nanoscience has been put forward as a natural solution for improving the specificity of heterogeneous catalysts. Modern organometallic chemistry has achieved unparalleled catalytic specificity in metal ion catalysts like Palladium by shaping their steric and electronic properties using bulky multiden-

tate ligands. [15] Nanoparticle catalysts may be capable of similar specificity, while maintaining the high purity conversion and recoverability of heterogeneous catalysts. [16, 17]

Tremendous strides have also been made towards the development of complicated multifunctional heterostructures, especially for biological applications. Several notable examples of this can be found in the work of our lab alone. We have pioneered the development of effective and flexible bioimaging probes by assembling nanoparticles using multiple components that are independently responsible for optimized fluorescence, solubility, and targeting. [18] To add even more complex functionality, we have explored the packaging of these fluorescence probes in micelles with magnetic nanoparticles to produce powerful, micron-scale, dual fluorescence/MRI probes. [19] And, we have made significant progress on the design of biodegradable organic nanparticles for multi-stage delivery strategies for cancer therapeutics. [20, 21] One of the unique properties of tumors is their leaky peripheral vasculature and poorly formed internal vasculature. Large degradable nanoparticles are being designed to preferentially enter the leaky vasculature of tumors, to degrade in the vicinity of the tumor, and to release small therapeutic molecules that can effectively diffuse into the poorly-formed tumor vasculature. Such complex delivery mechanisms are only possible because of the flexible, modular design strategies that are uniquely feasible at the nanoscale.

As we have seen in this section, nanostructures can take many forms, from plasmonic materials, like gold nanoparticles, to semiconductor nanocrystals, to catalytic nanoparticles, to organic nanostructures like dendrimers or block co-polymers, to complex crystalline structures like metal-organic frameworks or zeolites. Despite their varied compositions and applications, they all benefit from a central set of properties that are unique to the nanoscale. They all have high surface-to-area ratios, predictable and controllable tunability, and the capacity for great functional specificity and structural complexity. In this thesis, we will focus on the semiconductor nanocrystal, one of the simplest model systems of nanoscience, which helped initially reveal the unique beneficial properties of the nanoscale and is, even now, emerging as a central player

in the technological applications of nanoscience.

1.2 Semiconductor Nanocrystals are One of the Major Model Systems of Nanoscience.

The history of semiconductor nanocrystals stretches back to the early 1970's, when researchers first began examining the physics of lower-dimensional semiconductor crystals. [22] It was clear that improvements in electronic performance (i.e. Moore's Law [23]) were critically tied to shrinking the size of integrated circuits, and therefore the size of their semiconductor device components. However, the size of semiconductor crystals were clearly bounded by the atomic scale and band theory predicted that semiconductor physics would begin to change even as their size approached the nanoscale exciton Bohr radius of the semiconductor crystals. It was critical to understand how confinement effects might affect semiconductor behavior, both to address the challenges of shrinking traditional device technolgies and to determine whether confinement might offer opportunities for novel applications.

The first investigations of quantum confinement were enabled by the development of molecular beam epitaxy as a building tool for semiconductor heterostructures. Thin layers of semiconductor on the order of nanometers could be deposited and sandwiched between two large bandgap substrates, producing a confined two-dimensional semiconducting layer with a step function density of states well-predicted by the well-established effective mass theorem (Figure 1-1(b)). [24–26] These "quantum wells" were found to exhibit a tantalizingly large array of novel physics, including thickness-tunable band gaps, highly-stabilized excitons, the quantum hall effect, and resonant tunneling effects. [27] As quantum wells began to mature as a material and find applications in lasers, optical modulators, and electronics in the 1980's, [28] improved fabrication techniques also enabled the creation of further confined systems, including two-dimensionally confined "quantum wires" and three-dimensionally confined "quantum dots."

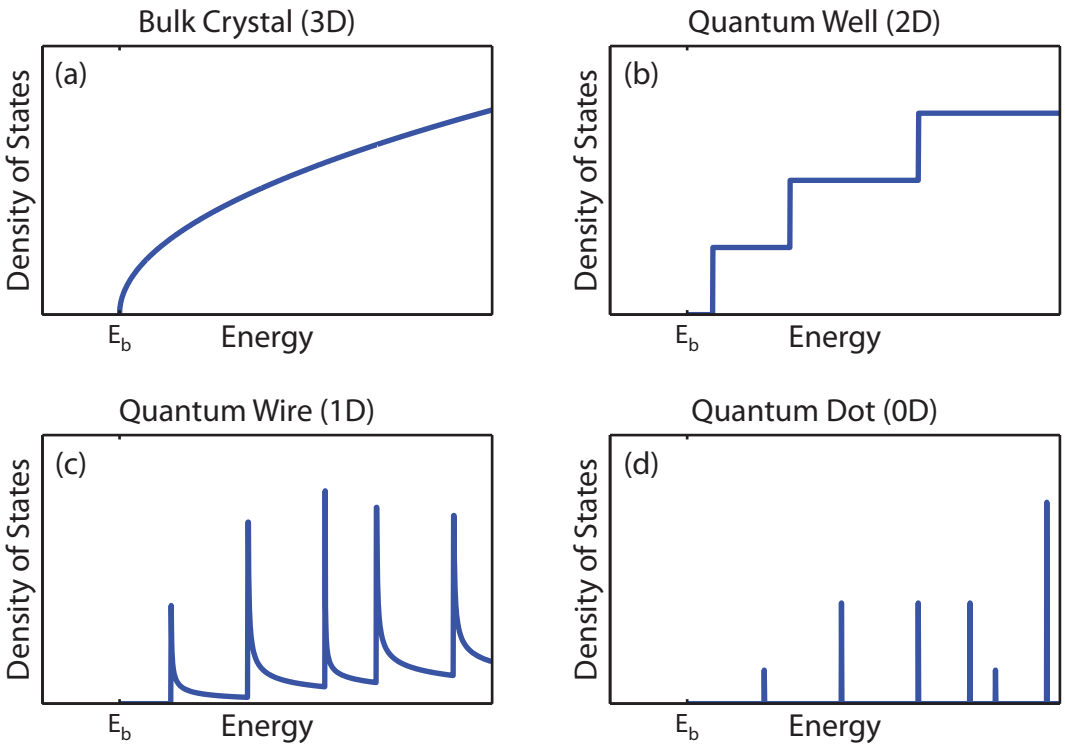

Figure 1-1: (a) The density of states of bulk semiconductors reflects the parabolic structure of the bands near the band edge. The effective mass theorem accurately captures the effect of quantum confinement in (b) one dimension, (c), two dimensions, and (d) three dimensions on the density of states near the band edge.

Early quantum dots took three major forms. Two of them were firmly rooted in the previous history of confined semiconductors. First, quantum dots could be fabricated by achieving three dimensional confinement via a fabrication-imposed potential. When a potential was applied across a quantum well that has been etched into a 10–25 nm island, Fermi-level pinning of the exposed walls of the quantum well produced a parabolic potential in the lateral dimension confining the exciton to the center of the well. [29] And second, quantum dots could also be produced via Stranski-Krastanov growth. [30] In this type of quantum dot, nanoscale islands of semiconductor spontaneously self-assembled upon deposition on a substrate because of strained surface interactions between the semiconductor and substrate, similar to how water droplets bead on the surface of a waxed car.[1] These islands can be covered with another insulating layer to stabilize and protect them, making them a highly robust and clean system for the investigation of quantum confinement.

But even before the advent of either lithographed or self-assembled quantum dots, a third synthetic technique had arisen out of the chemical community from the field of colloid science. In 1981, Ekimov et al. [31] discovered that monodisperse crystallites of CuCl could be precipitated in a glass matrix by heating a multicomponent silicate glass doped with copper and chlorine above the melting point of CuCl and cooling the glass after a well-defined period of time. When the average size of the CuCl particles was above 10 nm, their absorption spectrum matched that of bulk CuCl. But as the size of the particles decreased, their absorption features blue-shifted in accordance with predictions by the effective mass theorem. Similarly and independently,[2] Rossetti and Brus began investigating the size-dependent electronic properties of CdS nanocrystals that were colloidally precipitated in water. [36–38] These CdS particles, and other subsequently-developed II-VI nanocrystals such as CdSe and ZnS, imme-

[1] This is actually an example of Volmer-Weber growth where the sample's intermolecular forces clearly dominate surface adhesion. In practice, self-assembled quantum dots use Stranski-Krastanov growth, an intermediate growth regime where a thin wetted layer of sample is left amidst the beaded quantum dot structures.

[2] It is also worth noting the work of Henglein and co-workers in Germany, which also began in the early 1980's, focused on the synthesis and chemical investigation of novel and varied colloidal systems (such as ZnS, Cd_3P_2, Zn_3P_2, and Cd_3As_2, among others, [32–35]) and eventually spawned the modern-day groups of Horst Weller and Paul Mulvaney.

diately attracted interest in the community because of their solution-phase synthesis and tunable fluorescence. During the late 1980's and early 1990's, a flurry of synthetic development improved sample monodispersity via confined colloidal growth in reverse micelles and zeolites, [39–41] reduced surface effects and broadened solubility via ligand surface passivation, [42] and eventually culminated in the high quality, convenient, and reliable hot-injection synthesis proposed by Murray and Bawendi. [43]

The first efforts to understand the fundamental physics of nanocrystals essentially treated them exactly like the other two forms of quantum dots that were produced in the physics community, which is to say, like a flawless semiconductor crystal surrounded by an infinite potential barrier. In such a simple model representation, the electronic properties of nanocrystals could be predicted by straight-forward application of now-conventional solid state theory, including the effective mass theorem, [25] Luttinger-Kohn Hamiltonian, [44] and the magnetic field treatments of Pidgeon and Brown. [45] In fact, this line of theory turned out to be extraordinarily successful at predicting the basic optical properties of nanocrystals. Throughout the late 1980's and 1990's, the effective mass theorem treatment of semiconductor nanocrystals was built from the basic confinement of a parabolic band, [46] to include treatments of all of the semiconductor bands near the band gap, [47] and to account for shape anisotropy, [48] polarized emission, [49] and electron-hole exchange interactions. [50–52] This theory remains a mainstay of modern spectroscopic investigation today, and has been experimentally validated time and again with increasing rigor.[3] [53, 54]

But even from the beginning, it was understood experimentally that nanocrystals had distinct physical and electronic properties compared to other quantum dots and that they could not simply be treated as isolated chunks of perfect semiconductor. Due to a combination of their colloidal synthesis and small size compared to other quantum dots, the optical properties of nanocrystals were found to be highly defined by their surface structure and surface coordination. Fluorescence from the nanocrystal band edge was particularly sensitive to surface treatments, and could be

[3]The effective mass treatment of nanocrystals is summarized in a helpful review by Efros. [9]

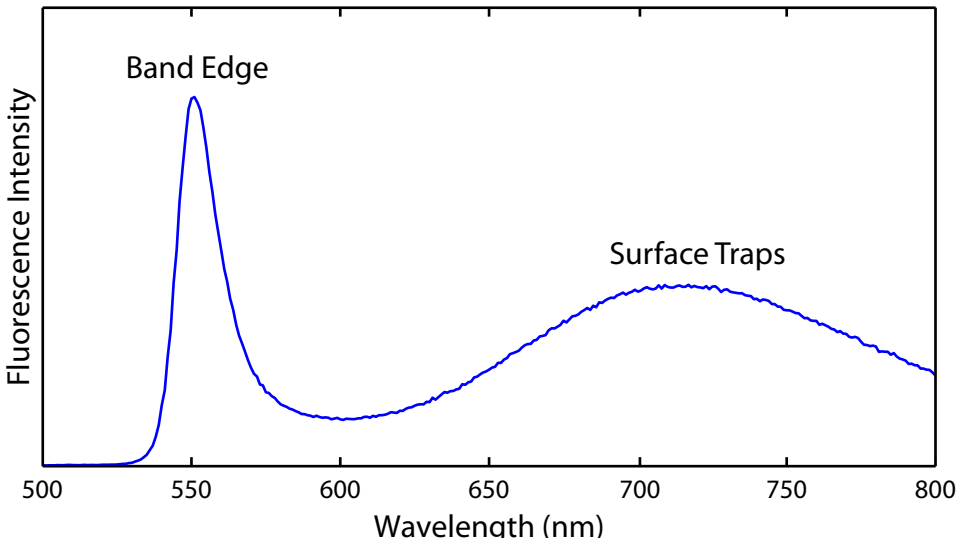

Figure 1-2: Early nanocrystals exhibited two major fluorescence features: a narrow feature caused by fluorescence from the core electronic states of the nanocrystal (i.e. band edge emission), and a broad, red-shifted feature caused by fluorescence from surface trap states.

greatly enhanced by the adsorption of certain weak bases such as tertiary amines to the nanocrystal surface. [55] In addition to the band edge fluorescence, nanocrystals also exhibited a strong, broad, red-shifted fluorescence feature attributed to intrinsic, mid-gap electronic "trap" states localized on the surface of the nanocrystal (Figure 1-2). [56–59] The poor quantum yield of trap fluorescence and anticorrelation with band edge emission suggested that surface trapping processes were the primary loss channel for quantum dot fluorescence. [60] Appropriate surface modification was essential for enhancing the overall quantum yield of nanocrystal samples and improving the suitability of nanocrystals for optoelectronic applications.

Later, when researchers began to investigate semiconductor nanocrystals using single-molecule spectroscopy, they discovered even more subtle and confounding fluorescence dynamics tied to surface effects. At the single-nanocrystal level, nanocrystal fluorescence was found to dramatically fluctuate in both intensity (i.e. fluorescence intermittancy or "blinking") and spectral position (i.e. spectral diffusion) on timescale ranging from milliseconds to sometimes hundreds of seconds. [61–64] These phenomena suggested that the nanocrystal surface was far more mutable than researchers had previously imagined and far more complex and important than existing micro-

scopic theories were prepared to accomodate. Theoretical models for the blinking phenomenon, for example, needed to hypothesize the existance of surface trap or mid-gap states with properties unsubstantiated by effective mass theory. [65–69] Although the fluorescence intermittancy and spectral diffusion of nanocrystal fluorescence have been exhaustively characterized experimentally and described phenomenologically, [70] the fundamental physics of nanocrystal surfaces and their core/surface interactions remains poorly understood and is still a topic of considerable investigation.

Several atomistic theories have been invoked to better capture the whole picture of nanocrystal photophysics. [71] Early atomistic models, including the tight-binding and semiempirical pseudopotential methods, adapted existing solid state theories to solve for nanocrystal electronic states given their precise atomic geometries (including ligand passivation sites). In the conventional tight-binding model, an infinitely large Hamiltonian matrix is (abstractly) assembled using a basis that is approximately given by the valence atomic orbitals of the atoms in the unit cell. [8] This approach can directly applied to nanocrystals by (actually) assembling a similar Hamiltonian for the exactly configuration of the thousands of atoms in a prospective nanocrystal. [72–75] Similarly, the semiempirical pseudopotential method of Wang and Zunger [76] was adapted from the empirical pseudopotential method developed in the late 1950s to account for the complicated potentials imposed on the valence electrons of bulk crystals by their core electrons and nuclei. [77] Again, the solution for nanocrystals was to build the exact same theoretical problem using a finite potential surface based on an exact nanocrystal geometry instead of the periodic unit cell potential. Both of these methods, especially the semiempirical pseudopotential method, have quantitatively improved on the theoretical results of the effective mass treatment, [78] and enabled the study of certain surface effects using theory within the solid state paradigm.

And finally, driven by improved computing resources in recent years, researchers have begun to use ab initio electronic structure calculations such as density functional theory to examine the finer electronic features of semiconductor nanocrystals. Modern simulations can accomodate on the order of one thousand atoms, which is beginning

to approach the size of the nanocrystals that are usually studied in the lab. It is important to note the anecdotal nature of current investigations; divergence from ideal atomic configurations (as undoubtedly occurs in actual polydisperse nanocrystal samples) has tended to produce wild, unpredictable, and possibly unphysical results.[4] But when the atomic geometry is careful chosen, density functional theory has been able to reproduce confinement effects; [80, 81] to reveal the character of surface traps and the energetic landscape of the surface ligands; [79, 82, 83] and even to provide practical insight into dynamic phenomena such as fluorescence intermittency [84], carrier transport, and other excited state processes. [85] As computing resources continue to improve, ab initio methods will probably continue to play an expanding role in the investigation of the basic physics of these nanoscale systems.

Despite the persistence of several deep, poorly understood phenomena, our current level of conceptual understanding of semiconductor nanocrystals is still miles ahead of what would have been thought possible when nanocrystals were first being synthesized in the 1980's. Early syntheses produced highly polydisperse samples with poor optical properties and non-uniform morphology, which made it difficult to determine their intrinsic properties. In the next section, we discuss the vast improvements in nanocrystal synthesis over recent decades and how they have produced modern samples with dramatically improved size monodispersity, morphological regularity, fluorescence quantum yield, and fluorescence resiliency. The result is an ideal model system for probing nanoscale physics: a system that is easy to probe experimentally via spectroscopy and that exhibits a broad array of physical phenomena that can be manifested in more complicated or less synthetically optimized nanoscale systems.

[4] An example procedure for establishing a geometry is carefully explained in Ref. [79]

1.3 The Simplicity and Flexibility of Nanocrystals Also Make Them Desirable Fluorophores for Optoelectronic Applications.

Compared to other quantum-confined semiconductors, nanocrystals have shown unique promise as fluorophores and electronic materials in many mainstream optoelectronic applications. Their chemical synthesis is inexpensive, results in macroscopic quantities of free nanocrystals (i.e. not bound to a deposition substrate), and could ultimately lend itself to production in conventional chemical reactors. Their band alignments are highly tunable via quantum confinement, making them versatile components in devices. And, they are high quality fluorophores with high quantum yields, emission wavelengths across the visible and infrared (400–5000 nm), narrow fluorescence linewidths, and better fluorescence durability than competing organic fluorophores. In this section, we will discuss the development of the modern nanocrystal and the current outlook on the applications of nanocrystals.

1.3.1 The Modern Nanocrystal Architecture

Since the initial hot injection synthesis that introduced a straight-forward route to monodisperse, high quality nanocrystal cores, several additional synthetic advancements have shaped an architectural paradigm for semiconductor nanocrystals that offers both high quality optical characteristics and flexible chemical and physical properties. A schematic representation of the modern nanocrystal is shown in Figure 1-3. We begin by discussing the development of each of these components of the nanocrystal architecture.

The core. The nanocrystal core is the architectural component that is primarily responsible for containing the exciton and for defining the major fluorescence properties of the nanostructure. Modern core synthesis relies on the same strategy as the initial hot injection procedure. A solution of metal precursor is prepared at high temper-

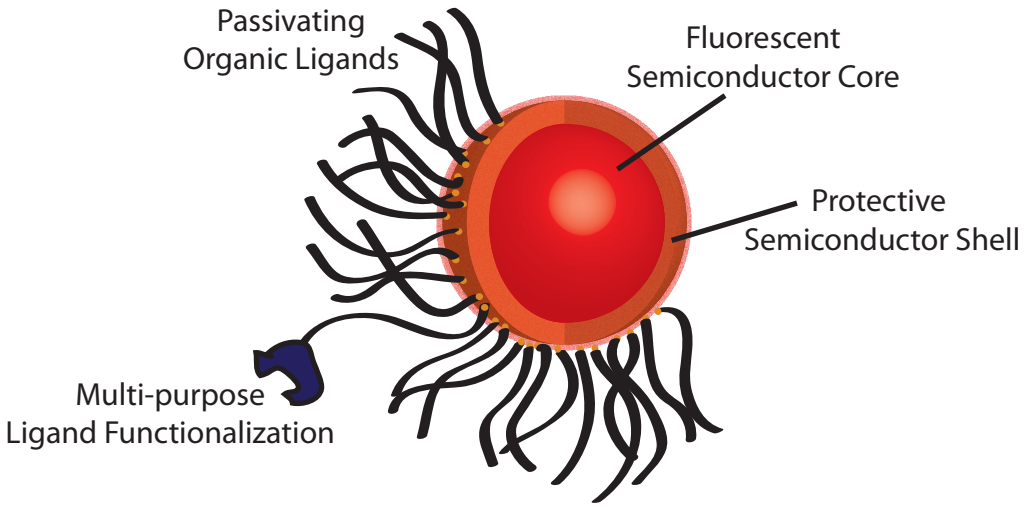

Figure 1-3: Schematic representation of the modern semiconductor nanocrystal architecture. Each component of the architecture can be tuned to shape the properties of the heterostructure, improving its overall fluorescence performance and flexible application.

ature in a solvent of long, coordinating aliphatic ligands. Then, the other precursor is rapidly injected to create a supersaturated solution. These precursors decompose to form monomer species, which nucleate at the time of injection to lower the solution concentration below supersaturation and prevent further nucleation. During the remainder of the synthesis, the existing particles continue to grow at roughly the same rate using the remainder of the monomer species and thereby maintain sample monodispersity. When the cores reach the desired size, the solution is cooled to arrest growth.

In addition to refinements in precursor selection and reaction conditions to reduce polydispersity, air-sensitivity, and reagent instability, toxicity, and pyrophoricity, [86] several qualitative synthetic advancements have been introduced to further adapt this general procedure. Major concerns have been raised concerning the scalability and reproduceability of a hot injection/arrested growth scheme because it relies on a small reaction volume that quickly homogenizes. Cao et al. [87] and Yang et al. [88] have proposed the replacement of hot injection with temperature-controlled precursor activation. In this way, a large solution of non-reactive precursors can be prepared ahead of time and the reaction initiated by raising the solution temperature to a

certain threshold. Similarly, Owen and coworkers [89, 90] have proposed replacing arrested growth with precisely engineered reaction conditions. They found that reaction conditions can be used to tune the total number of nucleated particles, resulting in monodisperse nanocrystal samples of predefined size if the reaction is allowed to proceed to completion. This innovation removes the guesswork of arrested growth schemes.

However, the most important advancement in core synthesis has been the synthetic development of a diverse array of material systems. Early synthetic efforts focused on CdSe nanocrystals because they naturally exhibited superior optical and physical properties and could be tuned to fluoresce across the visible (where obvious applications existed and where high quality detector technologies were available for characterization). Even now, the CdSe nanocrystal is by far the most-optimized synthesis. Nevertheless, nanocrystal synthesis using other materials has the potential to both reduce nanocrystal toxicity and broaden the range of fluorescence wavelengths. CdS and ZnSe nanocrystals have been explored as possible UV emitters; [91, 92] InP and Si nanocrystals have been explored as possible cadmium-free visible-emitting alternatives to CdSe; [93, 94] PbSe, PbS, InAs, and Cd_2As_3 nanocrystals have been explored as possible short-wave infrared-emitting phosphors between 1000–1500 nm; [95–97] and HgTe nanocrystals have been explored as a possible mid-infrared emitting phosphor between 3–12 µm. [98]

Because growth paradigms tend to be slightly different in these systems, their synthetic development has often required major changes to the synthetic procedure. III-V materials such as InAs and InP have proven particularly difficult to syntheisize with high monodispersity because the high reactivity of the available precursors makes it extremely difficult to separate the nucleation and growth stages of nanocrystal synthesis. [96, 99] Recent solutions have included engineering reagents with slowed conversion into nanocrystal precursors, and the use of continuous injection techniques to provide ample growth material without approaching precursor saturation. The synthesis of high quality, monodisperse cores made from InAs and other emerging materials remains an area of active research.

The shell. After it was known in the mid-1990's that surface trap states were severely affecting the fluorescence quantum yield of nanocrystals, several groups began experimenting with epitaxial shells as a way of isolating the fluorescent core electronic states from their environment. Early efforts focused on (Type I) wide-bandgap heterostructures such as CdSe/ZnS and CdSe/ZnSe core/shell nanocrystals to both block the carrier wavefunctions from penetrating to the nanocrystal surface and to approximate the infinite barrier used in effective mass treatments. [100–103] Although these heterostructures did indeed have dramatically better photostability and quantum yield, ZnSe shells were still prone to oxidation [101] and the CdSe/ZnS interface was subject to lattice strain that tended to produce imperfect epitaxial growth at (and therefore incomplete passivation of) the core/shell interface. [104]

It became clear that the highest priority for shell material selection should be epitaxial compatibility (i.e. the core and shell materials should share the same crystal structure and as close a lattice parameter as possible). For CdSe cores, the best epitaxial match was CdS. Visible (especially red) samples were quickly developed with quantum yields above 50 %, [105] and by using a combination of high reaction temperatures to anneal interfacial defects and unreactive precursors to slow shell growth, a recent synthesis by Chen et al. [106] has been developed that can produce particles with high monodispersity and quantum yields approaching 97 %. Nevertheless, one of the inherent problems associated with CdSe/CdS nanocrystals is that, unlike CdSe/ZnS nanocrystals, they are quasi-Type II heterostructures. Whereas the hole of the nanocrystal exciton is confined to the core, the closely-aligned conduction bands of CdSe and CdS allow the excited electron to delocalize throughout the heterostructure. CdSe/CdS nanocrystals are therefore still prone to surface-related fluorescence quenching mechanisms because their excited electrons still have access to the shell/ligand interface.

Two classes of solutions have been proposed to improve the photostability of CdSe/CdS heterostructures. First, special syntheses have been developed to grow CdS shells so thick that the core excited electron wavefunction does not extend all of the way to the surface. [107–109] These so-called "Giant" core/shell nanocrystals do not

exhibit phenomena related to surface interactions (specifically blinking), but their lack of electron confinement exclusively results in red-emitting particles and their decreased electron-hole overlap increases their radiative lifetime. And second, an additional thin ZnS shell has been grown on the surface of the CdS shell to block either carrier from reaching the surface. Both the distinct and graded alloy forms of the CdSe/CdS/ZnS heterostructure combine the beneficial interfacial properties of CdSe/CdS nanocrystals with the beneficial electronic properties of CdSe/ZnS nanocrystals. [110, 111]

Shell design for nanocrystal cores made from other materials has often been a more challenging problem. Certain materials such as InAs/CdSe, which features a Type I structure, identical crystal structure, and good matching of lattice parameters, readily lend themselves to high quality synthesis. [112, 113] However, PbSe and PbS nanocrystals in particular have been difficult materials for shell-growth syntheses because their rock salt crystal structures are not compatible with typical shell materials. In lieu of an appropriate natural shell material, the solution for the synthesis of core/shell materials has been to conduct partial cation exchange with cadmium to convert the outer layers of the nanocrystal to either CdSe or CdS. [114] Even though the rock salt crystal structure is not the most stable geometry for either of these shell materials, they have been shown to retain the original crystal structure of the core.

The ligands. The layer of ligands on the surface of nanocrystals fulfills two major roles: it passivates the surface of the nanocrystal, protecting it from oxidation and aggregation, and it defines the solubility characteristics of the nanocrystal. During synthesis, the nanocrystal surface is spontaneously coordinated by a combination of the large aliphatic solvent used for the high temperature synthesis and the original coordinating molecules of the metal precursors. Considerable research has been dedicated to understanding how surface coordination chemistry affects particle synthesis, characterizing the final native ligand surface, and understanding the connection between the physical surface coverage and the resulting optical passivation.

Early research on CdSe nanocrystal that were synthesized using technical grade

trioctylphosphine (TOP) as a solvent suggested that the post-synthesis nanocrystal surface was primarily passivated by a combination of TOP, which passivated the selenium surface atoms, and TOP oxide, which passivated the cadmium surface sites. [115] This appealing theory provided a clean explanation for the full passivation of the nanocrystal surface and suggested that the ligand layer was occupied exclusively with neutral L-type ligands that could be readily exchanged with different neutral ligands by adding an excess of the new ligand via Le Chatelier's principle. Nevertheless, problems with the conceptual picture quickly began to arise when theoretically sound ligand exchange procedures could not fully remove native ligands [116] and certain impurities in the (often old and/or degraded) technical grade TOP reagents were found to provide critical nanocrystal surface interactions. [117] Since these initial studies, nanocrystal surface passivation has been found to require a complex mixture of L-type ligands and X-type ligands, like phosphonic and phosphinic acids, [118–121] which provide charge balance in non-stoichiometric nanocrystals and stabilize the nanocrystal during synthesis. [122, 123] The judicious addition of different surface-binding species, can dramatically improve the optical properties of the nanocrystals, [124] and even tune the reactivity of different crystal faces to produce different nanocrystal shapes. [117, 125]

But whatever the precise surface properties are at the end of synthesis, it is guaranteed that the resulting nanocrystals will be coated with a thick fatty ligand layer that will increase interparticle spacing and restrict the nanocrystals to non-polar solvents. Ligand exchange has become an important tool for shaping how nanocrystals interact with their environment. For example, many optoelectronic devices require their optical materials to exhibit high carrier mobility. In these applications, native ligands are exchanged for much shorter ligands, such as ethylene dithiol, halides, or inorganic coordinating species, [126–128] which improve carrier mobility by allowing closer packing of nanocrystals in thick films and often decreasing the potential barrier between nanocrystals. Conversely, bioimaging applications require nanocrystals to be water soluble and non-toxic, and to exhibit stable fluorescence in aqueous environments. Here, native ligands are often exchanged by large multicoordinating polymers

like polyethylene glycol that provide water stability and form a permanent barrier between the semiconductor material and the biological environment. [129]

Despite the clear advances in ligand exchange, it remains a tricky and poorly-understood process. Ligand exchange procedures must address the presence of both L-type and X-type ligands, being careful to maintain charge balance on the nanocrystal surface and to choose new ligands whose affinities are neither too weak nor too strong. Ligand exchange with strictly neutral ligands such as amines or pyridines may not be able to remove the X-type binders without maintaining charge balance, [130] while strong or multidentate ligands like dihydrolipoic acid may cause etching of the nanocrystal surface, diminishing their optical properties and making them susceptible to degradation over time. [131] The development of broadly-applicable ligand exchange procedures that do not damage the nanocrystal surface and can reliably remove all of the different possible contributers to the native ligand shell remains an active area of research. [122, 130, 131]

Additional ligand functionalization. In some cases, nanocrystal applications can also benefit from even more specific environmental interactions. For example, chemical reactivity can be straight-forwardly programmed into the nanocrystal architecture by functionalizing the ligand molecules bound to the surface. After nanocrystal synthesis, these chemical handles can be used to attach the nanocrystal to other functional species. Notable examples of conjugation targets from our lab have included dye molecules to form nanocrystals capable of ratiometric pH-sensing via fluorescence resonance energy transfer, [132] and proteins to form fluorescent probes capable of biological labeling. [133] Nevertheless, early examples of nanocrystal conjugation produced particles that were too large to be useful in biological applications, relied on ligands with weak binding affinity to the nanocrystal surface, or were overly specific in scope.

Much of the recent work on nanocrystal functionalization has been dedicated to formulating general conjugation procedures that can be cleanly applied to any biological problem. Two key examples from our group are the development of the

polymeric imidazole ligand system (PIL) and the application of "click" chemistry in conjugation reactions. The PIL ligand provides a compact, stable, and versatile ligand surface by RAFT copolymerizing three types of monomer responsible for different functional roles. [18] Imidazole monomers are used as chemically inert nanocrystal binding sites, polyethylene glycol monomers are used to ensure aqueous solubility, and primary amine-containing monomers are included as conjugation handles that are unlikely to ineract with the nanocrystal surface. The ratios of these monomers during co-polymerization can be used to tune the strength of nanocrystal binding and the number of available amine groups. Then, "click" chemistry can provide a strategy for selective conjugation using the primary amines. [134] Because dienes are relatively rare in many natural compounts, converting the amine to norbornene, a Diels-Alder substrate, selectively targets a presynthesized diene site for conjugation.

1.3.2 Select Applications of Semiconductor Nanocrystals

The modular design paradigm of modern nanocrystals grants them unmatched flexibility to conform to the optical and electronic specifications of a wide array of different applications. Here, we focus on three major areas where nanocrystals can provide an advantage over established materials.

The first major area is in the field of semiconductor optoelectronic devices, where nanocrystals are used in lieu of bulk semiconductor films in solar cells, photodetectors, and light-emitting diodes. [135] In essence, the idea is that although nanocrystal films will have considerably lower carrier mobilities and higher trap state densities than bulk materials, they also feature several properties that may give their devices superior versatility. Nanocrystal researchers have particularly emphasized the solution processability of nanocrystals, which makes them compatible with inexpensive roll-to-roll printing device fabrication; their tunable direct bandgaps over mid-infrared, short-wave infrared, and visible wavelengths, which can produce devices with functionality outside normal device ranges and devices with precisely optimized RGB display properties; and their finely tunable band alignments that can be used to optimize device energetics. Among many examples, these properties have recently been

used to develop research-grade mid-infrared detectors, [136–138] modest performance research-grade solar cells (at 9.2 % power conversion efficiency), [139] and vivid and relatively efficient visible and infrared LEDs. [140, 141]

As emphasized by the caveats in the previous section, the real weakness of nanocrystals in optoelectronic devices has been their electronic properties. This is no surprise given that the optical properties of nanocrystals are defined by the confinement of the exciton. The second (and hugely successful) area of nanocrystal applications has been to use them as optical sensistizers in existing optoelectronic devices. These applications rely on both high quality fluorescence properties and the fact nanocrystals can absorb all light above their band edge. In this way, they can absorb any high energy photon and downshift it to a predefined fluorescence wavelength. The highest profile manifestation of this strategy has been in the recent generation of liquid crystal displays (LCDs). [142] LCDs work by illuminating the back of a screen with a bright white light and blocking the light at the pixel level to transmit an image. The image is projected in color by painting each pixel with an additional color filter that only transmits red, green, or blue. In this paradigm, color quality is dependent on the bandwidth of the color filter; if it is very narrow, it transmits a more vivid color with a lower brightness, and if it is very broad, it transmits a washed out color with a higher brightness. This tradeoff between brightness and color purity can be solved using a nanocrystal backlight, where the blue is provided by a gallium nitride LED [143] and the red and and green are provided by nanocrystals that downshift a fraction of the blue light. This "white" backlight is now actually composed of three narrow color bands that directly target the narrow color filters and allow for both high color purity and brightness. Similar downshifting schemes have also been used to sensitize infrared cameras to ultraviolet emission using infrared nanocrystals. [144–146]

The final major area of nanocrystal applications has been their use as fluorescent imaging agents, particularly in biological systems. Fluorescence microscopy has become a critical tool in modern biology because it is a zero to low background tool that can easily be multiplexed to image several species with different biological targeting. [147] As a result, a large library of visible fluorescent organic dyes and targeting strate-

gies have been developed for different biological problems, from fluorescent protein gene expression (the subject of the 2008 Nobel Prize in Chemistry) to direct attachment of dyes to biological species. Even so, nanocrystals offer a unique complement to this existing toolbox because, even though they are generally bulkier and exhibit longer fluorescence lifetimes than organic dyes, they are particularly resistant to photobleaching, exhibit narrower fluorescence linewidths, and can be straight-forwardly attached to biological species using the generalized strategy discussed in the previous section. These properties make them particularly suited to certain experiments like single-particle tracking that rely on stable and long-lasting fluorescence. [148]

But perhaps the greatest opportunity for nanocrystals in biological imaging is as a short-wave infrared fluorophore. Infrared imaging could be a particularly powerful tool for biology because the greater penetration depth of infrared light allows for non-invasive access deep within tissue. [149] With the recent rise (and deregulation) of sensitive InGaAs CCD cameras, it has finally become possible to implement this technique in practice. The emerging hurdle has been finding a high quality fluorophore in this wavelength regime. Infrared-emitting organic dyes are rare and have quantum yields $<0.1\,\%$, [150] carbon nanotubes are bulky and have quantum yields of $<1\,\%$, [151] and even small, high quality silver sulfide nanoparticles have quantum yields below $5\,\%$.[5] [153, 154] With these fluorescence specifications, infrared fluorescence spectroscopy cannot have the sensitivity and temporal resolution that biologists have come to expect from visible fluorescence spectroscopy. However, using the modern nanocrystal architectural paradigm, our group has been successful at translating most of the high quality optical properties of visible-emitting nanocrystals into the infrared. Current InAs/CdSe nanocrystals have quantum yields $\approx 30\,\%$, narrow fluorescence linewidths, and should eventually lend themselves to similar conjugation strategies as those explored earlier. [155]

[5] Note that many of the numbers in the given references are inflated by as much as an order of magnitude due to the controversy about the actual quantum yield of the organic dye IR-26, which is used in many of the dye-comparison quantum yield measurements. [150, 152]

1.4 Single-Molecule Spectroscopy Has Been a Central Tool Characterizing the Fluorescence Properties of Nanocrystals and for Investigating their Fundamental Photophysics.

Synthetic efforts to refine the optical properties of semiconductor nanocrystals for the applications discussed in the previous section have relied heavily on both convenient characterization techniques and an understanding of the underlying nanocrystal physics. A textbook example of this symbiotic relationship between synthetic development and basic physic research can be found in the low quantum yields of core-only nanocrystals. It was quickly established by the mid-1990's that the nanocrystal surface was the dominant source of the non-radiative recombination pathways that competed with fluorescence. The quantum yields of core-only nanocrystal samples were limited to ≈10%, [43] but could be improved to up to 50% by overcoating the cores with an epitaxial shell. [100–103] However, what was unclear at the time was whether the low quantum yields of core-only nanocrystals were inherent to the core-only nanocrystal architecture or whether they were caused by poor synthetic procedure, which produced particles with a wide distribution of intrinsic quantum yields. This was a critical question because if there were a sub-population of perfect core-only nanocrystals in each sample, it might be possible to devise an improved synthesis of these particles without resorting to heterostructure architectures at all.

This question was finally answered with the adoption of single-nanocrystal spectroscopy in the late 1990's, when Nirmal et al. [61] observed that the quantum yield of individual nanocrystals was universally dictated by time-dependent fluctuations between bright, highly-emissive nanocrystal states (later found to have near-unity quantum yield [156]) and dark, non-fluorescent states with near-zero quantum yield. Their finding suggested that there was no such thing as a perfect core-only nanocrystal with a permanent fully-passivated surface, and that perfect quantum yield samples could only be produced by eliminating the blinking phenomenon entirely. This insight

into the basic physics of nanocrystal fluorescence defined the nature of the problem for synthetic chemists and spurred the development of core/shell heterostructures. In fact, even today, when the publication of CdSe/CdS core/shell syntheses with near-unity quantum yield is practically commonplace, [106, 109, 111] the basic physics identified by single-nanocrystal spectroscopy still prevent the optimization of core-only nanocrystals, and the best core-only nanocrystal syntheses still cannot routinely produce samples with quantum yields above 50%. [86]

Since these early studies, single-nanocrystal spectroscopy has developed into a versatile class of experiments that has been used to characterize and inform on a broad array of nanocrystal properties. The reason for this versatility, much like the architecture of the nanocrystal itself, can be found in the modular structure of single-nanocrystal experiments. Figure 1-4 illustrates the experimental setup used in early investigations of fluorescence intermittancy. A single nanocrystal isolated on a substrate is illuminated with continuous wave excitation, and the resulting fluorescence is collected and binned over a given integration time to reveal how the fluorescence intensity changes over time. Despite the simplicity of this setup, it illustrates the basic structure shared by all single-nanocrystal experiments. Each type of single-molecule experiment must define an excitation type, microscope type, sample form, photon manipulation process, detector type, and data analysis technique. At each level, there are several options that can be used to shape and refine the type of information the experiment can reveal. In this section, we will briefly summarize the available options for designing a single-nanocrystal setup and discuss what types of information are accessible.[6]

Excitation Type. In addition to selecting an excitation wavelength well-matched to the sample's absorption spectrum and an excitation flux that will produce an optimal rate of excitation, an experiment designer must decide what type of laser to use for excitation.[7] The two major options are pulsed lasers, which excite the sample

[6]This discussion is heavily influenced by our recent review paper on the development of the single-nanocrystal spectroscopy toolbox. [157]

[7]In principle, excitation need not be strictly photoinduced. The sample could also be excited electrically, as in LEDs. Nevertheless, even in this case, it is still necessary to choose both an

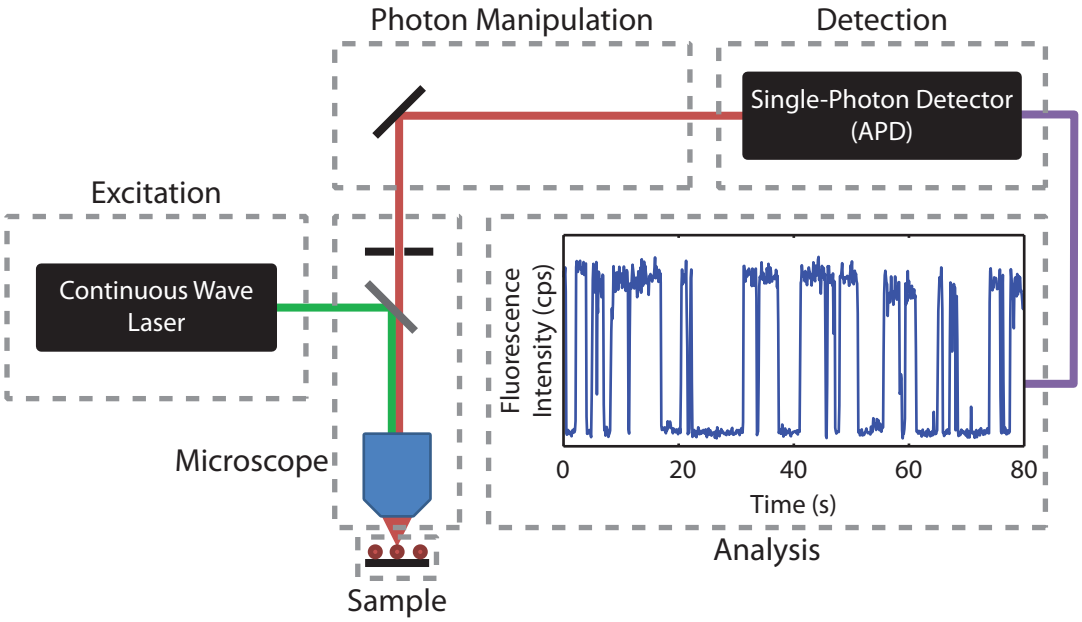

Figure 1-4: The experimental setup of the single-molecule setup used to investigate fluorescence intermittancy in single nanocrystals. This setup can be broken down into several modular experimental design segments that affect the nature of the information the experiment probes.

during short regularly-spaced intervals, or continuous-wave lasers, which constantly excites the sample with low intensity light. This decision usually hinges on whether it is important to know the precise time when absorption occured. If the experimenter is interested in measuring the time the nanocrystal spends in the excited state before fluorescence, pulsed excitation must be used. If not, continuous-wave excitation is preferable because its high duty cycle will provide a stronger fluorescence signal at a given excitation flux.

Microscope Type. The next decision is what kind of microscope to use to to deliver that excitation to the sample and collect the emission. Generally, single-nanocrystal experiments use epifluorescence microscopes, where excitation and fluorescence collection are accomplished by the same objective (as in Figure 1-4).[8] This

electrical voltage for excitation and whether to use a pulsed or continuous electrical waveform.

[8]Occasionally this is not feasible. Jensen and Bawendi's [158] nanocrystal optical trapping experiments, for example, initially used a transmission geometry to deliver two counter-propagating lasers: an infrared laser for optical trapping and a visible laser for optical excitation. This was ultimately found to be unneccesary because the two-photon cross section of the trapped nanocrystals

makes alignment much easier, delivers a tightly focused excitation spot with high excitation flux, and prevents the excitation of other nearby nanocrystals.

The two types of epifluorescence microscopes used in single-nanocrystal experiments are the widefield microscope, where the excitation source is defocused to excite a large area of the sample, and the confocal microscope, which excites a diffraction-limited area of the sample and focuses the collected fluorescence through a pinhole to ensure that the signal represents fluorescence from a single point on the sample. Widefield microscopy is generally used with a multi-element 2D array detector like a CCD camera to image multiple nanocrystals simultaneously (Figure 1-5), whereas confocal microscopy provides an ideal method for isolating the emission from an individual nanocrystal with minimal background or contribution from neighboring nanocrystals. As a side note, infrared confocal microscopes integrate elements from both types of microscopes. [159] Chromatic aberration in typical objectives will cause the visible excitation volume to be poorly overlapped with the infrared collection volume. These volumes can be overlapped to provide ideal confocal excitation by precisely defocusing the visible excitation source.

Sample Form. This is a relatively new parameter for single-nanocrystal experiments. Conventionally, single-nanocrystal samples have been fabricated by spin-coating a dilute solution of nanocrystals and polymer molecules (PMMA, etc.) on a glass or quartz substrate. [61] The result is a thin film of supporting polymer matrix embedded with a low concentration of spatially-distinguishable individual nanocrystals (As imaged in Figure 1-5). Film samples remain the default sample type for single-nanocrystal spectroscopy because they readily allow researchers to isolate fluorescence from a chosen nanocrystal on the film and to survey a large number of individual nanocrystals per sample. Nevertheless, there is plenty of room for innovation in thin film sample fabrication. Films may be embedded with electrodes or placed within magnets for electric and magnetic field studies, the temperature of films may be varied from 4–400 K for temperature-dependent studies, and films can even

was high enough to provide excitation with the infrared laser.

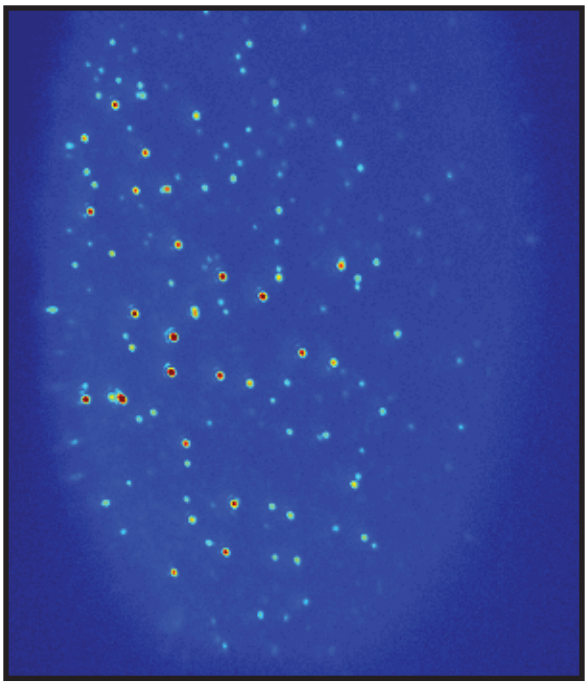

Figure 1-5: A widefield image of single CdSe/CdS nanocrystals dispersed in a PMMA film. The large blue oval is caused by film autofluorescence and/or laser scatter and represents the excitation area.

be integrated into flow cells to study chemical dynamics like cation exchange. [160]

Our group has also begun experimenting in recent years with solution-phase samples. In this strategy, a confocal microscope is used to collect emission from a small focal volume of a dilute solution of nanocrystals. Over the long term, the fluorescence collected from this volume will reflect the nanocrystal ensemble as a whole because of the free diffusion of particles into and out of the focal volume. But over the short term ($<$10 ms), the signal collected from the focal volume reflects the behavior of the relatively small number of nanocrystals in the focal volume at once. By analyzing the differences in the structure of the photon stream over short and long timescales, an experiment can be designed that measures the average properties of individual nanocrystals in the ensemble. Later, we will discuss several examples of this type of experiment that measure the average size of single nanocrystal, their average single-nanocrystal linewidth, and their average multi-exciton quantum yields.

Photon Manipulation. Once the fluorescence signal is collected by the microscope, it can be further manipulated using a variety of optical components to extract information about the photon stream emitted by the single or small collection of fluorophores. Although the simple setup shown in Figure 1-4 does not include any photonic signals processing, early experiments sometimes used linear polarizers to measure the polarization of fluorescence transitions or spectrometers to resolve the energy of each emitted photon. [161, 162] As single-molecule experiments have become more complicated, they have also integrated beamsplitters to split the fluorescence signal between multiple single-element detectors, and spectrally biased these channels using filters, interferometers, and duel monochromator setups. [157] With improvements in detector technologies, it has even become possible to split the photon stream to conduct multiple single-nanocrystal experiments at once. The opportunities for photonic signals processing in single-nanocrystal spectroscopy are endless, hampered only by limits on the total integration time imposed by setup or fluorophore stability, and human creativity and mathematical bravery.

Detector Type. There are two main types of detectors used for single-nanocrystal experiments. The first are multi-element array detectors, such as CCD cameras, that integrate a signal over a relatively long integration time ($>$50 ms). Their primary virtue is their parallelized detection scheme. Because they detect a large number of pixel values simultaneously, they can efficiently detect an image formed on the detector (like the widefield image in Figure 1-4) or a spectrum dispersed across the detector active area by a spectrometer, without the need for rastering or monochromator scanning. Spectrometer/CCD camera schemes have been instrumental in studying the fluorescence spectrum of single-nanocrystals, including their homogenoeous spectral features caused by fine structure splitting, multi-exciton emission, and exciton-vibrational coupling, and their spectral dynamics over timescales ranging from 50 ms to $>$100 s. [53] Their primary drawback is their temporal resolution, limited to the integration time of the frame. Photons detected during a frame's integration time are not time ordered, so spectral and intensity dynamics on timescales below the

integration time are time-averaged and obfuscated.

The second main type of detector that has been used for single-nanocrystal experiments is the Geiger mode single-element detector. These detectors, made from silicon avalanche photodiodes (APDs) for visible detection and either InGaAs APDs or superconducting nanowires single-photon detectors (SNSPDs) for infrared detection, detect the timing of individual emitted photons from the sample with sub-nanosecond precision. These detectors cannot inherently encode any spectral information about the photon or anything about its spatial origin, and the generally suffer from a variety of detection artifacts such as dead times and afterpulsing, but they can be used to time photon arrivals compared to laser excitation events and to investigate the fundamental statistical structure of sample's fluorescence via photon correlation. As we will see, a simple list of all of the photon arrival times on a detector during an experiment can be an incredibly insightful observable, especially when combined with the photon manipulation options discussed earlier.

We also note two particularly intriguing developing types of detectors that may prove exceptionally important for single-nanocrystal spectroscopy in years to come: transition edge sensors and array single-photon counters. The SNSPD is an example of a transition edge sensor run in Geiger mode. [163] A superconducting nanowire is cooled to slightly below its superconducting threshold, such that when a photon strikes it, it absorbs the heat from the photon and becomes resistive. The resistive transition registers as a spike in the current through the wire, which is read as a photon arrival if it surpasses a given threshold. However, in principle, the resistive spike could be analyzed further to yield the precise energy of the detected photon in addition to its arrival time. This strategy would produce a single-element detector with spectral resolution. Conversely, several APD manufacturers are working on fabricating arrays of APDs that could be used like a CCD camera in conjunction with a spectrometer. This strategy would produce a multi-element detector with high temporal resolution. Unfortunately, as of the time of writing, neither of these technologies have good enough specifications for application in single-nanocrystal spectroscopy.[9]

[9] If they are available at the time of reading, we are all very jealous.

Analysis Technique. After the fluorescence from the sample has been detected, the final step in the experiment is to compile the results into a physically-relevant observable for further analysis. These observables can be broadly fit into two categories: intensity-binned quantities and photon correlation functions.

Early work in single-nanocrystal spectroscopy focused on intensity-binning techniques. [61, 63] To form an intensity-binned observable, researchers discretized time into a series of integration periods and averaged the number of photon arrivals over each integration time to yield a fluorescence intensity. Key examples of this strategy are the blinking trace shown in Figure 1-4, the CCD camera image shown in Figure 1-5, and the single-nanocrystal spectrum shown in Figure 1-2. These observables tend to be simple to measure experimentally,[10] intuitive to interpret theoretically, and convenient for measuring long timescale fluorescence dynamics such as blinking and spectral diffusion ($>$100 ms).

Nevertheless, intensity-binning strategies suffer from two critical drawbacks. The use of an integration time necessarily sacrifices the inherent temporal resolution of the photon stream by averaging over many photon arrivals. Binning analyses have been known to produce artifacts when there are fluorescence dynamics on timescales faster than the integration time, including threshold artifacts in blinking traces and artificially broadened fluorescence lines in single-nanocrystal spectra. [64, 164] And, they cannot take advantage of the fact that single-photon detectors like APDs and SNSPDs precisely time the arrival of photons. A wealth of information should, in principle, be available by comparing the arrival times of photon to either the timing of their parent excitation pulses or the arrivial times of other photons.

Researchers began to access this photon timing information in single-nanocrystal experiments in the 2000's to early 2010's with two types of experiments. First, they began probing the population dynamics of the nanocrystal band edge using time-correlated single-photon counting (TCSPC). [156, 165] This experiment used the same experimental setup as in Figure 1-4, with two key differences. The continuous-wave

[10] A single nanocrystal's fluorescence intensity can usually be measure with an APD in approximately 50 ms, and its fluorescence spectrum can usually be measured using a CCD camera in approximately 1 s.

excitation was replaced with pulsed excitation to define the moment of absorption, and instead of analyzing the fluorescence intensity of the single nanocrystal by binning the photon arrivals over time, researchers compiled its photoluminescence (PL) decay trace by histogramming the temporal separation between each excitation pulse and the resulting fluorescence event (Figure 1-6(b)). Using TCSPC, researchers could directly measure the competition between non-radiative and radiative relaxation channels in single nanocrystals and characterize the variability and time-dependence in the duration of their excited states. These experiments revealed that, although the PL decay traces of nanocrystal samples were highly non-exponential,[11] the radiative rates were found to be surprisingly consistent within samples. The non-exponential behavior was found to be caused by temporal fluctuations in the non-radiative rate at the single-nanocrystal level, which were tied to single-nanocrystal blinking.

The second type of timing experiment was the biexciton quantum yield experiment. [166] It was well known in the mid-2000's that, like their bulk semiconductor crystal analogues, nanocrystals could accomodate multiple electron-hole pairs, simultaneously. However, due to their close proximity, these multiexcitons tended to recombine non-radiatively via Auger-like mechanisms rather than undergo multiple fluorescence events. The biexcitonic state, for example, had a markedly lower fluorescence quantum yield than the single excitonic state, and the overall quantum yield of a nanocrystal sample generally dropped precipitously when subjected to a higher excitation flux. This phenomenon could be probed experimentally using single-nanocrystal spectroscopy by histogramming the temporal separation τ between pairs of photons emitted from a nanocrystal excited by low flux pulsed illumination.

The resulting "antibunching" histogram in Figure 1-6(c) consists of multiple peaks spaced at the repetition rate of the laser because fluorescence events primarily occur shortly following excitation. Most of these peaks have the same intensity because they are caused by uncorrelated photon pairs produced by exciton fluorescence after

[11] Both radiative and non-radiative channels are regarded as first-order processes, which result in exponential decay traces in a homogeneous samples. Non-exponential behavior indicates subpopulations of nanocrystals caused by heterogeneity or time-dependence in the radiative or non-radiative rates.

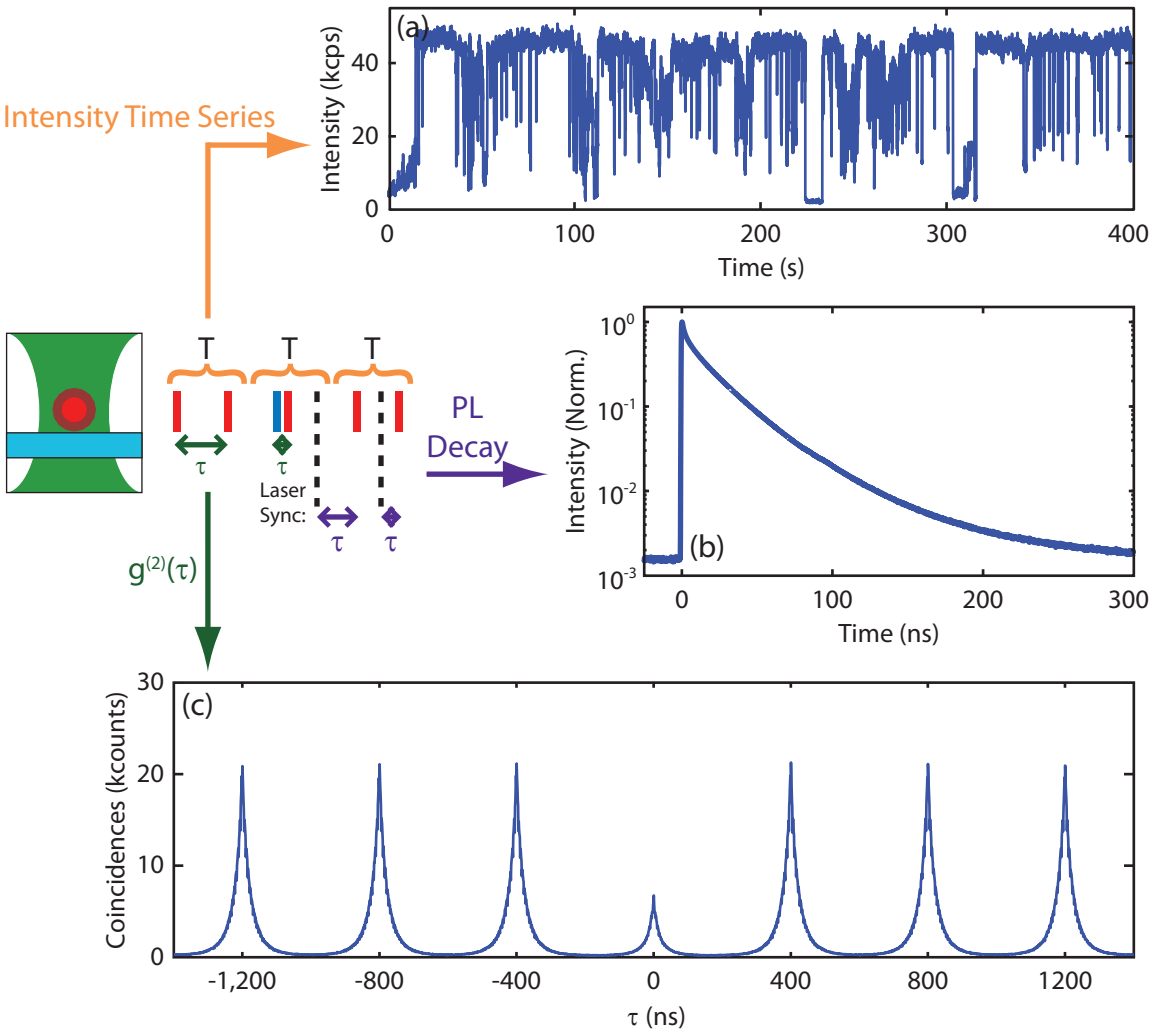

Figure 1-6: There are three major ways of analyzing the fluorescence intensity of single nanocrystals illuminated by pulsed excitation. Photon counts can be (a) binned over time to measure blinking dynamics, (b) timed with respect to the excitation pulse to measure the excited state dynamics, or (c) timed with respect to other photons to measure the biexciton quantum yield. Data collected by T.S. Bischof.

different excitation pulses. However, the center peak at $\tau = 0$ has special physical significance because it is necessarily caused by pairs of photons produced by the same excitation pulse. In order to register a count in the center peak, the nanocrystal must absorb two photons to form a biexciton and then undergo fluorescence twice, during both biexciton and exciton relaxation. As we will see later in the thesis, the ratio of the area center peak to the area of the side peaks directly reveal how much these Auger-like mechanisms adversely affect fluorescence.

Both TCSPC PL decays and the antibunching traces are un-normalized examples of the second-order cross-correlation function, defined by,

$$g^{(2)}_{a/b}(\tau) = \frac{\langle I_a(t) I_b(t+\tau) \rangle}{\langle I_a(t) \rangle \langle I_b(t+\tau) \rangle}, \tag{1.1}$$

where $I_{a/b}(t)$ is the intensity on channels a or b at time t, respectively, and $\langle \cdots \rangle$ denotes a time average over the integration time of the experiment. In TCSPC, one of the channels is the laser sync and one is the fluorescence signal, whereas in antibunching traces, both channels are the fluorescence signal. For discrete signals such as the photon stream or the excitation sync, Equation 1.1 is simply the histogram of the time separation between pairs of detection events between channels, normalized by the overall count rate on each channel. It is directly proportional to the conditional probability of detecting a count on channel b given that a count was already detected some time τ before on channel a. A value of unity is consistent with a random, uncorrelated stream of counts dictated by Poisson statistics. In contrast, a non-unity value reflects correlated structure in the signal, which may be tied to a variety of physical phenomena or experimental conditions.

A useful pedagogical example of correlation functions in action is fluorescence correlation spectroscopy (FCS). [167] In FCS, a confocal microscope is used to excite a small focal volume of fluorophores freely and rapidly diffusing in solution. Because the exchange of particles in the focal volume is rapid, the fluorescence intensity from the focal volume (at least over long timescales) appears to be steady and uninteresting (Figure 1-7(a)). However, although this intensity trace appears to be Poissonian,

we know that the underlying fluorophore diffusion physics ought to be encoded in the photon steam collected from the focal volume. On fast timescales, the fluorescence signal should consist of many rapid bursts of fluorescence as individual particles traverse the focal volume. This becomes evident when we generate a photon counting histogram (PCH) in Figure 1-7(b) using a very short integration time (on the order of the particle dwell time). [168, 169] The PCH illustrates that the fluorescence signal indeed exhibits more bright periods than would be expected from a Poissonian source,[12] and suggests that the underlying diffusion physics ought to be accessible. However, they do not appear to be encoded in the intensity-binned observable.

The answer is to analyze these short bursts of fluorescence using a correlation function. If we detect a photon, we know that there is a fluorophore in the focal volume, which means that there will be an enhanced conditional probability of detecting another photon for as long as the fluorophore remains in the focal volume. This point is reflected in the second-order correlation function measured in FCS (Figure 1-7(c)). FCS curves cleanly reveal several underlying sample parameters that are not obvious in the intensity-binned picture. The plateau value is inversely proportional to the average occupation of the focal volume, because if there are more particles in the focal volume, the first photon's revelation that there is at least one particle there is less insightful. The decay constant reveals the average dwell time of fluorophores in the focal volume, and can be tied to the fluorophore diffusion constant or hydrodynamic radius. And, the fluorescence lifetime of the fluorophores are even encoded in the FCS trace at short times in the form of an exponential rise from unity at $\tau = 0$ to the plateau value. This is because single fluorophores require a finite period of time to re-absorb and re-emit between fluorescence events. FCS illustrates the ease with which correlation analyses can reveal fast fluorescence dynamics that cannot be resolved using intensity-binning.

Unfortunately, correlation functions have the opposite drawback as intensity-

[12] This non-Poissonian distribution is actually caused by the shape of the focal volume. We sample a Poissonian distribution of particles in the focal volume during the integration times, but the each particle contributes a non-Poissonian distribution of photons depending on the possible trajectories it may take through the focal volume.

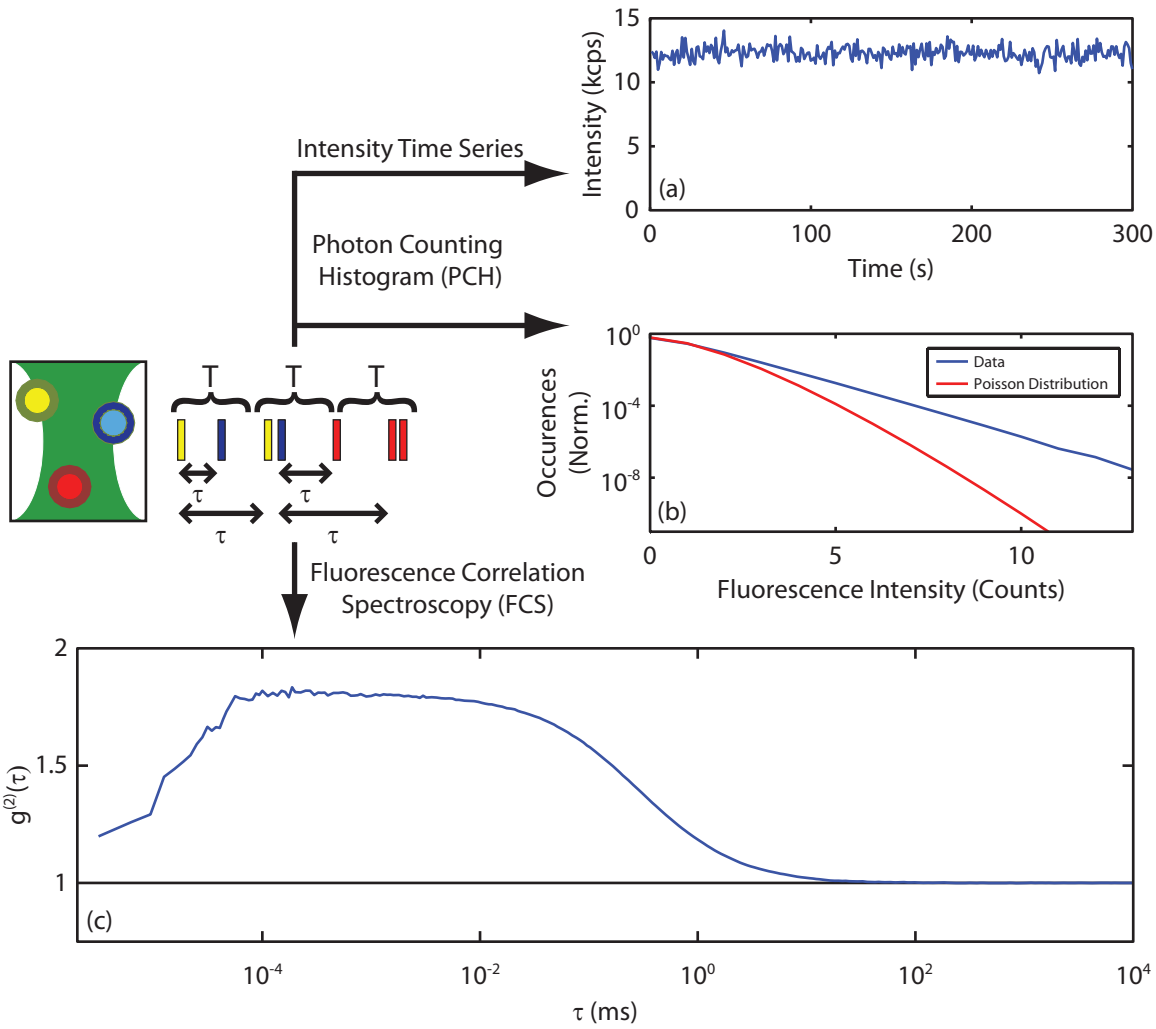

Figure 1-7: The fluorescence from a solution-phase focal volume can be analyzed using many techniques, including intensity binning techniques such as (a) intensity time series and (b) photon counting histograms (PCH). Nevertheless, only photon correlation methods such as (c) fluorescence correlation spectroscopy (FCS) give us direct access to both the particle occupation in the focal volume and the average dwell time of individual particles in the focal volume.

binning methods, in that their results can be obfuscated by long timescale dynamics. We have already discussed how rapid fluctuation in the lifetime of nanocrystals cause their PL decay to appear multi-exponential. [165] It has also been difficult to use intensity correlation functions to study the power law-distributed blinking dynamics of nanocrystals because they are strongly biased by long on- and off- events. [170] As a general rule, non-ergodic behavior in the sample fluorescence will cause the measured correlation function to be non-reproducible and difficult to analyze.

Several experiments have addressed this drawback by combining correlation and intensity-binning analyses. The prototypical example is the fluorescence lifetime-intensity distribution analysis used by Galland et al. [108, 171] to analyze blinking dynamics. In this treatment, they choose an integration time shorter than blinking dynamics, and use each integration time to simultaneously measure the fluorescence intensity and perform a rapid TCSPC lifetime measurement. With this information, they can clearly see how their correlation observable (the fluorescece lifetime) changes over time and varies alongside their intensity observable. Hybrid analyses such as these are now becoming commonplace in the literature as improving computing resources have allowed researchers to record all of the photon arrivals during an experiment in software for post-experimental analysis.[13] We will rely on hybrid analyses for most of the work presented here.

In this section, we have described the highly flexible modular structure of single-nanocrystal experiments and discussed many (but not all!) of the possible options that can be used to customize an experiment. These interchangeable experimental parts can be combined to measure a wide variety of different optical properties, both at the single nanocrystal level and averaged over the single nanocrystals in the sample. In the next section, we will summarize the important properties of nanocrystals, the basic physics that define them, and how they might be measured experimentally.

[13]Previously, poor computing resources often required observables to be compiled in hardware. Intensity-binning was accomplished using a DAQ counter card or CCD camera, and correlation functions were measured with dedicated correlation hardware or approximated with a start-stop TCSPC module.

1.5 Summary of the Properties of NCs and the Physical Effects at Play

Potential applications for semiconductor nanocrystals can have widely varying requirements for optimal performance. For instance, many device applications require the nanocrystal to be open and readily available to participate in carrier transport, where purely fluorescence applications generally require nanocrystals to be as isolated and protected from their environment as possible. Our ability to shape nanocrystals for different applications depends on our ability to characterize and precisely tune every aspect of nanocrystal performance. In this section, we review the important optical, electronic, and physical properties of nanocrystals and summarize them at the end in Table 1.1.

1.5.1 Basic Fluorescence Properties

Absorption Spectrum and Cross Section. The absorption spectrum of nanocrystal samples take a very simple and consistent form. It is defined on its red edge by the band gap energy, and increases with increasing absorption energy because of the degeneracy of higher lying transitions. There may be a small Stokes shift between the band-edge absorption and fluorescence, [172] and monodisperse samples may have featured absorption spectra near the band edge due to the discrete nature of the electronic states. The magnitude of the absorption cross-section is generally understood to scale with the amount of material in each nanocrystal, [173] and can be enhanced further by introducing shell material with the desired absorption spectrum. For example, an artificial Stokes shift has been introduced using thick-shelled CdSe/CdS heterostructures, where the CdS shell provides the lionshare of absorption and the CdSe core provides the fluorescence. [174]

The absorption spectrum of nanocrystals is generally characterized exclusively at the ensemble level using a UV-Vis, or higher-resolution/wider bandwidth absorption instrument (e.g. a Cary 5000 high performance UV-Vis-NIR spectrophotome-

ter). There has been some effort to measuring the absorption spectrum of single-nanocrystals, but these have not yet reached fruition due to the small absorption cross-section of individual nanocrystals. Without confining the excitation spot (using plasmonics, etc.), single-nanocrystals will generally absorb on the order of one in a million excitation photons.

Fluorescence Wavelength. The fluorescence wavelength of a nanocrystal sample is defined by its core material and the extent of quantum confinement (i.e. core size and the degree to which the band-edge wavefunction delocalizes into the shell). It is measured directly at the ensemble level using a steady state spectrofluorometer (e.g. a Horiba Fluoromax or infrared equivalent), and can be inferred from the absorption spectrum or from the physical size of the nanocrystals in the sample as measured by TEM and other sizing techniques. In principle, the fluorescence wavelength can be measured by surveying the fluorescence spectra of individual particles using single-nanocrystal spectroscopy, but this is a tedious and less accurate method for measuring an inherently ensemble quantity.

Fluorescence Linewidth. The fluorescence linewidth of a nanocrystal sample is a much easier quantity to measure than it is to understand. Whereas it is straightforwardly and accurately revealed in the ensemble fluorescence spectrum, it is defined by a confluence of different physical effects that can be difficult to characterize individually. The linewidth can be divided into four components: inhomogeneous broadening, homogeneous broadening, high excitation broadening, and spectral diffusion.

The degree of inhomogeneous broadening is defined by the polydispersity of the sample, which causes the consituent nanocrystals to have a distribution of different fluorescence wavelengths. Traditionally, changes in the overall ensemble linewidth during shell growth or in other contexts has been wholly attributed to changes in polydispersity. [175] While recent findings have contradicted the view that it is the sole effect at play, [176] it can be a significant source of line-broadening in poorly-optimized syntheses. Size polydispersity has often been characterized using TEM

and other sizing techniques, but single-nanocrystal spectroscopy provides a means for directly quantifying inhomogeneous broadening. This can be accomplished by surveying a large number of individual particles using conventional single-nanocrystal spectroscopy, or by using our recently-developed solution-phase photon-correlation Fourier spectroscopy (PCFS) measurement. [176, 177] The latter is a more convenient, higher signal-to-noise approach with much better ensemble statistics.

The extent of homogeneous broadening, or the average single-nanocrystal linewidth, has recently been identified as a major contributor to the ensemble linewidth that can change dramatically from one sample to the next. At room temperature, it is defined by a combination of the exciton fine structure, which determines the energy spacing between the band-edge bright states, and the strength of exciton-phonon coupling, which broadens the fluorescence linewidth from each of the bright state transitions. The exciton fine structure is dependent on a number of parameters, including the nanocrystal size (and electron-hole overlap), shape anisotropy, and core crystal structure, and can be measured using low-temperature single-nanocrystal spectroscopy. [53, 71] The exciton-phonon coupling strength also appears to depend on a number of architectural parameters and can be measured using ultrafast, Raman, or low-temperature single-nanocrystal spectroscopy. [176, 178] And, the average single-nanocrystal linewidth as a whole can be characterized in the same fashion as the degree of heterogeneous broadening, using either conventional single-nanocrystal spectroscopy or solution-phase PCFS.

There are also two additional sources of ensemble line-broadening that may be observed in specific circumstances. First, under very high excitation flux, nanocrystals can form higher-order excitons that emit from higher electronic states. [109, 179] This broadens the fluorescence lineshape, and has been used as an experimental handle for observing multiexciton recombination using conventional single-nanocrystal spectroscopy. And second, spectral diffusion and charging effects can cause power-dependent broadening of the single-nanocrystal lineshape due to dynamic Stark shifting of the band edge states and the red-shifted fluorescence of trion states, respectively. Spectral diffusion does not appear to be a significant source of line-broadening

in core/shell nanocrystals at room temperature, [177] but the large 5–25 meV binding energy of trion states could introduce significant width in the time-averaged or ensemble spectrum. [180–183] Both spectral diffusion and trion fluorescence have primarily been investigated using low temperature single-nanocrystal spectroscopy.

Fluorescence Quantum Yield. The overall efficiency of fluorescence is expressed by the quantum yield of the sample, given by the ratio of the number of photons emitted to the total number of photons absorbed. Almost all applications of nanocrystals require, or at least would benefit from, a high fluorescence quantum yield. It is measured at the ensemble level using an integrating sphere, or sometimes a dye comparison experiment. This is another observable where even though its ensemble characterization is well-established (although perhaps not always well-implemented), the actual physical story behind the observable is a bit unclear. At low excitation flux, it has generally been understood to be defined by a combination of fluorescence intermittancy (blinking) and the existence of a population of entirely non-fluorescent particles, either produced by the sample synthesis or quenched afterwards by oxidation. [184, 185] This understanding was shaped primarily by single-nanocrystal blinking experiments, which observed that the brightest blinking states of nanocrystal samples had very mono-exponential fluorescence PL decay traces with very consistent time constants, suggesting that these bright states had nearly unity quantum yield. [156]

Nevertheless, this picture is complicated by several factors. First, it is not easy to characterize the relative impacts of the blinking and non-emissive particles. Blinking behavior is highly non-ergodic and so the average on-fraction of nanocrystals can vary widely within samples, [185] and there is not a good characterization technique for identifying the fraction of the sample that is non-emissive. Second, more recent samples seem to indicate that more phenomena may be at play. Several groups have reported thick-shelled CdSe/CdS nanocrystal syntheses that appear to produce non-(or rarely-)blinking particles that have surprisingly low quantum yields ($\approx 50\%$). [107, 186] There is no clear reason why these syntheses should have a significant

fraction of non-emissive particles, but their PL decays are still very mono-exponential. And third, the quantum yield is highly excitation-flux dependent due to the power-dependence of blinking, and to the low quantum yields of multiexcitonic states. [187] It is usually not obvious, in practice, how a sample with a high quantum yield at low excitation flux (as measured by an integrating sphere or dye comparison) will perform under high flux conditions. We will discuss these effects in greater detail when discussing fluorescence saturation.

Fluorescence Lifetime. The fluorescence lifetime of nanocrystals can be measured by ensemble or single-nanocrystal time-correlated single-photon counting (TCSPC), and is most critically defined by the core material of the nanocrystal. Visible samples made from CdSe generally have lifetimes on the order of 30 ns, while infrared-emitting materials have lifetimes that are one or two orders of magnitude longer. [156, 188, 189] Once the core material is chosen, the lifetime of particles can be further increased by the degree of electron-hole overlap (i.e. nanocrystal size, heterostruture, and polarizability and susceptibility to local electric fields), but, apart from Type-II structures that explicitly separate the electron and hole, these effects rarely affect the lifetime by an order of magnitude. [190] The lifetime can have subtle effects on many areas of nanocrystal performance. It dictates the susceptibility of nanocrystal fluorescence to competing non-radiative pathways, can cause streaking effects in fast integration time applications such as confocal imaging, and plays an important role in defining the high-excitation flux properties of the sample.

Fluorescence Saturation. As we will discuss in more detail in Chapter 6, one of the current weaknesses in the fluorescence of nanocrystals is their decreased brightness under high flux excitation. This stems from a number of unrelated phenomena. First, blinking is an (at least partially) photoinduced process, which causes the on-fraction of nanocrystals to decrease with increasing excitation flux. [191] Second, nanocrystals have longer fluorescence lifetimes than many other fluorophores like organic dyes. This causes their single-exciton fluorescence to saturate at lower overall brightness.

[192] And finally, their multiexciton quantum yield is often an order of magnitude lower than their exciton quantum yield, which means that they are unable to reap this possible source of additional fluorescence inaccesible to many other competing fluorophores. [193]

Because of the confluence of these many physical phenomena, parsing the relative contributions to the saturation properties of nanocrystal samples can be an involved process. The total saturation properties of the sample can be measured by simply measuring the fluorescence intensity of a sample as a function of excitation flux. The effect of blinking on saturation can be measured by analyzing single-nanocrystal blinking traces, or by performing ensemble statistical aging experiments (see next section). The effect of the fluorescence lifetime can be measured using either single-nanocrystal or ensemble TCSPC. And the effect of the multiexciton quantum yield of saturation, the subject of Part II of this thesis, can be measured by a number of techniques, including single-nanocrystal and solution-phase antibunching measurements, single-nanocrystal saturation measurements, and transient PL and transient absorption measurements.

Fluorescence Longevity/Stability. Finally, one of the strengths of nanocrystals compared to other molecular and nanoscale fluorophores is their fluorescence longevity and stability under harsh optical conditions. The use of an epitaxial shell can confer optical stability to individual nanocrystals in air on the order of tens of minutes to hours under single-molecule excitation fluxes. Nevertheless, even with a protecting shell, nanocrystals are still prone to blinking and can still oxidize in air. Due to its non-ergodic dynamics and unbalanced on- and off-time distributions, blinking causes a photoinduced dimming of many nanocrystal samples on the order of hours to days. [184, 185] This dimming process can be characterized with statistical aging experiments, can be prevented by augmenting the blinking statistics of the sample, and is otherwise accounted for by assuming the sample will eventually reach the long-time equilibrium brightness. Oxidation has been harder to characterize because of its irreversible and somewhat unpredictable behavior, but it can be easily prevented by

packaging the nanocrystal sample in an air-free environment.

1.5.2 Inter-Nanocrystal and Device-Relevant Properties

So far, we have focused entirely on the optical properties of individual nanocrystals. However, if they are going to be incorporated into optoelectronic devices such as LEDs or solar cells, we also need to be concerned with how nanocrystals carriers will enter and leave the nanocrystals and how they will diffuse through a thick nanocrystal film. Several important characteristics of nanocrystal films have been identified as particularly important for nanocrystal optoelectronic applications.

Carrier Mobility. The carrier mobility describes how quickly carriers can diffuse through a nanocrystal film. Due to the quantum confinement of the carriers inside the nanocrystal, carriers can not freely flow through a film as they would in a bulk crystal. Instead, they must tunnel through the barrier between neighboring nanocrystals and essentially "hop" through the film one nanocrystal at a time. If this process is not efficient, carriers take longer to move through the film and become more susceptible to quenching mechanisms that lower device efficiency. The carrier mobility has been one of the most studied electronic observables because nanocrystal films have considerably lower mobility than most other electronic materials. It is generally measured indirectly using either field-effect transistor measurements or directly using time-of-flight measurements and is primarily dictated by nanocrystal parameters that affect the tunneling barrier between nanocrystals. Carrier mobility can be increased by decreasing the inter-nanocrystal spacing via shorter coordinating ligands, [194], by using smaller nanocrystals to increase the leakage of electronic wavefunction into the potential barrier, [195], or even by lowering the height of the potential barrier using inorganic ligand systems such as $Sn_2S_6^{4-}$. [127, 196, 197] The mobility is also affected by the longer range energetic properties of the film. Polydisperse or trap-rich films can cause carriers to get stuck in energetic wells throughout the film and slow the overall rate of carrier diffusion. [198]

Band Alignment. Despite the challenges of engineering high mobility, low trap density films, the flexibility of the nanocrystal architecture can allow for a careful tailoring of the electronic properties of the film that far exceeds conventional semiconductor crystals. Not only can the bandgap of the film be continuously tuned via the size of the constituent nanocrystals, but there is also some flexibility in affecting the alignment of the band gap with respect to the vacuum energy. Both ultraviolet photoelectron spectroscopy [199, 200] and voltammetry/scanning tunning spectroscopy [201] have been used to show that ligand exchange could be used to perturb the interfacial dipole between the nanocrystal and its environment and shift the absolute energy of the nanocrystal conduction and valance bands. This potential for band engineering was recently leveraged by Chuang et al. [202] to achieve then-record power conversion efficiencies for nanocrystal solar cells.

Majority Carrier and Carrier Density. Most current optoelectronic applications of nanocrystals simply use them as an absorption or emission layer in the device architecture, which is sandwiched between other materials, if necessary, to facilitate electron or hole injection/extraction. [203] In recent years, several groups have also begun focusing on controlling the carrier density of nanocrystal films to increase their conduction and controlling the identity of the majority carrier in the film for the fabrication of nanocrystal materials for p-n junctions. This effort has taken two forms. First, driven by observations that environmental changes could turn ostensibly ambipolar films into n- or p-type materials, [126, 204] several investigations have focused on using nanocrystal stoichiometry to intentionally fabricate inherently n- or p-type materials. These efforts have shown that n-type films can be reliably fabricated by increasing the ratio of cations in each nanocrystal, whereas p-type materials can be reliably fabricated by increasing the ratio of anions. [205–207] Second, other investigations have focused on incorporating heterovalent dopants into nanocrystals. [208] The principle behind this approach is identical to that of bulk semiconductor doping: by incorporating atoms with either more or fewer valance electrons into the crystal lattice, you can create a (relatively large) extrinsic population of carriers in the

conduction or valance bands. In fact, more broadly, advances in nanocrystal doping techniques have begun to drive the development of many novel nanocrystal materials with exotic electronic, [209] optical, [210] and magnetic properties. [211, 212]

Trap Density and Distribution. The trap state density is a particularly important property nanocrystal optoelectronic films because trap states provide deep energetic wells that confine free carriers. This both decreases overall carrier mobility by preventing them from reaching the interfaces of the device, and introduces sites for carrier recombination that directly impact the efficiency of the device. [213] In fact, although surface trap states are the primary cause of the poor fluorescence properties of core-only nanocrystals, they are even more destructive in close-packed films because they not only quench carriers generated in their nanocrystal, but also any carrier that diffuse through their nanocrystal on the way to a device interface. Even the extremely high mobility films made using the early inorganic ligand system by Kovalenko et al. [127] were susceptible to carrier quenching and did not produce high quality devices. The reduction of carrier traps in nanocrystal films has been a particularly difficult challenge because the reduction of carrier traps is, at least conventionally, at odds with the enhancement of carrier mobility. Researchers have had considerable success eliminating carrier trapping in nanocrystal samples for use as optical materials because they can effectively remove detrimental surface interactions using either thick or high-bandgap passivating shells. However, this approach cannot be used in nanocrystal films for optoelectronic interactions because the elimination of surface interactions inherently eliminates the ability for nanocrystal excitons and free carriers to diffuse between nanocrystals.

Decreasing the effect of surface traps without dramatically lowering carrier mobility has been a central area of research over the past five years. The trap profile of a nanocrystal film can be measured using a number of specialized techniques. For example, the total density of trapped carriers in a film can be measured using steady state photocurrent measurements, [213, 214] and the energy distribution of empty traps can be measured using time-resolved infrared spectroscopy, [128, 215] infrared

photoluminescence and electroluminescence spectroscopy, [216] or surface photovoltage spectroscopy. [217] These techniques have been used to identify several effective methods for reducing trap density that have actively improved the device performance of nanocrystal solar cells. For example, the use of halide surface passivation instead of previous inorganic ligand systems has been shown to both reduce the energetic depth of deep trap states and improve carrier mobility, [128] and oxidative treatments of the nanocrystal film has been shown to eliminate deep traps and increase the open-circuit voltage of nanocrystal solar cells. [218] Nevertheless, understanding the basic physics of carrier trapping and how it can affect carrier recombination and mobility, both generally and in specific devices, is still an active area of research that is important to the future prospects of nanocrystal optoelectronic devices. [219]

Multiple Exciton Generation. Finally, one of the major potential benefits of nanocrystals that have driven their development in solar cells is their potential for multiexciton generation. Conventional single-junction solar cells are theoretically limited to an efficiency of 30% because they rely on a single carrier extraction energy given by the bandgap of the material. [220] This Shockley-Queisser limit represents a tradeoff between absorption and energy extract, where a higher bandgap material would absorb less of the solar spectrum but extract more energy from each absorbed photon and a lower bandgap material would absorb more of the solar spectrum but extract less energy from each absorbed photon. However, in a material capable of multiple exciton generation, a single hot exciton can be converted to two near-band-edge excitons, thereby reducing thermalization losses and enabling theoretical efficiencies as high as 45%. [221] Multiple exciton generation (or carrier multiplication) is a rare event in bulk materials due to rapid thermalization and weak Coulomb interactions, but early predictions suggested that nanocrystals might have slower thermalization rates due to the lower density of phonon modes and enhanced Auger interactions due to their quantum confinement.

Unfortunately, except in very specific cases where the nanocrystal architecture is engineered to prevent thermalization, [222] nanocrystals thermalization rates have

been found to be on par with the bulk because of additional Auger-like thermalization pathways that can help excited carriers bridge electronic energy gaps without phonon-coupling. [223, 224] As a result, when the multiple exciton generation efficiency has been measured in nanocrystals by using transient photoluminescence or transient absorption experiments to probe the magnitude of the biexciton feature as a function of excitation wavelength (under stirred conditions),[14] nanocrystals have exhibited only modest improvements compared to their bulk analogues. [225, 226] The main problem has been that even though the Auger interaction does increase with increasing confinement, so does the excitonic band gap. This means that the absorbed photons capable of generating multiple excitons are pushed to higher wavelengths that are less represented by the solar spectrum and has led to only modest improvements in the efficiency of nanocrystal devices. [227] Multiple exciton generation is still an active area of research in some corners and may still ultimately be useful for increasing the efficiency of nanocrystal solar cells, [228] but as Nair et al. [221] emphasizes, this potential is mainly on the basis of identifying a new nanocrystal material whose bulk crystal has a high carrier multiplication yield at solar-relevant wavelengths and a very small bandgap that can be can be tuned via confinement to the optimal value. They recommended InSb as such a prospective material.

1.5.3 Biologically-Relevant Properties

There are also several important properties regarding how nanocrystals physically interact with their environment. These are particularly critical in biological applications of nanocrystals, where nanocrystals are required to be small, non-perturbative, targetable probes both in vitro and in vivo, but many of these physical properties will also be relevant in other nanocrystal applications (especially solubility).

[14] The multiple exciton generation efficiency could also be measured using a similar principle by measuring center-to-side peak area ratio of an antibunching experiment as a function of excitation wavelength. The generation of multiple excitons would break the absorption Poisson distribution and cause the peak area to increase with excitation wavelength.

Overall Size. The physical size of the individual nanocrystals, including their core, shell, and ligands, can be an important parameter in many nanocrystal applications because it determines the overall packing density of fluorophores in the physical sample. It takes on even more importance in biological applications because the size of the particles also affects their ability to diffuse into confined spaces, [229] their clearance in vivo, [230, 231] and the overall inertial perturbation that they have on their labeled substrates. In solution-phase work (including biological applications), the relevant size metric is the hydrodynamic radius, which can be measured using either fluorescence correlation spectroscopy or dynamic light scattering, [232] and takes into account both the size of the nanocrystal architecture and solvent interactions, which can increase the effective size of nanocrystals. The hydrodynamic diameter can be reduced by either reducing the core/shell/ligand footprint of the nanocrystals or, more critically, by reducing solvent interactions by engineering neutral particles using either neutral or zwitterionic ligands. [233] Choi et al. [230] reported that serum proteins could adsorb to their charged nanocrystals in vivo, increasing their hydrodynamic radius by almost 15 nm.

Solubility. Obviously, in all applications, it is important for nanocrystals to be soluble in the solution used to produce the final nanocrystal component. But whereas many device applications may use organic solvents that are inherently compatible with nanocrystals such as toluene or hexanes to fabricate their nanocrystal films, nanocrystals used for biological applications must be engineered to be soluble in aqueous media. This means that the native ligands of these nanocrystals must necessarily be exchanged with some other ligand that can provide water solubility. Considerable research has been dedicated to designing ligand exchange procedures that maintain the optical properties of the nanocrystal, provide good biocompatibility, and enable the binding specificity discussed in the next section. Successful ligand systems have generally provided water solubility using either poly-(ethylene glycol) chains or zwitterionic functionalization, and provided stable anchoring to the nanocrystal surface using multidentate coordinating structures such as dihydrolipoic acid or polyimidi-

zoles. [18, 234–236]

Binding Specificity. Another important physical property for targeting applications is the binding specificity of the nanocrystal labels. This property can be broken down into two distinct components: how well the labels bind to their targets and how poorly the labels bind to anything else. Desirable binding affinity is usually built into the nanocrystal architecture by incorporating conjugation sites in the ligand systems discussed in the previous section. These conjugation groups, either simple functional groups like amines, thiols, or carboxylic acids or more complicated groups like the norbornene group with more reactive specificity and poor affinity for the nanocrystal surface, [113, 134, 237] can be directly attached to biological species such as proteins. [133] Low non-specific binding is achieved using the same strategies used to achieve smaller properties, namely by ensuring that the surface of the nanocrystal is charge neutral and not chemically reactive.

Cytotoxicity (and Toxicity). There has been very reasonable concern about the toxicity of nanomaterials in general, and in particular of heavy metal-containing materials like most nanocrystals. [238] It is therefore very unlikely that nanocrystals will be approved for use in humans in the near or intermediate future, and even outside of human applications, toxicity can still play a major role in defining the suitability of nanocrystals for various applications. In device applications, regulatory agencies have been worried about the potential for human contact with the nanocrystal materials and the potential for heavy metal pollution after device disposal. Even if the nanocrystal material is well-isolated, high tech trash has become a major source of heavy metal contamination in developing countries. [239] As a result, display applications of the synthetically-mature cadmium-containing nanocrystals have had to contend with possible regulation via the European RoHS directive that regulates the use of hazardous substances in electronics. [240] In biological applications, because the short-term nature of imaging experiments, the concern is simply to avoid the possibility of acute toxicity or cytotoxicity that may interrupt experiments or per-

Fluorescence Properties	Relevant Physical Parameters and Phenomena
Absorption Spectrum	Core size, shell absorption
Fluorescence Wavelength	Core material and size, delocalization into shell
Fluorescence Linewidth	Exciton-phonon coupling, exciton fine structure, spectral diffusion/charging, polydispersity
Fluorescence Quantum Yield	Blinking, fraction of non-fluorescent particles, various non-radiative processes, multiexcitons
Fluorescence Lifetime	Core material, electron-hole overlap
Fluorescence Saturation	Fluorescence lifetime, multiexciton quantum yield blinking
Fluorescence Stability	Blinking, surface oxidation
Device Properties	**Relevant Physical Parameters and Phenomena**
Carrier Mobility	Inter-particle potential (shell thickness, ligand), particle spacing, trap density
Film Trap Density	Surface passivation
Majority Carrier/Carrier Density	Dopant ions and concentration, nanocrystal stoichiometry
Carrier Multiplication Yield	core material, carrier confinement
Biological Properties	**Relevant Physical Parameters and Phenomena**
Overall Size	core/shell size, ligand bulk
Solubility	ligand functionalization
Binding Specificity	particle charge, ligand functionalization
Cytotoxicity	core/shell isolation

Table 1.1: Summary of the optical, electronic, and phyical properties of nanocrystals and the relevant parameters and phenomena that define them.

turb the biological activity being studied. The consensus suggests that nanocrystal biocompatibility can be achieved regardless of core or shell material by ensuring that the ligand coverage on the surface of the nanocrystal is permanent and as complete as possible. [241] For example, Weilnau et al. [242] reported that their ZnS nanocrystals were initially biologically compatible, but became progressively more cytotoxic over time as their nanocrystals were kept in suspension in a phosphate-buffered saline solution.

1.6 Thesis Overview

In this introductory chapter, we discussed how the scientific value of semiconductor nanocrystals lies is two major directions, both as a historically important and con-

ceptually critical model system for the investigation of the fundamental physics that defines many nanoscale systems and as a well-optimized and highly flexible optical and electronic material that may be useful for a broad spectrum of applications. We also identified single-nanocrystal spectroscopy as a powerful and versatile tool for both the elucidation of nanocrystal physics and the the characterization of many of the poorly-understood properties critical for optimizing nanocrystals for applications. This thesis will present two investigations that illustrate how single-nanocrystal spectroscopy can provide insight into practically any aspect of the optical behavior of nanocrystals.

In Part I, we illustrate the power of single-nanocrystal spectroscopy as a tool for the elucidation of basic physics by investigating the rapid spectral diffusion of individual nanocrystals at cryogenic temperatures. This phenomenon has so far evaded our understanding because of its widely variable behavior within nanocrystal samples and its unique requirements for high spectral and temporal resolution. We will show that photon-correlation Fourier spectroscopy (PCFS), a recently-developed single-nanocrystal technique that combines interferometry with photon correlation analysis, can give us all of the necessary tools to characterize these spectral dynamics and to assemble a complete picture of the phenomenon in individual nanocrystals. In Chapter 2, we review the current understanding of rapid spectral diffusion and discussing its theoretical connection to our broader understanding of nanocrystals, we discuss the experimental difficulties that have interfered with previous investigations of rapid spectral diffusion, and we provide a conceptual explanation of how the PCFS experiment works. In Chapters 3 and 4, we work through the theoretical and mathematical details of PCFS, including possible artifacts and sources of systematic error, and how PCFS can be combined with conventional single-nanocrystal spectroscopy to study the full range of spectral dynamics. Then, in Chapter 5, we present the experimental details of our investigation, our results, a discussion of what information can be extracted from these results, and their physical consequences. This part consists of the work presented by Beyler et al. [243]

In Part II, we illustrate the power of single-nanocrystal spectroscopy as a tool

for characterizing the optical properties of nanocrystals by devising a solution-phase antibunching experiment to measure the ensemble-averaged biexciton quantum yield of nanocrystal samples. As we discussed earlier, the low biexciton quantum yield of nanocrystals is one of the primary characteristics that hinder their optical performance under high excitation flux conditions. Our experiment provides a much-needed tool for quickly and reliably assessing the results of synthesis that should aid in the synthetic optimization of biexciton fluorescence. In Chapter 6, we present an overview of previous experimental tools for measuring the biexciton quantum yield of nanocrystal samples and provide a conceptual explanation of our experiment. In Chapter 7, we derive the mathematical result of the experiment and discuss several possible artifacts that may affect the measurement. Then, in Chapter 8, we present the experimental details of our investigation, an experimental verification of the technique, and two small investigations that demonstrate the utility of the experiment. This part consists of the work presented by Beyler et al. [244]

And finally, in Part III (Chapter 9), we illustrate the vast potential for the future development of single-nanocrystal spectroscopy experiments by presenting three possible modifications to the conventional PCFS experiment that could enhance the capabilities of our current single-nanocrystal toolbox. For each variant, we will discuss the potential need for innovation, derive the experimental result, and present my personal opinion and outlook with regards to the experiment.

Part I

Investigating the Local Environment of Semiconductor Nanocrystals

Chapter 2

Background on Spectral Diffusion in Nanocrystals at Low Temperature

One of the most fundamental and enduring challenges in the elucidation of basic nanocrystal physics has been how to conceptualize the surface and immediate local environment of the nanocrystal. In Chapter 1, we discussed how uncertainties about how to treat the nanocrystal surface have complicated the development of accurate and insightful electronic structure models for these systems. It has been equally tricky to understand the chemistry and dynamics of the surface. Many dynamic processes, including ligand exchange, carrier trapping, and oxidation, have real and tangible effects on the optical properties of the nanocrystal, and control over surface chemistry and passivation is necessary for the synthesis of high quality nanocrystals. The ongoing challenge underlying the study of many of these problems has been that it is difficult to study the nanocrystal surface directly. Surface electronic states are not readily addressable using spectroscopy because of their low oscillator strength transitions compared to the core states, the concentration of surface atoms and surface-bound ligands is usually very low in the overall nanocrystal sample, and the nanocrystal surface itself is heterogeneous and varies between nanocrystals. Nevertheless, recent innovations in experimental techniques have allowed researchers to begin to tackle many of the myriad of surface-related processes.

Electron-mediated characterization techniques such as transmission electron mi-

croscopy (TEM) have been the experimental workhorse for investigating the structure of the semiconductor portion of the nanocrystal because they have the superior spatial resolution required to resolve the shape of nanoscale objects. Although TEM has been used for decades to characterize the degree of shape and size polydispersity in nanocrystal samples, [43] recent advances in high resolution TEM have achieved atomic-level resolution and opened the door for in-depth investigations of the physical structures of nanocrystals. In the last four or five years, TEM investigations have directly measured the lattice strain caused by overcoating individual CdSe nanocrystals with ZnS, [245] mapped the shape of the core/shell interface in PbSe/CdSe nanocrystals synthesized using partial cation exchange, [246, 247] conclusively demonstrated the oriented attachment of specific PbSe crystal faces to form ordered superlattices, [248] proven the atomic flatness of CdSe nanoplatelets and identified the physical origin of their helical folded structure, [249, 250] revealed the surprisingly transient structure of photoexcited CdS clusters, [251] and even directly observed in real time the growth of individual platinum nanocrystals in a graphene liquid cell. [252] These atomic-level investigations have brought clarity and unprecedented concreteness to the actual structure and physical behavior of nanocrystals.

Unfortunately, TEM-based techniques suffer from two critical blindspots. First, because organic molecules have poor TEM contrast, TEM cannot be used to investigate the ligand shell of the nanocrystal. To investigate the structure and dynamics of the passivating layer of nanocrystals, researchers have relied on techniques such as NMR [253] and x-ray photoelectron spectroscopy [254, 255] that measure the average structural connectivity of the nanocrystals in a sample. These techniques are sensitive to organic and metal-organic bonds, can distinguish between bound and unbound ligands in a nanocrystal solution, and can be used to identify the lability of surface-bound ligands and to identify the chemical transformation enacted during ligand exchanges. [256] The second blind spot is that none of the aforementioned structural techniques can report on the connection between the physical state of the system and the optical properties of the system. TEM may report that the lattice strain between a CdSe core and its ZnS shell has caused severe distortions in the

equilibrium position of the interfacial atoms, but it cannot reveal whether (or how) the observed strain will adversely affect the fluorescence from the CdSe core electronic states. Surface techniques such as NMR may be able to quantify the presence of many ligand species on the surface of the nanocrystal, but they cannot directly report on how this physical surface passivation affects optical behavior.

The unclear connection between the structural and optical properties of nanocrystals has interfered with the investigation of many different types of interactions between the nanocrystal surface and core excitons. Using purely optical techniques including transient photoluminescence and transient absorption, researchers have identified the important role of the nanocrystal surface in determining the dominant mechanisms of hot carrier relaxation, dictating the rate of carrier trapping, and causing the highly detrimental effects of biexciton formation on nanocrystal fluorescence. [224, 257, 258] These phenomena profoundly affect the fluorescence properties of the nanocrystals for applications, but have generally only been treated theoretically on a phenomenological basis. There is clear need to begin to build a more concrete connection between the optical behavior and structural characteristics of nanocrystals to clarify the structural goals of high quality nanocrystal syntheses.

Single-nanocrystal spectroscopy may be an important tool for bridging this gap between our understanding of the chemistry and structural physics of nanocrystals and our understanding of their optical behavior. The time-dependent optical properties of individual nanocrystals have been found to reflect many of the transient surface phenomena that have been tricky to measure through other means. Moreover, single nanocrystal spectroscopy gives us a way of correlating many different optical observables produced by a single nanocrystal configuration and gives us a way of characterizing the distribution of optical properties produced by the heterogeneity in surface structure within a sample. In fact, correlated TEM/single-nanocrystal blinking investigations have already been used to identify certain structural features that appear to be correlated with blinking behavior. [259]

In this Chapter, we will take a closer look at the investigation of a poorly-understood single-nanocrystal optical phenomenon that may provide unique insight

into carrier trapping and other surface effects: the spectral diffusion of single nanocrystals at low temperature. This observable has been found to report on the peripheral dynamics of the nanocrystal via fluctuations in the local electric field and therefore can provide an optical/spectroscopic probe of surface phenomena with a degree of spatial resolution. We begin with a review of the previous literature on nanocrystal spectral dynamics. We will then discuss the major experimental problems that have been associated with measuring these spectral dynamics and several possible solutions. Finally, we conclude with an overview of the solution explored here, a technique called photon-correlation Fourier spectroscopy.

2.1 What We Know about Spectral Diffusion in Semiconductor Nanocrystals

Spectral diffusion was first observed by Empedocles and Bawendi [63] when they looked to study the quantum-confined Stark effect at the single-nanocrystal level. In their experiments, they measured the fluorescence spectrum of individual core-only and ZnS-shelled CdSe nanocrystals at 10 K and demonstrated that the emission wavelength could be shifted by the application of an electric field. The field-dependence of the center wavelength revealed a large excited state polarization, consistent with the core states being delocalized over the entire nanocrystal, and a non-zero excited state dipole, which due to the spherical symmetry of nanocrystals, was interpreted as the existence of a local electric field. They observed two distinct, but related types of spectral dynamics. First, during their experiments, the fluorescence spectrum occasionally underwent large, spontaneous spectral shifts on the order of 10 meV, which were accompanied by a change in the excited state dipole of the nanocrystal. The magnitude of these spectral shifts was estimated to be consistent with the change in electric field caused by the addition or removal of carrier from the nanocrystal surface. And second, the low temperature spectrum did not exhibit a lifetime-limited linewidth. Instead, its linewidth was around 1–3 meV and could be broadened fur-

ther by applying an electric field. This linewidth behavior was consistent with a rapidly varying local electric field on timescales faster than the integration time of the experiment.

Several later investigations have clarified the nature of both of these types of spectral dynamics. Neuhauser et al. [260] identified a connection between the large spectral shifts and fluorescence intermittancy events. They found that large spectral shifts were statistically more likely to occur during blinking events. In the context of the charging model of blinking, this suggested that the large spectral shifts may be induced during the carrier trapping and detrapping processes involved with nanocrystal core charging and neutralization. Furthermore, when nanocrystals were synthesized with fluorescent trion states, an additional mechanism of spectral diffusion directly associated with trion formation was also identified. During trion formation and neutralization, the fluorescence spectrum has been observed to red- or blue-shift by the trion binding energy of the core states ($\sim$20 meV for the postive trion in CdSe core/shell particles, and $\sim$5 meV for the negative trion).[1] [181–183]

There have also been several clever investigations of the rapid form of spectral dynamics, even though conventional experiments do not have the temporal resolution to resolve them. Gomez et al. [261] found that the room temperature fluorescence linewidth, which they claimed was defined by rapid spectral dynamics,[2] was independent of dielectric environment, suggesting that it was caused by dynamics within the core/shell/ligand architecture. Empedocles et al. [64] identified the rapid spectral dynamics as a photoinduced, but thermally assisted process at tempertures between 10 K and 40 K, enabled using the excess energy from hot carrier thermalization in the fluorescence cycle. Fernée et al. [262, 263] provided additional statistical evidence for the discrete, photoinduced character of rapid spectral dynamics, but also observed instances of spontaneous spectral shifts they identified as energetically downhill events.

[1] To my knowledge, no one has reproduced the analysis of Neuhauser et al. using samples with trion emission to confirm that core charging was responsible for the blinking events that were correlated with large spectral dynamics.

[2] This is contrary to our more recent understanding that ties the room temperature linewidth to the extent of exciton-phonon coupling and to the nanocrystal fine structure. Nevertheless, they do still show that the spectral dynamics they observe on camera timescales at room temperature are also independent of the dielectric environment.

And, Plakhotnik et al. [264] modeled the rapid spectral dynamics as a diffusion process and found that its probability distribution function broadened according to a sub-diffusion power law with widely variable exponent.[3]

And finally, in a somewhat contentious pair of reports, Müller et al. [265, 266] drew a causal connection between rapid spectral dynamics and the large spectral shifts by studying the spectral dynamics of CdSe/CdS seeded rods. They found that the fluorescence linewidth defined by rapid spectral dynamics was strongly correlated with the average spectral position defined by the large spectral shifts. On this evidence, they suggested a unified model of spectral diffusion, where large spectral jumps were caused by the hopping of trapped charges along the length of the seeded rod, and the rapid spectral dynamics were caused by small jitter in the exact position of the trapped charges. The spectral position was therefore defined by the distance between the trapped charge and the CdSe seed and the spectral linewidth was defined by the total magnitude of the dynamic electric field fluctuations caused by the rapid jitter of the charge at its given physical position. However, Gómez et al. [261] have noted that the same behavior is manifested in spherically-symmetric core/shell nanocrystals. The correlation between spectral position and linewidth could simply be a result of the second-order nature of the Stark effect. Just as Empedocles and Bawendi were able to modulate the linewidth using an applied electric field, the magnitude of the rapid spectral dynamics may simply be responding to a change in the overall static local electric field. Whether rapid spectral jitter is caused by the same physical process as the discrete spectral jumps or simply scaled by the magnitude of the local electric field is still not entirely clear.

At present, there are two major theories that have been proposed to explain the rapid spectral dynamics of nanocrystals at low temperature. The first is the charge-trapping model, originally proposed by Empedocles and Bawendi [63, 64] and supported by Müller et al. [265, 266], where the large discrete spectral jumps are caused by the trapping and de-trapping of carriers on the surface of the nanocrystal

[3]Unlike in blinking statistics, a power law is not a strange or surprising result in diffusion physics. One-dimensional Brownian motion produces a probability distribution function that broadens as a power law with an exponent of 0.5.

and the rapid spectral dynamics are caused by the diffusion of the carriers through the manifold of available trap sites on the surface of the nanocrystal. The second is the ligand-perturbation model, recently suggested by Fernée et al. [263], which suggests that the rapid form of spectral dynamics may not be related to charge-trapping at all. Instead, they propose that rapid spectral diffusion events occur when the relaxation of hot carriers dumps energy into specific vibrational modes on the surface of the nanocrystal, which are capable of inducing minor reorganizations of ligands on the surface of the nanocrystal. The cause of the dynamic Stark shift is therefore the fluctuation in the local electric field in the nanocrystal caused by the reorganization of the surface dipoles. One of our major goals for this project has been to try to identify ways of experimentally distinguishing between these two physical pictures, which ultimately requires a better way of measuring and characterizing rapid spectral dynamics.

It is also important to note a related line of investigation aimed at identifying the intrinsic linewidth hidden underneath the rapid spectral dynamics. In addition to being a physically interesting observable in and of itself, the intrinsic linewidth is also important for determining the overall magnitude of rapid spectral dynamics. Conventional single-nanocrystal spectroscopy has not been used to measure a linewidth less than 120 μeV because of rapid spectral dynamics. [64] However, narrower linewidths have been measured using other techniques like spectral hole burning, [267, 268] ultrafast spectroscopy, [269, 270] resonant photoluminescence excitation experiments that measure the linewidth quickly and without allowing hot carrier thermalization, [271, 272] and photon-correlation and/or interferometry. [273–275] The consensus seems to place the intrinsic linewidth of single nanocrystals at low temperatures between 1–30 μeV, but also suggests that it is probably a sample-dependent quantity. Processes like spin-flip dephasing may be a major source of line-broadening in CdSe/CdS nanocrystals and would be affected by architectural parameters such as shell thickness. [269, 270]

To summarize, three sources of spectral dynamics have been observed in the fluorescence spectra of single nanocrystals at low temperature (Figure 2-1). Large and

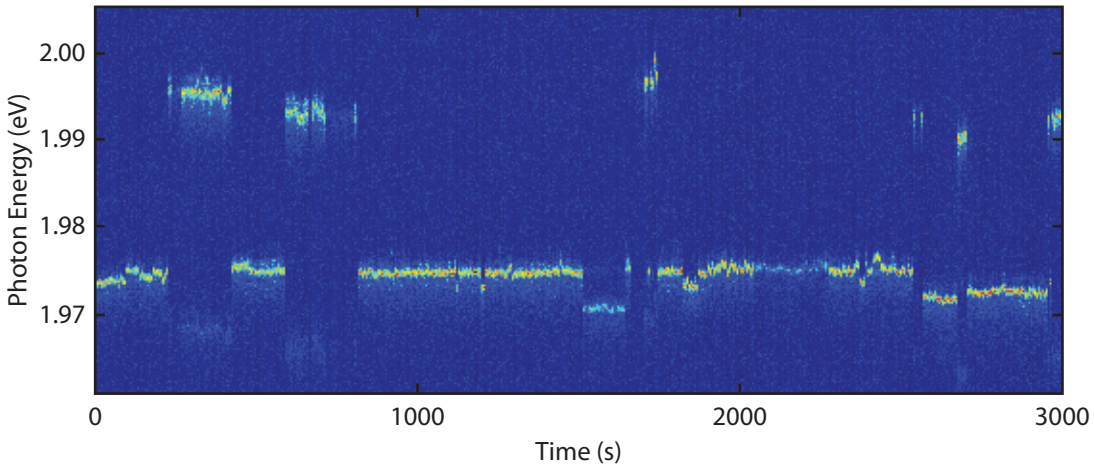

Figure 2-1: A time series of integrated spectra illustrating three types of spectral dynamics in single nanocrystals at low temperatures (4 K): large, discrete binary shifts due to trion formation and neutralization, smaller discrete shifts attributed to carrier trapping, and rapid diffusion over a small energy range.

very infrequent binary switching in spectral location have been observed and tied to trion formation. Large, but variable, spectral shifts have been observed and tied to the trapping or detrapping of carriers in the in periphery of otherwise neutral nanocrystals. And small but rapid spectral jitter has been observed and tied to either the diffusion of carriers within the trap manifold or to ligand rearrangement on the surface of the nanocrystal. A thorough understanding of these three mechanisms could yield important insight into the salient features of nanocrystal surface structure and its connection to their optical properties.

2.2 The Problem

The study of nanocrystal spectral dynamics has been strongly limited by the temporal resolution of conventional single-nanocrystal spectroscopic techniques. Ideally, the single-nanocrystal spectrum could be entirely studied using a setup similar to that shown in Figure 2-2. In this setup, a single nanocrystal is confocally excited on a substrate in a cryostat, the fluorescence emission is collected and frequency-resolved with a spectrometer, and the spectrum is detected by imaging the frequency-dispersed signal using a CCD camera. This experimental procedure is easy to implement, can

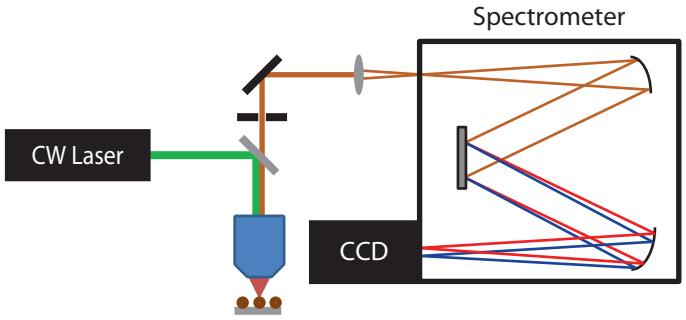

Figure 2-2: A schematic of a conventional single-nanocrystal spectroscopy setup. Fluorescence from a single-nanocrystal in confocal microscope is spectrally resolved with a spectrometer and integrated on a CCD camera.

yield a single-nanocrystal spectrum in less than a second, and can measure a spectrum with arbitrary resolution depending on the chosen gratings and spectrometer path length. Moreover, the resulting time series of spectra generated by taking a series of spectral integrating times is easy to interpret and straight-forwardly reveals spectral time-dependence. This setup is therefore the ideal tool for studying spectral dynamics that are both slow and large in magnitude, including the infrequent spectral jumps caused by trion formation or charge trapping.

Nevertheless, this experiment suffers from the inherent temporal limitations of intensity-binning techniques (Figure 2-3). In order to resolve the shape of a spectrum, a large number of fluorescence counts must be collected and binned. This creates a trade-off between the spectral resolution, given by the bin spacing in the spectral domain (i.e. the number of bins receiving the counts), the temporal resolution, given by the integration time (i.e. the number of total counts received), and the signal-to-noise of the spectrum (i.e. the number of counts per bin). The tradeoff is exacerbated when you consider that standard cryostat setups using low-numerical aperture air objectives tend to have overall collection/detection efficiencies below 5%. Over 25,000 fluorescence events must be allowed to occur to measure a spectrum with only 500 counts, and this requires even more absorption events if the quantum yield of the emitter is less than unity. This is a serious problem for investigating spectral fluctuations that are small and fast like the rapid spectral diffusion of nanocrystals, because resolving individual spectral diffusion events simultaneously requires high

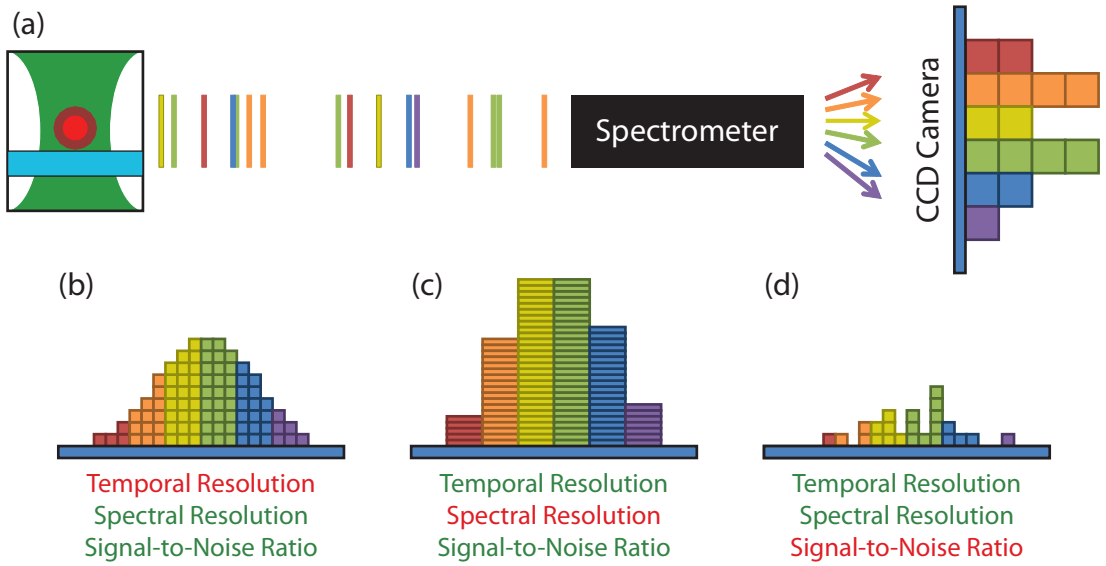

Figure 2-3: Conventional single-nanocrystal spectroscopy is limited by an inherent tradeoff between spectral resolution, temporal resolution, and signal-to-noise ratio.

temporal resolution, high spectral resolution, and high signal-to-noise to pinpoint very small changes in the center wavelength of a spectrum.

2.3 Improving Temporal Resolution Using Photon Correlation

Photon correlation provides an elegant strategy for bypassing the inherent temporal limitations of conventional single-molecule spectroscopy. Although intensity correlation functions themselves have no inherent spectral resolution, spectral discrimination can be added into a photon correlation experiment by introducing spectral bias into the detection channels using bandpass filters, monochromators, or interferometers. One of the first examples of spectrally-biased correlation measurements in single-nanocrystal spectroscopy was presented by Fisher et al. [276] They added spectral filtering to the standard single-nanocrystal antibunching experiment to demonstrate that a blue-shifted spectral feature in the high-excitation flux nanocrystal spectrum was caused by the 1P-1P nanocrystal fluorescence of triexcitons. By correlating the photon arrivals from the blue-shifted fluorescence with the photon arrivals in the

main peak produced by biexcitons and excitons, they showed that the blue-shifted feature exhibited ordered-emission characteristic of multiexcitons (i.e. triexcitons decay to form biexcitons, which decay to form excitons). A similar filtering scheme was recently used by Galland et al. [277] to independently investigate the antibunching behavior of spectrally-resolved fluorescence from different parts of a CdSe/CdS "dot-in-bulk" heterostructure.

Several spectrally-resolved correlation experiments have also been used to investigate spectral diffusion in a variety of nanostructures. The earliest example we will discuss here is the photon-correlation Fourier spectroscopy technique described in the next section that was developed by Brokmann et al. [278] and first implemented by Coolen et al. [273, 279], but there are a couple of simple later examples worth mentioning. The first key example used a dual monochromator setup instead of bandpass filters to precisely tune the spectral profiles of two detection channels and isolate the red or blue side of a epitaxial quantum dot fluorescence spectrum that was broadened by spectral diffusion (Figure 2-4). [280–282] The intensity correlation function of the spectrally-biased channels exhibited additional photon-bunching that was absent from the intensity correlation function of the entire fluorescence spectrum because of the periods of time the spectrum spent outside the channel's spectral window during spectral diffusion. By comparing the overall intensity correlation function of the emitter to the intensity correlation of the signal within the spectral window, it was possible to identify both the timescale of spectral dynamics and the underlying homogeneous linewidth of the fluorescence.

Another key example was recently used by Wolters et al. [283] to investigate the spectral dynamics of nitrogen vacancies in diamond.[4] In this system, a narrow intrinsic fluorescence spectrum has been found to discretely and randomly samples a broad time-averaged spectrum. To directly measure the kinetics of this sampling process, they spectrally biased their detection channels using an interferometer whose path-length difference was being scanned in the region between the coherence lengths of the intrinsic and time-averaged spectra (Figure 2-5). If a diffusion event had

[4]Also note the related experiment of Abbarchi et al. [284]

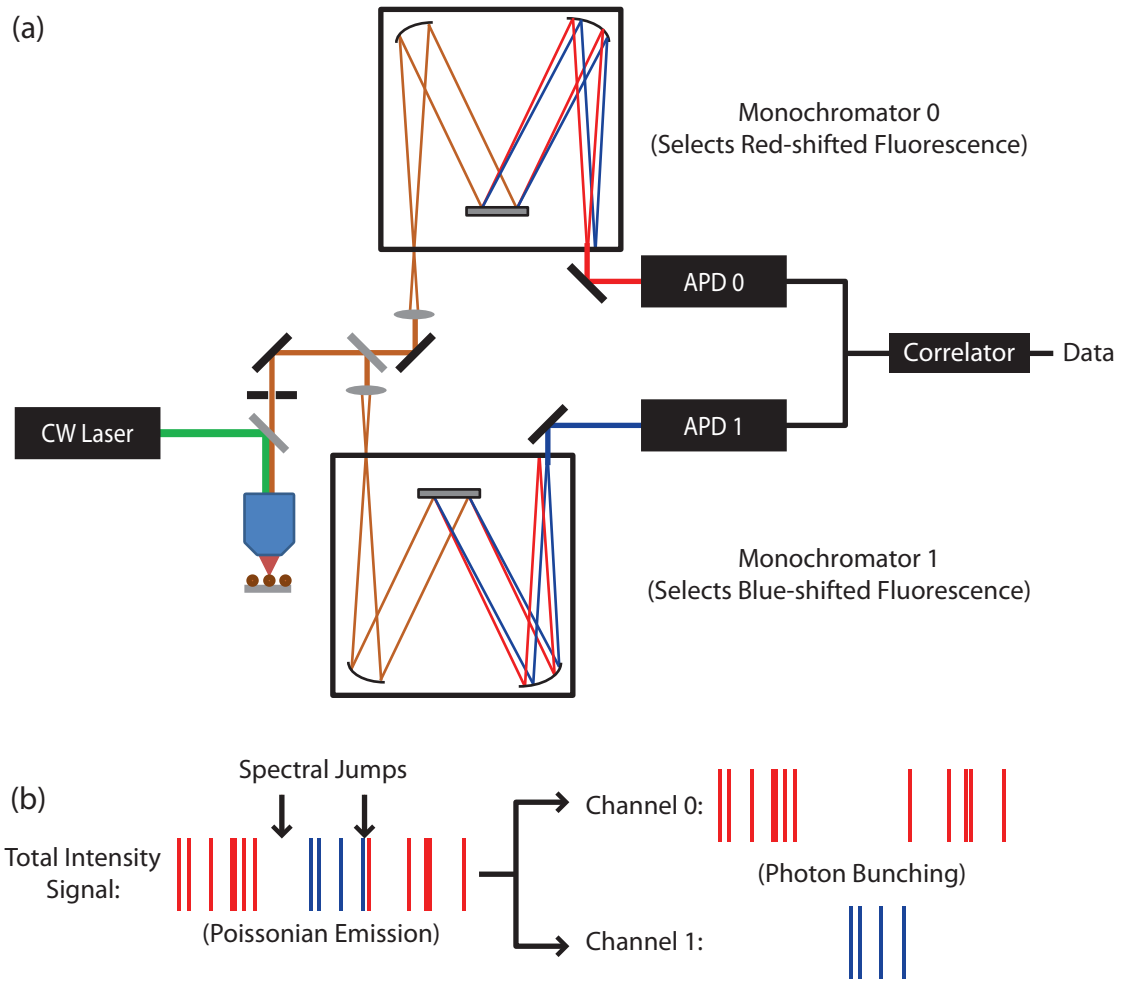

Figure 2-4: By spectrally biasing the channels of a correlation experiment using a dual monochromator setup, rapid spectral dynamics are manifested as difference between the intensity-cross correlation function and the total intensity autocorrelation function of the emitter.

occured between two photon arrivals, the interferometer would not influence their likelihood to be detected on a given detection channel because, on average, their spectra would reflect the time-averaged spectrum. However, if a diffusion event had not occured between two photon arrivals, the enhanced spectral coherence between the photon pairs would cause them to be mapped to the same interferometer arm. This manifests as an anticorrelation feature in the cross-correlation function between the detection channels because these coherent photon pairs tend to map to either one detector or the other, depending on the exact spectral position of the given intrinsic spectrum within the time-averaged spectrum and the precise path-length difference of the interferometer during the scan. The decay constant of this anticorrelation feature in the intensity cross-correlation of the two interferometer arms is directly related to the kinetics of the underlying discrete spectral diffusion process.

These two correlation experiments are valuable for investigating rapid spectral dynamics with relatively simple physics because they can reveal information on timescales inaccessible to conventional single-molecule spectroscopy, they are conceptually intuitive and straight-forward to interpret, and they are experimentally easy to implement with high signal-to-noise. Nevertheless, they are single-point correlation measurements that rely on a presupposed physical model for the spectral dynamics. In both cases, experimenters assumed that the intrinsic spectrum had a Lorentzian lineshape and discretely sampled the time-averaged spectrum via uncorrelated spectral jumps. Their experiment provided no means for measuring the underlying homogeneous lineshape (or even linewidth, in the case of the interferometer-based measurement), or any means for testing the mechanism of the spectral dynamics. Either experiment could just as easily have been analyzed in the context of a more complex stochastic process or even a continuous diffusion process.[5]

In cases where the diffusion physics is unknown or more complicated, or the underlying shape of the intrinsic fluorescence spectrum is of interest, a more powerful technique is required. In the next section, we provide an experimental and theoretical

[5]That they measured a simple exponential decay in their correlation functions is strong evidence that the story is not more complicated in these systems.

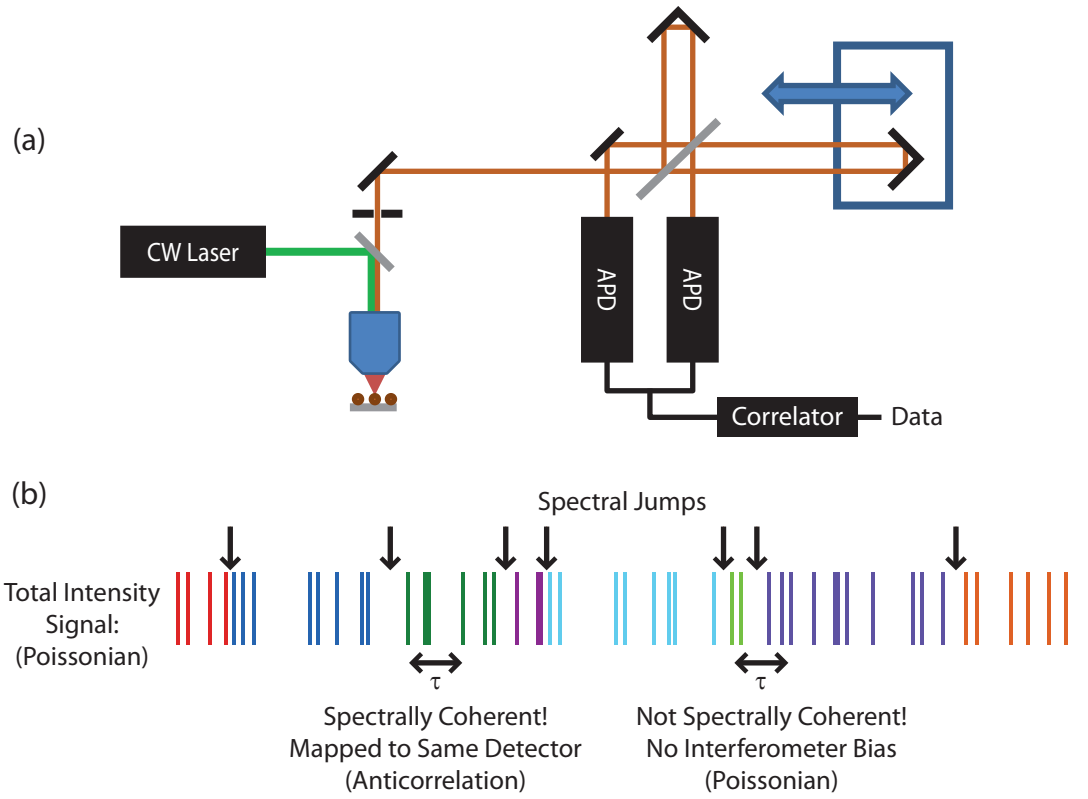

Figure 2-5: Simple spectral dynamics can be measured by cross-correlating the outputs of an interferometer whose path-length difference is positioned between the coherence lengths of the intrinsic and time-averaged spectra. Photon pairs across spectral jumps are unbiased by the interferometer, whereas photon pairs arriving between spectral jumps are mapped to the same detector and cause an anti-correlation in the intensity cross-correlation.

overview of photon-correlation Fourier spectroscopy (PCFS), a technique that can be used to directly analyze the mechanistic details of rapid spectral dynamics and can reveal the underlying homogeneous lineshape of single emitters.

2.4 Overview of Photon-Correlation Fourier Spectroscopy

The idea behind PCFS is very similar to the simple interferometry experiment reported by Wolters et al. [283] An interferometer can be used to probe the spectral coherence between pairs of photons as a function of their temporal separation, thereby revealing spectral features and dynamics on the timescales of photon timing rather than relying on an integration-based technique. As a result, the experimental setup of PCFS is identical to that of Figure 2-5. A single emitter isolated on a substrate is illuminated with continuous-wave excitation in a confocal microscope. The emission is sent into a two-output Michelson interferometer, detected on two single-photon-counting avalanche photodiodes, and analyzed using correlation hardware.

However, there are three key differences between the experiment of Wolters et al. [283] and PCFS. First, because nanocrystals are known to exhibit intensity fluctuations in addition to spectral fluctuations, the intensity cross-correlation between the interferometer outputs will contain features caused by total signal fluctuations in addition to the desired features caused by spectral fluctuations. We will account for this by also measuring the intensity autocorrelation of the total signal that passes through the interferometer, to correct for intensity-related features. Second, rather than scanning the interferometer path-length difference through an arbitrary region between the coherence lengths of the intrinsic and time-averaged spectra, we will pick a specific path-length difference and introduce a small dither over a few interference fringes about that path-length difference. The importance of the dither will be discussed in detail later, but the idea is that the photon pair coherence we measure will be closely representative of that at the given average path-length difference and

not averaged over a large range of path-length differences. Finally, and most importantly, we will measure the photon pair coherence via the intensity cross-correlation as a function of *both* temporal separation and interferometer path-length difference. This is the key that PCFS uses to unlock lineshape information about the intrinsic single-emitter spectrum and its dynamics.

To understand how PCFS works, it is important to first understand how an interferometer transforms spectral information into intensity information. When a signal enters an interferometer, it is split into two paths, allowed to propagate over two different path lengths, and recombined to give a final signal. Because of the path-length difference between the two beam paths, a phase shift is introduced between the two halves of the signal, which causes either constructive or destructive interference on one of the interferometer outputs (Output A) and the opposite effect on the other (Output B) to conserve energy.[6]

The extent of constructive or destructive intereference depends on two factors: the path-length difference between the halves of the signal and the spectrum of the signal. When monochromatic light at a wavelength of 600 nm is sent through an interferometer (Figure 2-6), complete constructive interference is observed on Output A when the path-length difference is given by an integer number of wavelengths (e.g. 0, 600, 1200 nm) and destructive interference is observed when the path-length difference is given by a half-integer number of wavelengths (e.g. -300, 300, 900 nm). However, if the light is polychromatic, each fraction of the signal will have its own points of constructive and destructive interference at slightly different path-length differences. All of the signal is necessarily in phase and undergoing complete constructive/destructive interference at zero path-length difference (the so-called white fringe), but over longer path-length-differences, the dispersion in the points of constructive and destructive interference will cause the total degree of interference to decrease and eventually average away. The broader the spectrum of the signal, the faster this decoherence occurs with increasing path-length difference, and the narrower the spectrum, the slower this

[6] An additional π phase shift is introduced on one of the outputs on the basis of the number of reflections that are required to direct the beam into that output.

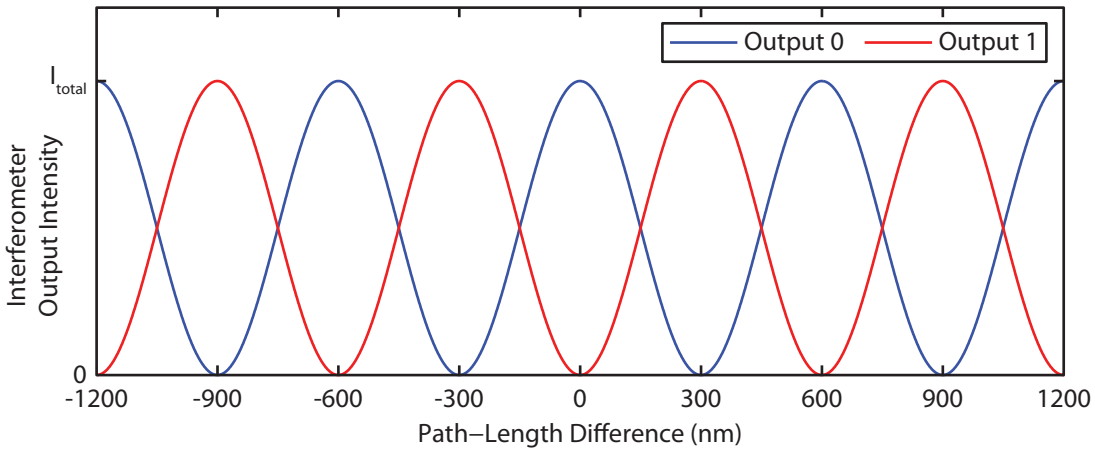

Figure 2-6: When Poissonian, monochromatic light is aligned into an interferometer, the interferometer outputs can be subject to complete constructive or destructive interference, depending on the relative phases introduced by the two arms of the interferometer. The spacing between the regions of constructive and destructive interference depends on the wavelength of the monochromatic light.

decoherence occurs.

As a result, the intensities of the outputs of an interferometer are closely related to the Fourier transform of signal's spectrum. For a potentially dynamic spectrum $s(\omega, t)$ with a constant fluorescence intensity, the intensities of the interferometer outputs $I_{A/B}(\delta, t)$ are given by,

$$I_{A/B}(\delta, t) = \frac{1}{2}\left(1 \pm FT_{cos}[s(\omega, t)]_{\omega \to \delta}\right), \tag{2.1}$$

where δ is the path-length difference of the interferometer and $FT_{cos}[\cdots]_{\omega \to \delta}$ denotes the real part of the Fourier transform with respect to ω. From this equation, we can see that measuring the *intensities* of the interferometer outputs as a function of path-length difference can give us the shape of the spectrum, but how does this work for their intensity cross-corelation?

We will begin by determining what we would see if we measured the intensity cross-correlation between outputs A and B for a constant signal with no intensity or spectral fluctuations. Consider the Gaussian spectrum in Figure 2-7(a), characterized by center frequency ω_0 and linewidth σ. Its intensity interferogram is given by its Fourier

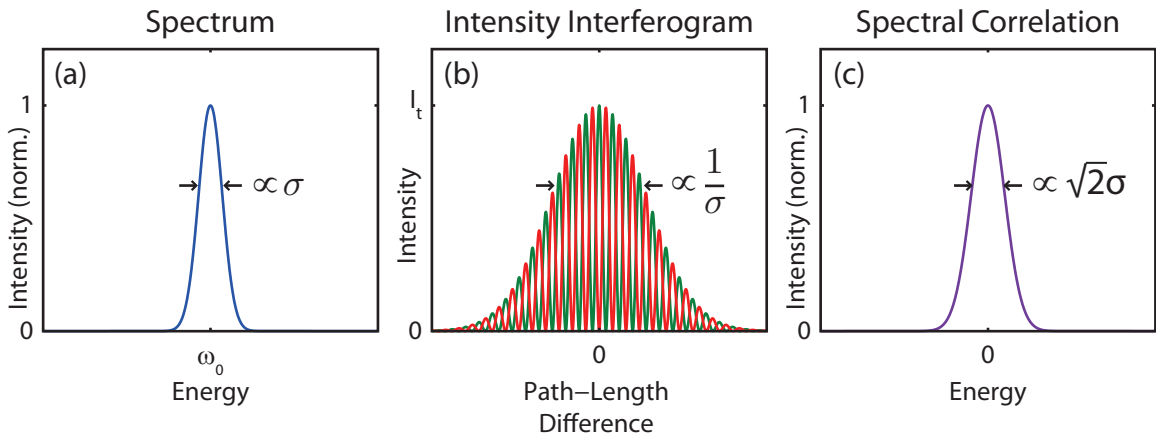

Figure 2-7: The (a) spectrum and (b) corresponding intensity interferogram of a Gaussian spectrum with center freqency ω_0 and linewidth σ. The interferogram has a carrier frequency proportional to ω_0 and a linewidth inversely proportional to σ. (c) The corresponding spectral correlation is a Gaussian function centered on zero with linewidth given by $\sqrt{2}\sigma$.

transform (Figure 2-7(b)), which is a Gaussian lineshape with a width proportional to $\frac{1}{\sigma}$ and a carrier frequency proportional to ω_0.[7]

Our goal is to measure the intensity cross-correlation function between the output channels, so what happens if we evaluate Equation 1.1 for $\tau = 0$ at some arbitrary path-length difference δ_0, which happens to correspond to a fringe maximum in the carrier frequency of the spectrum? The result is worked out in Figure 2-8(a), and we cannot be very pleased with it. Remember that intensity correlation functions are constructed to identify fluctuations in a signal. Even though our intensity outputs clearly reflect some spectral information about the signal (in their uneven intensities), because the signal is constant, the numerator and the denominator are equal and we measure an uninteresting Poissonian correlation function.

The solution is to introduce a controlled oscillation into the path-length difference we call a dither, which will convert the uneven output intensities into intensity fluctuations. In Figure 2-8(b), we show what happens if we calculate the intensity cross-correlation while we simply scan the interferometer path-length difference over

[7]Units can be tricky in energy-based Fourier transforms and require careful attention, so we are being intentionally vague here instead.

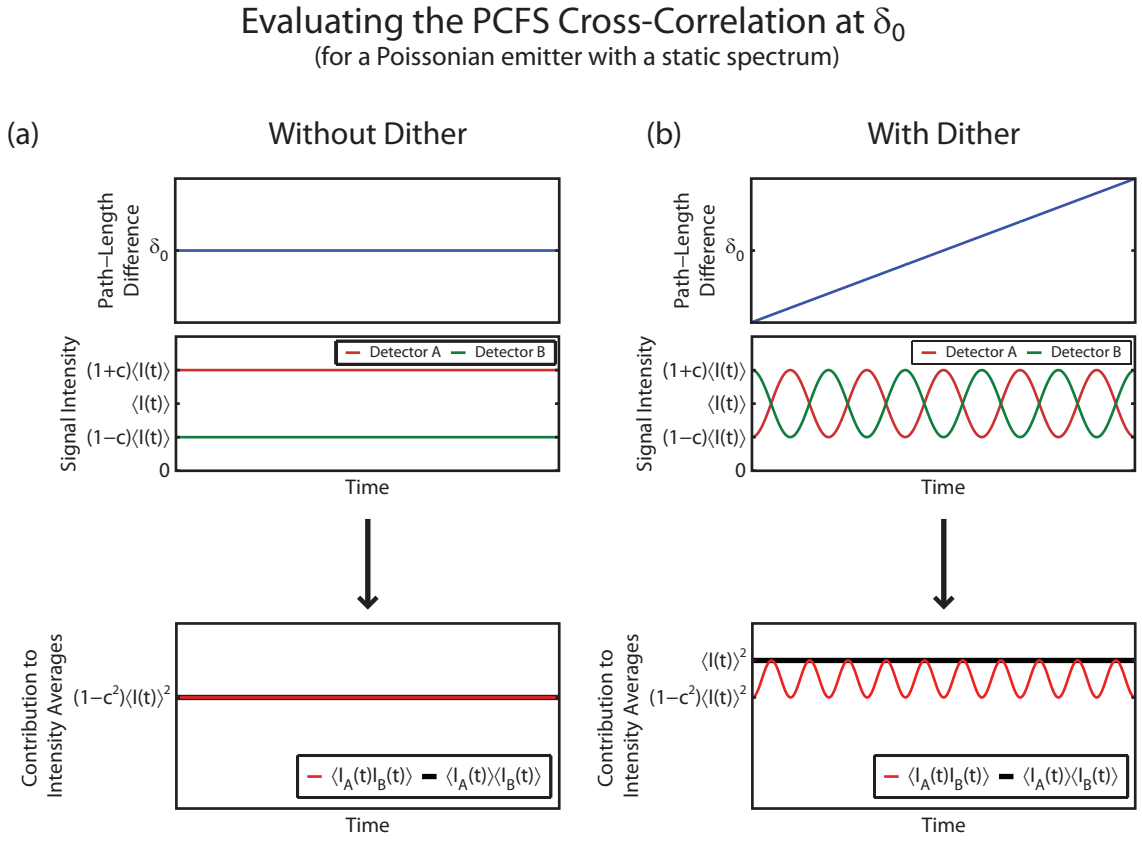

$$g^{AB}(\tau \to 0) = \frac{\langle I_a(t) I_b(t+0)\rangle}{\langle I_a(t)\rangle\langle I_b(t+0)\rangle} = \frac{(1-c^2)\langle I(t)\rangle^2}{(1-c^2)\langle I(t)\rangle^2} = 1$$

$$g^{AB}(\tau \to 0) = \frac{\langle I_a(t) I_b(t+0)\rangle}{\langle I_a(t)\rangle\langle I_b(t+0)\rangle} = \frac{(1-\langle c^2 cos^2(kt)\rangle)\langle I(t)\rangle^2}{\langle I(t)\rangle^2} = 1 - \frac{1}{2}c^2$$

Figure 2-8: Worksheet evaluating the PCFS cross-correlation at $\tau = 0$ for a static, Poissonian spectrum with and without scanning the interferogram. (a) Without scanning the interferometer, there are no intensity fluctuations in the signal and the numerator and the denominator of the cross-correlation function cancel. (b) When the interferometer is scanned over several fringes, intensity fluctuations are introduced to the two interferometer outputs proportional to the average coherence of the signal. Now, the product of the interferometer outputs deviates from the square of the average signal and the spectral coherence is mapped into the cross-correlation function. Note that c represents the magnitude of the fringes in the intensity interferogram at a given path length difference (e.g. from Figure 2-7(b)), so by measuring the cross-correlation of the interferometer outpus as a function of path-length difference, we are measuring the square of the envelope of the Fourier transform of the spectrum.

an integer number of carrier frequency periods.[8] If we evaluate the cross-correlation at $\tau = 0$, our result suddenly reflects the spectral coherence of the signal!

So, now that we can encode spectral information in our intensity cross-correlation, we can take a closer look at what spectral information we are actually collecting. This requires a bit of mathematical gymnastics. For the sake of argument, let's consider the general case where we have a spectrum $s(\omega)$ whose Fourier transform can be recast as a product of a carrier frequency term $e^{i\omega_0\delta}$, which conveys the average emission wavelength, and a real and positive envelope function $FT[s_{env}(\omega)]$, which contains the lineshape information. The Gaussian spectrum from Figure 2-7 is a perfect example. In the previous paragraph, we showed that the anticorrelation in $g(\tau = 0, \delta)$ after dithering is given by one half the square of the envelope of the spectrum's interferogram (i.e., the quantity $\frac{1}{2}c^2$). Thus,

$$g(\tau = 0, \delta) = 1 - \frac{1}{2} FT[s_{env}(\omega)]^2 \tag{2.2}$$

$$= 1 - \frac{1}{2} \left(e^{i\omega_0\delta} FT[s_{env}(\omega)] \right) \left(e^{-i\omega_0\delta} FT[s_{env}(\omega)] \right) \tag{2.3}$$

$$= 1 - \frac{1}{2} FT[s(\omega)] FT[s(\omega)]^* \tag{2.4}$$

$$= 1 - \frac{1}{2} FT[p(\zeta)], \tag{2.5}$$

where * denotes a complex conjugate, and where in the final step, we have merged the product of two Fourier transforms using the autocorrelation theorem of Fourier transforms. The resulting quantity $p(\zeta)$ is the spectral correlation or autocorrelation of the spectrum. And, in fact, due to certain experimental details we will explore in Chapter 3, this expression will hold for all τ much shorter than the time it takes to scan from one fringe to the next. When the τ-dependance is reintroduced to the equation, the spectral correlation is defined by,

$$p(\zeta, \tau) = \left\langle \int_{-\infty}^{\infty} s(\omega, t) s(\omega + \zeta, t + \tau) \, \mathrm{d}\omega \right\rangle, \tag{2.6}$$

[8] This simple picture assumes a narrow spectrum where the envelope of the interferogram does not vary over a small number of interference fringes.

where $\langle \cdots \rangle$ is the time-average over the integration time of the experiment. This simple demonstration shows that using PCFS, we can sketch out the spectral correlation of a signal measured on timescales approaching $\tau = 0$, presumably much faster than the integration time of conventional single-nanocrystal spectroscopy. But the questions remain, what is the meaning of the spectral correlation and how does it handle the rapid spectral dynamics that obfuscate conventional measurements?

The spectral correlation represents the histogram of energy differences between pairs of signal photons as a function of their temporal separation. This can be understood on the basis of how we compile it experimentally during PCFS. As with all single-nanocrystal cross-correlation measurements, we compile the intensity cross-correlation at each path-length difference by histogramming the temporal separations between all pairs of photons we detect across the interferometer outputs. The anti-correlation feature we analyze in PCFS, as shown by Figure 2-8, is produced by the spectral coherence between these pairs of photons, which causes them to map to the same output rather than opposite outputs. In this way, we are only probing the relative spectral coherence between the photon pairs, rather than the absolute spectral coherence of the entire signal. We only care how the pairs of photons map with respect to each other, not how they map to other photon pairs. This is how we can measure spectral information without waiting long enough to probe the entire signal. Whereas in Fourier transform spectroscopy, measuring the output intensities as a function of path-length difference reveals the Fourier transform of the time-averaged spectrum, in PCFS, measuring the cross-correlation of the output intensities as a function of path-length difference reveals the Fourier transform of the distribution of energy separations between pairs of photons. In Figure 2-9 we show how this conceptual picture of the spectral correlation connects to the mathematical expression in Equation 2.6.

2.5 How We Use the Spectral Correlation

The primary benefit of the spectral correlation is its temporal resolution. We can determine the average spectral relationship between pairs of photons that are spaced

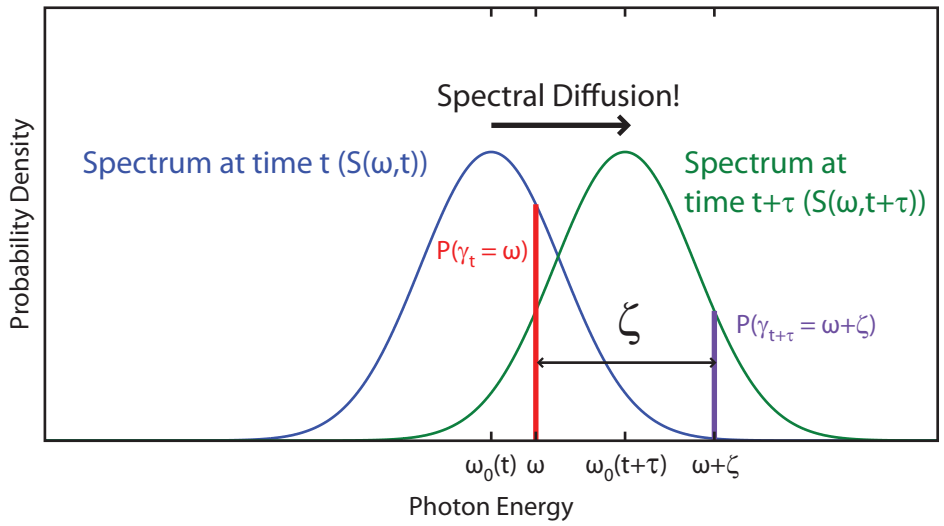

Joint probability of detecting one photon at time t with energy ω, and another photon at time t+τ with energy ω+ζ :
(considering the probability density functions of photon energies (i.e. spectra) at each time)

$$= P(\gamma_t = \omega) \times P(\gamma_{t+\tau} = \omega+\zeta)$$
$$= S(\omega,t) \times S(\omega+\zeta,t+\tau)$$

Probability of detecting two photons at times t and t+τ, respectively, whose energy difference is ζ :
(considering all possible energies of the first photon)

$$= \int S(\omega,t) \times S(\omega+\zeta,t+\tau)\, d\omega$$

Overall probability that any two photons temporally separated by τ are also spectrally separated by ζ :
(considering that with ergodicity, the time average samples all possible results)

$$= \left\langle \int S(\omega,t) \times S(\omega+\zeta,t+\tau)\, d\omega \right\rangle \equiv p(\zeta,\tau)$$

Figure 2-9: Worksheet building the mathematical definition of the spectral correlation in Equation 2.6 using our conceptual interpretation of the spectral correlation.

much closer in time than the integration time required to resolve the spectrum overall. This property allows us to pick out the average single-nanocrystal linewidth from a solution-phase PCFS (S-PCFS) measurement by comparing how the spectral correlation evolves in concert with the FCS trace. [176, 177, 285] Single emitters in solution are free to diffuse into and out of the focal volume during the measurement. In a conventional spectroscopy measurement, this rapid particle exhange in the focal volume is much faster than viable integration times, resulting in the mesurement of an ensemble spectrum. Even with arbitrarily fast spectral integration times, you would still have to contend with the fact that there are often multiple particles in the focal volume at once.

However, FCS demonstrates our ability to use correlation methods to identify the fraction of a signal caused by single emitters as they enter and leave the focal volume. By using S-PCFS to compare the spectral correlation produced by photon pairs at long τ, when photon pairs are necessarily from different particles, to the spectral correlation at short τ when FCS suggests that photon pairs may be from the same particle, we can tease out the average spectral correlation of single particles within the ensemble. This technique has been used to precisely and conveniently characterize spectral polydispersity in nanocrystal samples and to investigate how different synthetic procedures and nanocrystal architectures affect the single-nanocrystal linewidth. It is described in detail in J. Cui's thesis. [286]

But more importantly for this thesis, the spectral correlation also allows us to take a closer look at the rapid spectral dynamics of single-emitters isolated on a substrate and their underlying intrinsic fluorescence linewidth. Consider a single emitter undergoing rapid spectral dynamics. Again, if we tried to measure the integrated spectrum using conventional single-nanocrystal spectroscopy, these rapid spectral dynamics would occur much faster than a viable integration time and our spectrum would be artificially broad. Instead, using PCFS, we can choose to focus on photon pairs that were emitted by the nanocrystal very closely together in time. These photon pairs will be more spectrally coherent than the time-averaged spectrum because very little spectral diffusion was allowed to occur during such a short time. In

fact, by waiting only for photon pairs τ much less than the timescale of spectral dynamics, we can systematically compile the autocorrelation of the underlying intrinsic spectrum.[9]

Then, once we have identified the underlying intrinsic linewidth, we can slowly increase τ to see how the spectrum diffuses over time. As we'll see when we do the math in the next Chapter, the spectral correlation is given by the convolution of the autocorrelation of the intrinsic spectrum with the probability density function of the spectral dynamics. That is, the probability distribution of how far a spectrum is liable to move from an arbitrary starting point in a given period of time. The probability density function is one of the canonical observables of diffusion processes and can give us key insight into the mechanism of spectral dynamics. Whereas distinguishing between discrete and continuous rapid spectral diffusion mechanisms, for example, is impossible using single-point correlation experiments and requires complicated statistical inference using spectrum-based experiments, these types of spectral diffusion each have their own distinct qualitative footprint in the spectral correlation.

In Figure 2-10, we show modeled spectral correlation functions for three possible types of spectral dynamics. In all three cases, the single emitter's fluorescence spectrum is characterized by a 20 meV Lorentzian intrinsic lineshape that is subject to millisecond timescale spectral dynamics. Nevertheless, each spectral correlation exhibits distinct qualitative features tied to the character of the given spectral diffusion process. Figure 2-10(a) shows the temporal evolution of the spectral correlation of a spectrum diffusing according to a Wiener process (i.e., Brownian motion). The well-known probability density function for this continuous process is simply a single Gaussian function whose full-width at half-max (FWHM) broadens as $\tau^{0.5}$.

In contrast, Figure 2-10(b) shows the spectral correlation for a spectrum diffusing according to the simple discrete model assumed by Sallen et al. [280] and Wolters et al. [283], where the intrinsic spectrum randomly samples the time-averaged spectrum

[9] It is worth noting that depending on our integration time, we can even afford to wait for photon pairs spaced orders of magnitude in time closer than are generally observed based on the average count rate. In this work, our signal intensities are on the order of 10 kcps, or one count every 100 µs, but in some cases, we still have the signal-to-noise to measure the spectral correlation using photon pairs emitted a microsecond apart.

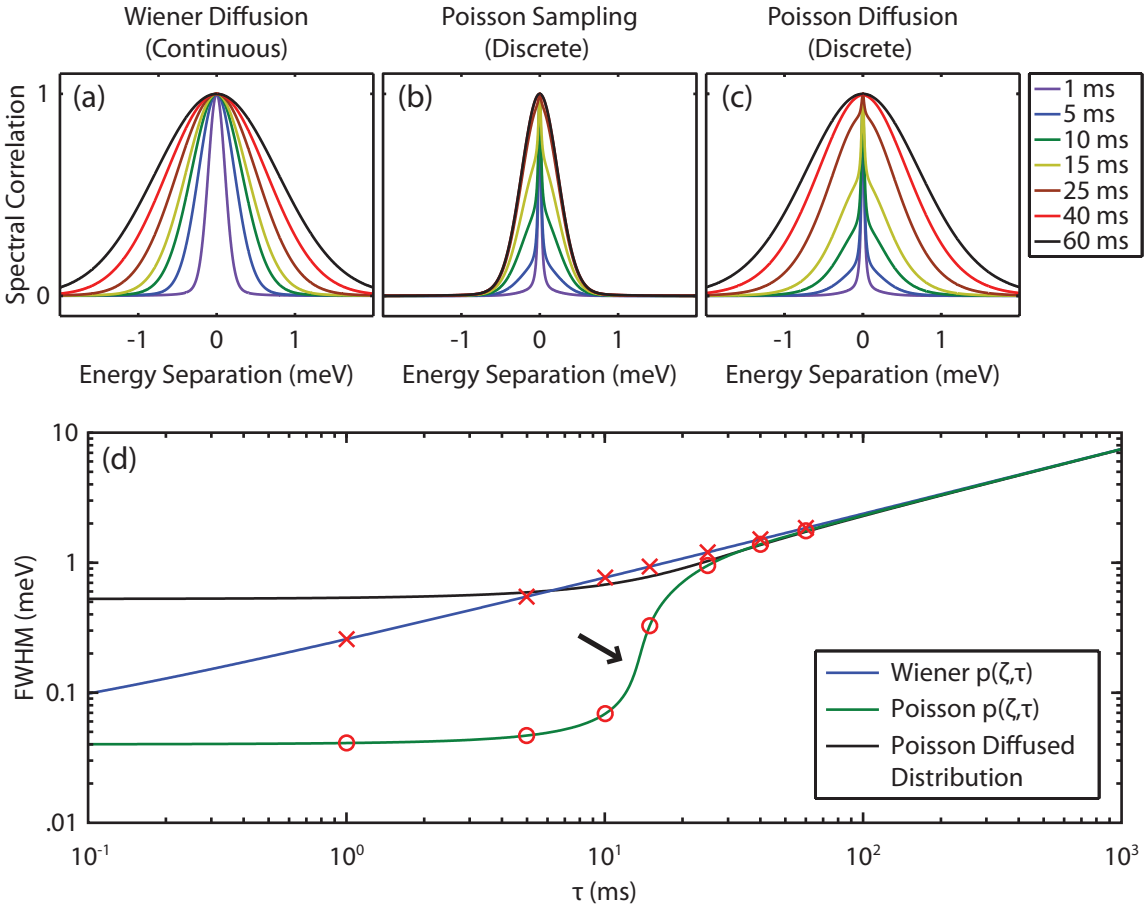

Figure 2-10: The spectral correlation of a single-nanocrystal will be qualitatively different if its spectral diffusion proceeds according to (a) continuous diffusion, (b) the random sampling of a fixed distribution, or (c) discrete diffusion. Discrete diffusion mechanisms can be identified by the existence of multiple distinct distributions of energy shifts corresponding to zero, one, and many spectral diffusion events. (d) This creates a unique evolution of the FWHM of the spectral correlation over time and, specifically, introduces an inflection feature that can serve as evidence for discrete diffusion (see arrow).

according to Poisson statistics. The discrete nature of this model manifests itself in the spectral correlation as a population transfer between two subpopulations of photon pairs. At short τ, the spectral correlation is dominated by the population of photon pairs without a diffusion event between them, which contribute a narrow "nondiffused" distribution (i.e. the autocorrelation of the intrinsic spectrum). Then, as τ increases, probability density is transferred to the population of photon pairs with one or more diffusion event between them. These contribute a constant broad "diffused" distribution given by the autocorrelation of the time-averaged spectrum. The relative weights of these two distributions with τ is closely related to the kinetics of the discrete spectral dynamics, and can be used to extract the time constant of the discrete Poissonian process.

Figure 2-10(c) shows the spectral correlation for a more complicated discrete mechanism, where the spectrum diffuses according to a discrete Gaussian random walk model also governed by Poisson statistics. At short τ, its spectral correlation closely resembles that of the discrete sampling model, characterized by a population transfer from a narrow nondiffused distribution to a broad, Gaussian diffused distribution. However, at intermediate τ, it becomes possible for multiple diffusion events to occur between photon arrivals. Because multiple diffusion events in this mechanism allow the spectrum to move further from its starting point, the diffused distribution begins to broaden and become non-Gaussian.[10] And finally, as the probability of not having a diffusion event vanishes and the probability of many diffusion events increases, the central limit theorem causes the spectral correlation to become Gaussian again and broaden continuously as $\tau^{0.5}$.[11]

There are two key features of this analysis that are important to keep in mind. First, in practice, subtle changes in the shape of the spectral correlation such as the population transfer feature of discrete mechanisms may not necessarily be as obvious as in Fig. 1(b), especially if the diffused and non-diffused distributions have similar linewidths or the measurement has a poor signal-to-noise ratio. Even in these cases,

[10] It is given by a Poissonian distribution of Gaussian functions, which is not a Gaussian function.
[11] Now, it is given by a Gaussian distribution of Gaussian functions, which is a Gaussian function.

some information can be gained from analyzing the evolving FWHM of the spectral correlation (Figure 2-10(d)). Random walk models like the Wiener and Discrete Poisson model will feature a constant broadening of the spectral correlation over many orders of magnitude in time, whereas discrete models like the Discrete Sampling and Discrete Poisson models will feature characteristic inflection points in the FWHM of the spectral correlation on the timescale of the diffusion process. The latter occurs as the FWHM transitions from being defined by the width of the nondiffused distribution to being defined by the width of diffused distribution.

Second, it is important to emphasize that over the long timescales accessible by conventional methods, it is impossible to distinguish between the continuous and discrete random walk models, and it is impossible to distinguish between the discrete sampling model and a particularly broad intrinsic linewidth. Only by measuring spectral dynamics on the actual timescales of the prospective discrete diffusion events using PCFS can we clearly resolve these different spectral diffusion mechanisms.

2.6 The Mission

In this Chapter, we have discussed how the low temperature spectral dynamics of nanocrystals may serve as a useful phenomenon for understanding the subtle physics of nanocrystal surface dynamics. These dynamics fall into three distinct physical categories: charging events that produced large binary shifts in the fluorescence spectrum, trapping events that produced infrequent discrete spectral jumps of variable magnitude, and poorly-understood surface dynamics that produce small spectral jitter. We have been able to infer that the rapid spectral jitter is probably composed of many rapid discrete shifts on millisecond timescales, faster than the integration time required to compile a spectrum using conventional single-molecule spectroscopy, and we have been able to track the correlated effects of these discrete dynamics as they form quasi-continuous subdiffusion of the spectrum over hundreds and thousands of seconds. However, our ability to study this phenomenon in depth has been hindered by the lack of suitable spectroscopic techniques for clearly resolving individual

diffusion events.

There are two primary objectives of Part I of this thesis. First, we will use PCFS to directly observe whether rapid spectral diffusion occurs through the hypothesized discrete mechanism. This effort will demonstrate the practical utility of PCFS in revealing the mechanistic details of subsecond processes in heterogeneous systems. Second, we will combine PCFS with conventional single-molecule spectroscopy to form a single-molecule experiment that can simultaneously measure spectral dynamics across eight orders of magnitude in time ranging from microseconds to hundreds of seconds. We will use this technique to observe the rapid spectral diffusion process of nanocrystals across its discrete and quasicontinuous regimes, forming a unified description of this phenomenon. This work serves as a proof-of-concept for the wholesale characterization of spectral dynamics in individual nanocrystals, and presents the experimental and theoretical tools necessary for a more exhaustive investigation of the effects of nanocrystal architecture on rapid spectral dynamics.

The remainder of this Part is split into three Chapters. Chapter 3 provides a detailed and rigourous derivation of the PCFS experiment as it is implemented in our lab, giving special attention to the role of the dither in PCFS and the known sources of systematic error in PCFS. Chapter 4 provides a quick theoretical look at the connection between the spectral correlation measured by PCFS and the time series of integrated spectra measured by conventional single-nanocrystal spectroscopy. And finally, in Chapter 5, we provide the practical details of our experimental parameters and setup, present our experimental results, and discuss the conceptual consequences of our findings.

Chapter 3

Theory Behind Photon-Correlation Fourier Spectroscopy

Now that we have discussed the need for photon-correlation Fourier spectroscopy (PCFS) and presented a conceptual overview of the technique, we will work through the mathematical details of the experiment and discuss several finer conceptual details important for the reliable and responsible application of PCFS. We begin with a new derivation of the experiment that accurately captures our implementation of the experiment. Then, we conclude with several short discussions on the choice of dither waveform, artifacts and inherent instrument functions in PCFS, correcting for detector dark counts, how to handle possible correlations between spectral and intensity fluctuations, extracting information about the spectral diffusion behavior from the spectral correlation, and understanding the connection between the spectral autocorrelation and the intrinsic spectrum.

3.1 Derivation of Photon-Correlation Fourier Spectroscopy

The derivation of PCFS has developed over time to account for several changes in the experimental procedure and the properties of the samples being measured. The

original derivation by Brokmann et al. [278] derives PCFS using a scanning interferometer and assumes a very narrow spectrum. This derivation was later extended to solution-phase samples by Brokmann et al. [285] and rephrased intuitively in L. F. Marshall's thesis. [287] Marshall's thesis also used the intuition gained from the solution-phase derivation to design a correction for intensity fluctuations that bias the intensity cross-correlation function analyzed in PCFS. More recently, Cui [286] derived the solution-phase PCFS experiment classically considering the diffusion of an underlying spectrum $s(\omega, t)$ rather than a stream of discrete photons with stochastically-determined energies. This allows us to rephrase the PCFS spectral correlation as a convolution of the autocorrelation of the underlying homogeneous spectrum and the probability distribution function of spectral and/or physical diffusion.

In this derivation, we will explicitly account for the dithering procedure used in current PCFS implementations. Although this change significantly complicates the derivation, it allows us to carefully analyze the theoretical requirements for the dither waveform and to explain some of the artifacts that may affect PCFS results.

3.1.1 Notation

For the purposes of this derivation,

- $\langle \cdots \rangle$ denotes a time average over the integration time of a correlation measurement.
- $\mathcal{F}[f(\omega)]_{g(t)}$ denotes a Fourier transform of $f(\omega)$ from energy ω to interferometer path-length difference δ,[1] and evaluated at path-length difference $g(t)$.
- $\mathcal{F}[f(\omega)]^*_{g(t)}$: the complex conjugate of $\mathcal{F}[f(\omega)]_{g(t)}$.
- $f(\omega) \circ g(\omega)$ denotes an energy cross-correlation (with respect to ω, not time).
- $f(\omega) \otimes g(\omega)$ denotes an energy convolution.

The single emitter analyzed by PCFS will be defined by its :

- $S(\omega, t)$: time-dependent spectrum.

[1] Interferometer path-length difference is a proxy for time via the speed of light in the interferometer. This conversion is accounted for with appropriate choice of energy/distance units (i.e. wavenumbers and centimeters, respectively).

- $I(t) = \int S(\omega, t)\,\mathrm{d}\omega$: time-dependent intensity.
- $s(\omega, t) = S(\omega, t) / \int S(\omega, t)\,\mathrm{d}\omega$: normalized spectrum.
- $\omega_0(t) = \int \omega s(\omega, t)\,\mathrm{d}\omega$: average fluorescence energy.
- Fluorescence lineshape $\tilde{s}(\omega)$, such that : $s(\omega, t) = \delta(\omega - \omega_0(t)) \otimes \tilde{s}(\omega)$.
- $P(\zeta, \tau) = \left\langle \int S(\omega, t) S(\omega+\zeta, t+\tau)\,\mathrm{d}\omega \right\rangle$: spectral correlation of the unnormalized spectrum.
- $\tilde{P}(\zeta, \tau) = \frac{P(\zeta,\tau)}{\langle I(t) I(t+\tau)\rangle}$: normalized spectral correlation of the unnormalized spectrum.
- $p(\zeta, \tau) = \left\langle \int s(\omega, t) s(\omega + \zeta, t + \tau)\,\mathrm{d}\omega \right\rangle$: spectral correlation of the normalized spectrum.
- $g(\tau) = \frac{\langle I(t) I(t+\tau)\rangle}{\langle I(t)\rangle \langle I(t+\tau)\rangle}$: autocorrelation of the fluorescence intensity.

And, the PCFS experiment itself will be defined by its :

- δ_0 : average path-length difference for a correlation measurement.
- T : integration time of each correlation function.
- $x(t)$: periodic dither form[2] with period $\hat{T}$.
- $\delta(t) = \delta_0 + x(t)$: time-dependent path-length difference.
- $I_{a/b}(t) = \frac{1}{2} I(t)(1 \pm \mathcal{F}_{\mathbf{cos}}[s(\omega, t)]_{\delta(t)})$: time-dependent interferometer output intensities.
- $g^{\times}(\delta_0, \tau) = \frac{\langle I_a(t) I_b(t+\tau)\rangle}{\langle I_a(t)\rangle \langle I_b(t+\tau)\rangle}$: intensity cross-correlation of the interferometer outputs.
- $c(\tau) = \frac{1}{\hat{T}} \int_0^{\hat{T}} cos\big(\langle \omega_0(t)\rangle (x(t) - x(t+\tau))\big)\,\mathrm{d}t$: dither contribution to cosine transform of the spectral correlation.
- $d(\tau) = \frac{1}{\hat{T}} \int_0^{\hat{T}} sin\big(\langle \omega_0(t)\rangle (x(t) - x(t+\tau))\big)\,\mathrm{d}t$: dither contribution to sine transform of the spectral correlation..

[2] A non-periodic waveform can be captured by setting $\hat{T}$ equal to T.

3.1.2 Assumptions

We will rely on three key assumptions concerning the behavior of the studied single-emitter:

1. **The linewidth of the time-averaged spectrum $\langle S(\omega,t)\rangle$ is narrow compared to the average fluorescence energy $\langle\omega_0\rangle$.**

This assumption is necessary to rephrase the interferogram of the average spectrum as a broad envelope function modulated by a rapid carrier frequency given by $\langle\omega_0\rangle$, and to assert that the envelope magnitude does not vary over a small number of carrier oscillations. If the envelope is slowly modulated compared to the carrier frequency, the average intensity of the interferogram over several fringes will be rigorously zero. This mathematical assertion will be required for several simplifications throughout the derivation.

Nevertheless, in practice and especially in room temperature samples, the envelope of the time-averaged intensity interferogram may vary slightly over a carrier period. There are two major consequences that may stem from this result: 1) terms proportional to the average of the intensity interferogram may not formally go to zero (producing an artifact that is not yet well-understood), and 2) terms proportional to the envelope will be averaged over the dither, broadening the measured interferogram. The effect of the this second consequence is revealed in this derivation and will be discussed in more detail later.

2. **The observed spectral dynamics of the emitter are ergodic.**[3]

There are two major reasons why ergodicity is required in the spectral dynamics of the emitter. First, the PCFS interferogram is compiled by sequentially measuring

[3]For the purposes of this thesis, we use ergodicity to mean that the evolution of the system samples the system's phase space over the integration time of the experiment, rather than over all time. In this way, a system is considered ergodic if many subsequent correlation measurements will all return approximately the same result. I apologize if this usage offends the more rigorous-minded members of the audience.

correlation functions at a variety of interferometer path-length differences. If each of these correlation functions do not report on the same behavior, the PCFS interferogram may be distorted and unpredictable shape artifacts may be introduced into the spectral correlation after inverse Fourier transform. Second, non-ergodic spectral diffusion may cause $\langle\omega_0\rangle$ to change from measurement to measurement, changing the ideal dither amplitude over time. The latter effect is generally not significant in the case of nanocrystal spectral dynamics because of their relatively small magnitude (a 20 meV shift about an average emission wavelength of 600 nm only changes the fringe spacing by about 1%).

The ergodicity assumption is particularly relevant in nanocrystals at low temperatures, which exhibit several different types of spectral dynamics. In Figure 6-5 of L. F. Marshall's Thesis, [287] she demonstrates how infrequent, large spectral shifts on the order of $\sim$10 meV can result in qualitative changes in the fast timescale spectral dynamics and result in segmented, often non-sensical PCFS interferograms. To avoid this effect, PCFS interferograms must be assembled using only emission from distinct spectral positions with similar spectral behavior.

3. **The spectral dynamics of the emitter are independent from the fluorescence intensity fluctuations of the emitter.**

This final assumption concerning the behavior of the studied emitter is really just a notational and conceptual convenience that allows us to mathematically separate integrals containing both spectral and intensity information. Later in the chapter, we will rework the derivation without this assumption and discuss the interpretation of the resulting observable.

We will also rely on three assumptions about the experimental conditions used to study the emitter:

4. **The total magnitude of the dither waveform is small compared to the envelope of the single-emitter's average interferogram.**

Assumption 1 allows us to assert that the average of the intensity interferogram over a small number of carrier frequency cycles is zero. Here, we assert that we are using a dither waveform that actually takes advantage of this. If this is the case, then the dither can be taken to be sampling a sinusoid with magnitude given by the spectral coherence at path-length difference δ_0.

As with Assumption 1, it may not be possible to thoroughly meet this criterion in room temperature samples. This will introduce the same artifacts as a failure to meet Assumption 1, and may be mitigated by dithering over as few fringes as possible.

5. **For the chosen dither waveform:** $\frac{1}{\hat{T}} \int_0^{\hat{T}} \cos(\langle \omega_0(t) \rangle \delta(t))\, \mathrm{d}t = 0$**.**

If all of the other assumptions are satisfied, then the dither is sampling a sinusoidal interferogram. This assumption simply mandates that the time average over the dither causes all terms proportional to the interferogram to vanish. The simplest dither form that satisfies this mathematical condition is a triangle wave with a magnitude given by an integer number of fringes – this is the waveform that we have traditionally used in our group. However, any dither form that satisfies the above equation should produce an accurate PCFS interferogram. In contrast to the earlier assumptions, errors caused by not precisely choosing the correct dither magnitude can be mitigated by dithering over as many fringes as possible.

6. **The integration time of each correlation measurement T is an integer multiple of the dither period $\hat{T}$.**

And finally, we require that each correlation measurement sample an integer number of dither periods to ensure that the equation given in Assumption 5 also holds for averages over the integration time of each correlation measurement. This condition should be easy to meet experimentally with a high degree of precision.

3.1.3 Derivation

Consider the case where the fluorescence signal from a single emitter is sent through an interferometer with time-varying path-length difference $\delta(t) = \delta_0 + x(t)$. The intensity cross-correlation of the interferometer outputs as a function of τ and δ_0 is given by,

$$g^{\times}(\delta_0, \tau) = \frac{\big\langle I_a(t) I_b(t+\tau) \big\rangle}{\big\langle I_a(t) \big\rangle \big\langle I_b(t+\tau) \big\rangle}. \tag{3.1}$$

The intensities of the two outputs of the interferometer are given by the total intensity of the emitter and the Fourier transform of the spectrum at the given time and path-length difference according to the well-known interferometry result,

$$I_{a/b}(t) = \frac{1}{2} I(t)(1 \pm \mathcal{F}_{\mathbf{cos}}[s(\omega, t)]_{\delta(t)}). \tag{3.2}$$

Inserting Equation 3.2 into Equation 3.1 yields,

$$g^{\times}(\delta_0, \tau) = \frac{\Big\langle I(t) I(t+\tau) \Big(1 + \mathcal{F}_{\mathbf{cos}}[s(\omega, t)]_{\delta(t)}\Big) \Big(1 - \mathcal{F}_{\mathbf{cos}}[s(\omega, t+\tau)]_{\delta(t+\tau)}\Big) \Big\rangle}{\Big\langle I(t) \Big(1 + \mathcal{F}_{\mathbf{cos}}[s(\omega, t)]_{\delta(t)}\Big) \Big\rangle \Big\langle I(t+\tau) \Big(1 - \mathcal{F}_{\mathbf{cos}}[s(\omega, t+\tau)]_{\delta(t+\tau)}\Big) \Big\rangle}. \tag{3.3}$$

The denominator can be immediately simplified by noting that the time-dependence of the path-length difference, given by the dither form $x(t)$ has been chosen to average equally over the interference fringes of the time-averaged spectrum. Thus, the denominator is given by,

$$= \Big\langle I(t) \Big(1 + \mathcal{F}_{\mathbf{cos}}[s(\omega, t)]_{\delta(t)}\Big) \Big\rangle \Big\langle I(t+\tau) \Big(1 - \mathcal{F}_{\mathbf{cos}}[s(\omega, t+\tau)]_{\delta(t+\tau)}\Big) \Big\rangle \tag{3.4}$$

$$= \big\langle I(t) \big\rangle \big\langle I(t+\tau) \big\rangle. \tag{3.5}$$

Similarly, the numerator can be expanded by taking advantage of the fact that averages are distributive, yielding,

$$= \big\langle I(t)I(t+\tau)\big\rangle + \big\langle I(t)\mathcal{F}_{\mathbf{cos}}[s(\omega,t)]_{\delta(t)}\big\rangle - \big\langle I(t+\tau)\mathcal{F}_{\mathbf{cos}}[s(\omega,t+\tau)]_{\delta(t+\tau)}\big\rangle$$
$$- \big\langle I(t)I(t+\tau)\mathcal{F}_{\mathbf{cos}}[s(\omega,t)]_{\delta(t)}\mathcal{F}_{\mathbf{cos}}[s(\omega,t+\tau)]_{\delta(t+\tau)}\big\rangle. \tag{3.6}$$

This expanded numerator contains two cross terms that are also first order in the Fourier transform of the spectrum and are averaged to zero by the dither form. Moreover, if the spectral and intensity fluctuations in the emitter are uncorrelated, we can separate the averages of the spectral and intensity terms by noting that the average of the product of two uncorrelated variables is the product of their averages. Applying these two simplifications and reassembling the complete cross-correlation,

$$g^{\times}(\delta_0,\tau) = \frac{\big\langle I(t)I(t+\tau)\big\rangle - \big\langle I(t)I(t+\tau)\mathcal{F}_{\mathbf{cos}}[s(\omega,t)]_{\delta(t)}\mathcal{F}_{\mathbf{cos}}[s(\omega,t+\tau)]_{\delta(t+\tau)}\big\rangle}{\big\langle I(t)\big\rangle\big\langle I(t+\tau)\big\rangle} \tag{3.7}$$

$$= \frac{\big\langle I(t)I(t+\tau)\big\rangle}{\big\langle I(t)\big\rangle\big\langle I(t+\tau)\big\rangle}\Big(1 - \big\langle \mathcal{F}_{\mathbf{cos}}[s(\omega,t+)]_{\delta(t)}\mathcal{F}_{\mathbf{cos}}[s(\omega,t+\tau)]_{\delta(t+\tau)}\big\rangle\Big) \tag{3.8}$$

$$= g(\tau)\left(1 - \big\langle \mathcal{F}_{\mathbf{cos}}[s(\omega,t)]_{\delta(t)}\mathcal{F}_{\mathbf{cos}}[s(\omega,t+\tau)]_{\delta(t+\tau)}\big\rangle\right) \tag{3.9}$$

Equation 3.9 emphasizes that the cross-correlation of the interferometer outputs measured by PCFS reflects not only the spectral information we desire (contained in the product of the cosine transforms), but also information about the intensity fluctuations of the emitter. Without knowing the intensity dynamics of the emitter, it will not be possible to determine whether changes in the cross-correlation are caused by changes in the spectral coherence or whether they are caused by intensity fluctuations like fluorescence intermittancy or microscope drift. Luckily, intensity fluctuations have a simple effect on the cross-correlation, which can be removed as long as we know the intensity autocorrelation of the overall fluorescence signal. The total intensity autocorrelation of the signal can be simultaneously monitored along-

side the cross-correlation by also measuring the autocorrelation of the sum signal of the two outputs $g_{a+b/a+b}(\tau)$. That is, as long as the detectors are well-balanced,

$$I_{a+b}(t) = \frac{1}{2}I(t)(1 + \mathcal{F}_{\mathbf{cos}}[s(\omega,t)]_{\delta(t))} + \frac{1}{2}I(t)(1 - \mathcal{F}_{\mathbf{cos}}[s(\omega,t)]_{\delta(t))} \tag{3.10}$$

$$= I(t), \tag{3.11}$$

And,

$$g_{a+b/a+b}(\tau) = g(\tau). \tag{3.12}$$

To summarize, the spectral contribution to the cross-correlation of the interferometer outputs can be isolated from intensity fluctuations by calculating the ratio of the intensity cross-correlation to the the autocorrelation of the sum signal of the two outputs at each path-length difference δ_0:

$$1 - \frac{g^{\times}(\delta_0,\tau)}{g(\tau)} = \left\langle \mathcal{F}_{\mathbf{cos}}[s(\omega,t)]_{\delta(t)} \mathcal{F}_{\mathbf{cos}}[s(\omega,t+\tau)]_{\delta(t+\tau)} \right\rangle \tag{3.13}$$

We now turn to evaluating the significance of the spectral contribution to the cross-correlation, given by the right side of Equation 3.13. It would be tempting to immediately try to apply the convolution theorem to combine the product of the two Fourier transforms, but there are two major problems with this approach. First of all, strictly, they are cosine transforms, which will require a more complicated version of the convolution theorem. But second, and more importantly, because the dither changes the path-length difference of the interferometer between time t and time $t + \tau$, these cosine transforms are actually being evaluated at different points on the interferogram and cannot be simply combined. Our goal is to remove the time-dependence from the evaluation of the cosine tranform and to convert the cosine transforms to Fourier transforms, so that we can combine the Fourier transforms according to the convolution (or cross-correlation) theorem.

To do this, we need to dig inside the cosine transforms themselves. When we take a look at the integral representation of the first cosine transform, it becomes clear that we can move the dither into the integrand of the cosine transform using the angle sum trigonometric identity,

$$\cos(a+b) = \cos(a)\cos(b) - \sin(a)\sin(b). \tag{3.14}$$

Doing so yields,

$$\begin{aligned}
\mathcal{F}_{\mathbf{cos}}[s(\omega,t)]_{\delta(t)} &= \int_{-\infty}^{\infty} s(\omega,t)\cos(\omega\delta(t))\,\mathrm{d}\omega && (3.15)\\
&= \int_{-\infty}^{\infty} s(\omega,t)\cos(\omega(\delta_0 + x(t)))\,\mathrm{d}\omega && (3.16)\\
&= \int_{-\infty}^{\infty} s(\omega,t)\big(\cos(\omega\delta_0)\cos(\omega x(t)) - \sin(\omega\delta_0)\sin(\omega x(t))\big)\,\mathrm{d}\omega && (3.17)\\
&= \int_{-\infty}^{\infty} [s(\omega,t)\cos(\omega x(t))]\cos(\omega\delta_0)\,\mathrm{d}\omega\\
&\quad - \int_{-\infty}^{\infty} [s(\omega,t)\sin(\omega x(t))]\sin(\omega\delta_0)\,\mathrm{d}\omega && (3.18)\\
&= \mathcal{F}_{\mathbf{cos}}[s(\omega,t)\cos(\omega x(t))]_{\delta_0} - \mathcal{F}_{\mathbf{sin}}[s(\omega,t)\sin(\omega x(t))]_{\delta_0}. && (3.19)
\end{aligned}$$

Similar treatment of the second cosine tranform yields:

$$\begin{aligned}
\mathcal{F}_{\mathbf{cos}}[s(\omega,t+\tau)]_{\delta(t+\tau)} =& \mathcal{F}_{\mathbf{cos}}[s(\omega,t+\tau)\cos(\omega x(t+\tau))]_{\delta_0}\\
&- \mathcal{F}_{\mathbf{sin}}[s(\omega,t+\tau)\sin(\omega x(t+\tau))]_{\delta_0}. && (3.20)
\end{aligned}$$

This "simplification" has turned one term into four terms, but now the sine and cosine transforms in all four terms are evaluated at the same static path-length difference δ_0. Next, we rephrase all of the cosine and sine transforms as Fourier transforms by noting that the cosine transform is the real part of the Fourier transform and the sine transform in the imaginary part. This will turn four terms into sixteen terms, so

a bit of shorthand is required. We will drop the evaluation of the Fourier transforms at the common value δ_0, set the integrands of the cosine terms to A and B, respectively, and set the integrands of the sine terms to C/D, respectively. The left side of Equation 3.13 becomes,

$$=(\mathcal{F}_{\mathbf{cos}}[A]-\mathcal{F}_{\mathbf{sin}}[B])(\mathcal{F}_{\mathbf{cos}}[C]-\mathcal{F}_{\mathbf{sin}}[D]) \tag{3.21}$$

$$=\left(\frac{\mathcal{F}[A]+\mathcal{F}[A]^*}{2}-\frac{\mathcal{F}[B]-\mathcal{F}[B]^*}{2i}\right)\left(\frac{\mathcal{F}[C]+\mathcal{F}[C]^*}{2}-\frac{\mathcal{F}[D]-\mathcal{F}[D]^*}{2i}\right). \tag{3.22}$$

This can be expanded and regrouped to form terms that represent the real and imaginary parts of the Fourier products:

$$\begin{aligned}
= \quad & \frac{(\mathcal{F}[A]\mathcal{F}[C])+(\mathcal{F}[A]\mathcal{F}[C])^*}{4}+\frac{(\mathcal{F}[A]\mathcal{F}[C]^*)+(\mathcal{F}[A]\mathcal{F}[C]^*)^*}{4} \\
& -\frac{(\mathcal{F}[B]\mathcal{F}[D])+(\mathcal{F}[B]\mathcal{F}[D])^*}{4}+\frac{(\mathcal{F}[B]\mathcal{F}[D]^*)+(\mathcal{F}[B]\mathcal{F}[D]^*)^*}{4} \\
& -\frac{(\mathcal{F}[A]\mathcal{F}[D])-(\mathcal{F}[A]\mathcal{F}[D])^*}{4i}+\frac{(\mathcal{F}[A]\mathcal{F}[D]^*)-(\mathcal{F}[A]\mathcal{F}[D]^*)^*}{4i} \\
& -\frac{(\mathcal{F}[B]\mathcal{F}[C])-(\mathcal{F}[B]\mathcal{F}[C])^*}{4i}-\frac{(\mathcal{F}[B]\mathcal{F}[C]^*)-(\mathcal{F}[B]\mathcal{F}[C]^*)^*}{4i}.
\end{aligned} \tag{3.23}$$

Now that all of the terms have been recast as products of Fourier transforms evaluated at δ_0, we can combine the product terms using either the convolution theorem (for the left terms) or the cross-correlation theorem (for the right terms):

$$\begin{aligned}
=\frac{1}{2}\Big(& \mathcal{F}_{\mathbf{cos}}[A\otimes C]+\mathcal{F}_{\mathbf{cos}}[A\circ C]-\mathcal{F}_{\mathbf{cos}}[B\otimes D]+\mathcal{F}_{\mathbf{cos}}[B\circ D] \\
& -\mathcal{F}_{\mathbf{sin}}[A\otimes D]+\mathcal{F}_{\mathbf{sin}}[A\circ D]-\mathcal{F}_{\mathbf{sin}}[B\otimes C]-\mathcal{F}_{\mathbf{sin}}[B\circ C]\Big).
\end{aligned} \tag{3.24}$$

Before proceding with the derivation, it is important to a step back from our

shorthand and note that the use of the convolution and cross-correlation theorems has introduced an additional variable into our mathematics. The cross correlation is defined as,

$$A(\omega) \otimes C(\omega)[\zeta] = \int_{-\infty}^{\infty} A^*(\omega) C(\omega + \zeta)\, \mathrm{d}\omega \tag{3.25}$$

Before combining the products of the Fourier transforms, we had only one energy variable ω, which was the independent variable of both terms in the product, e.g. $\mathcal{F}[A(\omega)]\,\mathcal{F}[B(\omega)]$. Now, by introducing the cross-correlation, we have two energy variables: an absolute energy variable ω, which is integrated over all space inside the operation and does not persist after evaluating the cross-correlation, and a relative energy variable ζ, which is the independent variable of the cross-correlation. As an energy variable, ζ is treated in the same fashion as ω and is the independent energy variable in any Fourier transform of a energy cross-correlation or convolution.

Equation 3.24 can be condensed in three steps. First, we can combine pairs of these terms by reversing the angle sum trigonometric identity used to produce Equations 3.19 and 3.20. For example, the first and third terms can be combined via,

$$\begin{aligned} A \otimes C - B \otimes D = &\left(s(\omega,t)\cos(\omega x(t))\right) \otimes \left(s(\omega,t+\tau)\cos(\omega x(t+\tau))\right) \\ &- \left(s(\omega,t)\sin(\omega x(t))\right) \otimes \left(s(\omega,t+\tau)\sin(\omega x(t+\tau))\right) \quad (3.26) \\ = &\int_{-\infty}^{\infty} s(\omega,t)s(\zeta-\omega,t+\tau)\cos(\omega x(t))\cos\left((\zeta-\omega)x(t+\tau)\right)\,\mathrm{d}\omega \\ &- \int_{-\infty}^{\infty} s(\omega,t)s(\zeta-\omega,t+\tau)\sin(\omega x(t)) \quad (3.27) \end{aligned}$$

$$sin\left((\zeta-\omega)x(t+\tau)\right)\,\mathrm{d}\omega \tag{3.28}$$

$$= \int_{-\infty}^{\infty} s(\omega,t)s(\zeta-\omega,t+\tau)\cos\Big(\omega x(t) + (\zeta-\omega)x(t+\tau)\Big)\,\mathrm{d}\omega. \tag{3.29}$$

After combining the other three pairs of terms in a similar fashion, Equation 3.24

becomes,

$$
\begin{aligned}
=\frac{1}{2}\Big(&\mathcal{F}_{\mathbf{cos}}\left[\int_{-\infty}^{\infty} s(\omega,t)s(\zeta-\omega,t+\tau)\cos(\omega x(t)+(\zeta-\omega)x(t+\tau))\,\mathrm{d}\omega\right]\\
&+\mathcal{F}_{\mathbf{cos}}\left[\int_{-\infty}^{\infty} s(\omega,t)s(\omega+\zeta,t+\tau)\cos(\omega x(t)-(\omega+\zeta)x(t+\tau))\,\mathrm{d}\omega\right]\\
&-\mathcal{F}_{\mathbf{sin}}\left[\int_{-\infty}^{\infty} s(\omega,t)s(\zeta-\omega,t+\tau)\sin(\omega x(t)+(\zeta-\omega)x(t+\tau))\,\mathrm{d}\omega\right]\\
&+\mathcal{F}_{\mathbf{sin}}\left[\int_{-\infty}^{\infty} s(\omega,t)s(\omega+\zeta,t+\tau)\sin(\omega x(t)-(\omega+\zeta)x(t+\tau))\,\mathrm{d}\omega\right]\Big).
\end{aligned}
\tag{3.30}
$$

Second, we can distribute the time-average from Equation 3.13 and simplify each integral with respect to ω. Because the spectral fluctuations are independent from the dither, we can decouple the time averages of the spectral and dither contributions to the integrand, yielding,

$$
\begin{aligned}
=\frac{1}{2}\Big(&\mathcal{F}_{\mathbf{cos}}\left[\int_{-\infty}^{\infty} \big\langle s(\omega,t)s(\zeta-\omega,t+\tau)\big\rangle\big\langle \cos(\omega x(t)+(\zeta-\omega)x(t+\tau))\big\rangle\,\mathrm{d}\omega\right]\\
&+\mathcal{F}_{\mathbf{cos}}\left[\int_{-\infty}^{\infty} \big\langle s(\omega,t)s(\omega+\zeta,t+\tau)\big\rangle\big\langle \cos(\omega x(t)-(\omega+\zeta)x(t+\tau))\big\rangle\,\mathrm{d}\omega\right]\\
&-\mathcal{F}_{\mathbf{sin}}\left[\int_{-\infty}^{\infty} \big\langle s(\omega,t)s(\zeta-\omega,t+\tau)\big\rangle\big\langle \sin(\omega x(t)+(\zeta-\omega)x(t+\tau))\big\rangle\,\mathrm{d}\omega\right]\\
&+\mathcal{F}_{\mathbf{sin}}\left[\int_{-\infty}^{\infty} \big\langle s(\omega,t)s(\omega+\zeta,t+\tau)\big\rangle\big\langle \sin(\omega x(t)-(\omega+\zeta)x(t+\tau))\big\rangle\,\mathrm{d}\omega\right]\Big).
\end{aligned}
\tag{3.31}
$$

Then, because the time-averaged spectrum of the emitter is narrow (that is, its interferogram is broad compared to the dither magnitude), the spectral time-average will only be non-zero in a narrow region of ω. This selects out a very narrow region of the dither component, where $\omega \approx \big\langle \omega_0(t) \big\rangle$, and eliminates everything else.[4] We can therefore substitute $\big\langle \omega_0(t) \big\rangle$ for ω in the dither component and pull it outside of the the convolution/correlation integral. For example, the dither component of the the

[4] In essence, we are saying that from the perspective of the dither, the time-averaged spectrum is approximated by a Dirac δ-function. This is consistent with the idea that the interferogram can be approximated by a cosine over the travel of the dither.

first term becomes,

$$\cos(\omega x(t) + (\zeta - \omega)x(t+\tau)) \approx \cos\left(\left\langle\omega_0(t)\right\rangle x(t) + (\zeta - \left\langle\omega_0(t)\right\rangle)x(t+\tau)\right) \tag{3.32}$$

$$\approx \cos\left(\zeta x(t+\tau) + \left\langle\omega_0(t)\right\rangle(x(t) - x(t+\tau))\right). \tag{3.33}$$

Assembling the full expression yields,

$$\begin{aligned}
&= \frac{1}{2}\mathcal{F}_{\mathbf{cos}}\left[\left\langle\int_{-\infty}^{\infty} s(\omega,t)s(\zeta-\omega,t+\tau)\,\mathrm{d}\omega\right\rangle\left\langle\cos(\zeta x(t+\tau) + \left\langle\omega_0(t)\right\rangle(x(t) - x(t+\tau)))\right\rangle\right] \\
&+ \frac{1}{2}\mathcal{F}_{\mathbf{cos}}\left[\left\langle\int_{-\infty}^{\infty} s(\omega,t)s(\omega+\zeta,t+\tau)\,\mathrm{d}\omega\right\rangle\left\langle\cos(\zeta x(t+\tau) - \left\langle\omega_0(t)\right\rangle(x(t) - x(t+\tau)))\right\rangle\right] \\
&- \frac{1}{2}\mathcal{F}_{\mathbf{sin}}\left[\left\langle\int_{-\infty}^{\infty} s(\omega,t)s(\zeta-\omega,t+\tau)\,\mathrm{d}\omega\right\rangle\left\langle\sin(\zeta x(t+\tau) + \left\langle\omega_0(t)\right\rangle(x(t) - x(t+\tau)))\right\rangle\right] \\
&- \frac{1}{2}\mathcal{F}_{\mathbf{sin}}\left[\left\langle\int_{-\infty}^{\infty} s(\omega,t)s(\omega+\zeta,t+\tau)\,\mathrm{d}\omega\right\rangle\left\langle\sin(\zeta x(t+\tau) - \left\langle\omega_0(t)\right\rangle(x(t) - x(t+\tau)))\right\rangle\right]
\end{aligned} \tag{3.34}$$

Third, we take a closer look at the spectral integrals themselves. The second and fourth terms are the spectral correlation term $p(\zeta,\tau)$ we have been looking for. The first and third terms are slightly different beasts that we will call spectral convolutions, $q(\zeta,\tau)$. Not only do the spectral convolutions and spectral correlations generally have different lineshapes, but they also have different center ζ. Whereas the spectral correlation is centered on zero, the spectral convolution will be centered on $\left\langle 2\omega_0(t)\right\rangle$. This different center-frequency will cause them to interact differently with the dither.

To see this clearly, we can shift the time-dependence back into the evaluation space of the Fourier transform. The difference of the first and third terms can be expanded using the sum angle formula:

$$
\begin{aligned}
=&\mathcal{F}_{\mathbf{cos}}\left[q(\zeta,\tau)\Big\langle \cos(\zeta x(t+\tau)+\big\langle\omega_0(t)\big\rangle(x(t)-x(t+\tau)))\Big\rangle\right]\\
&-\mathcal{F}_{\mathbf{sin}}\left[q(\zeta,\tau)\Big\langle \sin(\zeta x(t+\tau)+\big\langle\omega_0(t)\big\rangle(x(t)-x(t+\tau)))\Big\rangle\right] \qquad (3.35)\\
=&\Big\langle\mathcal{F}_{\mathbf{cos}}\left[q(\zeta,\tau)\cos(\zeta x(t+\tau))\cos(\big\langle\omega_0(t)\big\rangle(x(t)-x(t+\tau)))\right]\Big\rangle\\
&-\Big\langle\mathcal{F}_{\mathbf{cos}}\left[q(\zeta,\tau)\sin(\zeta x(t+\tau))\sin(\big\langle\omega_0(t)\big\rangle(x(t)-x(t+\tau)))\right]\Big\rangle\\
&-\Big\langle\mathcal{F}_{\mathbf{sin}}\left[q(\zeta,\tau)\sin(\zeta x(t+\tau))\cos(\big\langle\omega_0(t)\big\rangle(x(t)-x(t+\tau)))\right]\Big\rangle\\
&-\Big\langle\mathcal{F}_{\mathbf{sin}}\left[q(\zeta,\tau)\cos(\zeta x(t+\tau))\sin(\big\langle\omega_0(t)\big\rangle(x(t)-x(t+\tau)))\right]\Big\rangle, \qquad (3.36)
\end{aligned}
$$

and because the second trigonometric factor of each term is now independent of ζ, it can be pulled out of the Fourier transform, yielding,

$$
\begin{aligned}
=&\Big\langle \cos(\big\langle\omega_0(t)\big\rangle(x(t)-x(t+\tau)))\\
&\times\int_{-\infty}^{\infty}q(\zeta,\tau)\Big(\cos(\zeta x(t+\tau)\cos(\zeta\delta_0)-\sin(\zeta x(t+\tau))\sin(\zeta\delta_0)\Big)\,\mathrm{d}\zeta\Big\rangle\\
&-\Big\langle \sin(\big\langle\omega_0(t)\big\rangle(x(t)-x(t+\tau)))\\
&\times\int_{-\infty}^{\infty}q(\zeta,\tau)\Big(\sin(\zeta x(t+\tau)\cos(\zeta\delta_0)+\cos(\zeta x(t+\tau))\sin(\zeta\delta_0)\Big)\,\mathrm{d}\zeta\Big\rangle. \qquad (3.37)
\end{aligned}
$$

Finally, contracting the dither contribution to the integrand using the sum angle formula reforms the Fourier transforms with a time-dependent evaluation,

$$
\begin{aligned}
=&\Big\langle \cos(\big\langle\omega_0(t)\big\rangle(x(t)-x(t+\tau)))\int_{-\infty}^{\infty}q(\zeta,\tau)\cos\Big(\zeta(\delta_0+x(t+\tau))\Big)\,\mathrm{d}\zeta\Big\rangle\\
&-\Big\langle \sin(\big\langle\omega_0(t)\big\rangle(x(t)-x(t+\tau)))\int_{-\infty}^{\infty}q(\zeta,\tau)\sin\Big(\zeta(\delta_0+x(t+\tau))\Big)\,\mathrm{d}\zeta\Big\rangle \qquad (3.38)\\
=&\Big\langle \cos(\big\langle\omega_0(t)\big\rangle(x(t)-x(t+\tau)))\mathcal{F}_{\mathbf{cos}}[q(\zeta,\tau)]_{\delta_0+x(t+\tau)}\Big\rangle\\
&-\Big\langle \sin(\big\langle\omega_0(t)\big\rangle(x(t)-x(t+\tau)))\mathcal{F}_{\mathbf{sin}}[q(\zeta,\tau)]_{\delta_0+x(t+\tau)}\Big\rangle. \qquad (3.39)
\end{aligned}
$$

Having removed the dither contribution from the integrand of the Fourier transform, we can use the properties of the emitter to remove the time-dependence from the Fourier transform. Let the spectral convolution be given by the convolution of a δ-function carrying its average value and a lineshape term $\tilde{q}(\zeta,\tau)$. Once again, we can assert that the Fourier transform of the spectral component's lineshape is broad compared to the dither form to segregate the effect of the dither from the spectral quantity:[5]

$$\begin{aligned}
=&\Big\langle \cos(\big\langle\omega_0(t)\big\rangle(x(t)-x(t+\tau)))\mathcal{F}_{\mathbf{cos}}[\tilde{q}(\zeta,\tau)\otimes\delta(\zeta-\big\langle 2\omega_0(t)\big\rangle)]_{\delta_0+x(t+\tau)}\Big\rangle \\
&-\Big\langle \sin(\big\langle\omega_0(t)\big\rangle(x(t)-x(t+\tau)))\mathcal{F}_{\mathbf{sin}}[\tilde{q}(\zeta,\tau)\otimes\delta(\zeta-\big\langle 2\omega_0(t)\big\rangle)]_{\delta_0+x(t+\tau)}\Big\rangle \qquad (3.40)\\
=&\Big\langle \cos(\big\langle\omega_0(t)\big\rangle(x(t)-x(t+\tau)))\cos(\big\langle 2\omega_0(t)\big\rangle(\delta_0+x(t+\tau)))\Big\rangle\Big\langle\mathcal{F}_{\mathbf{cos}}[\tilde{q}(\zeta,\tau)]_{\delta_0+x(t+\tau)}\Big\rangle \\
&-\Big\langle \sin(\big\langle\omega_0(t)\big\rangle(x(t)-x(t+\tau)))\sin(\big\langle 2\omega_0(t)\big\rangle(\delta_0+x(t+\tau)))\Big\rangle\Big\langle\mathcal{F}_{\mathbf{sin}}[\tilde{q}(\zeta,\tau)]_{\delta_0+x(t+\tau)}\Big\rangle. \qquad (3.41)
\end{aligned}$$

Identical treatment of the correlation terms yields the same result, but with a minor sign change and without the δ-function shift, i.e.,

$$\begin{aligned}
=&\Big\langle \cos(\big\langle\omega_0(t)\big\rangle(x(t)-x(t+\tau)))\Big\rangle\Big\langle\mathcal{F}_{\mathbf{cos}}[p(\zeta,\tau)]_{\delta_0+x(t+\tau)}\Big\rangle \\
&+\Big\langle \sin(\big\langle\omega_0(t)\big\rangle(x(t)-x(t+\tau)))\Big\rangle\Big\langle\mathcal{F}_{\mathbf{sin}}[p(\zeta,\tau)]_{\delta_0+x(t+\tau)}\Big\rangle. \qquad (3.42)
\end{aligned}$$

Ultimately, we would prefer to focus on the spectral correlation for two reasons. First, it is not modulated by the additional high-frequency (co)sine term, which we suspect will either vanish or behave erratically if the dither is not tightly controlled. And second, unlike the spectral convolution, it will generally be entirely symmetric and

[5] If this were strictly true, the Fourier transform of $\tilde{q}(\zeta,\tau)$ or $p(\zeta,\tau)$ would be explicitly time-independent over its evaluation at $\delta_0+x(t+\tau)$. Here, we allow for subtle time-dependence by splitting the time averages, and assuming that higher-order effects due to coupling between the time averages are negligible.

therefore captured entirely by the cosine transform term.[6]

Therefore, if we want to measure only the spectral correlation terms, we must make sure that the convolution terms rigorously average to zero. Unfortunately, whether the addition of the carrier frequency in the spectral convolution necessarily causes it to vanish over the course of the experiment is not obvious to me. Taking a closer look at the dither average from Equation 3.41, where we will rewrite $\langle \omega_0(t) \rangle$ as ω_0 for convenience and drop the arbitrary phase shift term δ_0,

$$= \Big\langle \cos(\omega_0(x(t) - x(t+\tau))) \cos(2\omega_0 x(t+\tau)) \Big\rangle \tag{3.43}$$

It is obvious from Assumption 5, that the second term will average to zero over the course of a dither period, but it is not obvious without knowledge of the exact dither form whether there could be interactions between the first and second term that could produce an overall non-zero average. As such, we will simply institute a seventh assumption to cover our bases, namely,

7. $\frac{1}{\hat{T}} \int_0^{\hat{T}} \cos(\langle \omega_0(t) \rangle (x(t) - x(t+\tau))) \cos(\langle 2\omega_0(t) \rangle (\delta_0 + x(t+\tau))) \, \mathrm{d}t = 0$**, and**
   $\frac{1}{\hat{T}} \int_0^{\hat{T}} \sin(\langle \omega_0(t) \rangle (x(t) - x(t+\tau))) \sin(\langle 2\omega_0(t) \rangle (\delta_0 + x(t+\tau))) \, \mathrm{d}t = 0$**.**

This assumption will probably follow from the earlier ones with reasonable choice of dither form, but it never hurts to double-check. With this restriction, the convolution terms strictly vanish, and we can reassemble the entire Equation 3.13 to get:

$$1 - \frac{g^{\times}(\delta_0, \tau)}{g(\tau)} = \frac{1}{2} c(\tau) \Big\langle \mathcal{F}_{\mathbf{cos}}[p(\zeta, \tau)]_{\delta_0 + x(t+\tau)} \Big\rangle - \frac{1}{2} d(\tau) \Big\langle \mathcal{F}_{\mathbf{sin}}[p(\zeta, \tau)]_{\delta_0 + x(t+\tau)} \Big\rangle, \tag{3.44}$$

[6] The spectral autocorrelation of the intrinsic spectrum will be rigorously symmetric, the only question is whether the probability distribution function of the spectral dynamics is symmetric. Most simple models feature symmetric probability distribution functions, but we will discuss later how we could deal with asymmetry.

where $c(\tau)$ is defined as the dither contribution to the cosine term,

$$c(\tau) = \frac{1}{\hat{T}} \int_0^{\hat{T}} \cos\big(\langle\omega_0(t)\rangle(x(t) - x(t+\tau))\big)\,\mathrm{d}t, \tag{3.45}$$

and where $d(\tau)$ is defined as the dither contribution to the sine term,

$$d(\tau) = \frac{1}{\hat{T}} \int_0^{\hat{T}} sin\big(\langle\omega_0(t)\rangle(x(t) - x(t+\tau))\big)\,\mathrm{d}t. \tag{3.46}$$

For the sake of general cleanliness, if we consider a time-averaged spectrum whose interferogram is *much* broader than the dither magnitude, the time-averages on the spectral correlation vanish, yielding,

$$1 - \frac{g^{\times}(\delta_0, \tau)}{g(\tau)} = \frac{1}{2}c(\tau)\mathcal{F}_{\mathbf{cos}}[p(\zeta,\tau)]_{\delta_0} - \frac{1}{2}d(\tau)\mathcal{F}_{\mathbf{sin}}[p(\zeta,\tau)]_{\delta_0}, \tag{3.47}$$

This final expression closely resembles the results of previous derivations, but still feature a couple notable differences due to our general treatment of the dither form. In the next sections, we will highlight several conceptual points that have been raised over the course of this derivation, and discuss their consequences for the practical application of PCFS.

3.2 Chosing a Dither Waveform

One of the more notable features of this result is that it predicts the dither contribution to the measured cross-correlation function. This is important because the spectral-dependence of the cross-correlation is scaled by the total dither contrast; if $c(\tau)$ or $d(\tau)$ is zero, the corresponding transform of the spectral correlation will not even be represented in the cross-correlation. We begin our discussion of the effect of the dither on PCFS by evaluating $c(\tau)$ and $d(\tau)$ for three possible dither forms.

3.2.1 Several Dither Examples

Scanning Dither. The first implementations of PCFS did not use a dither waveform at all. [273, 279] Instead, they took correlation measurements while continuously scanning the interferometer. As we will see in the next section, a scanning procedure can have a negative impact on the resolution of the experiment by introducing an unneccessary interdependence between integration time, instrument function, and resolution. Nevertheless, scanning is a very convenient way to introduce a reliable and reproducible modulation into the interferometer path-length difference. Here, we capture the scanning result by considering a periodic linear increase in the path-length difference with period given by the integration time of the experiment (i.e. $T = \hat{T}$), such that over the integration time, the path-length difference is given by,

$$x(t) = v_0 t. \tag{3.48}$$

Inserting this expression into Equation 3.45 yields,

$$\begin{aligned} c(\tau) =& \frac{1}{\hat{T}} \int_0^{\hat{T}} \cos(\langle \omega_0(t) \rangle (x(t) - x(t+\tau))) \, \mathrm{d}t & (3.49) \\ =& \frac{1}{\hat{T}} \int_0^{\hat{T}} \cos(\langle \omega_0(t) \rangle (v_0 t - v_0 (t+\tau))) \, \mathrm{d}t & (3.50) \\ =& \frac{1}{\hat{T}} \int_0^{\hat{T}} \cos(\langle -\omega_0(t) \rangle v_0 \tau) \, \mathrm{d}t = \cos(\langle \omega_0(t) \rangle v_0 \tau), & (3.51) \end{aligned}$$

and inserting it into Equation 3.46 yields,

$$\begin{aligned} d(\tau) =& \frac{1}{\hat{T}} \int_0^{\hat{T}} \sin(\langle \omega_0(t) \rangle (x(t) - x(t+\tau))) \, \mathrm{d}t & (3.52) \\ =& \frac{1}{\hat{T}} \int_0^{\hat{T}} \sin(-\langle \omega_0(t) \rangle v_0 \tau) \, \mathrm{d}t & (3.53) \\ =& -\sin(\langle \omega_0(t) \rangle v_0 \tau), & (3.54) \end{aligned}$$

which gives the final PCFS solution,

$$1 - \frac{g^{\times}(\delta_0, \tau)}{g(\tau)} = \frac{1}{2}\cos(\langle\omega_0(t)\rangle v_0\tau)\mathcal{F}_{\mathbf{cos}}[p(\zeta,\tau)]_{\delta_0} + \frac{1}{2}\sin(\langle\omega_0(t)\rangle v_0\tau)\mathcal{F}_{\mathbf{sin}}[p(\zeta,\tau)]_{\delta_0}. \tag{3.55}$$

Two features are worthy of particular attention. First, the cosine transform term perfectly agrees with the result derived by Brokmann et al. [278], and we maintain a sine transform term where Brokmann et al. did not, simply because we acknowledge the possibility of an asymmetric spectral correlation (which will be discussed later). Second, this sine term appears to be pathological due to the odd-character of the sine prefactor. After all, intensity correlation functions should be symmetric in time and sines are not. However, the sine prefactor does actually make sense in the context of an asymmetric spectral correlation because it serves to counteract the time-inversion properties of the sine transform itself. Negating τ not only introduces a sign flip into the prefactor, but it also reflects the spectral correlation across the y-axis because the spectrum is now traveling in the opposite direction (which flips the sign of the sine transform). The product of the sine transform and sine prefector gives us a correlation feature that is symmetric in τ.[7]

Triangle Dither. Once we invented the concept of dithering in PCFS, the dither form we began using was the triangle dither. Instead of a continuous scan, we simply scanned the interferometer back and forth over a narrow path-length difference region, according to the waveform,

$$x(t) = A\left(\frac{2t}{\hat{T}} - 1 - \left\lfloor\frac{2t}{\hat{T}}\right\rfloor\right)(-1)^{\left\lfloor\frac{2t}{\hat{T}}\right\rfloor}, \tag{3.56}$$

[7]There is considerable subtlety in the sign of the correlation feature itself. But, we will not get into this here because we are going to avoid the issue of resolving asymmetric spectral correlations entirely.

where $\lfloor \cdots \rfloor$ denotes the floor function, and A is half the total path-length difference traveled during the dither. In fact, this is still the dither waveform used for the work in this thesis because it is easy to understand conceptually, its amplitude is easy to measure and calibrate at the white fringe, and it yields approximately the same result as the scanning version of the experiment.

To see this mathematically, we will consider a τ less than the dither period $\hat{T}$, and break up the integral expressions for $c(\tau)$ and $d(\tau)$ into the four piecewise units where the waveform at times t and $t+\tau$ evaluate to regions of either positive or negative slope. That is,

$$c(\tau) = \frac{1}{\hat{T}} \int_0^{\hat{T}} \cos(\langle \omega_0(t) \rangle (x(t) - x(t+\tau))) \, \mathrm{d}t \tag{3.57}$$

$$\begin{aligned} =& \frac{1}{\hat{T}} \Bigg(\int_0^{\hat{T}/2-\tau} \cos\left(A \langle \omega_0(t) \rangle \left(\left[\frac{2t}{\hat{T}} - 1 \right] - \left[\frac{2(t+\tau)}{\hat{T}} - 1 \right] \right) \right) \mathrm{d}t \\ &+ \int_{\hat{T}/2-\tau}^{\hat{T}/2} \cos\left(A \langle \omega_0(t) \rangle \left(\left[\frac{2t}{\hat{T}} - 1 \right] - \left[-\frac{2(t+\tau)}{\hat{T}} + 2 \right] \right) \right) \mathrm{d}t \\ &+ \int_{\hat{T}/2}^{\hat{T}-\tau} \cos\left(A \langle \omega_0(t) \rangle \left(\left[-\frac{2t}{\hat{T}} + 2 \right] - \left[-\frac{2(t+\tau)}{\hat{T}} + 2 \right] \right) \right) \mathrm{d}t \\ &+ \int_{\hat{T}-\tau}^{\hat{T}} \cos\left(A \langle \omega_0(t) \rangle \left(\left[-\frac{2t}{\hat{T}} + 2 \right] - \left[\frac{2(t+\tau)}{\hat{T}} - 3 \right] \right) \right) \mathrm{d}t \Bigg), \end{aligned} \tag{3.58}$$

where the first and third terms and second and fourth terms are identical because cosines are even functions. Thus, using a little bit of variable substitution,

$$\begin{aligned} =& \frac{2}{\hat{T}} \Bigg(\int_0^{\hat{T}/2-\tau} \cos\left(\frac{2A \langle \omega_0(t) \rangle \tau}{\hat{T}} \right) \mathrm{d}t \\ &+ \int_{\hat{T}/2-\tau}^{\hat{T}/2} \cos\left(A \langle \omega_0(t) \rangle \left(\frac{4t}{\hat{T}} + \left[\frac{2\tau}{\hat{T}} - 3 \right] \right) \right) \mathrm{d}t \Bigg) \end{aligned} \tag{3.59}$$

$$\begin{aligned} =& \frac{2}{\hat{T}} \Bigg(\int_0^{\hat{T}/2-\tau} \cos\left(\frac{2A \langle \omega_0(t) \rangle \tau}{\hat{T}} \right) \mathrm{d}t \\ &+ \int_0^{\tau} \cos\left(A \langle \omega_0(t) \rangle \left(\frac{4t}{\hat{T}} - \left[\frac{2\tau}{\hat{T}} + 1 \right] \right) \right) \mathrm{d}t \Bigg) \end{aligned} \tag{3.60}$$

$$
\begin{aligned}
=&(1-\frac{2\tau}{\hat{T}})\cos\left(\frac{2A\langle\omega_0(t)\rangle\tau}{\hat{T}}\right)\\
&+\frac{2}{\hat{T}}\cos\left(A\langle\omega_0(t)\rangle\left(\frac{2\tau}{\hat{T}}+1\right)\right)\int_0^\tau\cos\left(\frac{4A\langle\omega_0(t)\rangle t}{\hat{T}}\right)\,\mathrm{d}t\\
&-\frac{2}{\hat{T}}\sin\left(A\langle\omega_0(t)\rangle\left(\frac{2\tau}{\hat{T}}+1\right)\right)\int_0^\tau\sin\left(\frac{4A\langle\omega_0(t)\rangle t}{\hat{T}}\right)\,\mathrm{d}t \qquad (3.61)\\
=&(1-\frac{2\tau}{\hat{T}})\cos\left(\frac{2A\langle\omega_0(t)\rangle\tau}{\hat{T}}\right)\\
&+\frac{1}{2A\langle\omega_0(t)\rangle}\cos\left(A\langle\omega_0(t)\rangle\left(\frac{2\tau}{\hat{T}}+1\right)\right)\sin\left(\frac{4A\langle\omega_0(t)\rangle\tau}{\hat{T}}\right)\\
&+\frac{1}{2A\langle\omega_0(t)\rangle}\sin\left(A\langle\omega_0(t)\rangle\left(\frac{2\tau}{\hat{T}}+1\right)\right)\left(1-\cos\left(\frac{4A\langle\omega_0(t)\rangle\tau}{\hat{T}}\right)\right). \qquad (3.62)
\end{aligned}
$$

The reverse sweep of the triangle wave clearly adds complexity to the cosine dither contribution, but only when τ approaches the timescale of the dither period. This is due to the regions of time when the dither is scanning in one direction at time t, but the other direction at time $t+\tau$. When $\tau \ll \hat{T}$, the final two terms vanish and the first term reduces to the scanning dither result.

The reverse sweep also has a huge impact on the sine dither contribution. If we follow the same procedure to find $d(\tau)$, we would get the same four piecewise terms from Equation 3.58 with sines instead of cosines. However, because sines are odd instead of even, the corresponding terms cancel instead of add, yielding,

$$d(\tau) = 0. \qquad (3.63)$$

In general, we expect the asymmetric component of the spectral correlation to vanish for any dither waveform with a reverse sweep identical to its forward sweep.[8]

[8] If you are interested in maintaining the asymmetric component of the spectral correlation, the triangle wave can be substituted with a sawtooth wave (or asymmetric triangle wave). The math is largely the same, but the sine terms will no longer cancel.

Sine Dither. Finally, there has also been some interest in our group in using a sinusoidal dither. It can be easier to implement using linear stages, and because it is wholly continuous and differentiable, it can be implemented with higher fidelity and reproducibility.[9] Consider the dither waveform given by $x(t) = \frac{A}{2}\sin(\frac{2\pi t}{\hat{T}})$. Like the triangle wave, it is a symmetric dither, so,

$$d(\tau) = 0. \tag{3.64}$$

Its cosine dither contribution is given by,

$$\begin{aligned}
c(\tau) =& \frac{1}{\hat{T}}\int_0^{\hat{T}} \cos(\langle\omega_0(t)\rangle(x(t) - x(t+\tau)))\,\mathrm{d}t && (3.65)\\
=& \frac{1}{\hat{T}}\int_0^{\hat{T}} \cos\left(\frac{A\langle\omega_0(t)\rangle}{2}\left(\sin(\frac{2\pi t}{\hat{T}}) - \sin(\frac{2\pi(t+\tau)}{\hat{T}}\right)\right)\,\mathrm{d}t && (3.66)\\
=& \frac{1}{\hat{T}}\int_0^{\hat{T}} \cos\left(\frac{A\langle\omega_0(t)\rangle}{2}\left(\sin(\frac{2\pi t}{\hat{T}}) - \sin(\frac{2\pi t}{\hat{T}})\cos(\frac{2\pi\tau}{\hat{T}}) - \cos(\frac{2\pi t}{\hat{T}})\sin(\frac{2\pi\tau}{\hat{T}})\right)\right)\,\mathrm{d}t && (3.67)\\
=& \frac{1}{\hat{T}}\int_0^{\hat{T}} \cos\left(\frac{A\langle\omega_0(t)\rangle}{2}\left(\left[(1-\cos(\frac{2\pi\tau}{\hat{T}}))\right]\sin(\frac{2\pi t}{\hat{T}}) - \left[\sin(\frac{2\pi\tau}{\hat{T}})\right]\cos(\frac{2\pi t}{\hat{T}})\right)\right)\,\mathrm{d}t && (3.68)
\end{aligned}$$

This expression looks like a mess, but it turns out that it is the definition of a zeroeth-order Bessel function of the first kind,

$$\int_0^{2\pi} \cos(A\sin(x) - B\cos(x))dx = 2\pi J_0(\sqrt{A^2+B^2}), \tag{3.69}$$

which is better known as a sinc function. Applying this formula,

[9] That said, using a sine dither can also be a little theoretically concerning because it does not equally sample all path-difference points along the dither travel. Even if the time-averaged interferogram in the vicinity of the dither is well-approximated by a sine function, the dither may not strictly average away the terms that are first-order in the Fourier transform. Special attention should be paid to whether the sine dither obeys Assumptions 5 and 7.

$$c(\tau) = J_0\left(\frac{A\langle\omega_0(t)\rangle}{2}\sqrt{\left[(1-\cos(\frac{2\pi\tau}{\hat{T}}))\right]^2+\left[\sin(\frac{2\pi\tau}{\hat{T}})\right]^2}\right) \tag{3.70}$$

$$= J_0\left(\frac{A\langle\omega_0(t)\rangle}{\sqrt{2}}\sqrt{1-\cos(\frac{2\pi\tau}{\hat{T}})}\right) \tag{3.71}$$

This dither contribution behaves similarly to that of the triangle dither, except there will be an additional modulation of the overall magnitude over τ beyond the oscillation feature because of the Bessel function decay.

3.2.2 Properties of the Ideal Dither

All three of the dither waveforms explored here are valid options for implementing PCFS. Nevertheless, there are several concerns that must be taken into account when selecting parameters for the dither waveform, such as amplitude and period. There are four major properties that an ideal dither waveform should exhibit.

First, it obviously should satisfy the assumptions stated in the derivation that cause the $\langle\omega_0\rangle$ and $\langle 2\omega_0\rangle$ terms to vanish. In the case of the $\langle\omega_0\rangle$ terms, at least, this is simply a matter of ensuring that each interferometer output equally samples the peaks and troughs of the time-averaged interferogram. And luckily, the satifaction of this requirement can be easily verified experimentally by measuring the countrate on the two detection channels over the course of a correlation measurement. If the average countrate on each channel is equal to the average countrate that would have been measured outside of the sample's interferometric coherence length, the $\langle\omega_0\rangle$ terms will have vanished.

Second, the dither waveform should have the appropriate parity. This is a minor consideration only pertinent in certain irregular cases. We have shown that dither waveforms that scan only in one direction are capable of measuring an antisymmetric

component of the spectral correlation, whereas dither waveforms that equally sample scans in both directions entirely supress the anti-symmetric component. Therefore, if there is a possibility that a spectral diffusion mechanism has an asymmetric probability distribution function, this may be evaluated by comparing the PCFS results using a symmetric and an antisymmetric dither waveform.[10] My impression is that under normal circumstances, a symmetric waveform should be chosen because they are easy to reliably implement experimentally and because they may minimize the effects of minor non-ergodicity by suppressing the anti-symmetric component of the spectral correlation.

Third, the dither waveform should be slow. The above derivations demonstrate two important points concerning the choice of dither: each waveform has a unique functional contribution to the intensity cross-correlation, but they all contain oscillating features at the timescale it takes to move across an interference fringe. These oscillations can hamper the measurement of the spectral correlation because they introduce wide variations in the total interferometric contrast. All information about the spectral correlation is lost at the nodes $c(\tau)$ and $d(\tau)$, and the magnitude of the spectral feature is dramatically dimininished in their vicinity. In principle, our goal is to maximize the spectral correlation signal throughout the timescales of interest. This can be accomplished by choosing a dither waveform that is slow compared to the timescales of interest in the PCFS experiment.

Consider the case where $x(t) \approx x(t+\tau)$ for all t during the dither period and for all τ being measured for PCFS. In this case,

[10] Note that an antisymmetric dither will have to be rapid in order to capture the antisymmetric component of the spectral correlation because its sine prefactor vanishes as $\tau \to 0$.

$$c(\tau) = \frac{1}{\hat{T}} \int_0^{\hat{T}} \cos(\langle \omega_0(t) \rangle (x(t) - x(t+\tau))) \, \mathrm{d}t \tag{3.72}$$

$$\approx \frac{1}{\hat{T}} \int_0^{\hat{T}} \cos(0) \, \mathrm{d}t \tag{3.73}$$

$$\approx 1, \tag{3.74}$$

and,

$$d(\tau) = \frac{1}{\hat{T}} \int_0^{\hat{T}} \sin(\langle \omega_0(t) \rangle (x(t) - x(t+\tau))) \, \mathrm{d}t \tag{3.75}$$

$$\approx \frac{1}{\hat{T}} \int_0^{\hat{T}} \sin(0) \, \mathrm{d}t \tag{3.76}$$

$$\approx 0. \tag{3.77}$$

Given that $c(\tau)$ and $d(\tau)$ are averages of sines and cosines, these conditions yield the maximum amplification of the symmetric component of the spectral correlation and the complete elimination of the antisymmetric component, even for antisymmetric dither waveforms. This is the optimal result for a conventional PCFS experiment, and it can be achieved in a slow dither without the need for precise engineering of the dither waveform.

Fourth, for the reasons discussed in the next section, the three previous properties should be achieved using a dither waveform with the smallest amplitude possible. This will minimize the PCFS instrument function introduced by the dither waveform itself, which affects the investigation of samples with particularly broad fluorescence spectra.

3.3 Artifacts and Instrument Functions in PCFS

In practice, the spectral correlation measured by PCFS is susceptible to a wide variety of different artifacts and sources of distortion. Here, we enumerate and discuss the major examples that we have identified and have attempted to mitigate.

Transmission Profile of Setup. Before even considering the details of PCFS, the single emitter signal analyzed by the PCFS experiment can be biased by the transmission profile of the setup. Special care should, of course, be taken to ensure that emission filters, mirrors, and other optics are fully compatible with the spectral profile of the signal. Edgepass artifacts can be produced when the signal is at the edge of the spectral range of the optical components, and will artificially narrow the detected spectral correlations. Interference artifacts may also be possible when using optics like pellicles, which may introduce small oscillations into the spectral correlation. When the signal's time averaged spectrum is particularly broad, correction for the spectral response of the detectors may also be required.

Usually, transmission artifacts can be identified by measuring the ensemble fluorescence spectrum of the sample using an independent instrument, such as the Fluoromax, and ensuring that the published specifications of all optics provide high, featureless transmission in that spectral region. It may also be helpful when conducting solution-phase experiments to compare the spectral correlation of the ensemble to the autocorrelation of the spectrum as measured by the Fluoromax or other conventional spectroscopic experiment.

Interferometer Alignment and Calibration/Drift. Once the signal is passed into the interferometer, its behavior is also highly dependent on the alignment of the interferometer. In our derivation, we have assumed a perfectly aligned interferometer with perfect spatial overlap of the recombined signals over all path-length differences.

This ideal interferometer offers perfect constructive/destructive interference at zero path-length difference and accurately represents the decay of spectral coherence of the emitter as the path-length difference is increased. Unfortunately, real-life interferometers may not be perfectly aligned.

There are two major types of interferometer misalignment. First, the recombined signals may not be perfectly spatially overlapped at zero path-length difference. This will lead to a decrease in the total interferometric contrast, which adversely affects the signal-to-noise of the measured spectral correlation. Whereas the spectral component of an ideal PCFS intensity cross-correlation at zero path-length difference will have a total magnitude of (negative) 0.5, poor white fringe overlap will result in a correlation feature with magnitude less than 0.5. Control experiments have suggested to us that as long as the PCFS contrast at zero path-length difference is above 0.3, the shape of the PCFS interferogram will generally be unaffected by this type of misalignment. However, maximized interferometer contrast is still desiriable for maximized signal-to-noise ratios under similar experimental conditions.

Second, the propagation vector of the variable path length arm may not be co-linear with the stage propagation vector. This source of misalignment causes the spatial overlap of the recombined signals to change with path-length difference. If the signals are perfectly overlapped at zero path-length difference, the spectral coherence measured by the interferometer will decay artificially quickly with increasing path-length difference because of the increasingly poor spatial overlap (rather than an actual loss of spectral coherence). This results in an artificially narrow measured interferogram and an artificially broad measured spectrum. To avoid this misalignment effect, the interferometer should be aligned by centering the interference fringes *both* at the white fringe and at a path-length difference exceeding the coherence length of the sample. These alignments can be enacted by adjusting the spatial position of the interferometer retroreflectors to optimize white fringe overlap, and by adjusting

the input vector of the signal into the interferometer to optimize large path-length difference overlap.[11]

Poor white fringe overlap and non-colinearity can combine to produce a dazzling array of strange artifacts, including asymmetric spectral correlations (even when using a symmetric dither waveform) and even dips in the PCFS contrast in the vicinity of the white fringe. Many of these artifacts are poorly understood, but all are undesirable. In order to confirm proper alignment, certain control experiments should be performed after each interferometer alignment. If the PCFS setup will be used to measure a narrow signal such as the low temperature zero phonon line of nanocrystal fluorescence, PCFS should be performed on a known narrow signal, such as a laser, to gauge the white fringe contrast and to place an upper bound on the extent of non-colinearity.[12] If the PCFS setup will be used to measure a broad signal such as room temperature spectra, PCFS should be performed on a known and well-behaved nanocrystal sample, to gauge white fringe contrast, confirm spectral correlation symmetry, and to verify the measured lineshape of the known sample especially near the white fringe.

Finally, the measured PCFS interferogram may also be distorted by errors in stage positioning or by interferometer drift, which may cause systematic error in the actual path-length difference of each correlation measurement. Modern stages should have adequate positioning uncertainty and calibration for homodyne measurements like PCFS that do not need to resolve the carrier frequency of the fluorescence, but our setups have been seen to drift on the order of half a micron over hours of experimental time. To mitigate this effect, PCFS experiments should generally be conducted in a single sweep of the list of desired path-length differences for correlation measure-

[11] These are not decoupled degrees of freedom, so interferometer alignment becomes an iterative process much like a beam walk through a pair of irises.

[12] If the sample exhibits a linewidth narrower than the laser source, we will not know if that linewidth is physical or representative of the interferometer instrument function.

ments.[13] For particularly long experiments, multiple sweeps with shorter correlation integration times may be used, but each of these sweeps should be processed independently and only averaged after calculating the spectral correlation. Interferometer drift between scans may shift the white fringe over time and produce an artificially broad PCFS interferogram.

Dither Magnitude. Whereas poor interferometer alignment may limit the ability for PCFS to measure exceptionally narrow linewidths, the dither waveform places some limitations on how broad a linewidth PCFS can measure. Our assumptions posit that the time-averaged linewidth of the sample is narrow compared to its center frequency and that the dither waveform has a smaller magnitude than the curvature of the envelope of the time-averaged interferogram. But, what happens when we begin to push these assumptions a little bit?

The answer is contained in the time averages of Equation 3.44. Consider the cosine average,

$$\left\langle \mathcal{F}_{\mathbf{cos}}[p(\zeta,\tau)]_{\delta_0+x(t+\tau)} \right\rangle = \frac{1}{T}\int_0^T \int_{-\infty}^{\infty} p(\zeta,\tau)\cos(\zeta(\delta_0+x(t+\tau)))\,\mathrm{d}\zeta\,\mathrm{d}t. \tag{3.78}$$

This expression essentially notes that because of the dither waveform, we are not simply evaluating the Fourier transform of $p(\zeta,\tau)$ at a single point, but actually measuring a weighted-average of this Fourier transform over the time spent at each path-length difference $\delta_0 + x(t+\tau)$. In other words,

$$\left\langle \mathcal{F}_{\mathbf{cos}}[p(\zeta,\tau)]_{\delta_0+x(t+\tau)} \right\rangle = \int_{-\infty}^{\infty} \rho(x)\mathcal{F}_{\mathbf{cos}}[p(\zeta,\tau)]_{\delta_0+x}\,\mathrm{d}x, \tag{3.79}$$

where $\rho(x)$ is the probability distribution function of finding the dither waveform at the given path-length difference during the integration time of the correlation

[13] Older stages had inadequate positioning precision, so we previously used a three-scan procedure to average over positioning uncertainty. This is no longer necessary.

measurement. The calculation of $\rho(x)$ depends highly on the dither waveform being used. The triangle wave, for example, has a probability distribution function of,

$$\rho(x)_{\text{triangle}} = \frac{1}{2A}\text{rect}(2Ax), \tag{3.80}$$

where rect$(\cdots)$ represents a rectangular function, because each position on the dither is equally sampled during the forward and reverse sweeps.

Furthermore, Equation 3.79 can actually be seen as a cross-correlation in path-length difference, i.e.,

$$\left\langle \mathcal{F}_{\mathbf{cos}}[p(\zeta,\tau)]_{\delta_0+x(t+\tau)} \right\rangle = \rho(x) \circ \mathcal{F}_{\mathbf{cos}}[p(\zeta,\tau)]_x, \tag{3.81}$$

where δ_0 is the independent variable of the correlation and x is the integrated variable. In essence, the measured PCFS interferogram is the convolution of the actual PCFS interferogram and an instrument function given by $\rho(x)$. To measure a spectrally broad sample with a very narrow interferogram, it will be important to choose the smallest dither amplitude possible in order to decrease the width of the dither probability distribution function.

The interferometer alignment and dither waveform combine to form a Fourier transform conjugate pair of instrument functions for the PCFS experiment that limit the range of energy spacings that can be probed by the experiment. This is illustrated in Figure 3-1. The narrowest possible feature that can be resolved is given by the interferometer alignment, which is a multiplicative bandwidth feature in path-length difference and a convolution feature in energy. The broadest possible feature that can be resolved is given by the dither waveform, which is a convolution feature in path-length difference and multiplicative bandwidth feature in energy. Depending on the spectral characteristics of the sample, either or both of these PCFS instrument functions must be noted and characterized.

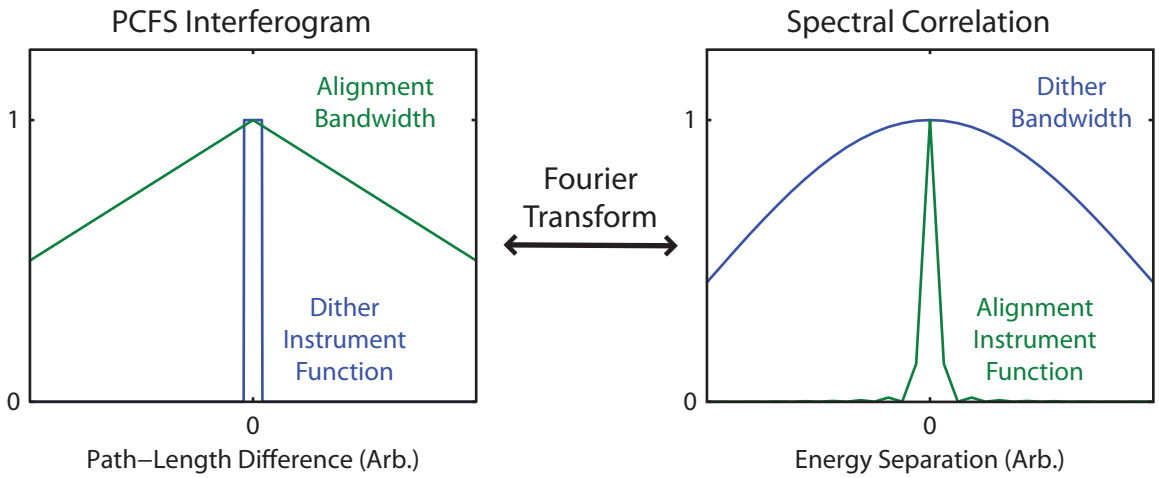

Figure 3-1: The interferogram measured by a PCFS experiment has been convolved with an instrument function defined defined by the dither and multiplied by a bandwidth profile defined by the interferometer alignment. After Fourier transform, the dither defines the bandwidth of the measured spectral correlation and the alignment defines the instrument function.

Afterpulsing. There are also two important sources of error for measuring the autocorrelation of the sum signal $g(\tau)$. The first is detector afterpulsing. When a photon is detected using an avalanche photodiode, it triggers the generation of a large number of excited electron-hole pairs on the active area of the detector. These carriers are sometimes trapped, and may trigger a second detection event when they de-trap. [288] This effect introduces a multi-exponential feature into intensity autocorrelation functions on the timescale of hundreds of nanoseconds (Figure 3-2), which is inversely proportional to the signal intensity in intensity correlation functions. For particularly weak signals on the order of thousands of counts per second, this decay feature can bleed into the microsecond-to-millisecond timescales investigated using PCFS.

The result of afterpulsing is an artificially increased autocorrelation of the sum signal that inflates the percieved anticorrelation between the detection channels. Because this feature is not dependent on path-length difference, it manifests in the PCFS interferogram as a constant offset value at short τ, which increases the $\zeta = 0$ value of the spectral correlation. This artifact may be obvious if the PCFS interferogram

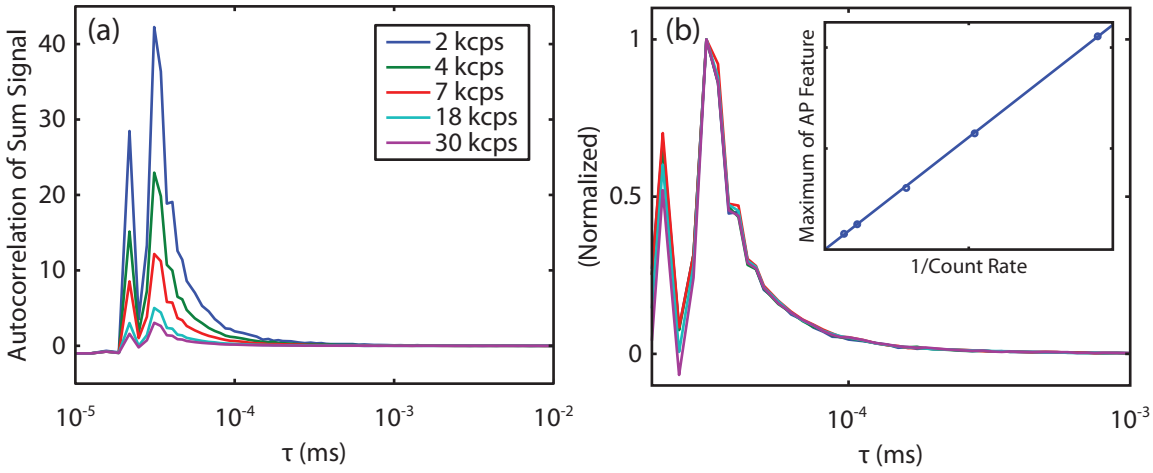

Figure 3-2: (a) Afterpulsing introduces a multiexponential decay into the autocorrelation of the sum signal. (b) the shape of this feature is remarkably consistent, but its magnitude scales inversely with signal intensity.

is measured far beyond the coherence length of the signal. But if not, the offset may cause the spectral correlation to appear artificially narrow and to exhibit false dynamics as the afterpulsing signature decays to zero (Figure 3-3).

There are two ways of handling afterpulsing artifacts. First, the precise functional form of the afterpulsing signature is a property of a given detector. Its shape (and magnitude) can be carefully characterized using a Poissonian source like a laser, and it can be reliably subtracted in post-processing. Second, many samples do not exhibit intensity fluctuations on sub-millisecond timescales. In these cases, the intensity correlation function used for PCFS analysis can be treated as flat in the temporal regions affected by afterpulsing.

It is also worth noting a second type of afterpulsing effect that manifests itself in intensity cross-correlations. The avalanche breakdown in a detector is often accompanied by the emission of above-bandgap light from the detector as the large number of hot carriers on the active area find each other and annihilate. This light can be recollimated by the detection optics, reverse-propagate through the setup, reflect off an optic, and reach the other detector, creating an instance of cross-detector

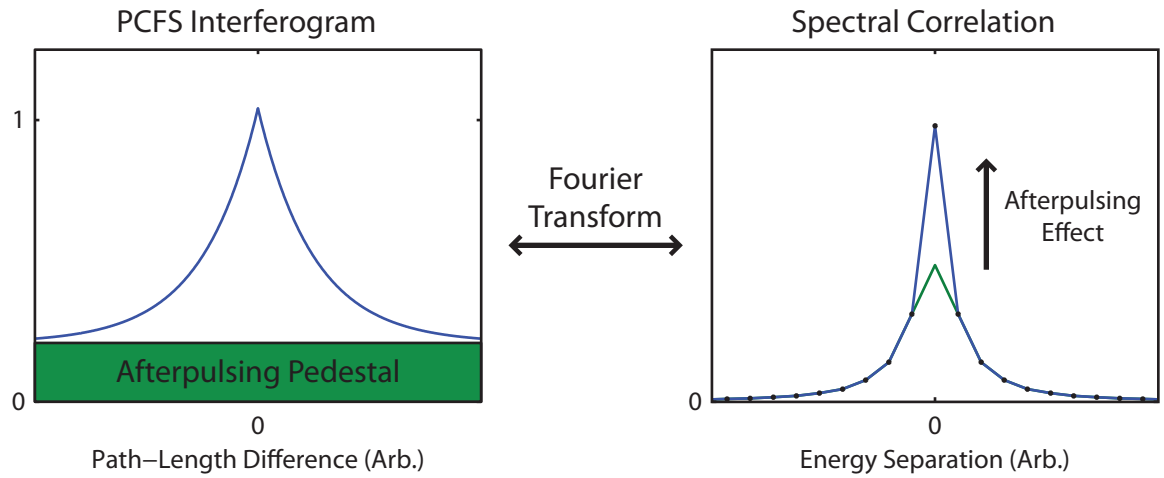

Figure 3-3: Afterpulsing introduces a δ-independent offset in the PCFS interferogram at short τ that artificially increases the magnitude of the $\zeta = 0$ data point. This can cause the spectral correlation to artificially narrow with decreasing τ as the magnitude of the afterpulsing feature increases.

afterpulsing. Unlike same-detector afterpulsing, it happens nearly immediately upon detection and manifests itself as a sharp peak in the cross correlation at the time it takes for the light to propagate through the setup ($\sim$ns) (Figure 3-4). Cross-detector afterpulsing occurs on timescales faster than those of interest to PCFS, but can be eliminated by spectrally filtering the near-bandgap photons.

Unbalanced Detectors. The expressions for the interferometer outputs that we used in the derivation assumed that the average countrate on each detector would be the same (i.e. the detectors are balanced). This may not strictly be the case in practice due to asymmetry in the interferometer beamsplitter or differences in detector quantum efficiency. Luckily, detector imbalance should have either no effect on the intensity cross-correlation, or in the case of asymmetric beamsplitting, only cause a predictable and uniform decrease in the maximum interferometric contrast. Unfortunately, unbalanced detectors do affect our ability to measure the intensity autocorrelation of the emitter. With unbalanced detectors, the intensity of the sum

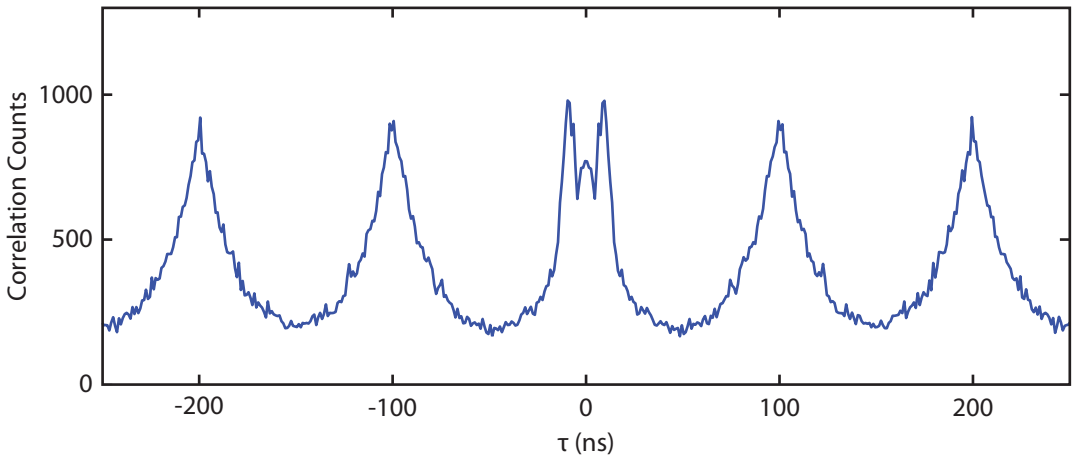

Figure 3-4: Near-infrared emission from the detector during an avalanche event can propagate through the setup and reach the other detector, generating a sub-10 ns cross-detector afterpulsing signature. This artifact does not affect either correlation function at PCFS-relevent τ.

signal is given by,

$$I_{a+b}(t) = \frac{A}{2} I(t)(1 + \mathcal{F}_{\mathbf{cos}}[s(\omega,t)]_{\delta(t))} + \frac{B}{2} I(t)(1 - \mathcal{F}_{\mathbf{cos}}[s(\omega,t)]_{\delta(t))} \tag{3.82}$$

$$= \frac{A+B}{2} I(t) + \frac{A-B}{2} \mathcal{F}_{\mathbf{cos}}[s(\omega,t)]_{\delta(t))} \tag{3.83}$$

$$\neq I(t). \tag{3.84}$$

The spectral component is not canceled out for unbalanced detectors and a dither feature is introduced to the autocorrelation of the sum signal proportional to the spectral coherence of the time-averaged spectrum.

This can probably be accounted for with precise knowledge of the time-averaged spectrum, but the best way of handling this artifact is to avoid it. Detector balance can be enforced by reducing the signal intensity of the more intense channel, or if the intensity dynamics of the sample are consistent, an autocorrelation function measured beyond the coherence length of the sample can be used to intensity-correct the entire interferogram.

3.4 A Correction for Detector Dark Counts

In addition to registering additional counts due to afterpulsing artifacts, detectors also introduce a fixed number of uncorrelated dark counts per second. At first, it may seem as though the addition of an uncorrelated signal to the true single-emitter signal should not affect the resulting intensity correlation functions. However, dark counts decrease the magnitude of correlation features in both the intensity cross-correlation and the autocorrelation of the sum signal. If there are intensity fluctuations in the single-emitter signal or drift in the microscope that affects the total count rate over correlation measurements, the overall effect of dark counts may vary from correlation measurement to correlation measurement. This should be a minor effect, but it is an easy one to correct for in all of the measured correlation functions.

Consider an arbitrary pair of channel A and B with intensities given by $I^M_{A/B}(t) = I_{A/B}(t) + \eta_{A/B}(t)$. Here, $I^M_{A/B}(t)$ represent the total measured intensities, $I_{A/B}(t)$ represent the "true" signals from the single emitter, and $\eta_{A/B}(t)$ represent the uncorrelated dark counts on each channel. The measured cross correlation of A and B is given by,

$$g^M_{A/B}(\tau) = \frac{\langle I^M_A(t) I^M_B(t+\tau)\rangle}{\langle I^M_A(t)\rangle\langle I^M_B(t+\tau)\rangle} \tag{3.85}$$

$$= \frac{\langle \left(I_A(t)+\eta_A(t)\right)\left(I_B(t+\tau)+\eta_B(t+\tau)\right)\rangle}{\langle I_A(t)+\eta_A(t)\rangle\langle I_B(t+\tau)+\eta_B(t+\tau)\rangle}. \tag{3.86}$$

Because the dark counts are uncorrelated with the actual single-emitter signal, we can distribute the time averages of their products. i.e.,

$$g^M_{A/B}(\tau) = \frac{\langle I_A(t)I_B(t+\tau)\rangle + \langle I_B(t+\tau)\rangle\langle\eta_A(t)\rangle + \langle I_A(t)\rangle\langle\eta_B(t+\tau)\rangle}{\langle I_A(t)\rangle\langle I_B(t+\tau)\rangle + \langle I_B(t+\tau)\rangle\langle\eta_A(t)\rangle + \langle I_A(t)\rangle\langle\eta_B(t+\tau)\rangle} \tag{3.87}$$

$$= \frac{\langle I_A(t)I_B(t+\tau)\rangle - \langle I_A(t)\rangle\langle I_B(t+\tau)\rangle}{\langle I^M_A(t)\rangle\langle I^M_B(t+\tau)\rangle} + 1 \tag{3.88}$$

$$= \frac{\langle I_A(t)\rangle\langle I_B(t+\tau)\rangle}{\langle I_A^M(t)\rangle\langle I_B^M(t+\tau)\rangle}\left(g_{A/B}(\tau)-1\right)+1, \tag{3.89}$$

where $g_{A/B}(\tau)$ is the cross correlaton of the actual single-emitter signal and where, generally, $g(\tau)-1$ is the infinity-corrected version of a correlation function measured by some correlators such as the ALV correlator we use in this work.

Inversion of this expression yields the general scaling correction factor for any correlation function subject to a known average dark count rate,

$$g_{A/B}(\tau) = \frac{\langle I_A^M(t)\rangle\langle I_B^M(t+\tau)\rangle}{\left(\langle I_A^M(t)\rangle - \langle \eta_A(t)\rangle\right)\left(\langle I_B^M(t+\tau)\rangle - \langle \eta_B(t+\tau)\rangle\right)}\left(g_{A/B}^M(\tau)-1\right)+1. \tag{3.90}$$

3.5 What if the Emitter has Correlated Spectral and Intensity Fluctuations?

One of the first assertions we made about the signal was that its spectral and intensity fluctuations were uncorrelated. We used this property to separate the intensity and spectral components of the time average in Equation 3.7 in order to form an uncorrelated product of the spectral component and the overall intensity correlation function of the emitter. This step simplified the interpretation of the spectral correlation, and has been regarded as reasonable, given that there are rarely intensity fluctuations on the timescale of the rapid spectral dynamics we want to use PCFS to study. But more generally, there may be a correlation between fluorescence intensity and spectrum. Here, we rework Equations 3.7–3.9 for the case of correlated spectral and intensity fluctuations and discuss the interpretation of the result.

First, we note that correlated fluctuations does not preclude us from forming the intensity correlation function. We can simply pull the intensity product time-average out of the numerator, leaving a copy in the denominator of the spectral component:

$$g^{\times}(\delta_0,\tau) = \frac{\big\langle I(t)I(t+\tau)\big\rangle - \big\langle I(t)I(t+\tau)\mathcal{F}_{\mathbf{cos}}[s(\omega,t)]_{\delta(t)}\mathcal{F}_{\mathbf{cos}}[s(\omega,t+\tau)]_{\delta(t+\tau)}\big\rangle}{\big\langle I(t)\big\rangle\big\langle I(t+\tau)\big\rangle} \tag{3.91}$$

$$= g(\tau)\left(1 - \frac{\big\langle I(t)I(t+\tau)\mathcal{F}_{\mathbf{cos}}[s(\omega,t)]_{\delta(t)}\mathcal{F}_{\mathbf{cos}}[s(\omega,t+\tau)]_{\delta(t+\tau)}\big\rangle}{\big\langle I(t)I(t+\tau)\big\rangle}\right). \tag{3.92}$$

Then, we can pull the intensity factors into the Fourier transforms to form the unnormalized time-dependent spectra,

$$= g(\tau)\left(1 - \frac{\big\langle \mathcal{F}_{\mathbf{cos}}[S(\omega,t)]_{\delta(t)}\mathcal{F}_{\mathbf{cos}}[S(\omega,t+\tau)]_{\delta(t+\tau)}\big\rangle}{\big\langle I(t)I(t+\tau)\big\rangle}\right). \tag{3.93}$$

This new expression can be manipulated exactly like the old one from Equation 3.13. The intensity product time-average will remain undisturbed in the denominator as we form the spectral correlation, and the unnormalized spectra can be manipulated exactly like the normalized spectra because there is no correlation between the intensity fluctuations of the emitter and the intensity fluctuations from the dither. When Equation 3.93 is fed into the rest of the PCFS derivation, Equation 3.47 becomes,

$$1 - \frac{g^{\times}(\delta_0,\tau)}{g(\tau)} = \frac{c(\tau)}{2\big\langle I(t)I(t+\tau)\big\rangle}\mathcal{F}_{\mathbf{cos}}[P(\zeta,\tau)]_{\delta_0} - \frac{d(\tau)}{2\big\langle I(t)I(t+\tau)\big\rangle}\mathcal{F}_{\mathbf{sin}}[P(\zeta,\tau)]_{\delta_0}, \tag{3.94}$$

where $P(\zeta,\tau)$ is the spectral correlation of the unnormalized spectrum. Now, we can pull the intensity product time-average into the Fourier transforms to form what we will call the intensity-averaged spectral correlation $\tilde{P}(\zeta,\tau)$. The interpretation of this quantity can be seen by presenting it in its integral representation,

$$\tilde{P}(\zeta,\tau) = \frac{P(\zeta,\tau)}{\big\langle I(t)I(t+\tau)\big\rangle} \tag{3.95}$$

$$= \frac{\left\langle \int_{-\infty}^{\infty} S(\omega,t)S(\omega+\zeta,t+\tau)\,\mathrm{d}\omega \right\rangle}{\left\langle I(t)I(t+\tau)\right\rangle} \tag{3.96}$$

$$= \frac{\int_0^T \int_{-\infty}^{\infty} S(\omega,t)S(\omega+\zeta,t+\tau)\,\mathrm{d}\omega\,\mathrm{d}t}{\int_0^T I(t)I(t+\tau)\,\mathrm{d}t}, \tag{3.97}$$

and switching the order of integration,

$$= \int_{-\infty}^{\infty} \frac{\int_0^T S(\omega,t)S(\omega+\zeta,t+\tau)\,\mathrm{d}t}{\int_0^T I(t)I(t+\tau)\,\mathrm{d}t}\,\mathrm{d}\omega \tag{3.98}$$

$$= \int_{-\infty}^{\infty} \frac{\left\langle \left[I(t)I(t+\tau)\right] s(\omega,t)s(\omega+\zeta,t+\tau)\right\rangle}{\left\langle \left[I(t)I(t+\tau)\right]\right\rangle}\,\mathrm{d}\omega \tag{3.99}$$

$$= \frac{\left\langle \left[I(t)I(t+\tau)\right] s(\omega,t)\circ s(\omega+\zeta,t+\tau)\right\rangle}{\left\langle \left[I(t)I(t+\tau)\right]\right\rangle}. \tag{3.100}$$

From Equation 3.100, we can see that $\tilde{P}(\zeta,\tau)$ is simply a weighted average of the spectral correlation by the intensities of the spectra at t and at $t+\tau$. Brighter spectral positions will contribute more heavily to the intensity-averaged spectral correlation because they produce more photons to be counted by our detectors. This is a property of all photon-counting experiments from PL decay traces to photon-correlation, and indeed of most integrated experiments, including conventional single-molecule spectroscopy. If there are intensity fluctuations that occur during spectral dynamics, they will need to be accounted for during the modeling of the spectral correlation.

3.6 Interpreting the Spectral Correlation

Finally, we conclude this PCFS theory chapter with a discussion of the interpretation of the spectral correlation, both in regard to spectral diffusion processes and with respect to the underlying spectral lineshape. To understand the significance of the spectral correlation, we can analyze a relatively simple model for the time-dependent fluorescence spectrum. Consider a fluorescence spectrum given by $s(\omega,t) = \delta(\omega-\omega_0(t)) \otimes \tilde{s}(\omega)$, where $\tilde{s}(\omega)$ is a constant, underlying spectral lineshape, and it

is convolved with spectral diffusion process described by $\delta(\omega - \omega_0(t))$. The spectral correlation will be given by,

$$p(\zeta,\tau) = \Big\langle \int_{-\infty}^{\infty} s(\omega,t)s(\omega+\zeta,t+\tau)\,\mathrm{d}\omega \Big\rangle \tag{3.101}$$

$$= \Big\langle \int_{-\infty}^{\infty} \left[\int_{-\infty}^{\infty} \delta(\omega' - \omega_0(t))\tilde{s}(\omega-\omega')\,\mathrm{d}\omega' \right] \tag{3.102}$$

$$\times \left[\int_{-\infty}^{\infty} \delta(\omega'' - \omega_0(t+\tau))\tilde{s}(\omega+\zeta-\omega'')\,\mathrm{d}\omega'' \right] \mathrm{d}\omega \Big\rangle \tag{3.103}$$

$$= \Big\langle \int_{-\infty}^{\infty} \tilde{s}(\omega-\omega_0(t))\tilde{s}(\omega-\omega_0(t+\tau)+\zeta)\,\mathrm{d}\omega \Big\rangle \tag{3.104}$$

$$= \Big\langle \int_{-\infty}^{\infty} \tilde{s}(\omega)\tilde{s}(\omega+\zeta-(\omega_0(t+\tau)-\omega_0(t)))\,\mathrm{d}\omega \Big\rangle \tag{3.105}$$

$$= \Big\langle \tilde{s}(\omega) \circ \tilde{s}(\omega)\left[\zeta - (\omega_0(t+\tau)-\omega_0(t))\right] \Big\rangle, \tag{3.106}$$

where the notation in the last equation signifies the evaluation of the autocorrelation of the intrinsic spectral lineshape at $\zeta - (\omega_0(t+\tau) - \omega_0(t))$. As $\tau \to 0$, the evaluation quantity evaluates to ζ, and the spectral correlation reduces to the autocorrelation of the intrinsic spectral lineshape. And, the τ-dependence can be isolated by rephrasing the spectral correlation as a convolution of this constant intrinsic lineshape term with a spectral diffusion term. i.e.,

$$p(\zeta,\tau) = \Big\langle \delta(\zeta' - (\omega_0(t+\tau)-\omega_0(t))) \otimes p(\zeta',\tau\to 0) \Big\rangle \tag{3.107}$$

$$= \Big\langle \delta(\zeta' - (\omega_0(t+\tau)-\omega_0(t))) \Big\rangle \otimes p(\zeta',\tau\to 0). \tag{3.108}$$

The time-dependent term is simply the time-averaged distribution of the spectral shift between the spectrum at time t and the spectrum some τ later, which in the case of ergodic spectral dynamics, is the probability density function of the spectral diffusion process. Thus, in the case where there are no spectral dynamics, the spectral correlation is simply the autocorrelation of the fluorescence spectrum, and in the case where the intrinsic spectrum is arbitrarily narrow, the spectral correlation is the

probability density function of the spectral dynamics.[14]

In this work, we will generally operate more towards the latter regime. We will show that the intrinsic spectral lineshape of our low temperature CdSe/CdS nanocrystals is ∼20 μeV, whereas the spectral dynamics these nanocrystals undergo is in the range of hundreds of μeV. This will produce a spectral correlation that resembles the probability density function of the spectral dynamics, but is slightly broadened and blurred by the small but finite intrinsic linewidth. In the remainder of this section, we will present the two models of spectral dynamics that will be used to demonstrate the qualitative features of discrete and continuous spectral diffusion mechanisms manifested in the spectral correlation $p(\zeta, \tau)$. We will describe each model, derive its corresponding $p(\zeta, \tau)$, and explain the physical significance of its model parameters.

3.6.1 The Wiener Model

Continuous spectral diffusion mechanisms will be represented by the one-dimensional Wiener process, the mathematical representation of Brownian motion. Its sole model parameter is the spectral diffusivity coefficient α, which characterizes the extent to which the spectrum is predisposed to diffuse. The $p(\zeta, \tau)$ for this process is well known [289]; it is the probability density function for a particle diffusing in one-dimension and starting at position $\zeta = 0$,

$$p(\zeta, \tau) = \frac{1}{\sqrt{2\pi\alpha^2\tau}} \exp\left(\frac{-\zeta^2}{2\alpha^2\tau}\right). \tag{3.109}$$

As evident from the expression, the FWHM of this $p(\zeta, \tau)$ increases according to a $\tau^{0.5}$ power law with prefactor proportional to the diffusivity constant. For the case of a finite intrinsic linewidth, the FWHM of the spectral correlation will reach a plateau at short τ depending on the width of the underlying spectrum.

[14] In practice, the autocorrelation of the intrinsic spectrum may be an averaged quantity, if there are temporal fluctuations in the fluorescence lineshape.

3.6.2 The Poisson Model

Discrete spectral diffusion mechanisms will be represented by a standard one-dimensional Poisson process. In this model, spectral diffusion occurs by discrete instantaneous events that occur temporally according to Poisson statistics (i.e. first-order jump kinetics) and induce energy shifts that sample a Gaussian jump distribution. This model is defined by two parameters: the standard deviation of the jump distribution σ and the first-order rate constant of the jump kinetics r.

The calculation of $p(\zeta, \tau)$ for a given τ is not straight-forward because it is constructed from multiple sub-populations of photon pairs. Each subpopulation of photon pairs is defined by the number of diffusion events n that occur between their photon arrivals. As in a standard Gaussian random walk, $p_n(\zeta)$, the contribution to $p(\zeta, \tau)$ from the nth sub-population, is given by convolving n jump distributions (in this case Gaussian distributions with standard deviation σ, *i.e.*

$$p_n(\zeta) = \frac{1}{\sqrt{2\pi n\sigma^2}} \exp\left(\frac{-\zeta^2}{2n\sigma^2}\right). \tag{3.110}$$

Since the jump kinetics are Poissonian, the probability of a given photon pair belonging to the sub-population with n spectral diffusion events is dictated by the Poisson distribution,

$$P(n, \tau) = \frac{(r\tau)^n}{n!} e^{-r\tau}. \tag{3.111}$$

Thus, we can express $p(\zeta, \tau)$ as

$$p(\zeta, \tau) = \sum_{n=0}^{\infty} P(n, \tau) p_n(\zeta) \tag{3.112}$$

$$= \sum_{n=0}^{\infty} \frac{(r\tau)^n}{n!} e^{-r\tau} \frac{1}{\sqrt{2\pi n\sigma^2}} \exp\left(\frac{-\zeta^2}{2n\sigma^2}\right). \tag{3.113}$$

This sum has no obvious closed-form solution, but its Fourier transform does:

$$FT[p(\zeta,\tau)]_{\zeta\to\delta} = FT\left[\sum_{n=0}^{\infty}\frac{(r\tau)^n}{n!}e^{-r\tau}\frac{1}{\sqrt{2\pi n\sigma^2}}\exp\left(\frac{-\zeta^2}{2n\sigma^2}\right)\right]_{\zeta\to\delta} \tag{3.114}$$

$$= \sum_{n=0}^{\infty}\frac{(r\tau)^n}{n!}e^{-r\tau}\exp(-2\pi^2 n\sigma^2\delta^2) \tag{3.115}$$

$$= e^{-r\tau}\sum_{n=0}^{\infty}\frac{(r\tau\exp(-2\pi^2\sigma^2\delta^2))^n}{n!} \tag{3.116}$$

$$= e^{-r\tau}\exp\left[r\tau\exp(-2\pi^2\sigma^2\delta^2)\right] \tag{3.117}$$

$$= \exp\left[-r\tau\left(1-\exp(-2\pi^2\sigma^2\delta^2)\right)\right]. \tag{3.118}$$

This expression is not easily inverse Fourier transformed analytically, but can be evaluated numerically. The result is a linear combination of an arbitrarily sharp distribution representing non-diffused photon pairs and a broad distribution representing the combination of all diffused photon pairs. The non-diffused distribution decays according to first-order kinetics, transferring probability density to the diffused distribution. We note that as $\tau \to 0$, this diffused distribution approaches $p_1(\zeta,\tau)$ and as $\tau \to \infty$, this distribution approaches the $p(\zeta,\tau)$ predicted by the Wiener model where $\alpha = \sigma\sqrt{r}$. In the intermediate regime, the diffused distribution is not Gaussian, as it is given by a linear combination of Gaussians with Poissonian weights.

The FWHM of this $p(\zeta,\tau)$ also has no obvious closed-form solution. However, in the quasi-continuous region at long τ, where it reduces to the Wiener $p(\zeta,\tau)$, its FWHM is given by a $\tau^{0.5}$ power law with prefactor proportional to $\sigma\sqrt{r}$ (we take this product as the effective diffusion constant). And finally, in the event of a finite intrinsic linewidth, the width of the non-diffused distribution will be given by the autocorrelation of the intrinsic spectrum, and the diffused distribution will be slightly broadened in the same fashion as the Wiener $p(\zeta,\tau)$.

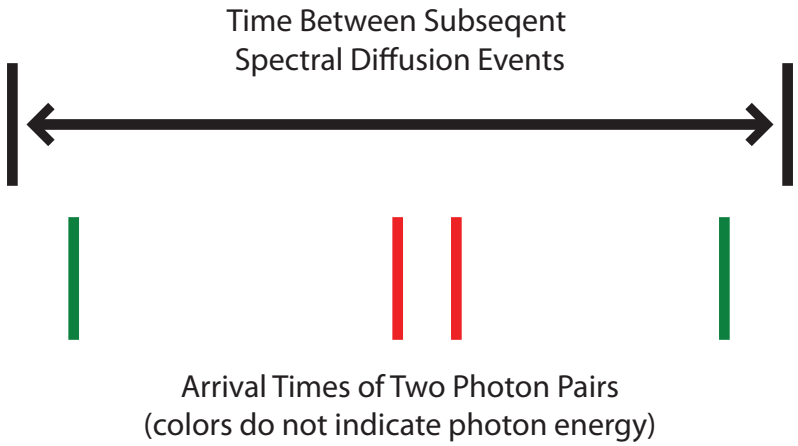

Figure 3-5: The spectral correlation reveals the fraction of photon pairs that arrive without a diffusion event between them. This is conceptually distinct from the waiting time distribution of spectral diffusion events that we would prefer to measure.

3.6.3 Extracting Spectral Jump Kinetics

The form of the Poisson model spectral correlation suggests that we should have a handle for measuring the kinetics of the discrete spectra jumps in the form of the integrated area of the non-diffused distribution. After all, this quantity represents the probability that a spectral diffusion event has not occured between photon arrivals as a function of their temporal separation, and must be connected to the distribution of times between diffusion events. Unfortunately, they are not one and the same. Consider the case where a spectral jump occurs every 1 s. We would like to know that the distribution of times between spectral diffusion events is given by an arbitrarily sharp peak at $T = 1\,\mathrm{s}$. However, our observable gives us a slightly different piece of information: the probability that an arbitrary pair of photons with temporal spacing τ does not bridge across a spectral diffusion event.

The cartoon shown in Figure 3-5 gives two examples of photon pairs that do not bridge spectral diffusion events. What should be clear from the cartoon is that they did not a priori have equal probabilities of being counted in the non-diffused distribution. For the green pair to be counted in the non-diffused distribution, its

first photon had to arrive shortly after the previous diffusion event so that its second photon could arrive before the next diffusion event. In contrast, the first photon of the red distribution could have arrived anytime during the space between diffusion events except the small fraction of time at the very end of the window. In general, the probability of a given photon pair being counted in the non-diffused distribution $f(\tau)$ for the regularly spaced diffusion event case is proportional to the size of the window for the first photon arrival, or,

$$f(\tau) = \begin{cases} 1 - \frac{\tau}{T} & : \tau < T \\ 0 & : \tau \geq T, \end{cases} \tag{3.119}$$

where T is the regular spacing between subsequent diffusion events.

As long as the fluorescence intensity of the emitter is independent of the times of the spectral diffusion events, this expression can be generalized for any distribution of times between subsequent diffusion events $g(T)$ as,

$$f(\tau) \propto \int_{\tau}^{\infty} (1 - \frac{\tau}{T})(Tg(T))\,\mathrm{d}T \tag{3.120}$$

$$\propto \int_{\tau}^{\infty} (T - \tau)(g(T))dT. \tag{3.121}$$

This equation is the product of the probability that the first photon falls in a time between diffusion events of length T (given by $Tg(T)$) times the probability that the second photon is not pushed over into the next window (given by $1 - \frac{\tau}{T}$). At its heart, this is essentially a convolution of the jump kinetics with a falling triangle edge.

Deconvolution processes are a bit tricky, so I have not had a lot of luck inverting this equation to give us a way of directly calculating the spectral jump kinetics from the area of the non-diffused distribution. But, there are a couple things we can do on this front. In simple cases, this expression can be simplified. For example, the area of the non-diffused distribution under the first-order kinetics of the Poisson model is

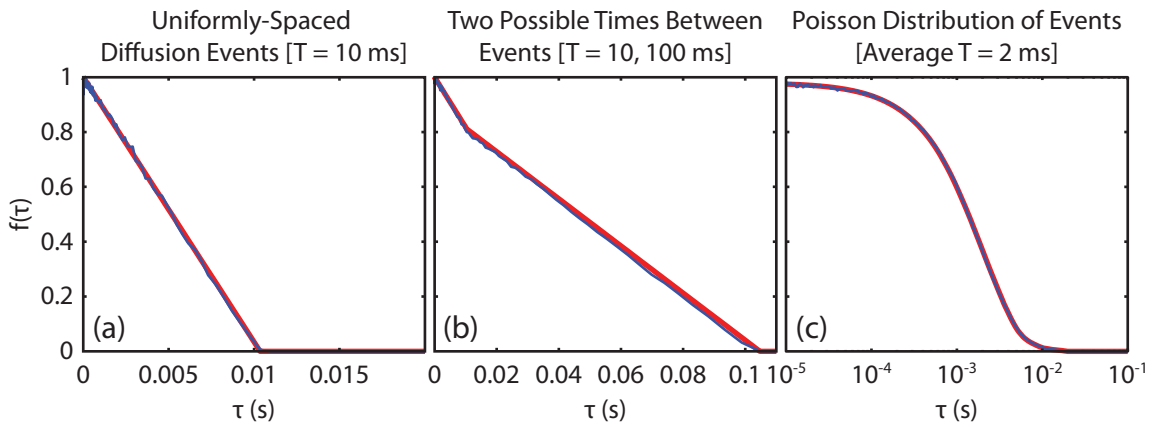

Figure 3-6: Equation 3.121 correctly predicts the amplitude of the non-diffused distribution for three different types of spectral diffusion kinetics.

given by,

$$f(\tau) \propto \int_{\tau}^{\infty} (T-\tau)(ke^{-kT})\,\mathrm{d}T \tag{3.122}$$

$$\propto \int_{\tau}^{\infty} kTe^{-kT}dT - \tau\int_{\tau}^{\infty} ke^{-kT}\,\mathrm{d}T \tag{3.123}$$

$$\propto \left[-\left(T+\frac{1}{k}\right)e^{-kT} + \tau e^{-kT}\right]_{\tau}^{\infty} \tag{3.124}$$

$$\propto e^{-kT}. \tag{3.125}$$

Thus, for the special case of first-order kinetics, the area of the non-diffused distribution as a function of τ is the kinetics of the spectral diffusion process. This is, by the way, borne out in the math behind the Poisson model spectral correlation in the previous section.

For more complicated kinetics, we can predict the form of the area of the non-diffused distribution using a simulation. For example, in Figure 3-6, we show the results of three simulations of simple kinetics models, including the regularly-spaced model, the Poisson model, and kinetics assembled by randomly choosing between a uniform short wait time T_1 and a uniform long wait time T_2. All three simulations verify the result from Equation 3.121.

3.7 Interpreting the Spectral Autocorrelation

In this work, we will not focus on the linewidth or lineshape of the underlying intrinsic nanocrystal spectrum. When considering the underlying spectrum, we will assume a Lorentzian lineshape (which is consistent with the measured data), and therefore quote a linewidth that is half of the spectral correlation as $\tau \to 0$.[15] However, in our room temperature solution-phase measurements (and possibly in future low temperature measurements) we have been directly interested in measuring and modeling the underlying intrinsic single-nanocrystal spectrum measured by PCFS via the spectral correlation. This effort has been met with a particularly insidious challenge that is worth discussing here.

The conventional wisdom regarding PCFS has been that we measure the spectral correlation instead of the spectrum, thus sacrificng the absolute emission energy of the spectrum for the superior temporal resolution of the spectral correlation. In truth, it is certainly the case that the the spectral correlation can be measured with superior temporal resolution because it only concerns the spectral relationship between pairs of photons that can be detected very closely together in time. It is also the case that because we have eschewed any absolute energy measure, we do not have access to the carrier frequency of the interferogram, and therefore the absolute emission energy of the spectrum. However, the more fundamental tradeoff that we have accepted by using a homodyne energy measure such as the spectral correlation is that we have sacrificed critical phase information about the intrinsic fluorescence lineshape.

To understand the consequences of this tradeoff, consider the case where we have measured the spectral correlation in a τ regime where it represents the autocorrelation of the intrinsic single-nanocrystal spectrum. The ultimate task at hand is to use this

[15] The autocorrelation of a Lorentzian lineshape is another Lorenzian with twice the FWHM. If the spectrum were Gaussian, the spectral correlation would be a Gaussian with a standard deviation that is $\sqrt{2}$ larger than that of the spectrum. Assuming a Gaussian lineshape would therefore slightly increase the measured intrinsic linewidth.

spectral autocorrelation to back out the single-nanocrystal lineshape itself, so that we can begin to understand the basic physics that defines it. The math we would be tempted to use is the following:

$$\mathcal{F}[p(\zeta, \tau \to 0)]_\delta = \mathcal{F}[\tilde{s}(\omega) \circ \tilde{s}(\omega)]_\delta \tag{3.126}$$

$$= \mathcal{F}[\tilde{s}(\omega)]^*_\delta \mathcal{F}[\tilde{s}(\omega)]_\delta \tag{3.127}$$

$$= |\mathcal{F}[\tilde{s}(\omega)]_\delta|^2. \tag{3.128}$$

This suggests that maybe we could get the spectral lineshape by simply inverting this equation. i.e,

$$\tilde{s}(\omega) = \mathcal{F}^{-1}\left[\sqrt{\mathcal{F}\left[p(\zeta, \tau \to 0)\right]}\right]. \tag{3.129}$$

But at a basic level, this is the problem. We cannot do that! Hopefully, there is a ghost of a childhood math teacher in your mind raising the alarm: "The square root of 4 is *plus or minus* 2!" This is the phase information we have lost about the fluorescence lineshape. In fact, because we are dealing with Fourier transforms and complex conjugates, the square root of 4 is actually $2(a + bi)$, for all a and b where $a^2 + b^2 = 1$. Moreover, we actually lack this phase information for all values of δ. Thus, the true expression for the spectral lineshape is actually,

$$\tilde{s}(\omega) = \mathcal{F}^{-1}\left[(a(\delta) + b(\delta)i)\sqrt{\mathcal{F}\left[p(\zeta, \tau \to 0)\right]}\right], \tag{3.130}$$

for any real $a(\delta)$ and $b(\delta)$ that produce a real and postive lineshape and satisfy the equation,

$$a(\delta)^2 + b(\delta)^2 = 1. \tag{3.131}$$

From a mathematical perspective, the moment we took the absolute value of $\mathcal{F}\left[\tilde{s}(\omega)\right]$ back in Equation 3.128, we lost the phase of the Fourier transform of the

spectrum in the complex plane.[16] This introduces ambiguity in our search for a unique solution, because we do not know what part of the integrand of the inverse Fourier transform ought to be handled by the cosine transform responsible for the even component of the spectrum and what part ought to be handled by the sine transform. Ultimately, any distribution of even- or oddness that produces a real and positive spectrum is consistent with the measured spectral correlation and could be the correct answer, and this possible solution space is captured by the set of all $a(\delta)$ and $b(\delta)$.

In essence, what has happened is that by measuring a fundamentally symmetric spectral quantity, we have lost all information about the even- or oddness of the underlying spectrum. There are an infinite number of possible lineshapes with varying degrees of asymmetry that can produce a measured spectral correlation and we cannot identify, a priori, which one of them is the correct one. We emphasize this point with three examples in Figure 3-7.

This leaves us in a difficult position with respect to our ultimate goal of recovering and analyzing the intrinsic single-nanocrystal lineshape. We cannot reliably reproduce the intrinsic spectrum, but surely we can extract something of value from the spectral autocorrelation. We have taken the analysis of the spectral autocorrelation in three distinct directions. First, in cases where we are looking for a trend in the behavior of the intrinsic linshape as a function of some synthetic parameter such as core size or shell thickness, we can simply consider the evolution of the spectral autocorrelation itself. Changes in the width and shape of the spectral autocorrelation will track with changes in the underlying spectra's width and shape. In this way, we can identify qualitative trends in linewidth without the need for modeling. This was the strategy primarily used by Cui et al. [176]

Second, we can make certain assumptions or approximations about the form of

[16] This also, by the way, eliminated any possibility of recovering any $e^{-i\omega_0\delta}$ term that could have told us the absolute emission energy of the spectrum.

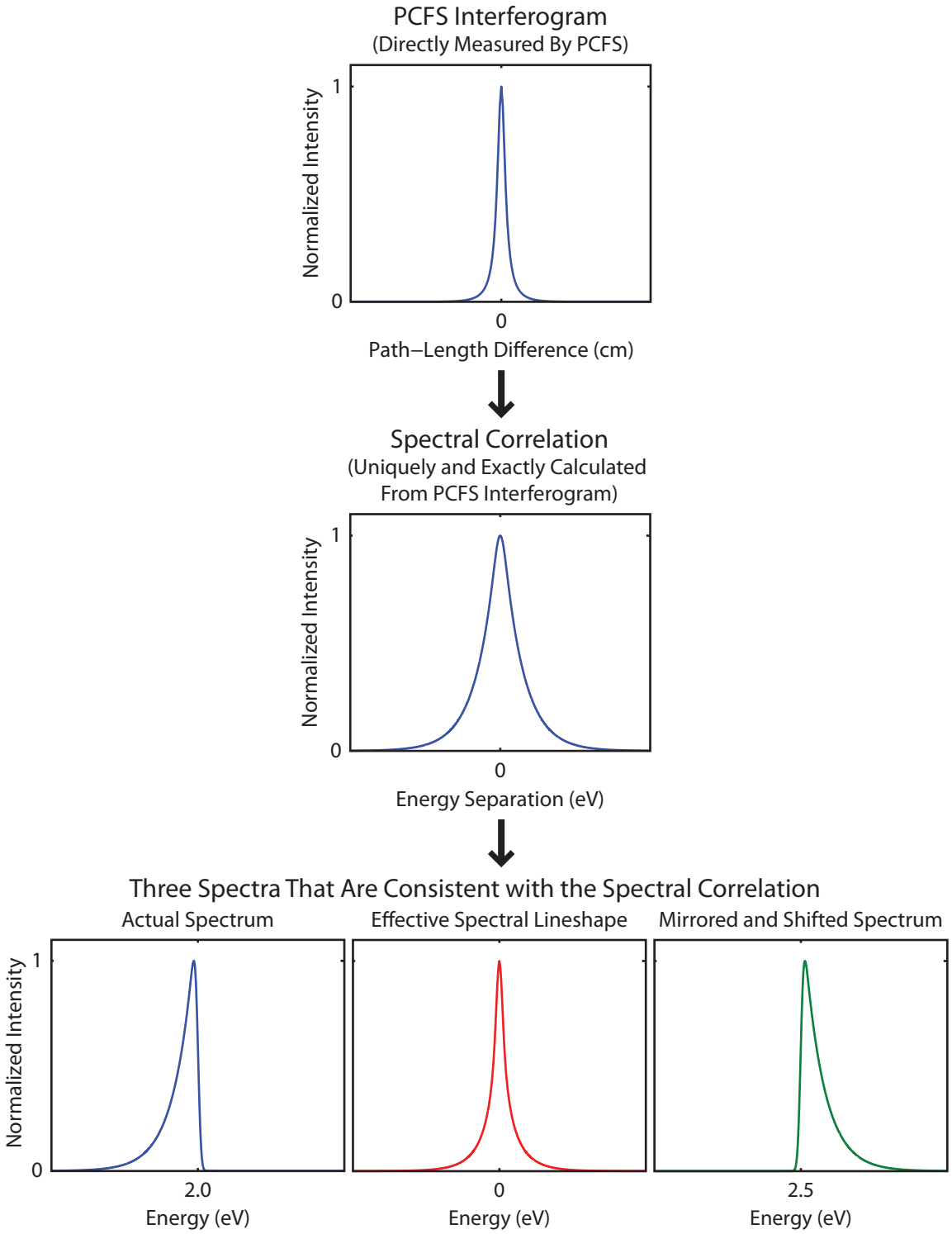

Figure 3-7: While the spectral correlation measured by PCFS is unique and exact, it does not contain enough information to precisely reconstruct the intrinsic spectrum of the emitter. The spectral correlation is consistent with an infinite set of possible spectra, including the symmetric solution (the effective spectral lineshape), the actual spectrum, and its reflection.

the underlying spectrum. For example, in this work, the spectral autocorrelation is closely Lorentzian. Although any number of lineshapes could, in principle, produce a Lorentzian spectral autocorrelation, a Lorentzian spectral lineshape seems to be a good, physically relevant guess. Similarly, conventional measurements have suggested that the room temperature lineshape is relatively symmetric. We can therefore make a reasonable estimation of the underlying spectral linewidth by finding the entirely symmetric solution to the spectrum that satisfies the measured spectral correlation. This is simply a matter of setting $a(\delta) = 1$ and solving Equation 3.129. The symmetric solution for the fluorescence spectrum, which we have named the effective spectral lineshape, is uniquely given by the spectral autocorrelation, and even though it is probably not the true underlying spectral lineshape, it should have a very similar linewidth. Thus, even though a lot of the shape information about the underlying spectrum may be lost in the spectral autocorrelation, it can still be a reliable and quantitative tool for characterizing single-nanocrystal linewidths.

Third, if we have our heart set on trying to extract shape information from the spectral correlation, we can directly model the spectral correlation itself using the underlying physics that define the spectral lineshape. For example, much like conventional lineshape modeling can predict the spectrum produced by a given vibrational spectral density, we have experimented with modeling our room temperature spectral autocorrelations using a physically-realistic phonon spectral density function. This has allowed us to directly connect the spectral autocorrelation to the basic exciton-phonon coupling physics that is understood to define the room temperature fluorescence spectrum. The task of extracting reliable estimates for the Huang-Rhys parameters of the spectral density is a complicated and subtle process, but it is at least mathematically possible.

In this Chapter, we have derived the PCFS experiment using a dither waveform, and discussed many of the theoretical complications and sources of artifacts that may

affect PCFS experiments. In the next Chapter, we will discuss one of the major practical complications that has hindered the application of PCFS: the requirement for ergodic spectral dynamics.

Chapter 4

Combining PCFS with Conventional Spectroscopy

Even though we need the temporal resolution of PCFS to resolve the rapid spectral dynamics of single nanocrystal at low temperatures, Figure 2-1 illustrates that these rapid dynamics still produce correlated spectral diffusion on the slower timescales accessible to conventional CCD spectroscopy. Any experiment aiming to capture the full range of rapid spectral dynamics must be capable of measuring both the basic dynamics at fast timescales and their correlated effects over longer timescales. Unfortunately, PCFS is not well suited for measuring long timescale dynamics. In this chapter, we will discuss the temporal limitations of PCFS and show that the full range of spectral dynamics can be captured by combining PCFS with conventional CCD spectroscopy.

4.1 Temporal Limitations of PCFS

Previously, we emphasized that the temporal resolution of correlation methods were fundamentally limited at fast timescales by the precision of photon timing. On the setup used for this work, photon timing is limited by the correlation hardware to

3.125 ns, but silicon APDs can be capable of timing as precisely as tens of picoseconds. Of course, on these fast timescales, the true limitation is not resolution so much as detecting enough photon pairs close enough together in time to actually sample the spectral coherence at such small τ with high enough signal-to-noise. A Poissonian source producing $5,000$ counts per second will only produce a photon pair with temporal spacing $\tau = 4 \pm 4$ns on average every five seconds. This may be okay for a single-point correlation measurement like an antibunching experiment, which can integrate signals for hours or as long as the nanocrystal remains optically active,[1] but in PCFS, we must collect a large number of correlation measurments at different path-length differences to resolve the spectral correlation. Taking 40 correlation measurements over the course of 40 minutes leaves only a minute per correlation measurement (which is good for only a dozen correlation counts at $\tau = 4 \pm 4$ns).

What may be less immediately obvious is that the short integration times for each correlation measurement also places significant upper bounds on the spectral dynamics that can be probed with PCFS. It will clearly never be possible to probe spectral dynamics on timescales longer than the integration time of the correlation measurement. This limits us to spectral dynamics on timescales less than 60 s in our hypothetical PCFS measurement. However, we are even more significantly limited in our temporal resolution by the assumptions we needed in the derivation of the PCFS experiment. First, we require investigated spectral dynamics to be ergodic so that each correlation measurement measures the same spectral behavior. Spectral dynamics over tens of seconds will not produce representative behavior over a 60 s integration time. And second, we instituted dither requirements that introduce dither nodes that interfere with the investigation of long timescale dynamics. A conservatively chosen triangle dither waveform, which completes three full periods over

[1] Especially under vacuum, nanocrystals will tend to bleach on the timescale of tens of minutes (this number is highly dependent on sample properties and varies widely from nanocrystal to nanocrystal).

five interference fringes during a 60 s integration time, will introduce a dither node at approximately $\tau = 1$s. Our ability to measure spectral dynamics on timescales greater than around half a second will be periodically interrupted by dither nodes (and, it should be noted, possibly corrupted by inconsistencies in the dither form). Although we may be able to marginally increase this upper bound on the timescales accessible by PCFS by selecting a more daring dither waveform, accessing spectral dynamics on timescales greater than seconds will simply not be possible with such short integration times.

Notable improvements in the temporal resolution at both long and short timescales can only really be achieved by increasing the integration time of each correlation measurement by either using fewer correlation measurements in the PCFS interferogram or by increasing the overall duration of the experiment. The former negatively impacts either the spectral window or spectral resolution of our experiment,[2] and the latter has not been feasible with the fluorescence stability of samples we have investigated so far. Practically, in this work, we are limited to using PCFS to investigate spectral dynamics on timescales ranging from microseconds to hundreds of millseconds.

4.2 Deeper Problems Measuring Multi-Timescale Dynamics

If our inability to capture the full range of rapid spectral dynamics using PCFS were not bad enough, we also have to cope with the existence of the other two forms of spectral dynamics, which can introduce infrequent changes in the spectrum probed in individual correlation measurements. These larger spectral shifts would not produce major artifacts in the spectral correlation measured for short τ as long as they did

[2] We will need a large spectral window and high spectral resolution for this work, but they may not be necessary for all investigations.

not cause changes in the behavior of the rapid spectral dynamics or the underlying intrinsic fluorescence lineshape. After all, as $\tau \to 0$, the fraction of photon pairs arriving on either side of the infrequent spectral shifts should vanish. However, in L. F. Marshall's thesis, [287] she showed preliminary data demonstrating that the spectral correlation undergoes significant changes when large spectral jumps occur. This result stands in agreement with the work of Empedocles and Bawendi, [63] which found that the integrated spectrum of single nanocrystals depended strongly on spectral position and was often notably broadened as the spectrum was red-shifted by tens of meV.

The upshot is that the charging and large jump forms of spectral diffusion may cause significant changes in the rapid spectral dynamics undergone by a single nanocrystal, and that in order to compile an artifact-free spectral correlation for a set of rapid spectral dynamics, a complete PCFS interferogram must be measured at a single large spectral jump position or charging state. This places even more significant limitations on how long a prospective PCFS experiment can last, depending on how likely large spectral shifts or charging events are to occur in a given sample, and requires that we have a strategy in place to identify spectral shifts and ensure that we are compiling a consistent PCFS inferferogram.

4.3 A Compound Experiment Can Reveal the Entire Range of Rapid Spectral Dynamics.

The solution to both capturing the full range of rapid spectral dynamics and ensuring that we are compiling a consistent PCFS interferogram is to split the single-nanocrystal signal and simultaneously perform PCFS and conventional single-molecule spectroscopy. Although splitting the signal will decrease the signal-to-noise ratio of both experiments, it grants us better oversight over the signal being analyzed by

PCFS and it provides a means for tracking spectral dynamics over longer timescales than an individual PCFS correlation measurement.

An example of a compound PCFS/Camera data set, which we will analyze in the next Chapter, is shown in Figure 4-1. Using both the intensity traces of the PCFS experiment and the time-series of integrated spectra from the CCD camera, we can see that the spectral position of the emitter changes halfway through the first PCFS measurement and switches back halfway through the second measurement. We can therefore stitch together the PCFS data from the two runs to construct two full and consistent PCFS interferograms. Furthermore, in addition to the PCFS interferograms, we also have hundreds of seconds of uninterrupted camera data about the trajectory of rapid spectral dynamics in each spectral position, which can report on how the spectra evolves over hundreds of milliseconds to hundreds of seconds and, if it is in agreement with the PCFS data, can further validate the consistency of our PCFS interferograms.

4.4 Determining the Spectral Correlation from a Time Series of Integrated Spectra

The only question that remains is how to resolve the disparate types of spectral data collected by PCFS and conventional spectroscopy. On one hand, we discussed in the previous Chapter that it is impossible to recover the spectrum from the PCFS spectral correlation. On the other hand, the spectral data measured by the CCD camera is averaged over the integration time of each frame, broadened by the spectrometer instrument function, and also contains broader spectral features like phonon sidebands that may not be captured in the narrow spectral window measured by PCFS. By choosing a narrow spectral window in PCFS, we can isolate the spectral diffusion of the narrow zero-phonon line (ZPL) and measure a spectral correlation that

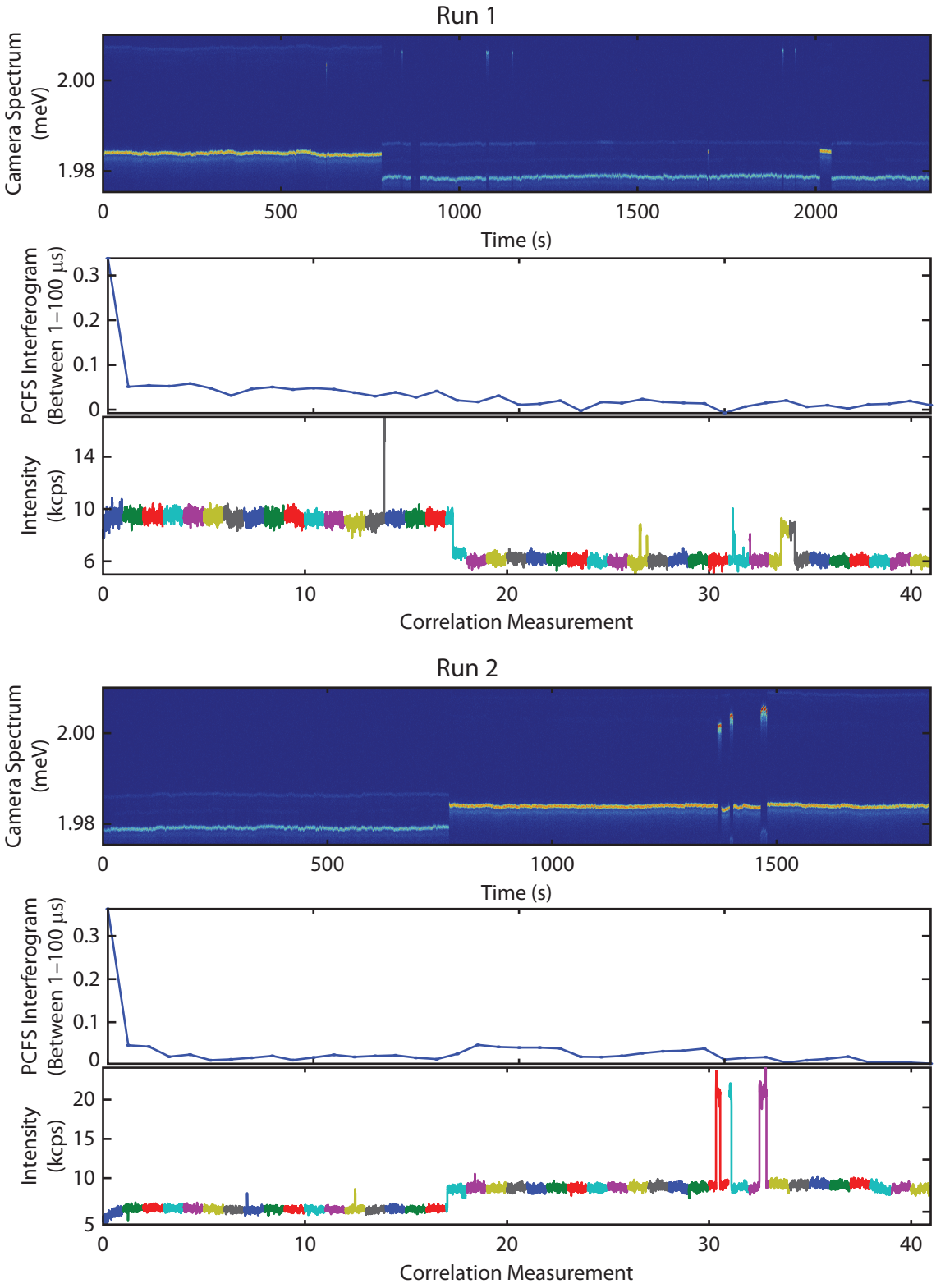

Figure 4-1: Two PCFS scans with camera data. The large spectral shift in the middle of each scan is evident from changes in the camera spectrum, the fluorescence intensity, and in the PCFS contrast at short τ. We can stitch together two consistent PCFS experiments by combining the similar data from each scan.There is an offset between the camera and PCFS data in the first run due by experimenter error.

approximates the probability density function of the spectral dynamics. In contrast, the spectral correlation directly calculated from the camera data will necessarily be broadened by the acoustic phonon side-band (and by the instrument function of the spectrometer). The solution is to use the spectral diffusion trajectories of the peak emission wavelength of the nanocrystal to isolate the behavior of the ZPL in the camera data and to measure the same spectral correlation quantity investigated by PCFS at fast timescales. This process, worked out in the next several sections, is heavily inspired by previous theoretical work by Plakhotnik and Walser. [290]

We first show that, without the confounding effects of the spectrometer instrument function or any incidental broad spectral features, the time series of integrated spectra can be used to approximate the spectral correlation on timescales greater than the integration time of each spectral frame. Then, we show that we can isolate the ZPL contribution, as we will do in PCFS, by constructing the spectral correlation using the histogram of energy shifts between frames.

4.4.1 Approximating the Spectral Correlation From the Average Correlation of Integrated Spectral Frames

Consider a series of N time-ordered spectra $s_T(\omega, t)$, each integrated for time T and referenced such that the jth frame in the series is given by $s_T(\omega, jT)$. The average spectral correlation of two integrated spectral frames separated by n frames $C(\zeta, nT)$ is given by,

$$C(\zeta, nT) = \frac{1}{N-n} \sum_{j=0}^{N-n-1} s_T(\omega, jT) \circ s_T(\omega, (j+n)T) \tag{4.1}$$

Each of these correlation terms can be rewritten in terms of $s(\omega, t)$, the homogeneous spectrum evaluated instantaneously at time t, as:

$$
\begin{aligned}
&[s_T(\omega, jT) \circ s_T(\omega, (j+n)T)](\zeta) \\
&\qquad = \int_{-\infty}^{\infty} s_T(\omega, jT) s_T(\omega+\zeta, (j+n)T)\,\mathrm{d}\omega && (4.2)\\
&\qquad = \int_{-\infty}^{\infty} \left[\int_0^T s(\omega, jT+t')\,\mathrm{d}t'\right]\left[\int_0^T s(\omega+\zeta, (j+n)T+t'')\,\mathrm{d}t''\right]\,\mathrm{d}\omega && (4.3)\\
&\qquad = \int_0^T \int_0^T \left[\int_{-\infty}^{\infty} s(\omega, jT+t') s(\omega+\zeta, (j+n)T+t'')\,\mathrm{d}\omega\right]\,\mathrm{d}t''\,\mathrm{d}t', && (4.4)
\end{aligned}
$$

For simplicity, we define $\mathcal{T}_1 = jT+t'$ and $\mathcal{T}_2 = (j+n)T+t''$. Further deconstructing the integrand by expressing the spectrum as the product of the fluorescence intensity $I(t)$ and the normalized spectrum $\hat{s}(\omega, t)$, we get

$$
\begin{aligned}
&= \int_{jT}^{(j+1)T} \int_{(j+n)T}^{(j+n+1)T} \int_{-\infty}^{\infty} I(\mathcal{T}_1)\hat{s}(\omega, \mathcal{T}_1) I(\mathcal{T}_2)\hat{s}(\omega+\zeta, \mathcal{T}_2)\,\mathrm{d}\omega\,\mathrm{d}\mathcal{T}_2\,\mathrm{d}\mathcal{T}_1 && (4.5)\\
&= \int_{jT}^{(j+1)T} \int_{(j+n)T}^{(j+n+1)T} I(\mathcal{T}_1) I(\mathcal{T}_2) \int_{-\infty}^{\infty} \hat{s}(\omega, \mathcal{T}_1)\hat{s}(\omega+\zeta, \mathcal{T}_2)\,\mathrm{d}\omega\,\mathrm{d}\mathcal{T}_2\,\mathrm{d}\mathcal{T}_1 && (4.6)\\
&= \int_{jT}^{(j+1)T} \int_{(j+n)T}^{(j+n+1)T} \left[I(\mathcal{T}_1) I(\mathcal{T}_2)\right]\left[\hat{s}(\omega, \mathcal{T}_1) \circ \hat{s}(\omega, \mathcal{T}_2)\right]\,\mathrm{d}\mathcal{T}_2\,\mathrm{d}\mathcal{T}_1. && (4.7)
\end{aligned}
$$

Taken individually, the integrand of each term in the sum from Eqn. 4.1 is highly specific to the spectral diffusion trajectory reflected in that term. However, if the observed spectral diffusion over nT is ergodic with respect to the total duration of the time series, then the average of all of these terms will reflect the ensemble of diffusion trajectories. Since the spectral diffusion of the single dot will be uncorrelated with the time and duration of the integration periods,

$$
C(\zeta, nT) = \left\langle \int_{jT}^{(j+1)T} \int_{(j+n)T}^{(j+n+1)T} \left[I(\mathcal{T}_1) I(\mathcal{T}_2)\right]\left[\hat{s}(\omega, \mathcal{T}_1) * \hat{s}(\omega, \mathcal{T}_2)\right]\,\mathrm{d}\mathcal{T}_2\,\mathrm{d}\mathcal{T}_1 \right\rangle \qquad (4.8)
$$

$$= \int_{jT}^{(j+1)T} \int_{(j+n)T}^{(j+n+1)T} \left\langle [I(\mathcal{T}_1)I(\mathcal{T}_2)] \, [\hat{s}(\omega, \mathcal{T}_1) * \hat{s}(\omega, \mathcal{T}_2)] \right\rangle \mathrm{d}\mathcal{T}_2 \, \mathrm{d}\mathcal{T}_1 \tag{4.9}$$

$$= \int_{jT}^{(j+1)T} \int_{(j+n)T}^{(j+n+1)T} \left[\langle I(\mathcal{T}_1) \rangle \langle I(\mathcal{T}_2) \rangle \times \frac{\langle I(\mathcal{T}_1) I(\mathcal{T}_2) \rangle}{\langle I(\mathcal{T}_1) \rangle \langle I(\mathcal{T}_2) \rangle} \right.$$
$$\left. \times \frac{\left\langle [I(\mathcal{T}_1)I(\mathcal{T}_2)] \, [\hat{s}(\omega, \mathcal{T}_1) * \hat{s}(\omega, \mathcal{T}_2)] \right\rangle}{\langle I(\mathcal{T}_1) I(\mathcal{T}_2) \rangle} \right] \mathrm{d}\mathcal{T}_2 \, \mathrm{d}\mathcal{T}_1 \tag{4.10}$$

The first factor is the square of the average intensity of the emitter, which is just a constant factor. Because the overall magnitude of $C(\zeta, nT)$ has no physical significance, being dictated by the count rate on the CCD, we will remove this factor by normalizing $C(\zeta, nT)$ to form $c(\zeta, nT)$. The second factor is the intensity autocorrelation of the total signal $g(\mathcal{T}_2 - \mathcal{T}_1)$. And, finally, the third factor is the ensemble average of the spectral correlation $p(\zeta, \mathcal{T}_2 - \mathcal{T}_1)$ that we measure in PCFS. Note that it is weighted by the intensities of the two spectral frames, just as the PCFS spectral correlation is weighted by the instantaneous fluorescence intensity. Thus,

$$c(\zeta, nT) = \frac{\int_{jT}^{(j+1)T} \int_{(j+n)T}^{(j+n+1)T} g(\mathcal{T}_2 - \mathcal{T}_1) p(\zeta, \mathcal{T}_2 - \mathcal{T}_1) \, \mathrm{d}\mathcal{T}_2 \, \mathrm{d}\mathcal{T}_1}{\int_{jT}^{(j+1)T} \int_{(j+n)T}^{(j+n+1)T} g(\mathcal{T}_2 - \mathcal{T}_1) \, \mathrm{d}\mathcal{T}_2 \, \mathrm{d}\mathcal{T}_1} \tag{4.11}$$

Finally, all of the above terms are related to $\mathcal{T}_2 - \mathcal{T}_1$. We can transform the double integral into an integral over t' (the time of the first spectral term) and an integral over $\tau = \mathcal{T}_2 - \mathcal{T}_1$ (the difference between the two spectral terms).

$$c(\zeta, nT) = \frac{\int_{(n-1)T}^{nT} \int_{nT-\tau}^{T} g(\zeta, \tau) p(\zeta, \tau) \, \mathrm{d}t' \, \mathrm{d}\tau}{T^2 \int_{(n-1)T}^{nT} \int_{nT-\tau}^{T} g(\zeta, \tau) \, \mathrm{d}t' \, \mathrm{d}\tau}$$
$$+ \frac{\int_{nT}^{(n+1)T} \int_{0}^{nT-\tau} g(\zeta, \tau) p(\zeta, \tau) \, \mathrm{d}t' \, \mathrm{d}\tau}{T^2 \int_{nT}^{(n+1)T} \int_{0}^{nT-\tau} g(\zeta, \tau) \, \mathrm{d}t' \, \mathrm{d}\tau} \tag{4.12}$$

$$= \frac{\int_{(n-1)T}^{(n+1)T} \left(1 - \frac{|\tau - nT|}{T}\right) g(\zeta, \tau) p(\zeta, \tau) \, \mathrm{d}\tau}{\int_{(n-1)T}^{(n+1)T} \left(1 - \frac{|\tau - nT|}{T}\right) g(\zeta, \tau) \, \mathrm{d}\tau} \tag{4.13}$$

As is so often the case, Equation 4.13 may look complicated, but it is simply a

bit of a strange weighted average of $p(\zeta, \tau)$ about $\tau = nT$. When $n \ll 1$, $c(\zeta, nT) \rightarrow p(\zeta, nT)$. This limit will also hold as $n \rightarrow 1$ as long as $p(\zeta, \tau)$ and $g(\tau)$ have little curvature in τ over $2T$.

4.4.2 Approximating the Spectral Correlation From the Histogram of Energy Shifts Between Frames

An alternative method for calculating the spectral correlation from the camera data is to use the peak positions of the integrated spectra rather than their overall lineshape. Even with poor signal-to-noise, curve fitting procedures should be able to very precisely determine the center position of a spectrum, and allow us to identify spectral shifts that are even smaller than the camera instrument function. Towards that end, we will show that $C(\zeta, nT)$ can be expressed as the convolution of $a(\zeta', T)$, the autocorrelation of the average spectral frame integrated for time T, and $h(\zeta', nT)$, the histogram of the energy shifts between all pairs of frames separated by n frames. If $a(\zeta', T)$ can be calculated via PCFS, we can remove broadening of the camera spectral correlation from the spectrometer instrument function and the phonon side-bands that are not considered in the PCFS $p(\zeta, \tau)$.

The integrated spectra used to construct $p(\zeta, \tau)$ in our data have roughly uniform fluorescence intensity and integrated spectral lineshape for a given large jump position because of the ergodicity on the timescale of seconds of most of the rapid diffusion dynamics. Therefore, we can ignore the intensity fluctuation considerations we treated in the previous section and represent a typical frame as

$$s_T(\omega, jT) = \delta(\omega' - \omega_0(jT)) \otimes \sigma(\omega', T), \tag{4.14}$$

where $\omega_0(jT)$ is the spectral position of the peak value of the frame and $\sigma(\omega')$ is the typical spectral lineshape over integration time T centered at $\omega_0 = 0$. The

autocorrelation of a pair of frames is therefore

$$
\begin{aligned}
& s_T(\omega, jT) \circ s_T(\omega, (j+n)T) \\
& \quad = [\delta(\omega' - \omega_0(jT)) \otimes \sigma(\omega', T)] \circ [\delta(\omega' - \omega_0((j+n)T)) \otimes \sigma(\omega', T)] \quad (4.15) \\
& \quad = [\delta(\omega' - \omega_0(jT)) \circ \delta(\omega' - \omega_0((j+n)T))] \otimes a(\zeta', T), \quad (4.16)
\end{aligned}
$$

where $a(\zeta', T)$ is the autocorrelation of $\sigma(\omega', T)$. The bracketed correlation represents a single contribution to a histogram of peak-value energy shifts $h(\zeta', nT)$, so averaging over all frames separated by nT yields

$$C(\zeta, nT) \simeq \frac{1}{N-n} a(\zeta', T) \otimes h(\zeta', nT). \quad (4.17)$$

Since both quantities are real and symmetric, the correlation and the convolution of these quantities are functionally identical.Therefore, because we showed in the previous section that $p(\zeta, \tau) \propto C(\zeta, nT)$, we can also conclude that $p(\zeta, \tau) \propto a(\zeta', T) * h(\zeta', nT)$.

Finally, we demonstrate that the contribution to $a(\zeta', T)$ from the ZPL can be isolated by calculating it from the PCFS data, where all other features contribute a fixed offset. To do this, we can note that $a(\zeta', T)$ is equivalent to $\hat{c}(\zeta, nT)$ from Eqn. 4.13 when $n = 0$. Here, however, the fluorescence intensity will not necessarily be uniform on sub-camera timecales, so $g(\tau)$ cannot be disregarded. But luckily, it is measured directly during the PCFS experiment. So,

$$
\begin{aligned}
a(\zeta', T) &= \frac{\int_{-T}^{T} (1 - \frac{|t|}{T}) g(\zeta', t) p(\zeta', t)\, \mathrm{d}t}{\int_{-T}^{T} g(\zeta', t)\, \mathrm{d}t} \quad (4.18) \\
&= 2\frac{\int_{0}^{T} (1 - \frac{t}{T}) g(\zeta', t) p(\zeta', t)\, \mathrm{d}t}{\int_{0}^{T} g(\zeta', t)\, \mathrm{d}t} \quad (4.19)
\end{aligned}
$$

It should be noted that the spectral correlation that is calculated on the camera

will still likely be broader than that measured by PCFS because of uncertainty in the fitting of the center-point of the spectrum. Part of our validation of this compound PCFS/Camera experiment will be to show that the trend of the width of the spectral correlation with τ across the PCFS and camera regimes, but that their magnitudes are offset by the uncertainty of the camera peak fit.

To summarize, the long timescale spectral dynamics of low temperature single nanocrystals threaten the ergodicity requirements needed to assemble a consistent PCFS interferogram. In this chapter, we have shown that combining PCFS and conventional CCD spectroscopy, we can avoid the detrimental effects of irreversible changes in nanocrystal spectral dynamics and we can simultaneously measure rapid spectral dynamics over as many as nine orders of magnitude in time ranging from microseconds to hundreds of seconds.

Chapter 5

Investigation of Rapid Spectral Diffusion in Semiconductor Nanocrystals

In the previous chapters, we summarized the current state of our understanding of rapid spectral dynamics in semiconductor nanocrystals and established the theoretical foundations of our experimental technique that combines photon-correlation Fourier spectroscopy (PCFS) and conventional single-nanocrystal spectroscopy. We now present the progress we have made using this technique to characterize and understand spectral dynamics. This chapter describes the results published by Beyler et al. [243] and will be divided into four parts. First, we will describe the technical details of our experimental setup and data analysis procedure. Second, we will present our major results and explain the tangible insight they provide concerning rapid spectral diffusion. Third, we will discuss the implications of these results for our conceptual understanding of spectral diffusion. And finally, we discuss possible future directions for investigating the spectral diffusion of low temperature nanocrystals using single-molecule techniques.

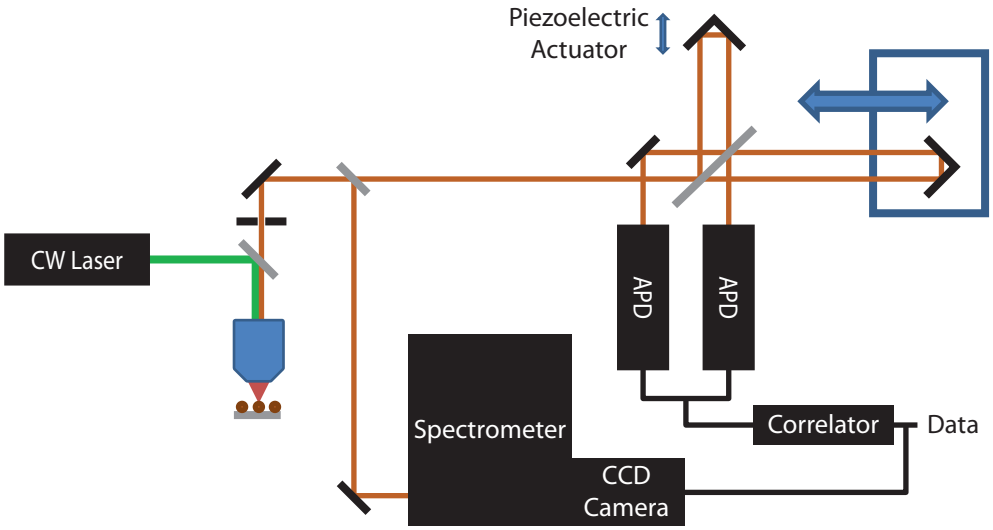

Figure 5-1: Schematic representation of the low temperature PCFS setup. The signal from a confocal microscope is split to simultaneously conduct PCFS and conventional single-molecule spectroscopy.

5.1 Experimental Setup and Data Analysis

5.1.1 Optical Setup

The experimental setup used for this investigation is shown schematically in Fig. 5-1.

A thin-film sample at single-nanocrystal dilution was fabricated on a 5 mm × 5 mm × 1 mm single-crystal quartz substrate, mounted using Apiezon N cryogenic vacuum grease to the cold finger of a Janis ST-500 cryostat, and cooled to ∼4 K.[1] The sample was excited using 514 nm continuous wave radiation from a Coherent 70C-Spectrum Argon/Krypton-ion gas laser via a home-built epifluorescence confocal microscope, equipped with a 550 nm long-pass dichroic beamsplitter, a long working distance air objective (Nikon, 0.7 NA),[2] and silver galvomirrors to scan the excitation spot over

[1] Apiezon N vacuum grease exhibits broadband visible fluorescence that can interfere with single-nanocrystal experiments. The cold finger we used was shaped like a washer, with a hole in the center where the excitation was focused. This assured good thermal contact between the sample and coldfinger without allowing for direct excitation of the vacuum grease. Nevertheless, the fluorescence linewidth of the vacuum grease is sufficiently broad that it only causes a constant background in both the spectral correlation and conventional spectral traces.

[2] The objective was mounted onto a piezoactuator to provide fine-tuning of the z-position of the objective.

the substrate. Collected fluorescence from a single nanocrystal on the sample was recollimated, passed through the dichroic beamsplitter, and spatially filtered using a pinhole (10 cm focal length focusing optic, 10 µm pinhole, 4 cm recollimating optic) to remove laser scatter and background grease and film autofluorescence.

Once the single-emitter fluorescence was isolated using the pinhole, the signal was split using an 10/85 (R:T) wedged beam splitter to simultaneously conduct the PCFS and conventional spectroscopy experiments. Ten percent of the signal was directed into the conventional spectroscopy setup, where the signal was spectrally-resolved using a Jobin Yvon Triax 320 spectrometer with 1200 l/mm grating, the spectrum was detected using a Princeton Instruments ProEM 512B CCD camera, and the experiment was managed in software by Princeton Instrument's WinSpec program. Five percent of the signal was lost due to reflection off of the back interface of the wedge. And, the remaining 85 % of the signal was directed into a two-output Michelson interferometer for the PCFS experiment.

The PCFS interferometer was constructed using a visible-wavelength two inch 50:50 (R:T) non-polarizing beamsplitting cube (Newport) and two two inch visible-wavelength total internal reflection retroreflectors (Thorlabs). The position for each correlation function was set by mounting one of the retroreflectors on a Newport DC servo linear translation stage (ILS100CC) with 1 µm unidirectional repeatability and 10 cm travel range.[3] The white fringe corresponded to an approximate position of −3.5 cm, offering 1.5 cm of symmetric travel across the white fringe and 8.5 cm asymetric travel away from the white fringe. The dither was introduced to the interferometer by mounting the corner of the other, stationary retroreflector to a piezoelectric actuator and driving the actuator with a waveform generator. The actuator introduced a small-angle tilt into the corner of the retroreflector that modulated the

[3]This stage precision is not strictly good enough for room temperature measurements, but certainly good enough for this work. Until we bought a non-contact ultra-precision linear stage, we performed room temperature measurements by scanning the interferogram three times and averaging the result to achieve sub-micron overall precision.

overall path-length of the interferometer arm.[4]

Once the interferometer paths were recombined, the two outputs of the interferometer were focused using 7.5 cm focal length achromatic doublets onto two Excelitas (formerly Perkins-Elmer) AQRH-16 single-photon counting modules (made using silicon avalanche photodiodes) with sub-50 cps dark counts and minimized afterpulsing (<1%). The resulting electronic signals from the detectors were split to yield two copies of the photon-counting signal. One of the electronic signals was counted by a DAQ to provide real-time intensity data for the confocal microscopy program, which controlled the galvomirrors, was used to select the single emitter before the experiment, and was monitored during the measurement to correct for cryostat drift during the measurement. The other electronic signal was sent to an ALV-7004/FAST real-time multiple-tau correlator to generate log-scale correlation functions in hardware.[5] The correlator was used to record both the 0+1 autocorrelation function (i.e. the autocorrelation of the sum signal of the interferometer outputs), and both the 0/1 and 1/0 interferometer cross-correlations.

5.1.2 The Sample

Because our goal was to measure the full spectral correlation reporting on rapid spectral dynamics without the obfuscating effects of charging or large spectral jumps, we required a nanocrystal sample that could be continuously excited for tens of minutes without bleaching or undergoing unwanted spectral dynamics. This is generally uncommon for most nanocrystal samples under vacuum at low temperature. As a result, we selected our nanocrystal sample for its superior optical properties rather than its underlying physics.

[4]One might worry that the retroreflector tilt could cause the interferometer paths to drift into and out of overlap. However, we observed no evidence for this in the intensities of the interferometer outputs using micron-scale dither waveforms. It would certainly be more reliable to introduce the dither waveform using the linear stage, but the stage used in this work was not precise enough.

[5]This correlator is generally used to perform FCS or DLS-style experiments.

The best available nanocrystals at the time of this work were CdSe/CdS core/shell nanocrystals with CdSe core synthesized according to Chen et al. [86] and epitaxial CdS shell grown according to Chen et al. [106] These nanocrystals were highly uniform and exhibited far less fluorescence intermittancy than previous nanocrystal samples at analogous shell thickness. The thicker-shell examples, in particular, exhibited very little fluorescence intermittancy under low flux excitation at room temperature and did not exhibit statistical aging over tens of thousands of seconds.[6] The sample used in this work was synthesized according to this synthetic procedure to yield particles that emitted at 640 nm at room temperature, with a 5.4nm diameter zinc blende CdSe core and a relatively thick, 8 monolayer CdS shells ($\sim$2.7 nm).

To further improve the fluorescence stability of this sample, single-nanocrystal films were fabricated using a poly(methyl methacrylate) polymer matrix and passivated at single-nanocrystal dilution with excess cadmium oleate. First, a cadmium oleate solution was synthesized by combining 1.25 mL cadmium oleate in octadecene and oleic acid (melted with a heat gun), 100 µL decylamine, and 8.75 mL toluene. The single-nanocrystal sample was synthesized by mixing 0.5 mL of 4% w/v of 100 kDa PMMA in toluene and 10 µL of the cadmium oleate solution, and dipping a pipet tip briefly into a transparent, golden crashed out nanocrystal solution and dipping that pipet briefly into the PMMA solution.[7] Then, this film was spin cast on the quartz substrate by fully covering the substrate with solution and spin casting the substrate at 1000 rpm for one minute.

In practice, however, it must be noted that these nanocrystals only barely exhibited the required fluorescence stability under vacuum at low temperature to perform

[6] Unlike giant-shell nanocrystals, fluorescence intermittancy in these samples was suppressed by reducing the frequency and duration of off-events, rather than eliminating the fluorescence quenching of the so-called dark state. This suggests superior surface properties that should lend themselves to reduced charging and fewer large spectral jumps at low temperature.

[7] While this procedure is not exactly rigorous, we were not overly concerned with controlling the exact nanocrystal concentration. We chose this procedure because it could regularly produce a solution with an average occupancy of $2-5$ in FCS without the need for serial dilution (which could strip the nanocrystals of labile ligands).

the full PCFS/Camera experiment. We were able to eventually measure the data presented here, but a more exhaustive survey of the variability of rapid spectral diffusion properties would not have been possible by using the full experiment to study this sample. After the publication of this work, Mulvaney et al. [111] noted that although CdSe/CdS nanocrystals usually exhibit high optical properties, they are still strongly susceptible to oxidation under vacuum. They showed that the beneficial optical properties of CdSe/CdS particles could be maintained under vacuum by growing an additional thin layer of ZnS over the CdS shell. Future investigations of spectral dynamics using PCFS should be much more feasible and straight-forward by either using the full experiment to study CdSe/CdS/ZnS nanocrystals, or by using a less-comprehensive, shorter PCFS experiment to study less synthetically optimized systems.

5.1.3 Experimental Parameters and Data Collection

The experimental conditions used to collect our data were required to balance many competing concerns. For instance, we chose to excite the sample with an excitation flux of $\sim$750 W/cm^2 to balance signal-to-noise with biexciton formation. On one hand, exciting the sample with a high excitation flux is highly desirable because the count rate of correlation functions scale quadratically with signal intensity. However, on the other hand, increasing the excitation flux also increases rate of biexciton formation, which may lead to fluorescence instability and biexcitonic fluorescence features. We estimate that our excitation flux generated a photon on average every $\sim$900 ns, yielding a manageable count rate of between 5–10 thousand counts per second per detector.[8] We observed no evidence for significant biexciton fluorescence in our conventional spectral traces during our experiments.

[8]The overall system detection efficiency of the APD channels of our setup is around 1 % because of the low collection efficiency of long working distance air objectives and because we split our signal over three detection channels.

The parameters of the conventional spectroscopy experiment were optimized for both the general surveillance of the single-nanocrystal spectrum and for the measurement of the long-timescale dynamics of the zero-phonon line (ZPL). On one hand, we required high enough spectral resolution to detect changes in the position of the ZPL during the progress of rapid spectra diffusion. On the other hand, the spectral window of the camera had to be wide enough that large spectral jumps or charging events would not cause the spectrum to leave the spectral window. Moreover, higher spectral resolution causes the spectrum to be dispersed over more pixels, thereby reducing the signal-to-noise of each integrated spectrum. It was imperative that we be able to pinpoint the position of the spectrum using an integration time accessible to PCFS in order to connect the data from the two experiments. During the entirety of the PCFS experiment, we collected a time series of integrated spectra with 250 ms integration time, 58 meV spectral window, 0.11 meV pixel resolution, and a 0.4 meV instrument function.[9]

Finally, the parameters of the PCFS experiment were chosen to balance our requirements for high signal-to-noise, high spectral resolution, wide spectral window, and finite experimental time. Forty-one correlation measurments were made stepping from zero path-length difference to a path-length difference of 4 cm. After discrete Fourier transform, this yielded a spectral window of 1.24 meV and a spectral resolution of 15.5 µeV in the measured spectral correlation. If the nanocrystal did not survive the entire set of 41 measurments, the interferogram could still be assembled with lower spectral resolution, and if the nanocrystal remained optically active after the entire series of correlation measurements, it could be repeated until the nanocrystal bleached to achieve higher signal-to-noise. This spectral resolution was high enough to approximately resolve the width of the ZPL in this sample,[10] and the

[9]The width of the ZPL was resolution-limited, but could be fit to identify the position of the spectrum with sub-pixel resolution.

[10]Note that if we measure a Lorentzian linewidth of ∼15 µeV, it will be manifested as a ∼30 µeV spectral correlation, which is well within our spectral resolution.

spectral window was broad enough to capture the full width of rapid dynamics, but narrow enough to avoid aliasing effects from the other, non-ZPL features in the low temperature spectrum.

Each correlation measurement was optimized to balance the desired temporal resolution of the experiment with the finite duration of the experiment. A triangle dither waveform over ∼4 µm in path-length difference was adopted to ensure satisfaction of the requirements for PCFS. Such a large dither form was ideal because it ensured that the interferogram would be averaged over many fringes, but its length scale was not even close to infringing on the very narrow (∼1 meV) spectral features measured in this work. For experiments that only used the PCFS interferogram to measure the spectral correlation, the integration time of each correlation measurement was 20 s and the dither period was 1 s. These conditions ensured clear satisfaction of the PCFS requirements and used a short integration time in order to complete the scan of 41 correlation measurements as fast as possible. However, they introduced a dither node at ∼40 ms that prevented the connection with camera timescales. For compound PCFS/Camera measurements, the dither period was slowed to 20 s and integration time increased to 40 s. These adjustments shifted the dither node to around ∼800 ms, and allowed for considerable overlap between the PCFS and camera timescales.

5.1.4 Data Analysis

The collected data was imported into Matlab for data analysis. Before the PCFS interferogram could be assembled, each correlation measurement was analyzed using the corresponding camera data and intensity traces to determine that it reflects a consistent spectral position (See Figure 4-1). Then, each correlation function was corrected for dark counts, according to the formula given in Section 3.4, each autocorrelation of the sum signal was afterpulse corrected, each cross-correlation was intensity-corrected using its corresponding corrected autocorrelation function, accord-

ing to Equation 3.47, and then then the corrected cross-correlations corresponding to the same path-length difference were averaged to produce a final set of unique, self-consistent PCFS interferogram measurements. For this work, afterpulse correction was implemented by measuring the afterpulsing signal in a high signal-to-noise measurement of a Poissonian laser. The afterpulsing feature was then removed from each correlation measurement by fitting the short-τ region of the autocorrelation with the afterpulsing signature plus a baseline term, and subtracting the properly scaled afterpulsing signature.

In order to apply the fast Fourier transform algorithm to the spectral correlation, the PCFS interferogram must be represented by a linear array of evenly spaced data points symmetrically distributed about zero path-length difference. This was achieved by reflecting the positive path-length difference data collected experimentally across the white fringe to approximate the negative path-length difference data (which is physically identical),[11] and linearly interpolating any (rare) gaps in the interferogram due to brief large spectral jumps or fluorescence intermittancy. Once the complete interferogram was assembled, each τ-slice was fast Fourier transformed to yield the corresponding slice of the spectral correlation.

The spectral correlation cross-section plots were generated by averaging the τ cross sections of the measured spectral correlation in the vicinity of the noted τ-value to improve the signal-to-noise of each cross sections. The linewidth of the spectral correlation with τ was determined by fitting each interferogram cross-section with a linear combination of exponential decays (i.e. Lorentzian peaks), Fourier transforming the fit, and calculating its FWHM via linear interpolation. And finally, this spectral correlation was used to approximate the autocorrelation of the integrated spectrum for

[11] In essence, we are enforcing that the spectral correlation is perfectly symmetric. There are other ways of doing this, including measuring both sides of the interferogram or taking the absolute value of the Fourier transform of the positive side of the interferogram. The former is not possible with our white fringe position (and a wasteful prospect, besides), and the latter eliminates the possibility of negative data points, which we need to accurately represent the interferogram baseline.

a camera frame by calculating the weighted average of the PCFS spectral correlation according to Equation 4.19. Additional analyses will be described as necessary, but no smoothing of the data in τ-space was ever used except in the generation the spectral correlation cross-section plots.

Finally, the camera data was analyzed by isolating the spectra frames corresponding to the desired spectral position, fitting each frame with a Gaussian function to determine the center-point of the spectrum over time, and calculating by brute force the histogram of shifts between center values as a function of frame separation. This histogram was convolved with the autocorrelation of the integrated spectrum as calculated by PCFS, and its FWHM was determined by linear interpolation.

It is worth noting that both the PCFS and Camera spectral correlations often exhibit small cross peaks that are not in keeping with our simple models of diffusion. In the camera data, this is generally caused by the occasional large, non-ergodic spectral shift. In the PCFS data, this may also be caused by non-ergodic effects, rapid switching between two preferred spectral positions (responsible for the blue-shifted side peaks in the integrated spectra shown in Figure 5-9), or aliasing of discrete acoustic side-peaks. Either way, the small intensity of these features cause them to have little effect on the FWHM of the spectral correlation.

5.2 Results and Discussion

We now present the results of our investigation and examine their important features. This section will rely heavily on the the theory introduced in Section 2.5, and in particular on the predicted behavior of the continuous Wiener model and discrete Poisson model presented in Figures 2-10. These figures have been reproduced in Figure 5-2 for convenience.

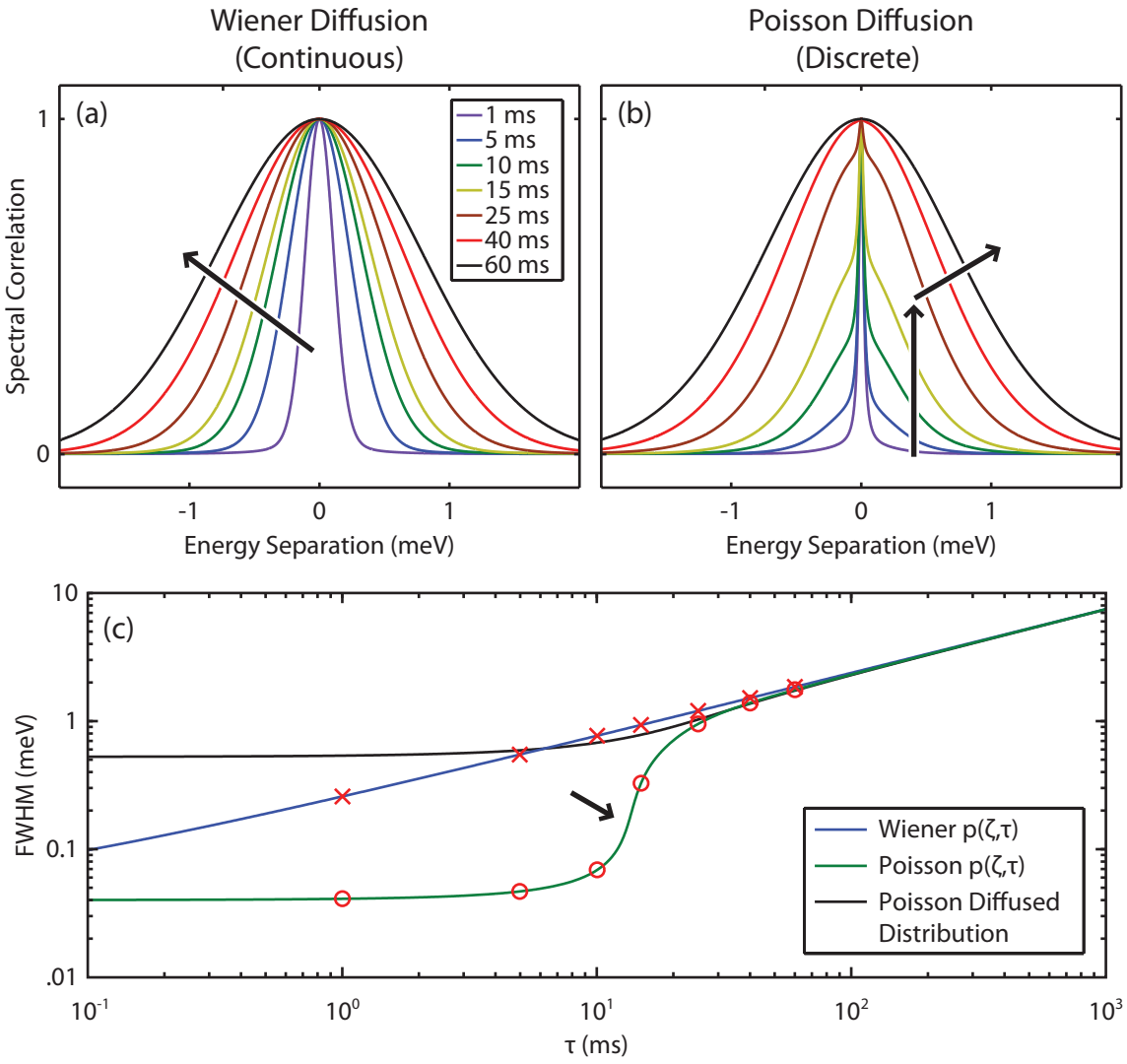

Figure 5-2: Reproduction of the Wiener and Poisson diffusion model results from Figure 2-10. Note the existence of two distinct distributions of photon pairs in the shape of the Poisson spectral correlation and the inflection feature in its FWHM, both of which are evidence of discrete behavior.

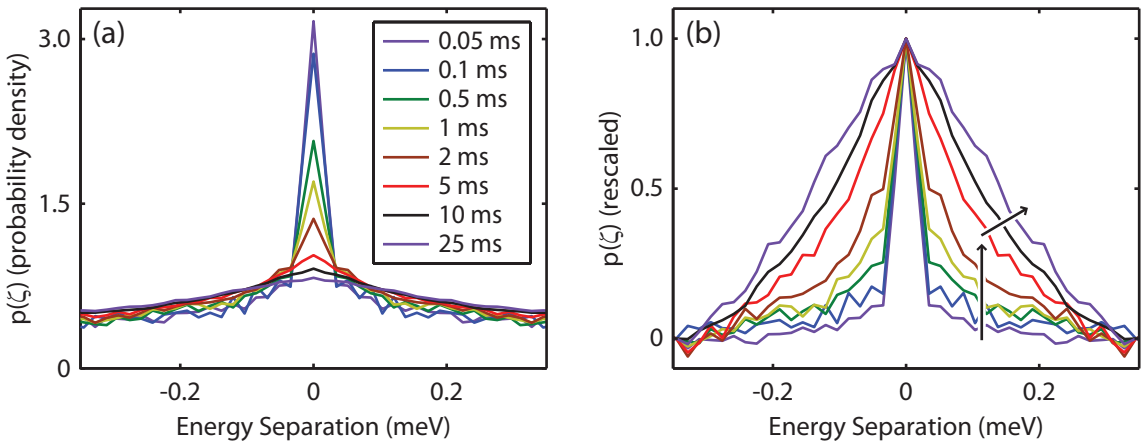

Figure 5-3: A spectral correlation of a low temperature nanocrystal exhibiting discrete spectral diffusion. The spectral correlation is (a) normalized by area as a probability density function, and (b) baseline-subtracted and normalized by amplitude to emphasize changes in shape.

5.2.1 Rapid Spectral Dynamics Are a Discrete Process.

One of the important features of rapid spectral diffusion that has been established in the literature is that it is a photo-assisted, and therefore presumably discrete process. In fact, several investigations have presented either statistical or anecdotal evidence that the spectral diffusion trajectories caused by rapid spectral dynamics are indeed composed of small discrete spectral jumps and periods of spectral stability. We begin by confirming this result, and showing that the discrete character of rapid spectral dynamics in semiconductor nanocrystals can be directly and clearly resolved in the spectral correlation measured by PCFS.

The PCFS spectral correlation of a single nanocrystal at 4 K is shown in Figure 5-3, normalized by area as a probability density function and baseline-subtracted and rescaled to emphasize changes in shape. Like in the Poisson model, the evolution of the spectral correlation exhibits two distinct temporal regimes corresponding to discrete and quasi-continuous behavior (see arrows). For $\tau \leq 2$ms, the evolution of the spectral correlation is characterized by a population transfer from a narrow peak representing the τ intervals over which no spectral dynamics have occured, and a broad peak

representing the τ intervals over which at least one discrete spectral diffusion event has occurred. The "non-diffused" contribution is given by the autocorrelation of the intrinsic spectrum of the nanocrystal, and is consistent with a $\sim$20 µeV Lorentzian homogeneous lineshape.[12] Then, for $\tau \geq 5$ms, the probability of not having a diffusion event in the τ interval has vanished and it becomes more and more likely that multiple diffusion events have occurred. This causes the spectral correlation to be manifested as a single distribution, which broadens and becomes more Gaussian as the average number of discrete jump events increases.

The transition between discrete and quasi-continuous diffusion in this nanocrystal occured at millisecond timescales, far faster than the temporal resolution of conventional single-molecule spectroscopy, but clearly resolved using PCFS.

5.2.2 The Discrete Spectral Jumps Exhibit Correlated Effects Over Several Orders of Magnitude in Time.

We can also follow the progress of progress of rapid spectral diffusion through its quasi-continuous regime by incorporating the conventional camera data. The time series of integrated spectra collected during a PCFS experiment on another nanocrystal is shown in Figure 5-4. Here, we see a startling array of different types of dynamics, including charging events causing the spectrum to shift between 1.975 eV and 1.995 eV, many smaller spectral jumps that may be accompanied by intensity fluctuations, and the small spectral jitter caused by rapid spectral dynamics. In order to assemble a spectra correlation that reports on a consistent set of rapid spectral dynamics, we only consider the behavior of the nanocrystal during its bright fluorescence at 1.975 eV (see

[12] It sort of looks like the non-diffused contribution is resolution-limited. It is not, but the second data point away from zero energy separation falls in line with the straight line connecting the peak to the baseline, so it appears to be hidden. This data point is actually about halfway up the peak, and significantly above the baseline noise.

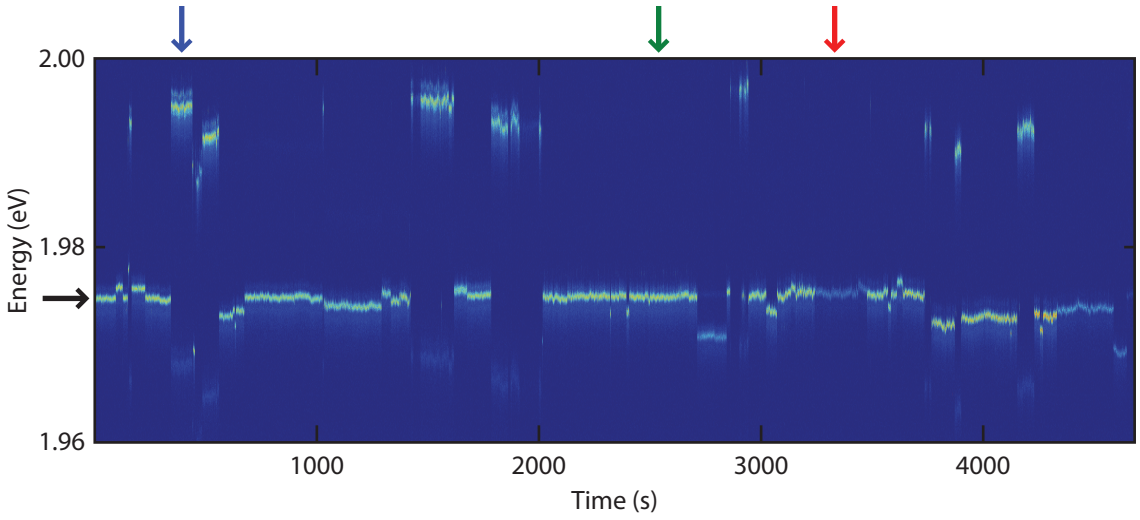

Figure 5-4: The time series of integrated spectra of a low temperature nanocrystal collected during PCFS. The nanocrystal exhibits several different types of spectal dynamics, which may change their dynamic behavior. We compile our PCFS data using only correlation measurements reporting on the bright fluescence state at 1.975 eV (see black arrow). The colored arrows indicate the times of the integrated spectra in Figure 5-9.

black arrow).[13]

The corresponding spectral correlations measured by PCFS and calculated from the camera data are shown in Figure 5-5. Unfortunately, the qualitative signature of discrete spectral diffusion is not as clearly evident in this data, due to a combination of the lower spectral resolution of this experiment and a slight narrower diffused distribution in the discrete regime. Nevertheless, at short τ, the spectral correlation for this nanocrystal is also consistent with a $\sim$20 µeV Lorentzian homogeneous lineshape, and the evolution of the linewidth of the spectral correlation in Figure 5-5(c) closely resembles the qualitative behavior of the Poissonian model show in Figure 5-2(c).[14] Both linewidth curves reach a plateau at the linewidth of the autocorrelation of the

[13] We will allow for discrete jumps as long as they do not affect the overall intensity, because they don't appear to have a large affect on the rapid spectral dynamics and because we strictly do not know whether they are a different phenomonon or simply extremely large instances of rapid spectral dynamics.

[14] There is a 91 µeV gap between the linewidths predicted by PCFS and the camera data, which is entirely consistent with the uncertainty we would predict from our integrated spectrum peak-fitting process. When that is accounted for, the two data sets are in complete agreement.

intrinsic spectrum at short τ, increase and undergo a point of inflection in the discrete regime where the diffused and non-diffused distributions have equal amplitude, and then adopt a power law broadening behavior during the quasi-continuous regime at long τ.

In this nanocrystal, the transition between discrete and quasicontinuous diffusion actually appears to occur on the timescale of tens or hundreds of milliseconds, meaning that conventional single-molecule spectroscopy should have the temporal resolution to observe some instances of discrete behavior. Nevertheless, the small magnitude of these spectral jumps compared to the spectral resolution of our conventional setup would generally obfuscate this behavior.[15] In Figure 5-6, we take a closer look at a stretch of the conventional time series data to look for discrete behavior, and come up relatively empty. However, by combining PCFS and conventional spectroscopy, we can measure the evolution of the spectral correlation over eight orders of magnitude in time, and reveal that its functional behavior is fully consistent with a discrete Poisson-like mechanism.

5.2.3 Salient Features of Rapid Spectral Diffusion Revealed by the Spectral Correlation

Our previous results illustrated that the evolution of the spectral correlation over eight orders of magnitude in time can be explained by a single physical process with a discrete spectral diffusion mechanism. Using the Poisson model as a guide, there are three major pieces of information that should define the diffusion process: the kinetics of the discrete spectral jumps, which are first-order in the Poisson model; the discrete jump distribution, which is a Gaussian distribution in the Poisson model; and the quasi-continuous power law exponent at long τ, which is 0.5 in the Pois-

[15] Achieving higher spectral resolution would cost us either signal-to-noise or temporal resolution. Neither of these would be acceptable.

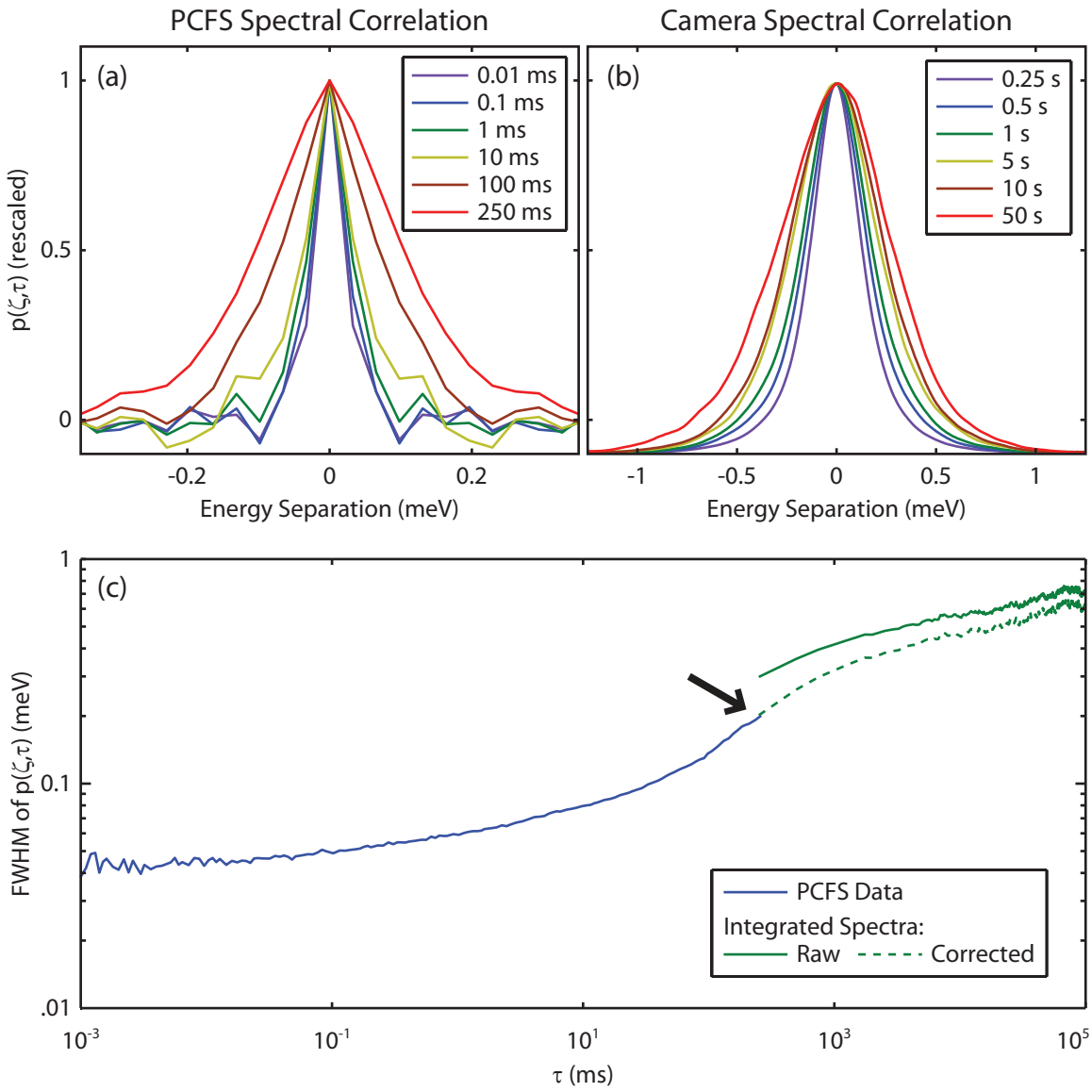

Figure 5-5: Compound PCFS/Camera data from the experiment conducted during the conventional data shown in Figure 5-4. (a) Spectral correlation from PCFS, (b) spectral correlation from the camera data, and (c) the FWHM of the spectral correlation across both data sets. The offset between the PCFS linewidth and the raw camera linewidth is consistent with the uncertainty in the spectral position in the camera data.

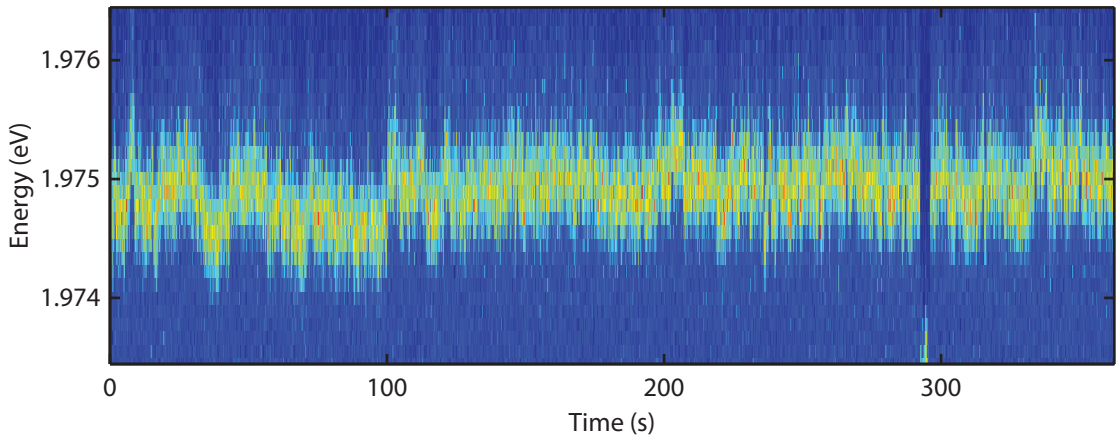

Figure 5-6: The rapid spectral dynamics from the data in Figure 5-5 are clearly seen in the conventional camera data, but their discrete spectral jumps are too small to be unambiguously resolved.

son model. All three pieces of information are simulaneously accessible using the compound PCFS/Camera experiment. In this section, we will discuss how they are manifest in the spectral correlation and what our results tell us about them.

Discrete Jump Kinetics The most important and fundamental piece of information about rapid diffusion that the spectral correlation gives us access to is the kinetics of the discrete spectral diffusion process. As we discussed in Section 3.6.3, the kinetics of spectral diffusion events are intimately tied to the τ-dependence of the area of the non-diffused distribution. Because the linewidth of the non-diffused distribution does not change in τ, the area of the non-diffused distribution is equivalent to its amplitude. In Figure 5-7, we show the spectral correlation for a different nanocrystal with particularly distinct diffused and non-diffused distributions. By normalizing the spectral correlation by area and plotting the amplitude of the non-diffused distribution, we can extract information about its diffusion kinetics.

Unlike in the Poisson model, the fraction of non-diffused photon pairs in this nanocrystal is well-captured by a stretched exponential with 0.5 ms time constant. This finding is consistent with the stretched-out point of inflection we observed in the

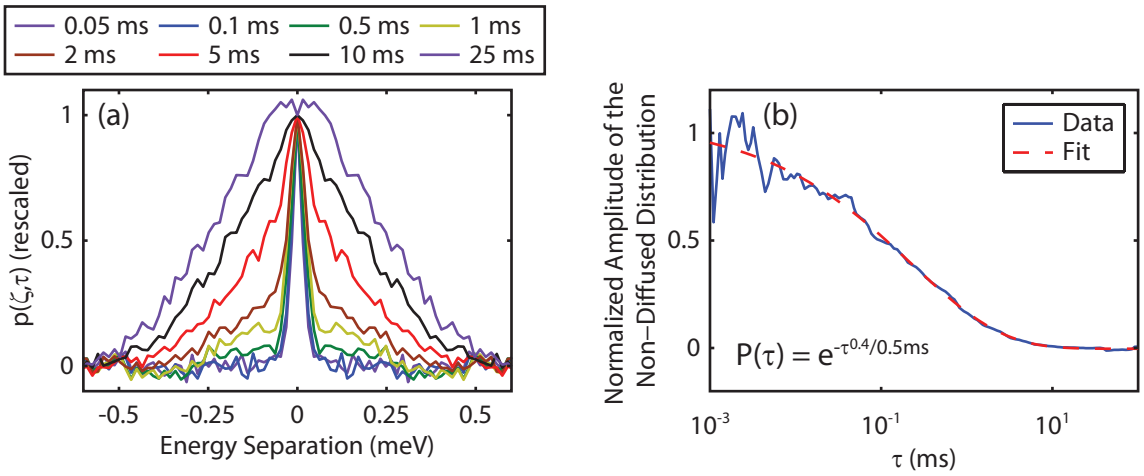

Figure 5-7: (a) PCFS spectral correlation for a low temperature nanocrystal exhibiting a clearly resolved diffused and non-diffused distribution. (b) Time-dependence of the amplitude of the non-diffused distribution, which appears to fit a stretched exponential with significant dispersion.

linewidth trace of the spectral correlation in Figure 5-5. There is something deeply baffling about this result. Not only is the stretched exponential a generally unphysical functional form for kinetics, but the quantity that we are considering is also not even the jump kinetics itself. As we determined back in Section 3.6.3, it is actually the spectra jump kinetics convolved with a falling edge.

The formulation of a kinetic model that functionally fits a stretched exponential in the fraction of undiffused photon pairs remains an unsolved problem, but there are three important qualitative points that we can draw from these results. First, stretched exponentials can sometimes arise in heterogeneous systems. It is likely that the multi-timescale kinetics we have observed in rapid spectral diffusion are caused by temporal variations in the rate of spectral dynamics. These temporal variations may, in fact, be intimately tied to the temporal variations in carrier trapping, which are understood to give rise to the power law kinetics of nanocrystal fluorescence intermittancy. Second, these kinetics results appear to be quite reproducible. In Figure 5-8, we show the jump kinetics that I have managed to extract from several of our available data sets. All of them show long-tail kinetic behavior that can be more

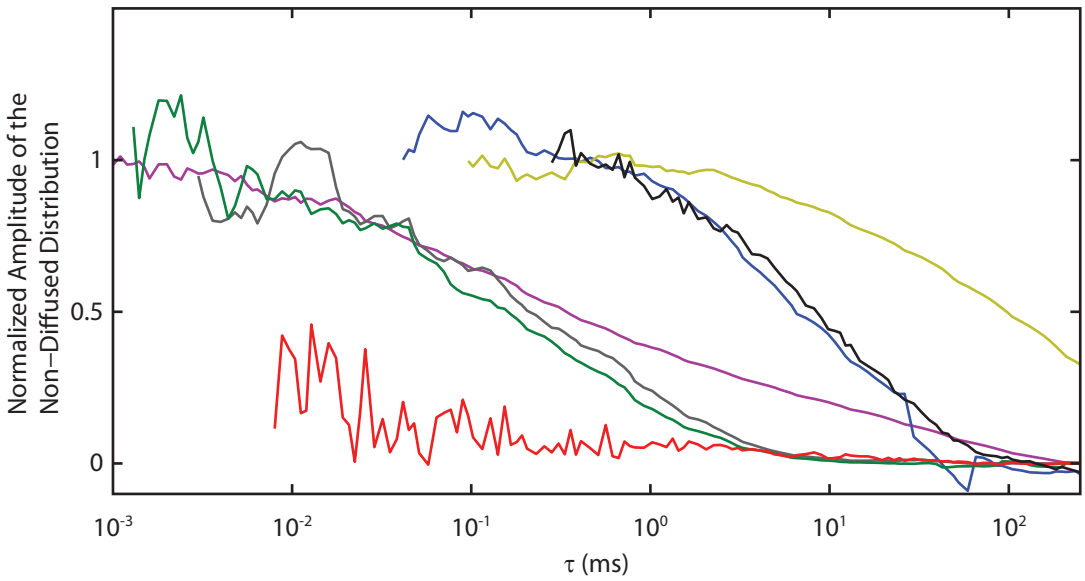

Figure 5-8: The time-dependence of the non-diffused distribution amplitude for several low temperature nanocrystals. Most of this data is very rough, but seems to suggest wide variability in spectral diffusion kinetics from nanocrystal to nanocrystal and even over time in individual nanocrystals.

or less captured by stretched exponentials. But third, the actual numerical values for the parameters of the stretched exponential seem to vary widely from nanocrystal to nanocrystal, even in this relatively homogeneous sample.

This is the first time that the kinetics of the discrete rapid spectral jumps have been measured, in part because PCFS remains the only technique with high enough temporal and spectral resolution to directly resolve jump events without arresting the diffusion process (for example, via resonant PLE).

Discrete Jump Distribution The distribution of spectral shifts produced by individual spectral diffusion events are also encoded in the diffused contribution to the spectral correlation. As we saw in Section 3.6.2 with the Poisson model, the diffused distribution broadens over time as multiple diffusion events occur over the time between photon arrivals and enable the spectrum to move even further from its starting point. Therefore, we can identify the jump distribution of a single event by measuring the lineshape of the diffused distribution as $\tau \to 0$, because, in this limit, the

likelihood of there being more than one diffusion event vanishes.

The lineshape of the diffused distribution as $\tau \to 0$ can be tricky to determine in practice because its overall amplitude goes to zero. However, it is an important physically-relevant parameter that is impossible to measure using a technique that cannot resolve individual spectral diffusion events because it speaks to the overall magnitude of individual spectral jumps. In the data we have collected for this sample, the diffused distribution appears to vary in the vicinity of 50–500 μeV. As we will discuss later, this approximate value can place critical constraints on what underlying physics could be responsible for rapid spectral diffusion.

Quasi-Continuous Diffusion Exponent Finally, using the camera data, we can also track rapid spectral dynamics throughout its quasicontinuous regime. In the Poisson model, each of the discrete spectral jump is uncorrelated, leading to a boring Gaussian quasicontinuous spectral correlation that necessarily broadens according to a $\tau^{0.5}$ power law and whose width prefactor is solely defined by its discrete jump kinetics and jump distribution. Our results corroborate previous findings that nanocrystal rapid spectral dynamics are subdiffusive over long τ, and diffuse according to a power law with an exponent that widely varies between 0.1 and 0.35, even in an otherwise homogeneous sample.

This subdiffusion necessarily indicates that there is some form of correlation between spectral diffusion events. It is important to note that this correlation may take many different forms. Correlation is often captured using autoregressive models, which add either frictional or self-correcting forces to diffusion trajectories. Fernee's observations of spontaneous "relaxation" of nanocrystals to previous spectral positions after photoexcitation may suggest a self-correcting character to rapid spectral dynamics. However, it is much more likely that the subdiffusion we observe here is caused by a confinement force rather than some jump-to-jump memory effect. In

practice, there will be an upper bound to the magnitude of the electric field that the environment can impose on the core states of the nanocrystal. This constrains the overall distance that a rapid spectral diffusion trajectory can travel from the zero-field transition energy and will introduce correlated subdiffusive effects into the measured spectral correlation.[16]

Although the quasi-continuous diffusion exponent can easily be measured using conventional spectroscopy (as we do here), there is a certain benefit to simultaneously measuring the exponent along with the discrete diffusion parameters that are manifested at short τ. It may not be that surprising that the quasi-continuous behavior is subdiffusive, but it is not clear why it should still be captured by a power law (as opposed to, say, the Ornstein-Uhlenbeck broadening profile of diffusion in a harmonic well) and why it should vary so widely from nanocrystal to nanocrystal. A more comprehensive study of the correlation between jump kinetics, jump distribution, and quasi-continuous exponent may shed some light on these issues.

5.2.4 The Intricate Interplay Between Spectral Diffusion Mechanisms

One of the striking results in the low temperature single-nanocrystal literature has been the strong dependence of the optical properties of the nanocrystals on their time-dependent fluorescence wavelength. For example, Empedocles and Bawendi [63] observed that both the strength of exciton-phonon coupling and the integrated linewidth defined by rapid spectral diffusion varied by a factor of four with spectral position in their core-only CdSe nanocrystals. In Figure 5-9, we show three integrated spectra

[16] In their spontaneous spectral diffusion paper, Fernee et al. [263] couch their findings in terms of an autoregressive model on the basis of the conditional probability data in their Figure 1. In fact, almost any subdiffusive model, whether frictional, self-correcting, or confined, can potentially reproduce the data in those figures. For instance, drawing random numbers between 0 and 1 will produce the same "memory" effects because if you draw 0.99, you know you have a very good chance of your next draw being less than the previous one.

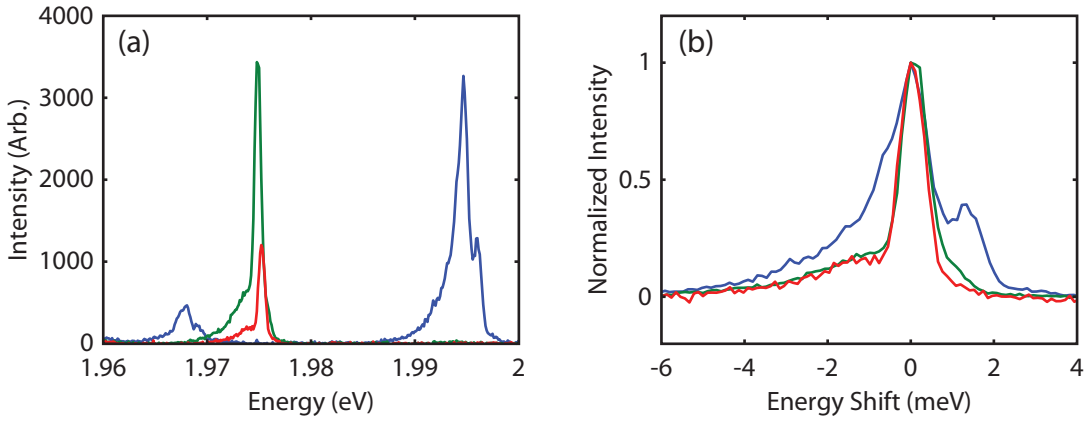

Figure 5-9: (a) Three integrated spectra from the time series in Figure 5-4, (b) shifted in absolute energy and normalized to emphasize changes in shape. The three spectra have different fluorescence intensities and rapid spectral dynamics. Note that the intensities of the side peaks on the blue side of the main ZPL are anticorrelated in time with the main ZPL peak. This suggests they are not features of the underlying intrinsic spectrum, but that they are caused by rapid switching between two distinct ZPL positions.

taken from the time series in Figure 5-4. These integrated spectra may not clearly have different exciton-phonon coupling strengths in this case, but they do clearly have different fluorescence intensities and rapid spectral diffusion magnitudes.

In fact, the variability in the linewidths of the integrated spectra in Figure 5-9 raises an important question about the wide variability in spectral diffusion parameters we observed earlier among nanocrystals in our supposedly homogeneous sample. Does this data suggest that the architectural properties of the nanocrystal that define their rapid spectral dynamics are subtle and not easily characterizable via other techniques, or that all nanocrystals are capable of adopting a wide variety of spectral diffusion behaviors, depending on the exact transient details of their surface structure? In our final experiment, we address this question by comparing the rapid spectral diffusion behavior of a single nanocrystal in two different discrete spectral positions.

Figure 5-10(a) shows the time series of integrated spectra for a single nanocrystal at low temperature. It exhibits all three types of spectral dynamics we have discussed.

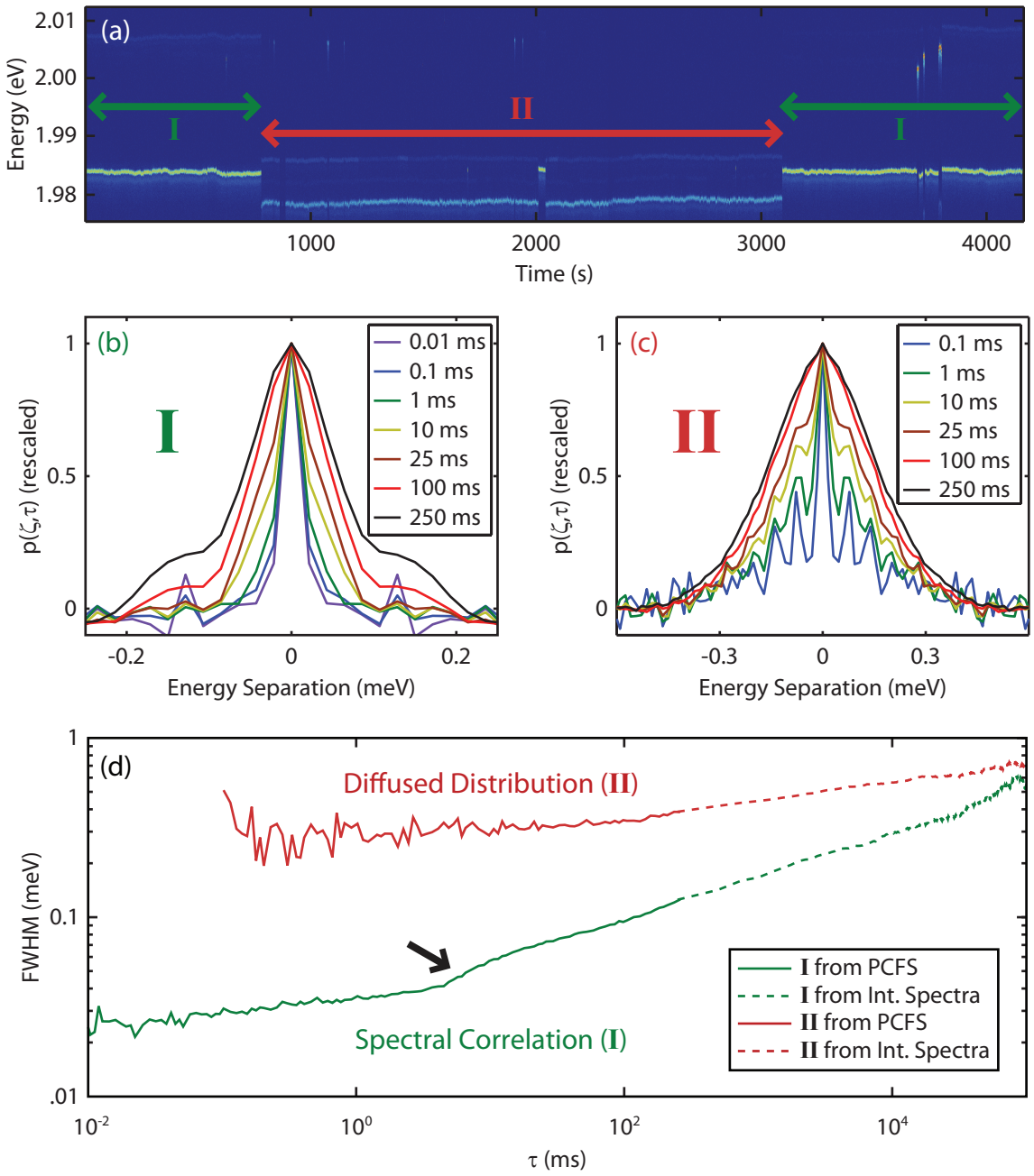

Figure 5-10: (a) Time series of integrated spectra for a single nanocrystal. (b)/(c) PCFS spectral correlations corresponding to spectral positions I and II. (d) Time-dependence of the FWHM of the spectral correlation of I and the diffused distribution of II across both the PCFS and camera data.

Charging causes an infrequent switching between the neutral, very bright state at ∼2.005 eV, and the comparitively dimmer, trion state at ∼1.985 eV.[17] Additional carrier trapping effects cause smaller discrete spectral jumps, which in this case, bridge two spectral positions separated by ∼7 meV.[18] And, rapid spectral dynamic cause clear spectral jitter in both of the long-lived spectral positions over time on the order of ∼1 meV.

The fluorscence from these different spectral positions exhibit different fluorescence properties, including different fluorescence intensities, acoustic exciton-phonon coupling strengths, and integrated linewidths.[19] All three of these parameters could track together without any more complicated microscopic physics if the local electric field on the nanocrystal was allowed to change with spectral position (as might be expected to occur during charging, or that certainly does occur during a spontaneous Stark-shifting event.) However, the spectral correlations corresponding to these spectral positions reveal a much deeper story. The spectral correlations of the two long-lived spectral positions, I and II, are shown in Figure 5-10(b,c). The linewidth of the spectral correlation of I, and the linewidth of the diffused distribution of the spectral correlation of II, are plotted across the PCFS and camera timescales in Figure 5-10(d).

Both spectral correlations exhibit the hallmarks of the discrete spectral diffusion behavior we observed in earlier nanocrystals. The shape of the spectral correlation of II during PCFS timescales clearly reflects the population transfer between a narrow, non-diffused distribution (corresponding to a nearly resolution-limited ∼15 µeV Lorentzian linewidth) and a broad diffused distribution, and the linewidth evolution

[17] This assignment is made on the basis of recent investigations that have reported stable trion emission in low-temperature CdSe/CdS samples, with a binding energy of ∼20 meV.

[18] It would be tempting to consider these the two trion states, but in CdSe/CdS samples, the other trion state has been reported to have a much lower binding energy of ∼5 meV, [181] which would put it at around ∼2.00 eV.

[19] There is also a faint, blue-shifted feature that seems to roughly, but not completely track with the spectral position of the ZPL. I am not going to read anything into that feature here.

of the spectral correlation of I reaches a plateau at short τ (again, corresponding to a $\sim$15 µeV Lorentzian linewidth) and exhibits the characteristic point-of-inflection feature of discrete diffusion at around $\tau = 5$ ms (see arrow). Furthermore, the non-diffused distributions in both spectral correlations seem to persist for orders of magntidue in time after the first appearance of diffusion behavior, corroborating previous observations of long-tail kinetics, and when the spectral correlations reach their respective quasi-continuous regimes, they broaden continuously according to subdiffusion power laws.

Nevertheless, within the qualitative confines of this discrete subdiffusion model with long-tail kinetics, the behaviors of the rapid spectral dynamics at these two spectral positions could not be more different. In spectral position II, the emitter undergoes fast, discrete sampling of a relatively fixed spectral distribution. By $\tau = 100$ µs, the integrated area of the non-diffused distribution has already almost vanished, yielding to a broad $\sim$300 µeV diffused distribution whose width does not increase further throughout PCFS timescales. Even in camera timescales, the diffused distribution only undergoes minor broadening to $\sim$700 µeV, in keeping with the subtle long timescale wiggles seen in the camera data. In contrast, the spectral dynamics of the emitter at position I are slower and more diffusive in character. The spectral correlation of I does not appear to change notably until almost 1 ms, and when it does, the discrete population transfer signature is almost impossible to distinguish because of a narrow diffused distribution with a width $\sim$50 µeV. But, once discrete diffusion events begin to occur in I, they undergo much more correlated behavior, which broadens the diffused distribution of I at a much more rapid rate (the quasi-continuous exponent of I is 0.24, compared to 0.11 for II). In the end, by $\tau = 100$ s, the two spectral correlations appear to reach very similar linewidths, but the discrete spectral jumps that produce this broadening are very different in character.

This experiment demonstrates that much, if not most, of the variability we observe

in the rapid spectral dynamics of our sample, could be explained by the variability of rapid spectral diffusion over time in individual nanocrystals due to the perturbative effects of charging and other surface-trapping processes. The strong interplay between charging, surface-trapping, and rapid spectral dynamics must be captured in any legitimate microscopic model of rapid spectral diffusion.

5.3 Summary of the Properties of Rapid Spectral Dynamics and Implications for its Physical Interpretation

Prior to this investigation, it was known that rapid spectral dynamics were caused by second-order Stark interactions between the core states responsible for fluorescence and fluctuating local electric fields. [63] These fluctuations were understood to be discrete, photo-induced events at low temperature, usually enabled by the $<$100 meV of energy released when the hot exciton relaxes to the band edge. [64, 262, 263] And, these fluctuations were found to induce overall spectral variations on the order of 1$-$10 meV in core-only or thin-shell nanocrystals, but only variations of $<$meV in thicker-shell samples. [64, 262, 263] These properties are consistent with two proposed physical models for spectral diffusion. In the first model, rapid spectral diffusion is caused by the diffusion of surface-trapped carriers, generated during large spectral jump events, through a manifold of trap states on the surface of the nanocrystal. [64, 265, 266] In the second model, rapid spectral diffusion is simply a manifestation of ligand dynamics on the surface of the nanocrystal, whose overall Stark effect on the core states is modulated by the total local field defined by the aforementioned trapped carriers. [263]

Our results make several important contributions to this base of knowledge. First

of all, we have confirmed the discrete character of the rapid spectral dynamics and showed that its correlated behavior over eight orders of magnitude in time is consistent with a single underlying physical mechanism. Our direct observation of this discrete process on timescales faster than those accessible by conventional single-nanocrystal spectroscopy, has allowed us to access, for the first time, the kinetics and spectal jump distributions of individual spectral diffusion events. The kinetics consistently exhibit multi-timescale behavior, suggesting temporal variations in the rate of rapid spectral diffusion that may be tied to the power law distribution of fluoresence intermittancy, and the magnitudes of discrete spectral diffusion events were found to vary in the vicinity of $50-300\,\mu$eV in our CdSe/(8ML)CdS sample. Finally, we identified fundamental differences in the character of rapid spectral diffusion between different spectral positions in low temperature single nanocrystal fluorescence. This result represents a fundamental interplay between rapid spectral dynamics and carrier trapping beyond the simple modulation of the overall spectral jump magnitude with overall local electric field caused by the second-order nature of the Stark effect.

It is not obvious that a ligand-only model of rapid spectral diffusion should be able to accomodate these additional findings. Although the structural similarities between the disordered ligand shell and polymers could potentially rationalize the multi-timescale kinetics of rapid spectral dynamics and the power law subdiffusion over long timescales, our high sample homogeneity and statistically large number of ligands surrounding each nanocrystal should not allow for order-of-magnitude variations in the spectral diffusion kinetics. There is also no clear reason why carrier trapping or charging events should cause fundamental changes in behavior of the ligand dynamics. It is possible that carrier rearrangments may modify the relaxation processes of the core excited state, thus changing the way that heat is dissipated to the periphery of the nanocrystal and therefore the perturbation of surface ligands. After all, the change in fluorescence intensity between positions I and II in Fig. 5-10

does clearly indicates a change in the non-radiative relaxation processes that compete with fluorescence. However, more evidence will be required to substantiate a ligand perturbation model.

On the other hand, little is known about the manifold of trap states on the surface of the nanocrystal, whether trapped carriers are actually free to diffuse through the manifold, or whether it features the correct heterogeneity in the radial distribution of probability density to cause the appropriate magnitude of Stark shift during a spectral diffusion event. The trapped carrier model is simply a phenomenological model with only weak ties to known nanocrystal surface physics. Nevertheless, it does cleanly rationalize (at a qualitative level) practically all of the properties we have described here. The heterogeneous character of the manifold could explain the multi-timescale kinetics and wide variability in spectral diffusion parameters, whereas the addition or subtraction of diffusing carriers from the surface of the nanocrystal could explain the severe, qualitative differences between rapid spectral dynamics across different spectral positions. In light of these considerations, we suggest the possibility of a hybrid model, where spectral dynamics are caused by the perturbation of trapped carriers on the surface of the nanocrystal by ligand rearrangment. This model combines the attractive features of both the ligand and carrier diffusion models.

Our discussion of the possible physical causes of rapid spectral diffusion should be punctuated with two notes of concern. First, recent evidence may have reopened the possiblity that rapid spectral dynamics are caused by charge trapping effects *outside* the nanocrystal architecture. Previous work by Gomez et al. [71] excluded this possiblity by examining the correlation between spectral position and spectral linewidth in room temperature samples. They observed large spectral shifts over around 15 meV attributed to carrier trapping effects, and saw a clear correlation between linewidth and spectral position, which suggested that the room temperature linewidth was being defined (or at least affected by) by rapid spectral dynamics.

In this context, their findings that the linewidth behavior was unaffected by the dielectric matrix indicate that the source of rapid spectral dynamics is inside the nanocrystal architecture. However, it is also known that the application of an electric field can dramatically increase the extent of exciton-phonon coupling, especially to LO phonon modes. Our recent work with solution-phase PCFS indicates that exciton-phonon coupling is one the major effects defining the room temperature linewidths, and that failure to passivate the surface of nanocrystals can dramatically broaden their room temperature linewidth. The results of Gomez et al. may actually reflect the enhancement of phonon coupling with applied field, rather than comment on the physical origin of rapid spectral diffusion.

Finally, although our results are entirely consistent with a single physical mechanism of spectral diffusion, they do not necessarily preclude the possibility of multiple mechanisms. Specifically, because most of our data draws a relatively clear distinction between the timescales of discrete and quasi-continuous diffusion, our data could also be consistent with a combination of two distinct diffusion mechanisms. At fast timescales, spectral dynamics could be governed by a discrete process that randomly samples a fixed distribution (with multi-timescale kinetics and the fixed distribution given by the diffused distribution as $\tau \rightarrow 0$). This mechanism would produce a constant broadened spectrum at long timescales, which could then undergo a second, continuous diffusion process to produce the so-called quasicontinous behavior observed over camera timescales. This second process could be identified because it would necessarily broaden the non-diffused distribution if there was any probability that the first discrete process had not occured on the timescale of continuous diffusion. So far, we have not identified any clear evidence that two distinct physical mechanisms are required.

5.3.1 What to Do with the Magnitude of Discrete Spectral Jumps

So far, we have done very little with the average magnitude of discrete spectral jumps that we measured via the width of the non-diffused distribution in the spectral correlation. In principle, this should be a very insightful observable because it should be able to tell us something about either the magnitude of the charge redistributions responsible for rapid spectral diffusion or their proximity to the core of the nanocrystal. In this section, we present some rudimentary modeling designed to shed light on the possible sources of spectral dynamics.

In a basic model of a neat nanocrystal, both the band-edge excited state and the ground state are spherically symmetric and do not have a net dipole moment. Nevertheless, real nanocrystals may have surfaces with partial charges and trapped carriers that impose a local electric field on the core of the nanocrystal. This (quasi-) permanent field interacts with the polarizability of the excited state to induce an excited state dipole moment and red-shift the fluorescence wavelength of the nanocrystal. Following the treatment of Empedocles and Bawendi, [63]

$$\Delta E = \alpha \xi^2, \tag{5.1}$$

where α is the polarizability of the excited state and ξ is the local electric field at the core of the nanocrystal. Thus, if we layer the electric field fluctuations responsible for rapid spectral diffusion $\xi(t)$ over the quasi-permanent sources of local electric field ξ_0, noting that these permanent sources generally have a much larger magnitude than the rapid field fluctuations, the Stark response appears to be pseudo-first-order in the fluctuating electric field, i.e.,

$$\Delta E(t) = \alpha\xi^2 \tag{5.2}$$

$$= \alpha(\xi_0 + \xi(t))^2 \tag{5.3}$$

$$= (\alpha\xi_0^2) + (2\alpha\xi_0)\xi(t) + (\alpha)\xi(t)^2 \tag{5.4}$$

$$\approx (\alpha\xi_0^2) + (2\alpha\xi_0)\xi(t). \tag{5.5}$$

This fact is important to recognize because even though the electric field from point sources or dipoles tend to decay very quickly with distance, their resulting Stark shift on the core states of a nanocrystal can be amplified if there is already a large permanent electric field imposed on the nanocrystal.

With this in mind, we can estimate the overall magnitude of spectral shifts predicted for the models we discussed earlier. We will the use the following approximations: a core radius of 2.7 nm, a shell thickness of 2.7 nm, a total crystal diameter of 5.4 nm, a polarizability of 300 nm^3,[20] a core/shell dielectric constant of 9, and, where applicable, a coordinating ligand dipole moment of ~ 1 D. We begin by determining the effect produced by trapping a carrier at radius r from the center of the nanocrystal. The Stark shift induced by such a trapped carrier is given by,

$$\Delta E[e\text{V}] = 1.29e \left[\frac{\text{nm}^2}{\text{V}}\right] \left(\xi_0 \left[\frac{\text{V}}{\text{nm}}\right] + \frac{1.44[\text{Vnm}]}{r^2}\right)^2 - 1.29\xi_0[e\text{V}]. \tag{5.6}$$

The results of Equation 5.6 are shown in Figure 5-11, for the case where the trapping event occurs in a neat nanocrystal with no internal electric field and for the case where a carrier of one charge is trapped directly opposite a previously trapped charge with opposite charge (i.e. a second trapping event whose field is aligned with the first trapped charge). The model predicts that a trapped charge on the surface of our

[20] This is the polarizability measured by Empedocles and Bawendi [63] for a CdSe particle with a 3 nm radius. The actual polarizability is probably slightly higher because of delocalization into the CdS shell

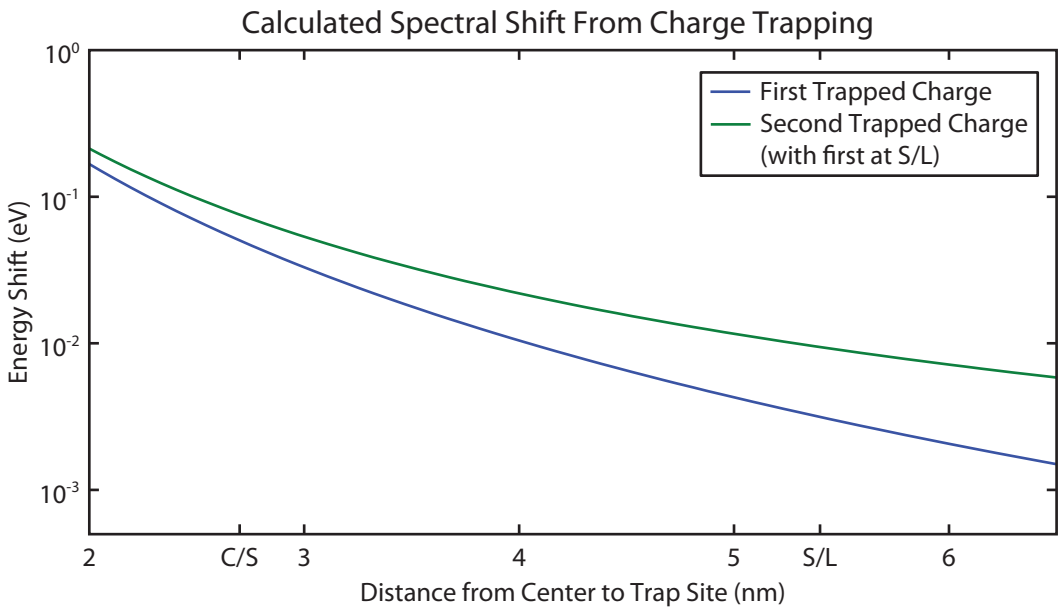

Figure 5-11: Predicted Stark shift induced by trapping either the first or second charge on the periphery of the nanocrystal. This toy model suggests that a first trapping event should induce a spectral shift around 3 meV and spectral shifts as high as 10meV in subsequent trapping events, depending on the geometry of the trapped charges.

CdSe/CdS nanocrystals would induce a spectral shift on the order of 3 meV (second charge up to 10 meV), which is consistent with our experimental results (especially given the back-of-the-envelope nature of our calculations). Next, to estimate the magnitude of rapid spectral dynamics we would expect in the charge trapping model, we calculate the change in field caused in both of these two cases by moving one of the charges 0.25 nm away from the surface of the nanocrystal (Figure 5-12). These results suggest that trapped carrier dynamics could, in principle, induce electric field fluctuation on the order of hundreds of microelectronvolts or millielectronvolts in our sample, as long as we are able to rationalize a 0.25 nm perturbation of surface charges.

The picture could potentially be rather different for the ligand model; it all depends on the nature of the ligand. If the ligand is a charged species like oleic acid, and the ligand dynamics responsible for rapid spectral diffusion is the pulling away of the ligand from the surface, the calculation can be quite similar to the charge-trapping

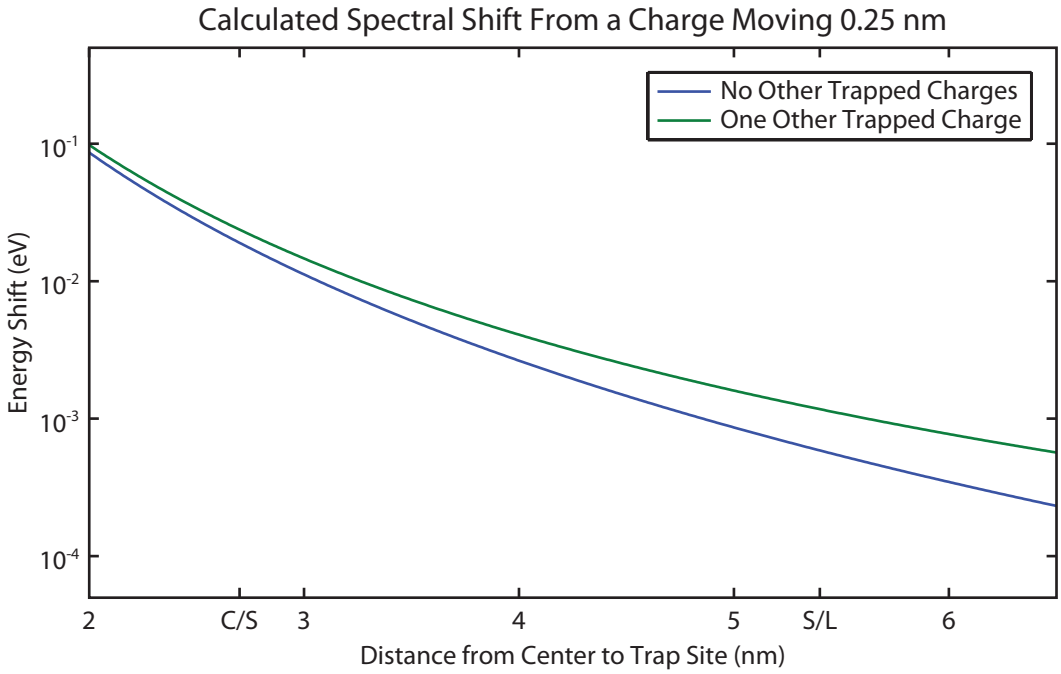

Figure 5-12: Spectral shifts predicted by perturbing the position of one of the trapped charges by about a Cd-S bond length. This charge trapping model for rapid spectral diffusion suggests discrete spectral jumps of around an meV, which is consistent with our data given the rough character of the model.

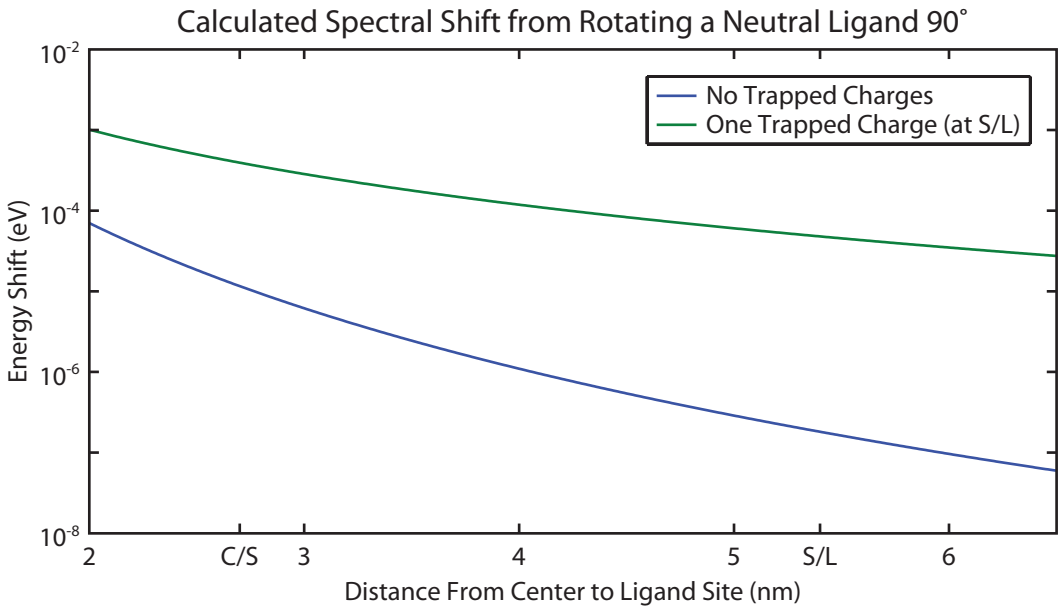

Figure 5-13: Spectral shifts predicted by rotating a ligand dipole 90° on the surface of the nanocrystal (as a function of a prospective surface radius). This model predicts a maximum discrete spectral shift of 0.1 µeV for a neat nanocrystal, and shifts as high as 100 µeV if there is a significant local electric field on the nanocrystal. Note that this is the most extreme case. Minor reorganization of the surface structure that only slightly perturbs the coordination bond vector will result in an even smaller spectral shift.

model (although you may, or may not expect the coordination site to pull 0.25 nm from the surface of the nanocrystal). However, if the ligand motion is more torsional, the effect on the core state fluorescence may be more like the rotation of a dipole electric field. The Stark shift caused by an extreme, 90° rotation of a ligand dipole, is given by,

$$\Delta E[e\mathrm{V}] = 1.29e\left[\frac{\mathrm{nm}^2}{\mathrm{V}}\right]\left(\xi_0\left[\frac{\mathrm{V}}{\mathrm{nm}}\right] + \frac{5.9\times10^{-2}[\mathrm{Vnm}^2]}{r^3}\right)^2 - 1.29e\xi_0[e\mathrm{V}]. \qquad (5.7)$$

and plotted in Figure 5-13, for a neat nanocrystal and a nanocrystal with one charge trapped on its surface. This model shows that if rapid spectral diffusion is caused by ligand dynamics on the surface of the nanocrystal, there must be a significant local electric field on the nanocrystal that strongly polarizes the nanocrystal exciton. This

field could either be caused by trapped charges or the distribution of Cd and Se atoms (or charged ligands) on the surface of the nanocrystal. Either way, with additional experimentation and more careful theoretical modeling, the average magnitude of the discrete spectral shifts should ultimately be an important observable for determining the physical cause of rapid spectral dynamics.

5.4 Future Directions

The full compound PCFS/Camera experiment we have used here to capture the full shape of the spectral correlation has been particularly valuable in these preliminary investigations because it has allowed us to piece together a unified and self-consistent picture of rapid spectral dynamics over eight order of magnitude in time. However, it would be impractical to try to use such a time-intensive experiment to characterize the full range of spectral behavior exhibited by a given sample, and even less practical to use it to tease out the subtle differences between samples. Not only would this endeavor be emotionally taxing, but it would also be severely prone to selection bias because it is only possible to probe nanocrystals and spectral positions that are stable for tens of minutes.

There are two obvious easier and faster versions of our experiment that we can use to study less stable behavior and to more quickly survey larger numbers of nanocrystals. For instance, by choosing fewer correlation measurements spaced further apart in path-length difference, we can explicitly target the narrow non-diffused contribution to the spectral correlation and measure its decay in amplitude as a function of τ. This experiment reveals the discrete jump kinetics with a shorter integration time, higher-signal-to-noise ratio, or both. Similarly, if the associated camera setup had much higher resolution (albeit a concerningly narrow spectral window), it could be possible to calculate the spectral correlation of the camera data directly from the

time series of integrated spectra, rather than relying on peak fitting and the PCFS connection. The peak fitting process we have used here gives us superior precision with our relatively low-resolution setup, but it sacrifices signal-to-noise because each frame, with its hundreds of photon counts, is reduced to a single histogram count. Direct calculation of the spectral correlation from the camera data would reveal the long timescale behavior with a much shorter total integration time.

Using these shorter versions of our compound experiment, it should be possible to characterize the average parameters of rapid spectral diffusion of a sample and determine their variability. This would enable us to determine the effect of nanocrystal architecture on rapid spectral dynamics, and by varying parameters such as core size, shell thickness, ligand passivation, and host matrix, it should be possible to determine the physical cause of rapid spectral dynamics once-and-for-all. For the record, due to the wide variability of rapid spectral dynamics we see in our monodisperse sample of CdSe/CdS nanocrystals, I advocate the use of single-nanocrystal sampling over an averaging experiment like solution-phase PCFS (or its substrate analogue that we will discuss later) for the elucidation of basic physics. Averaging over many different types of diffusion behavior will wash out any distinctive features of the spectral correlation. After all, the average of a bunch of power laws with different exponents is not a power law.

There are also three, less related directions that I have been interested in but unable to follow through on. The first, now that we can regularly determine the linewidth of the non-diffused distribution of the spectral correlation, is to use PCFS to study the homogeneous linewidth of the ZPL emission at low-temperature. Other groups have argued about the intrinsic linewidth of nanocrystals, and specifically about why CdSe/CdS nanocrystals should have a broader intrinsic linewidth than other nanocrystals. We can directly address these questions using PCFS. The second, is to take a closer look at the long-timescale "rapid" spectral dynamics of nanocrystals.

In this work, we only followed τ to 100 s, but the spectral correlation was still clearly broadening further. At some point, we anticipate that the spectral correlation will reach a plateau width representing the maximum electric field that the rapid spectral dynamics can impose on the nanocrystal. It might be interesting to confirm this idea experimentally and to know what governs that upper limit. Third, we have exclusively studied rapid spectral dynamics at 4 K. Other investigations have found that increasing the temperature causes the spectral dynamics to increase in magnitude and to occur on faster timescales. However, our room temperature work with S-PCFS does not reveal any phenomenon that resembles rapid spectral diffusion at room temperature. There is an intriguing opportunity to do some conceptual bridge-building between the conceptual pictures of spectral diffusion at low temperature at room temperature.[21]

And, finally, I personally think it would be interesting, now that single-nanocrystal spectroscopy technology has improved so dramatically, to revisit the Stark-effect style measurements of Empedocles and Bawendi. [63] For one thing, our ability to draw insight from the average magnitude of spectral jumps is hindered by the fact that we do not actually know what the magnitude of the local electric field around our single nanocrystals are. By combining PCFS and/or camera measurements with Stark-effect measurements, we may be able to better pinpoint the location of the rapid spectral dynamics. And for another thing, our better camera technology should allow us to dramatically increase the temporal resolution of a Stark-effect measurement. Empedocles and Bawendi presented a telling figure where they could see a spontaneous change in the local electric field around the nanocrystal by sweeping an applied field. Today, it could be possible to resolve the local electric field around nanocrystals with a temporal resolution of a second, allowing for real-time measurement of the evolution

[21] For example, if low temperature spectral diffusion is caused by the diffusion of carriers through a trap manifold, maybe there should not be any spectral diffusion at room temperature because these carriers can easily thermally de-trap.

of the local field.

Part II

Investigating the Biexciton Quantum Yield of Semiconductor Nanocrystals at the Ensemble Level

Chapter 6

Background on the Biexciton Quantum Yield of Semiconductor Nanocrystals

The recent developments in synthesis that we discussed in the Introduction have addressed (or at least begun to address) many of the sub-optimal properties of semiconductor nanocrystals. The current arsenal of nanocrystal materials feature particles that can emit throughout the visible and short-wave infrared; exhibit high or even near-unity quantum yield, compact geometries, and surface functionalizability; and can event be free of toxic materials such as cadmium, arsenic, and lead (although it is not yet possible to have all of these properties in one). One of the properties that has proven to be a bit tricky to address has been their performance under high-excitation flux conditions. This is particularly problematic in device applications like LEDs, where it is often desirable to minimize the active area of the diode, and biological applications like confocal imaging, where high excitation flux is used to achieve shorter integration times and therefore higher temporal resolution.

Fundamentally, the problem that nanocrystals face is their long fluorescence life-

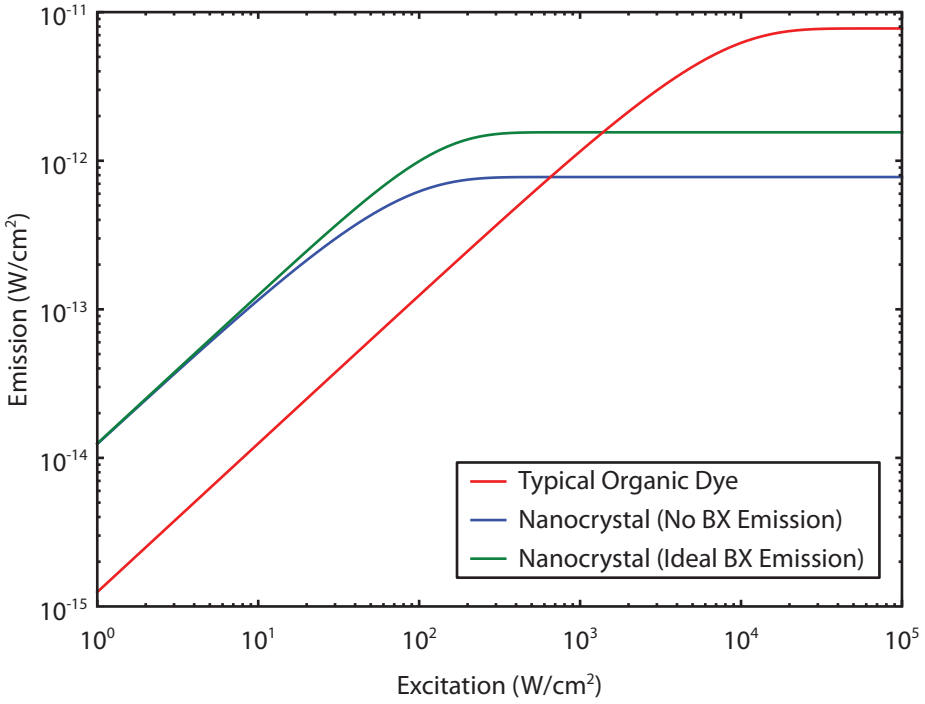

Figure 6-1: At low excitation fluxes, nanocrystals exhibit greater brightness than many organic dyes due to their higher absorption cross section. However, at high excitation flux, nanocrystal exciton fluorescence reaches saturation at much lower brightness than organic dyes due to their longer fluorescence lifetime. [192] This drawback could be overcome by efficient multiexciton fluorescence. Data from model developed by T.S. Bischof.

times, which can range from tens of nanoseconds for visible-emitting samples to hundreds of nanoseconds or microseconds for infrared-emitting samples. [156, 188, 189] If nanocrystals are relegated to behaving as single-photon emitters like organic dyes, their long radiative lifetimes will cause their fluorescence to reach saturation at orders of magnitude lower excitation flux and produce many fewer total photons. [192] Instead, we would prefer to think about nanocrystals as multi-photon sources, capable of sustaining multiple excitations simultaneously. This would, in principle, allow nanocrystals to overcome fluorescence saturation and dramatically improve their brightness under high-flux excitation. Figure 6-1 illustrates how efficient biexciton fluorescence alone could increase the high-flux brightness of nanocrystals by a factor of four due to the faster radiative rate of the biexcitonic state.

From a practical perspective, however, for most of their history, nanocrystals have not been multi-photon emitters. Even though it has been possible to generate multiexcitons in nanocrystals, their close proximity in the core of the nanocrystal enhances the probability of Auger-like and other non-radiative recombination channels that compete with biexciton fluorescence. [193, 291, 292] The quantum yield of biexciton fluorescence has routinely been between one and two orders of magnitude lower than the quantum yield of exciton fluorescence, making its contribution to the total fluorescence output of the nanocrystal almost negligible, even at high excitation flux. Moreover, the ability to generate multiexcitons is a double-edged sword because it also means that the rate of absorption in the nanocrystal does not saturate with the fluorescence. Under high-flux conditions, these practically non-radiative biexcitonic states are constantly being formed and dumping energy into their local environment, enhancing the probability of blinking events or photodamage. High-excitation flux applications of nanocrystals require better control of multiexciton fluorescence, not only to enhance their overall brightness, but also to prevent the detrimental effects of multiexcitons on their fluorescence stablity.

6.1 What Do We Know About Auger-Like Processes?

Auger-like non-radiative recombination in nanocrystals has been a topic of considerable study in the spectroscopy literature over the last 15 years. Early investigations were particularly interested in this process because of the role that nanocrystal charging was understood to play in blinking dynamics.[1] [66] As nanocrystals continued to mature synthetically and blinking effects were reduced, the role of Auger-like processes have continued to be addressed in the literature in the context of promoting

[1]The original charging model of blinking has been called into question, [293, 294] and that story has become a bit more complicated since these original papers. [108, 171] But, it is certainly still the case that a charged nanocrystal will generally have a lower quantum yield because of Auger-like interactions between the exciton and the free charge.

multiple exciton generation (the reverse process that generates two excitons from one high energy exciton) and multiexciton fluorescence (our motivation here).

In broad strokes, the rate of Auger recombination is governed by two factors: the strength of the Coulomb interactions between the three carriers (i.e. their proximity) and the momentum-matching condition that couples the initial three-particle wavefunction to the final, high-curvature excited state. [295] Any architectural change that affects either the proximity of the carriers or the curvature of their wavefunctions should be tied to a change in the Auger rate. The Auger rate has been dramatically decreased in several investigations by decreasing the Coulomb interaction between the carriers, including by increasing particle volume [296, 297] and by decreasing the electron/hole overlap in type-II and quasi-type-II heterstructures. [298, 299] In fact, these investigations have reported increases in the Auger lifetime by orders of magnitude. Nevertheless, these approaches have been found to be somewhat suboptimal because of the wider implications attached to the magnitude of the Coulomb interaction. Nanocrystal size impacts the Coulomb interaction responsible for Auger recombination, but it also defines the emission wavelength; the electron/hole overlap impacts the Coulomb interaction responsible for Auger recombination, but it also defines the rate of single exciton fluorescence.

Cragg and Efros [300] have suggested decreasing the rate of Auger recombination via the momentum-matching constraint instead. It is well-known that otherwise monodisperse nanocrystal samples generally have highly heterogeneous Auger rates, which result in multiexponential PL decay curves and wide variability in the biexciton/exciton quantum yield ratio from dot-to-dot. [187, 193] This variability is probably due the poorly-controlled interfacial properties of nanocrystals, which can introduce abrupt potential boundaries that introduce curvature into the band-edge wavefunctions and provide better momentum-matching between the initial and final states of the Auger process. [300, 301] The existence of a small minority of nanocrys-

tals with nearly unity biexciton quantum yield suggests that better synthetic control of the nanocrystal surface properties could significantly improve the multiexciton fluorescence quantum yield of samples. A recent investigation has put this principle into practice, demonstrating that the biexciton quantum yield of CdSe/CdS nanocrystals could be both increased and made more homogeneous within the sample, by inserting an intentionally alloyed CdSeS layer between the core and pure CdS shell. [186] The optimization of nanocrystal syntheses with superior interfacial properties could therefore result in nanocrystals with very efficient multiexciton fluorescence and high suitability for high-excitation flux applications.

6.2 How Do We Measure Multiexciton Fluorescence?

One of the major reasons why the optimization of the multiexciton quantum yield has not received more attention in the synthetic literature is because it is a subtle observable that is relatively difficult to measure. It has generally been measured using one of three approaches, all of which require special spectroscopy expertise and/or considerable time on the part of the experimenter. The inherent difficulty of characterizing multiexciton behavior has relegated the study and optimization of multiexciton fluorescence to the relatively small number of nanocrystal research groups who have expertise in both synthesis and spectroscopy.

The first method for characterizing multiexciton dynamics is to use transient photoluminescence or transient absorption experiments to measure the average population lifetime of the biexcitonic state. [292, 296, 301, 302] In this strategy, the PL decay trace or ground state bleach is measured under low excitation flux to measure the population dynamics of the excitonic state. Then, the excitation flux is increased to determine how the decay or bleach is affected by the addition of multiexcitons. By comparing the high- and low-flux data, it is possible to isolate the population decay

of the biexcitonic state and calculate its Auger lifetime and quantum yield. This approach directly measures the population dynamics of multiexcitonic states, the more physically-relevant observable, and, as an ensemble technique, it can immediately speak to the average behavior of multiexcitons within a given sample. However, it relies on the careful modeling of multiexponential decay traces, requires ultrafast capabilities, and is prone to charging and other high excitation flux artifacts. [303] The accuracy of the analysis is fundamentally based on the idea that the excitonic behavior of the sample is consistent at low and high excitation flux, even though high flux excitation is known to cause photodamage, increased blinking, and other effects that may change the functional form of the excitonic population dynamics.[2] Moreover, translating the often highly multiexponential population dynamics of the biexcitonic state into a precise measurement of the biexciton quantum yield of the sample is a difficult prospect, at best.

The second method for characterizing the multexciton dynamics of a sample is to model its fluorescence intensity saturation as a function of excitation flux (as in Figure 6-1). [187] This strategy can be applied to a thick film or concentrated solution of nanocrystals to measure the average sample properties or it can be applied to individual nanocrystals. As an ensemble method, saturation modeling directly addresses the essential applications-oriented question, namely, how bright we can make the nanocrystal sample, using a very simple and inexpensive optical setup. However, saturation models will generally need to parameterize the absorption cross-sections and quantum yields of higher multiexcitons in order to capture the data, generating a many-variable fit with little quantitative precision in any given parameter, and, as a high-flux ensemble technique, it may also conflate the multiexciton information we desire with excitonic effects such as photodamage, charging, and blinking. Fluores-

[2]For instance, the excitonic baseline of the Transient PL data presented by Bae et al. [186] appears to notably change with excitation flux, even though they stir their sample. This may be actually be caused by long-lived biexcitons, but it is difficult to know for sure.

cence saturation can also be performed on single nanocrystals in a single-nanocrystal microscope. [187] This strategy is more resilient to blinking and other excitonic effects and allows the experimenter to monitor variability within the sample, but it also uses a more complicated optical setup, requires the experimenter to measure a large number of nanocrystals to achieve statistical significance, and is still prone to uncertainty in its many-variable fits.

The final method for characterizing multiexciton dynamics is to use single-nanocrystal photon-correlation experiments (SNC-$g^{(2)}$) to measure the fluorescence quantum yield of the biexcitonic state in individual nanocrystals. [166] As discussed in the introduction, SNC-$g^{(2)}$ experiments excite a single nanocrystal with pulsed excitation and measure the relative probability of detecting either two photons after a single excitation pulse, caused by fluorescence from both the biexcitonic and excitonic states, or detecting single photons in two subsequent excitation pulses, both from excitonic states. As long as the absorption by the nanocrystal during each excitation pulse is Poissonian, the ratio of these probabilities is equivalent of the ratio of the quantum yields of the biexciton and exciton. This experiment directly measures the most purely biexcitonic, applications-relevant observable without the need for modeling, namely, how much biexciton fluorescence suffers due to the competing many-body non-radiative channels, and it does so under low excitation flux with high resilience to excitonic effects.[3] Nevertheless, the SNC-$g^{(2)}$ experiment requires a single-photon correlation setup, and it is a relatively long experiment to perform ($\sim$5–30 min, depending on the blinking dynamics of the nanocrystal and the required signal-to-noise). The long duration of the experiment introduces a concerning avenue for selection bias effects, because studied nanocrystals must remain optically active long enough to complete the experiment, and it also makes the process of measuring the average quantum yield ratio of a sample extremely time consuming,

[3] As long as only the photon pairs drawn from the bright state are considered.

because of the wide variability of biexciton quantum yield within nanocrystal samples. [187, 193, 304]

All of these techniques have clear benefits and drawbacks that can make each one of them the appropriate tool for a given type of investigation. However, none of them offer a straight-forward, plug-and-play means for characterizing the biexcitonic behavior resulting from a given synthesis, with high accuracy and precision. Such a tool would be extremely helpful and convenient for any efficient sythetic effort to optimize the surface properties of nanocrystal samples for ideal multiexcitonic fluorescence.

6.3 The Plan

Our goal is to develop a convenient and reliable experiment for measuring the average biexciton fluorescence quantum yield of a sample of nanocrystals. This experiment should combine the beneficial features of the SNC-$g^{(2)}$ experiment, including the direct measurement of the biexciton/exciton quantum yield ratio, low excitation flux conditions, resilience to artifacts, and the use of a single-nanocrystal microscope that can also be used to measure a variety of other sample properties, with the beneficial features of ensemble measurements, including high sample statistics, short experimental time, and the lack of user selection bias. Furthermore, to aid in synthetic optimization, our experiment should be capable of measuring the sample-averaged quantum yield ratio with high precision to identify subtle changes from sample to sample, and be capable of measuring the biexcitonic properties of synthetically underdeveloped materials. As we will demonstrate, all of these properties can be achieved in a single experiment by using the conceptual framework of SNC-$g^{(2)}$ to study a dilute solution of nanocrystals.

6.4 Conceptual Summary of the Solution-Phase $g^{(2)}$ Measurement

Photon-antibunching measurements were initially used in the 1970's to confirm the quantum nature of light. In their investigation of gas-phase sodium atoms, Kimble et al. [305] showed that when they excited a dilute atomic beam using a CW dye laser, the autocorrelation function of the emission decreased towards $g^{(2)}(\tau) = 0$ as $\tau \to 0$. This finding was inconsistent with a classical result, which would predict a maximum in the autocorrelation function as $\tau \to 0$, and instead consistent with quantum theory both with regards to the single atomic emitter and the quantized radiation field. The idea was that the detection of a first photon collapses the emitter wavefunction into the ground state, rendering it non-emissive until it can be re-excited. As a result, quantum mechanics predicts that, for a single-quantum emitter, $g^{(2)}(0) = 0$, and that $g^{(2)}(\tau)$ should then increase with τ according to the PL decay of the emitter.

The experimental manifestation of antibunching was made more conceptually explicit using pulsed excitation. [306, 307] Here, the single-quantum emitter is excited at distinct temporal intervals. According to quantum theory, an individual two-level emitter should only be able to absorb a single photon per pulse and emit a single photon in the period of time following excitation. The resulting autocorrelation of the emitted signal should therefore be captured by a series of peaks spaced at the repetition period of the laser, with each peak being defined by the autocorrelation of the PL decay. But in the case of a single-quantum emitter, there should not be a peak at $\tau = 0$ because it is impossible for multiple excitation-emission cycles to occur following a single excitation pulse.[4] The pulsed and continuous-wave excitation forms of the antibunching experiment are functionally very similar, but the pulsed version

[4]This assumes that the excitation pulse is much shorter than the PL decay. If it is not, there may be a small peak at $\tau = 0$ corresponding to the case where the emitter fluorescences during the excitation pulse and still has an opportunity to be re-excited.

offers a quantitative advantage because antibunching is measured by comparing the magnitudes of the center and side peaks rather than functionally fitting a continuous antibunching signature.

With the rise of single-molecule spectroscopy, the antibunching experiment became an important tool for spectroscopists to demonstrate that they were indeed studying an individual single-quantum emitter, rather than an aggregate, or to identify how many single-quantum emitters were being investigated. Figure 6-2 illustrates that, even if there are multiple single-quantum emitters in the focal volume, there is a distinctive difference in the number of recombination pathways that can provide correlation counts in the center and side peaks of the autocorrelation function. In fact, if the emitters have uniform brightness, the ratio of the magnitudes of the center peak $g_0^{(2)}$ and side peak $g_{T_{rep}}^{(2)}$ is simply given by,

$$\frac{g_0^{(2)}}{g_{T_{rep}}^{(2)}} = 1 - \frac{1}{n}, \tag{6.1}$$

where n is the number of single-quantum emitters in the focal volume.

Nair et al. [166] later adapted this antibunching measurement to investigate the biexciton quantum yield of individual nanocrystals by noting that the multiexciton emission of individual nanocrystals was actally fairly similar to having multiple emitters in the focal volume. After all, in the event that a nanocrystal could independently absorb and emit arbitrarily large numbers of photons, the fluorescence from the nanocrystal should not exhibit any antibunching at all.[5] In the low excitation flux limit, where the nanocrystal is never excited more than twice in a single pulse, this idea could be used to compare the relative brightness of the nanocrystal biexciton

[5]Note that because the biexciton and exciton are not independent emitters, the number of pathways for each correlation peak is different from the independent emitter case in Figure 6-2. Under low flux excitation, a nanocrystal with unity biexciton/exciton quantum yield and no higher multiexciton emission will exhibit no antibunching, rather than the two-independent-emitter behavior. You can rationalize this by noting that the higher multiexcitons are never created during the experiment, so their low quantum yield is never reported.

(a)

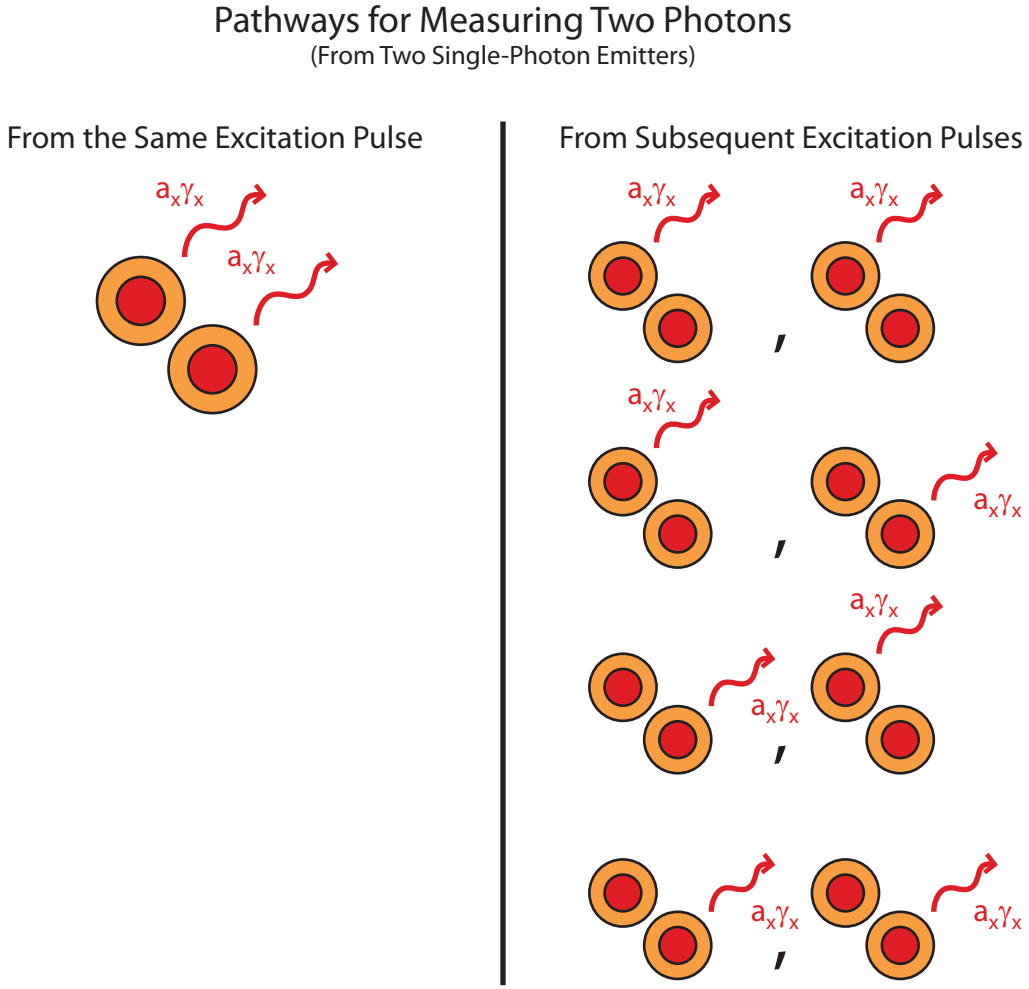

(b)

	Center Peak Area	Side Peak Area	Peak Area Ratio
2 Emitters	$a_x^2\gamma_x^2$	$\frac{1}{2}\left[4a_x^2\gamma_x^2\right]$	$\frac{1}{2}$
n Emitters	$\frac{1}{2}(n^2-n)(a_x^2\gamma_x^2)$	$\frac{1}{2}\left[n^2a_x^2\gamma_x^2\right]$	$1-\frac{1}{n}$

Figure 6-2: (a) Number of pathways that produce two photons from two single-photon emitters after a single excitation pulse and in subsequent excitation pulses. (b) General mathematical expression for the peak area ratio with either two or n single-photon emitters.

(a)

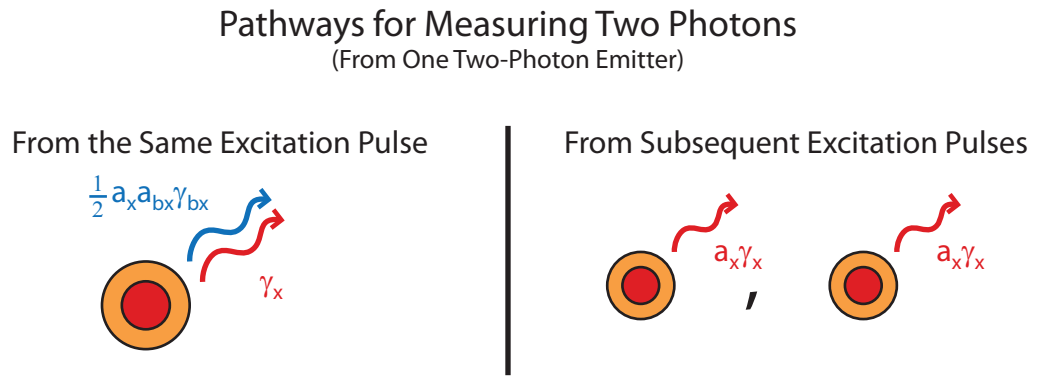

(b)

	Center Peak Area	Side Peak Area	Peak Area Ratio
1 Emitter	$\frac{1}{2}a_{bx}a_x\gamma_{bx}\gamma_x$	$\frac{1}{2}\left[a_x^2\gamma_x^2\right]$	$\frac{a_{bx}a_x\gamma_{bx}\gamma_x}{a_x^2\gamma_x^2} \approx \frac{\gamma_{bx}\gamma_x}{\gamma_x^2}$

Figure 6-3: (a) Number of pathways that produce two photons from a two-photon emitter after a single excitation pulse and in subsequent excitation pulses. (b) Mathematical expression for the peak area ratio for one two-photon emitter under low excitation flux.

and excition (Figure 6-3). Nair et al. showed that if the absorption cross-sections of the biexcitonic and excitonic states were the same, a comparison of their relative brightness simply reduced to a comparison of their quantum yields, i.e.,

$$\frac{g_0^{(2)}}{g_{T_{rep}}^{(2)}} = \frac{\left\langle \gamma_x \gamma_{bx} \right\rangle}{\left\langle \gamma_x \gamma_x \right\rangle} \sim \frac{\gamma_{bx}}{\gamma_x}, \tag{6.2}$$

where γ_x represents the quantum yield of the excitonic state, γ_{bx} represents the quantum yield of the biexcitonic state, and $\left\langle \cdots \right\rangle$ represents the time average over the integration time of the experiment, taking into account intensity fluctuations due to blinking and other effects.

The analysis of Nair et al. [166] requires that there be only a single nanocrystal in the focal volume. There is little ambiguity in the regime typical of nanocrystals, where the biexciton quantum yield is much less than the exciton quantum yield. Based on Equation 6.1, multiple particles of similar brightness cannot produce an antibunch-

ing ratio less than 0.5, and the observation of a < 0.5 peak area ratio can serve as both confirmation of the single-nanocrystal identity and an accurate measure of the quantum yield ratio.[6] Unfortunately, if the peak area ratio is greater than 0.5, low excitation flux measurements cannot be used to determine if the antibunching feature has been eroded by the existence of multiple particles in the focal volume or by efficient biexciton fluorescence. In this case, some other experimental method would be required to confirm that the sample is a single particle and that the biexciton/exciton quantum yield ratio is indeed greater than 50%.[7]

Nevertheless, if we know, through whatever means, how many particles are in the focal volume, it is straightforward to parse the sources of eroded antibunching from multiple particles and from multi-photon emission. In Figure 6-4, we visually derive the significance of the peak area ratio for the case of two (identical) two-quantum emitters in the focal volume. The cruicial point is that the peak area ratio is broken up into two parts: the first part representing contributions to the center peak from different particles and the second part representing the average antibunching behavior expected for each of the individual particles in the focal volume. All that we need to know to back out the average quantum yield ratio is the fraction of the total number of photon pairs in each peak that originate from the same particle, which is directly related to the number of particles in the focal volume.

This fact is essential for understanding the antibunching feature produced by a solution-phase sample where particles are free to diffuse through the focal volume. Even though we may not know at any given moment how many particles are in the focal volume, autocorrelation analysis can tell us what the average occupation of the

[6] It should be kept in mind that a sub-0.5 peak area ratio can be produced by two particles with very different brightnesses. A good example would be if there were a second nanocrystal on the periphery of the excitation spot. Luckily, such a second particle would be spatially-resolved in a confocal scan.

[7] The good news is that the antibunching feature of a single particle with high biexciton quantum yield should have a different excitation-flux-scaling than two particles with low biexciton quantum yield. This is discussed in T.S. Bischof's thesis.

(a)

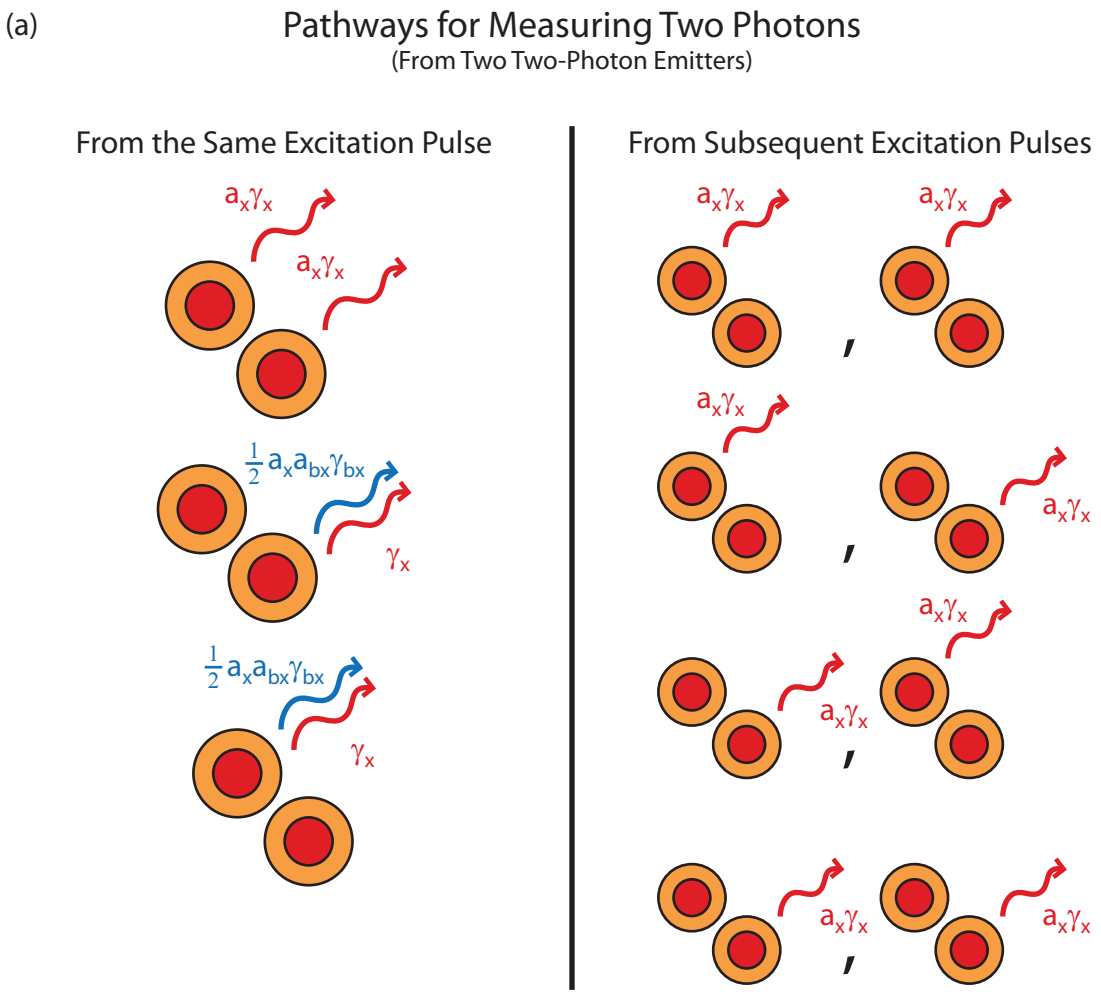

(b)

	Center Peak Area	Side Peak Area	Peak Area Ratio
2 Emitters	$a_x^2\gamma_x^2 + a_{bx}a_x\gamma_{bx}\gamma_x$	$\frac{1}{2}\left[4a_x^2\gamma_x^2\right]$	$\frac{1}{2}(1+\frac{\gamma_{bx}\gamma_x}{\gamma_x^2})$
n Emitters	$\frac{1}{2}(n^2-n)(a_x^2\gamma_x^2) + \frac{n}{2}a_{bx}a_x\gamma_{bx}\gamma_x$	$\frac{1}{2}\left[n^2a_x^2\gamma_x^2\right]$	$1-\frac{1}{n}\left(1-\frac{\gamma_{bx}\gamma_x}{\gamma_x^2}\right)$

Figure 6-4: (a) Number of pathways that produce two photons from two two-photon emitter after a single excitation pulse and in subsequent excitation pulses. (b) General mathematical expression for the peak area ratio with n two-photon emitters under low excitation flux.

focal volume is. Figure 6-5 shows the continuous-wave FCS curve from Figure 1-7(c), annotated with its important characteristics. As we discussed in the Chapter 1, the FCS curve is proportional to the conditional probability of detecting a second photon given that some particle in the focal volume had emitted a photon some time τ before. At all times, there is a constant, uncorrelated probability of detecting a photon from a different particle, regardless of the optical behavior of the particle that emitted the first photon. This fixed probability is captured by the Poissonian background of the FCS autocorrelation function. However, there is an additional *correlated* probability that the same particle will emit a second photon, which is governed by the physics of that emitter. This correlated probability is given by the amplitude of the FCS autocorrelation function above the Poisson background, which vanishes at short τ because of antibunching, vanishes at long τ because of particle diffusion, and has an overall magnitude at intermediate τ given by the inverse of the average occupation of the focal volume. [167] Furthermore, just as the fixed sample antibunching feature does not reach zero in the case of multiple independent emitters, several investigations have been able to tie incomplete solution-phase antibunching to dye and/or nanocrystal aggregation. [308, 309]

FCS therefore gives us exactly the information we need to know in order to unpack the peak area ratio of a solution-phase sample. The total fraction of photon pairs that are contributed to the center and side peaks of a pulsed-excitation autocorrelation function from different particles in the focal volume is given by the area of side peaks at τ beyond the diffusion time of the fluorophores in the sample, and the average quantum yield ratio of fluorophores in the sample is given by the peak area ratio after this constant background is subtracted from the center and side peak magnitudes. That is,

$$\frac{\left\langle \gamma_x \gamma_{bx} \right\rangle}{\left\langle \gamma_x \gamma_x \right\rangle} = \frac{g_0^{(2)} - g_{\tau\to\infty}^{(2)}}{g_{T_{rep}}^{(2)} - g_{\tau\to\infty}^{(2)}}, \tag{6.3}$$

where, in the normalized version of the autocorrelation function, the Poissonian back-

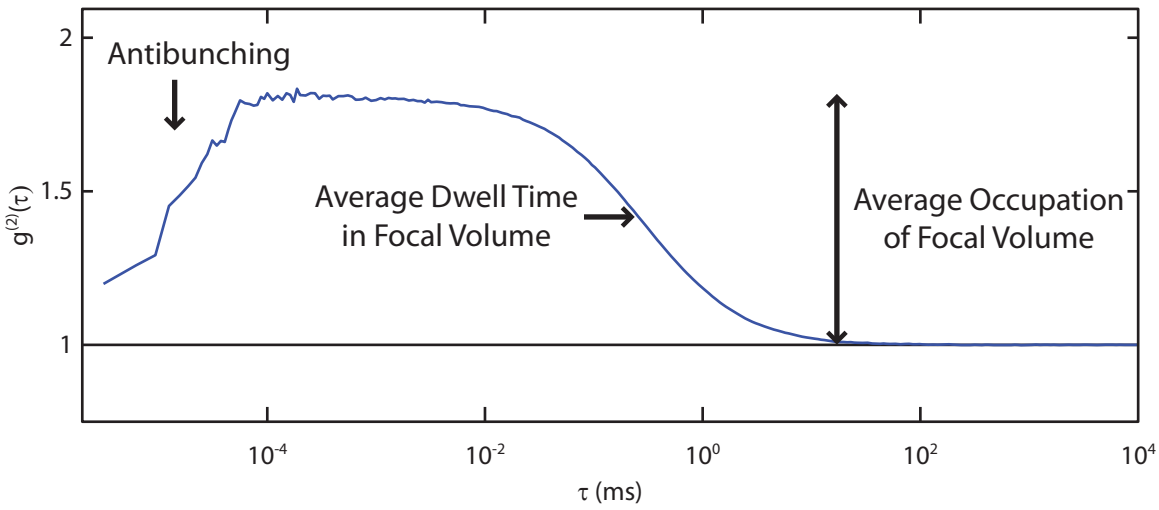

Figure 6-5: FCS trace from Figure 1-7(c), annotated with the physical information that can be extracted from it.

ground $g^{(2)}_{\tau\to\infty}$ is unity. We can further relate this expression to that derived in Figure 6-4 by noting that the in the normalized form of the autocorrelation function the area of the side peak is given in FCS as $1+\frac{1}{\langle n\rangle}$, and rearranging this expression to yield,

$$\frac{g^{(2)}_0}{g^{(2)}_{T_{rep}}} = \frac{\langle n\rangle}{\langle n\rangle+1} + \frac{1}{\langle n\rangle+1}\frac{\langle \gamma_x\gamma_{bx}\rangle}{\langle \gamma_x\gamma_x\rangle}. \tag{6.4}$$

This equation does not quite match the fixed particle case from Figure 6-4 because FCS features a Poisson distribution of emitters in the focal volume, not a fixed number.[8] But, the deeper difference between the fixed and diffusing cases is that whereas the average of the quantum yield terms in the fixed particle case is simply the average of the properties of the n particles in the focal volume, the diffusing case averages the quantum yield values of all of the particles that diffuse through the focal volume during the measurement. Not only does a solution-phase $g^{(2)}$ approach give us the quantitative precision of a $g^{(2)}$ measurement, but it also gives us the large and representative sample size of solution-phase or ensemble measurements.

In the next Chapter, we will extend the formalism of Nair et al. [166] to show that

[8]This will be evident in the math in the next Chapter.

their quantum yield ratio result used to study biexciton fluorescence in nanocrystals can be cleanly and predictably translated to a solution-phase sample.

Chapter 7

Theory Behind the Solution-Phase $g^{(2)}$ Experiment

We now describe the theoretical details of the solution-phase $g^{(2)}$ experiment. We will begin with a derivation of the significance of the center to side peak area ratio of the pulsed-excitation autocorrelation function of the fluorescence from a focal volume of emitters freely diffusing in solution. Then, we will discuss several topics relating to the practical application of the experiment, including how to calculate the uncertainty in the measured quantum yield ratio, considerations that dictate the choice of average occupation, some tricks for making long measurements, and how to handle samples with particularly long radiative lifetimes. This chapter is heavily influenced by, and sometimes directly copied from, the supplemental material in Beyler et al. [244]

7.1 Derivation of the Solution-Phase $g^{(2)}$ Experiment

7.1.1 Notation

Consider a solution-phase sample composed of particles that are each defined by the following properties:

- $\vec{a} = (a_1, a_2, ..., a_n, ...)$: the absorption cross sections of their $(n-1)$X multiexcitonic state for absorbing a photon and transitioning to their nX multiexcitonic state. All of them will be considered uniform and constant in time at value a.

- $\vec{\gamma} = (\gamma_1, \gamma_2, ..., \gamma_n, ...)$: the quantum yields of their nX multiexcitonic state for emitting a photon while relaxing to their $(n-1)$X multiexcitonic state.

- $p(t)$: the time-dependent rate of excitation, based on $\vec{a}$ and the diffusion trajectory of the particle.

The sample itself and our microscope will be defined by the following experimental parameters:

- V_0 : the arbitrarily large reference volume defined for the purposes of the derivation.

- $PSF(\vec{r})$: the point spread function of excitation flux in the microscope.

- N_0 : an instantaneous number of particles in the *reference* volume.

- $\phi(t) = \gamma_1 p(t)$: the FCS detectivity function.

- V : the focal volume of the microscope, defined in Equation 7.64.

- $\langle n \rangle$: the average occupancy in the focal volume.

We will also be interested in several correlation observables, including:

- $P_i(n, p(t))$: the probability that the ith nanocrystal in the focal volume will generate n photons after a given excitation pulse, given its average excitation rate $p(t)$.

- $P_T(n, N_0, \{p_i(t)\})$: the total probability that the N_0 particles in the reference volume will generate n photons after a given excitation pulse, given their average excitation rates $\{p_i(t)\}$.

- $G^{(2)}(T,t)$: the probability of generating a correlation count in the peak at $\tau = T$ after the excitation pulse (or pair of pulses) at time t.

- $G^{(2)}(T)$: the average probability over the integration time of the experiment of generating a correlation count in the peak at $\tau = T$. i.e. $G^{(2)}(T) = \left\langle G^{(2)}(T,t) \right\rangle$.

- $g_\tau^{(2)}$: the integrated area of the normalized autocorrelation function over the correlation peak at τ. This is given by $g_\tau^{(2)} = \frac{G^{(2)}(\tau)}{G^{(2)}(T \to \infty)}$.

Furthermore, for the purposes of this derivation,

- $\mathrm{Poi}(m,p)$: the Poisson distribution, evaluated at m with an average value of p.

- $\left\langle \cdots \right\rangle$: time average over the integration time of the experiment.

7.1.2 Assumptions and Requirements

Four assumptions and requirements are needed to satisfy the mathematical approximations used for our derivation.

1. **The experiment must be performed under low excitation flux.**

Each excitation pulse is required to induce many fewer than one excitation both in each particle and in the focal volume as a whole, where the threshold conventionally used for this requirement is approximately one excitation per ten excitation pulses.[1] The limit is strictly required to hold for each particle to eliminate the existence of higher order excitions and to enable straightforward simplification of the Poisson distribution. With this condition, we can discard terms that are higher than second-order in excitation flux and arrive at a fixed result that is independent of the precise excitation flux used. This is critical because particles will diffuse through the focal

[1] An average excitation rate of one tenth is regarded as a strong and safe threshold. In practice, and especially with low quantum yield samples, experimental deviation from the low flux limit is sometimes not observed until the excitation flux approaches the order of one excitation per pulse.

volume and experience wide variations in their excitation flux. If the contribution that each particle makes to the peak area ratio fluctuates with excitation flux, the interpretation of the peak area ratio will be strongly contingent on both the shape of the focal volume and the total excitation flux through it. We do not want that.

The requirement that low flux excitation be maintained for the focal volume as a whole may not be strictly necessary; we will later show that high occupancies do not appear to cause measurable experimental deviation from our theoretical results. However, it is a very convenient requirement from a mathematical perspective, and I have not been very interested in playing with it further. As we will find later, there is no reason to conduct the experiment at high average occupancy unless the signal is very weak, so both low flux requirements will generally be satisfied under similar conditions.

2. **All relevant nX states have the same, time-independent absorption cross section.**

This assumption ensures that a Poisson distribution of excitons will be produced by individual excitation pulses. On its face, it may seem like a strange claim. However, in the low flux limit, it really only needs to apply to the excitonic and biexcitonic states, and it can be easily achieved in nanocrystals by using excitation photons with energy much greater than the nanocrystal band gap. I suspect that breaking this requirement simply adds some sort of relative absorption prefactor to each quantum yield term. If you can carefully characterize the relative absorption, you can probably correct for non-Poissonian absorption. We also require that the absorption cross sections be time-independent because we have no evidence for large fluctuation in absorption, and honestly, that would be a huge pain. This will probably become obvious when we start to consider fluctuations in the excitation flux due to particle diffusion.

3. **The laser repetition period is much longer than the emitter lifetime but much shorter than the emitter dwell time.**

The requirement that the repetition period be much longer than the emitter lifetime is taken directly from the SNC-$g^{(2)}$ theory. Essentially, we want to ensure that each particle reaches the ground state before the next excitation pulse to avoid cross-pulse multiexciton formation. This sort of effect would disrupt our Poissonian distribution of excitations from the previous assumption by converting some of the exciton population into biexcitons. Our second requirement that the laser repetition period be shorter than the emitter dwell time is needed because if diffusion is allowed to occur between subsequent excitation pulses, the particle may leave the focal volume before the second pulse and decrease the overall magnitude of the side peak. This would cause an overestimate of the quantum yield ratio. We will discuss later how to handle cases where both of these requirements cannot be met simultaneously.

4. **There is no sample aggregation and the occupation of the focal volume is therefore Poissonian.**

We require the diffusion of particles in the focal volume to be uncorrelated and ergodic so that cross-particle photon pairs always contribute to the Poisson background and can be cleanly subtracted. Aggregation will cause correlation between the fluorescence behavior of different particles, causing them to masquerade as single particles with very high multiexciton quantum yield and to inflate the measured quantum yield ratio in the exact same fashion as having multiple particles in the focal volume of a fixed-sample correlation measurement. Aggregation can be identified by the large spikes in fluorescence intensity they produce as they diffuse through the focal volume, or more rigorously by using photon-counting histogram. We will later confirm that our sample preparation does not generally cause aggregation by demonstrating that

serial dilution does not affect our measured peak area ratio,[2] and by demonstrating that we can measure a quantum yield ratio of approximately zero in certain samples.[3]

7.1.3 Derivation

Our strategy will be to calculate the peak-integrated $g^{(2)}(\tau)$ based on the average result from a single excitation pulse or pair of excitation pulses. In essence, since

$$g^{(2)}(\tau) = \frac{\langle I(t)I(t+\tau)\rangle}{\langle I(t)\rangle\langle I(t+\tau)\rangle}, \tag{7.1}$$

the area of the center peak of $g^{(2)}(\tau)$, $g_0^{(2)}$, will be equal to the average number of correlation counts generated during a given single pulse $G^{(2)}(\tau = 0)$ divided by the square of the average number of photons produced during a single pulse. Similarly, the area of the side peak of $g^{(2)}(\tau)$, $g_{T_{rep}}^{(2)}$, will be equal to the average number of correlation counts generated across two successive excitation pulses $G^{(2)}(\tau = T_{rep})$ divided by the square of the average number of photons produced after a single pulse. We note that the denominator term in both of these quantities is the average number of correlation counts you would expect to occur across two pulses if the behavior of the focal volume were uncorrelated between pulses (as will occur in solution as $\tau \to \infty$ because of particle diffusion). Thus,

$$g_0^{(2)} = \frac{G^{(2)}(0)}{G^{(2)}(\tau \to \infty)}, \tag{7.2}$$

and,

$$g_{T_{rep}}^{(2)} = \frac{G^{(2)}(T_{rep})}{G^{(2)}(\tau \to \infty)}. \tag{7.3}$$

[2]Serial dilution has often been tied to aggregation and other types of sample degradation because it can reduce the availability of labile ligands for surface passivation.

[3]This test obviously only works if the sample itself has no biexciton emission. If aggregation were adversely affecting our results, it would be impossible to measure a zero biexciton quantum yield because of the correlated photon pairs produced by aggregated particles. [308]

We begin by deriving the values of $G^{(2)}(0)$, $G^{(2)}(T_{rep})$, and $G^{(2)}(\tau \to \infty)$ for a single particle fixed inside the focal volume, reproducing the results presented elsewhere,[166] and then use these results to derive their values for a single particle diffusing through the focal volume, and finally, for a Poisson distribution of particles in the focal volume.

A Fixed Single Particle

Consider a single fluorophore fixed at a given position in the focal volume and defined by its excitonic absorption cross-section vector at the given excitation wavelength $\vec{a} = (a_1, a_2, ..., a_n, ...)$, which represents the absorption cross section of the $(n-1)$X multiexcitonic state for absorbing another photon to form an nX state, and its quantum yield vector $\vec{\gamma} = (\gamma_1, \gamma_2, ..., \gamma_n, ...)$, which expresses the probabilities that the fluorophore emits a photon when relaxing from its nX multiexcitonic state to its $(n-1)$X state. We have assume that the absorption cross section vector is approximately constant and uniformly given by the parameter a. But, we do not make any assumptions about the value or time-dependence of the quantum yield vector. In fact, we suspect that it may be time-dependent due to the intensity fluctuations that nanocrystals tend to exhibit. The probability that this fluorophore emits n photons following an excitation pulse at time t will generally take the form,

$$P(n) = \sum_{m=0}^{\infty} A(m)E(n,m), \tag{7.4}$$

where $A(m)$ represents the probability that the emitter absorbs exactly m photons, given $\vec{a}$ and the excitation flux at its position in the focal volume, and where $E(n,m)$ represents the probability that these m excitons result in the emission of n photons. The absorption component of this expression takes a simple form given our assumption that the absorption cross sections of all multiexcitonic states are the same. Under these conditions, the formation of multiple excitons in the nanocrystal are indepen-

dent and $A(m)$ can be approximated by a Poisson distribution whose average excitation rate p is dependent on the absorption cross section a and the excitation flux at its positions $PSF(\vec{r})$, i.e.,

$$A(m) = \mathrm{Poi}(m, p) = \frac{p^m e^{-p}}{m!}. \tag{7.5}$$

Furthermore, because the experiment is conducted in the low excitation flux regime, we can discard any terms that are third-order in p or above, including all terms involving $A(m > 2)$.

The emission component of Equation 7.4 is simply dictated by combinatorics and can be constructed by enumerating the probabilities of all possible exciton relaxation pathways. For example, there are two relaxation pathways that result in a biexciton producing exactly one photon: either a photon is emitted during the biexciton relaxation but not during the exciton relaxation (with probability $\gamma_2(1-\gamma_1)$) or a photon is emitted during the exciton relaxation but not during the biexciton relaxation (with probability $\gamma_1(1-\gamma_2)$). Combining this rationale with Equation 7.5 yields the probability of getting certain numbers of photons from a particular pulse, given p,

$$P(0, p) = \mathrm{Poi}(0, p) + \mathrm{Poi}(1, p)(1-\gamma_1) + \mathrm{Poi}(2, p)(1-\gamma_2)(1-\gamma_1), \tag{7.6}$$

$$P(1, p) = \mathrm{Poi}(1, p)(\gamma_1) + \mathrm{Poi}(2, p)\left[\gamma_1(1-\gamma_2) + \gamma_2(1-\gamma_1)\right], \tag{7.7}$$

$$P(2, p) = \mathrm{Poi}(2, p)\gamma_1\gamma_2, \tag{7.8}$$

$$P(n \geq 3, p) = 0, \tag{7.9}$$

or expanded to second-order in p:

$$P(0,p) = 1 - \gamma_1 p + \left[\frac{1}{2}(\gamma_1 - \gamma_2) + \frac{1}{2}\gamma_1\gamma_2\right] p^2, \tag{7.10}$$

$$P(1,p) = \gamma_1 p + \left[\frac{1}{2}(\gamma_2 - \gamma_1) - \gamma_1\gamma_2\right] p^2, \tag{7.11}$$

$$P(2,p) = \frac{1}{2}\gamma_1\gamma_2 p^2, \tag{7.12}$$

$$P(n \geq 3, p) = 0. \tag{7.13}$$

These expressions give us the means for calculating the contributions to $G^{(2)}(0)$, $G^{(2)}(T_{rep})$, and $G^{(2)}(\tau \to \infty)$ from the excitation pulse at time t (assuming that the immediately preceding excitation pulse produce roughly the same behavior). Under low excitation flux, the only way to produce center peak correlation counts is to get two photons from a single excitation pulse. This result will actually produce two correlation counts in the peak-integrated correlation function (one at positive and one at negative time separation). Thus,

$$G^{(2)}(0,t) = 2 \times P(2,p) \tag{7.14}$$

$$= 2 \times \left[\frac{1}{2}\gamma_1\gamma_2 p^2\right] \tag{7.15}$$

$$= \gamma_1\gamma_2 p^2. \tag{7.16}$$

Similarly, the only way to produce side peak correlation counts that is less than third-order in p is to produce a single photon in two subsequent excitation pulses. This process only produces a single correlation count because the positive and negative

time separation counts occupy distinct correlation peaks. Thus,

$$G^{(2)}(T_{rep}, t) = P(1,p) \times P(1,p) \tag{7.17}$$

$$= \left(\gamma_1 p + \left[\frac{1}{2}(\gamma_2 - \gamma_1) - \gamma_1\gamma_2\right] p^2\right)^2 \tag{7.18}$$

$$\approx \gamma_1\gamma_1 p^2. \tag{7.19}$$

Both of these expressions can be averaged over the integration time of the experiment by noting that only the quantum yield parameters are time-dependent and they may vary in a correlated fashion. This average is therefore given by,

$$G^{(2)}(0) = \langle G^{(2)}(0,t)\rangle \tag{7.20}$$

$$= \langle\gamma_1\gamma_2\rangle p^2, \tag{7.21}$$

and,

$$G^{(2)}(T_{rep}) = \langle G^{(2)}(T_{rep}, t)\rangle \tag{7.22}$$

$$= \langle\gamma_1\gamma_1\rangle p^2. \tag{7.23}$$

Furthermore, although not necessary for calculating the peak area ratio, we can also calculate the denominator of the correlation function:

$$G^{(2)}(\tau \to \infty) = \langle I(t)\rangle^2 \tag{7.24}$$

$$= \langle 0 \times P(0,p) + 1 \times P(1,p) + 2 \times P(2,p)\rangle^2 \tag{7.25}$$

$$= \left\langle \left(\gamma_1 p + \left[\frac{1}{2}(\gamma_2 - \gamma_1)\right] p^2\right)\right\rangle^2 \tag{7.26}$$

$$\approx \langle\gamma_1 p\rangle^2 \tag{7.27}$$

$$= \langle\gamma_1\rangle^2 p^2. \tag{7.28}$$

The peak area ratio in a fixed single-molecule $g^{(2)}$ experiment is therefore,

$$\frac{g_0^{(2)}}{g_{T_{rep}}^{(2)}} = \frac{\langle \gamma_1 \gamma_2 \rangle}{\langle \gamma_1 \gamma_1 \rangle}, \tag{7.29}$$

which is the result derived by Nair et al. [166]

A Single Diffusing Particle

Few changes are required to consider a solution-phase focal volume containing strictly one particle at a time diffusing in solution. Correlation counts still always originate from the same particle excited with low flux excitation, but now the actual excitation flux is allowed to vary over time, sampling the point spread function of the focal volume as the particle diffuses. Moreover, if we allow for particle exchange in the focal volume, any time average over the integration time of the experiment becomes an average over all possible intensity states of a single particle and over all of the particles in the ensemble.

To treat this case mathematically, we use the reference volume strategy applied in solution-phase experiments such as photon counting histogram analysis. [168, 169] Consider a reference volume V_0, encompassing the focal volume of the microscope and sufficiently large that all emitted photons will be from within the reference volume. If a single particle is confined to the reference volume, it will experience a time-dependent excitation flux given by the excitation point spread function $PSF(\vec{r})$ at its position at time t and therefore a time-dependent excitation rate $p(t)$. During a sufficiently long experiment, the particle will uniformly sample all of V_0, experiencing an average excitation rate of

$$\langle p(t) \rangle = \frac{1}{V_0} \int_{V_0} a \times PSF(\vec{r}) \, \mathrm{d}\vec{r}. \tag{7.30}$$

To calculate the peak area ratio produced by these circumstances, we express

the contributions to $G^{(2)}(0)$ and $G^{(2)}(T_{rep})$ from a single pulse (or pair of subsequent pulses) in terms of the instantaneous excitation flux experienced by the particle at that time t, and then average this result over the entire reference volume the particle is allowed to sample.

Modifying Equation 7.16 and Equation 7.19, the contributions to the center and side correlation peaks from a single pulse or pair of pulses at time t are given by,

$$G^{(2)}(0,t) = \gamma_1\gamma_2 p(t)^2, \tag{7.31}$$

and,

$$G^{(2)}(T_{rep},t) = \gamma_1\gamma_1 p(t)^2, \tag{7.32}$$

and because the fluorescence properties of the particle are independent of its position in the reference volume, the overall correlation signal measured during the experiment is,

$$G^{(2)}(0) = \langle\gamma_1\gamma_2 p(t)^2\rangle \tag{7.33}$$

$$= \langle\gamma_1\gamma_2\rangle\langle p(t)^2\rangle, \tag{7.34}$$

and,

$$G^{(2)}(T_{rep}) = \langle\gamma_1\gamma_1 p(t)^2\rangle \tag{7.35}$$

$$= \langle\gamma_1\gamma_1\rangle\langle p(t)^2\rangle. \tag{7.36}$$

When the peak area ratio is calculated, the excitation flux terms cancel, yielding the same result as in the fixed single-molecule case. This cancelation is strictly contingent on being in the low flux limit at all points in the excitation point spread function.

N_0 Diffusing Particles

To derive the value for the peak area ratio in an actual solution-phase experiment, we must address the possibility that more than one particle will be in the reference volume at once. Consider the case where there are exactly N_0 emitters in the reference volume, but the identities of these emitters may change over the duration of the experiment. Each particle is characterized by its own independent position and absorption cross section vector (i.e., its own independent $p_i(t)$), and its own independent quantum yield vector $\vec{\gamma}^{(i)}$. The probability of n photons being emitted from the entire reference volume after a given pulse or pair of pulses at time t can be compiled based on the independent probabilities that each of the N_0 fluorophores emits 0, 1, or 2 photons. In the low flux limit where many fewer than one excitons are created on average in the entire reference volume, we only need to consider the probabilities that two or fewer photons are emitted. These probabilities $P_T(n, N_0, \{p_i(t)\})$ are given by:

$$P_T(0, N_0, \{p_i(t)\}) = \prod_{i=1}^{N_0} P_i(0, p_i(t)), \tag{7.37}$$

which is simply the probability that none of the emitters emit a photon,

$$P_T(1, N_0, \{p_i(t)\}) = \sum_{i=1}^{N_0} \left[P_i(1, p_i(t)) \prod_{j \neq i}^{N_0} P_j(0, p_j(t)) \right], \tag{7.38}$$

which is the sum of the probabilities that one of the particles emits a photon, but none of the other ones do,

$$\begin{aligned} P_T(2, N_0, \{p_i(t)\}) = & \sum_{i=1}^{N_0} \left[P_i(2, p_i(t)) \prod_{j \neq i}^{N_0} P_j(0, p_j(t)) \right] \\ & + \sum_{i=1}^{N_0 - 1} \sum_{j=i+1}^{N_0} \left[P_i(1, p_i(t)) P_j(1, p_j(t)) \prod_{k \neq i,j}^{N_0} P_k(0, p_k(t)) \right], \end{aligned} \tag{7.39}$$

which is the sum of the probabilities of two distinct cases: the case where a single particle emits two photons and all of the other particles emit zero photons, and the case where two particles emit one photon and all of the other particles emit zero photons, and,

$$P_T(n \geq 3, N_0, \{p_i(t)\}) = 0. \tag{7.40}$$

Although these expressions are clearly more complicated than their single-nanocrystal analogues in Equations 7.10-7.13, they can be used in the same fashion to calculate the average number of correlation counts for an average pulse or pair of pulses for a reference volume containing N_0 particles, $G^{(2)}(0, N_0)$, $G^{(2)}(T_{rep}, N_0)$, and $G^{(2)}(\tau \to \infty, N_0)$. We still assume a low flux limit where many fewer than one excitation is generated in the focal volume during each pulse, so the only way of generating a center peak correlation count is to generate two photons from the reference volume after a single excitation pulse and the only way of generating a side peak correlation count is to generate one photon from the reference volume on two subsequent excitation pulses. Moreover, we extensively use the independence of the behavior of different particles: the average of a product of two terms involving different particles is the product of the averages of the two terms. Thus, the average center peak correlation signal is given by,

$$\begin{aligned}
G^{(2)}(0, N_0) =& 2 \times \left\langle \sum_{i=1}^{N_0} \left[P_i(2, p_i(t)) \prod_{j \neq i}^{N_0} P_j(0, p_j(t)) \right] \right. \\
&\left. + \sum_{i=1}^{N_0-1} \sum_{j=i+1}^{N_0} \left[P_i(1, p_i(t)) P_j(1, p_j(t)) \prod_{k \neq i,j}^{N_0} P_k(0, p_k(t)) \right] \right\rangle \qquad (7.41) \\
=& 2 \times \sum_{i=1}^{N_0} \left[\langle P_i(2, p_i(t)) \rangle \prod_{j \neq i}^{N_0} \langle P_j(0, p_j(t)) \rangle \right] \\
&+ 2 \times \sum_{i=1}^{N_0-1} \sum_{j=i+1}^{N_0} \left[\langle P_i(1, p_i(t)) \rangle \langle P_j(1, p_j(t)) \rangle \prod_{k \neq i,j}^{N_0} \langle P_k(0, p_k(t)) \rangle \right] \qquad (7.42) \\
=& 2N_0 \times \langle P(2, p(t)) \rangle \langle P(0, p(t)) \rangle^{N_0-1}
\end{aligned}$$

$$+ (N_0)(N_0-1)\langle P(1,p(t))\rangle^2\langle P(0,p(t))\rangle^{N_0-2}, \tag{7.43}$$

where $\langle P(n,p(t))\rangle$ denotes the average probability that a single particle emits n photons, averaged over all particle identities and all positions in the reference volume (note that because of ergodicity and particle exchange, the identity of the ith particle changes over time and $\langle P_i(n,p(t))\rangle$ is rigorously equivalent to $\langle P_j(n,p(t))\rangle$). Similarly, the average side peak correlation signal is given by,

$$G^{(2)}(T_{rep},N_0) = \left\langle \left[\sum_{i=1}^{N_0} P_i(1,p_i(t)) \prod_{j\neq i}^{N_0} P_j(0,p_j(t))\right]\left[\sum_{i=1}^{N_0} P_i(1,p_i(t)) \prod_{j\neq i}^{N_0} P_j(0,p_j(t))\right]\right\rangle \tag{7.44}$$

$$= \sum_{i=1}^{N_0}\left[\langle P_i(1,p_i(t))^2\rangle \prod_{j\neq i}^{N_0}\langle P_j(0,p_j(t))^2\rangle\right] + \sum_{i=1}^{N_0}\sum_{j\neq i}^{N_0}\left[\langle P_i(1,p_i(t))P_i(0,p_i(t))\rangle\langle P_j(1,p_j(t))P_i(0,p_j(t))\rangle \prod_{k\neq i,j}^{N_0}\langle P_k(0,p_k(t))^2\rangle\right] \tag{7.45}$$

$$= N_0 \times \langle P(1,p(t))^2\rangle\langle P(0,p(t))^2\rangle^{N_0-1} + (N_0)(N_0-1)\langle P(1,p(t))P(0,p(t))\rangle^2\langle P(0,p(t))^2\rangle^{N_0-2}, \tag{7.46}$$

where $\langle P(n,p(t))^2\rangle$ denotes the average probability that a single particle emits n photons in two subsequent pulses, again averaged over all particle identities and all positions in the reference volume. The two terms in Equation 7.46 correspond to the possibilities that the two photons produced by the reference volume in subsequent pulses came (1) from the the same particle, or (2) from different particles. Finally,

the square of the average intensity following a single excitation pulse is given by,

$$G^{(2)}(\tau \to \infty, N_0) = \left\langle \sum_{i=1}^{N_0} \left[P_i(1, p_i(t)) \prod_{j \neq i}^{N_0} P_j(0, p_j(t)) \right] \right\rangle^2 \tag{7.47}$$

$$= N_0^2 \times \langle P(1, p(t)) \rangle^2 \langle P(0, p(t)) \rangle^{2N_0 - 2}. \tag{7.48}$$

Note that Equations 7.43, 7.46, and 7.48 all reduce to their single-nanocrystal analogues from the previous section.

A Poisson Distribution of Diffusing Particles (Real Life)

We can now construct the results from a realistic reference volume, composed of a Poisson distribution of particles freely and independently diffusing in solution. To do this, we average Equations 7.43, 7.46, and the total intensity from Equation 7.48 over the Poisson distribution describing the number of particles that will occupy the reference volume over the course of the measurement. In this way, the average probability of registering a correlation count in the center peak region over an entire solution experiment, given an average occupancy of the reference volume $\langle N_0 \rangle$, is

$$G^{(2)}(0, \langle N_0 \rangle) = \sum_{n=0}^{\infty} \mathrm{Poi}(n, \langle N_0 \rangle) \times G^{(2)}(0, n) \tag{7.49}$$

$$= \left[2\langle N_0 \rangle \langle P(2, p(t)) \rangle + \langle N_0 \rangle^2 \langle P(1, p(t)) \rangle^2 \right] e^{-(1 - \langle P(0, p(t)) \rangle) \langle N_0 \rangle}, \tag{7.50}$$

the average probability of registering a correlation count in the side peak region is,

$$G^{(2)}(T_{rep}, \langle N_0 \rangle) = \sum_{n=0}^{\infty} \mathrm{Poi}(n, \langle N_0 \rangle) \times G^{(2)}(T_{rep}, n) \tag{7.51}$$

$$= \left[\langle N_0 \rangle \langle P(1, p(t))^2 \rangle + \langle N_0 \rangle^2 \langle P(1, p(t)) P(0, p(t)) \rangle^2 \right] e^{-(1 - \langle P(0, p(t))^2 \rangle) \langle N_0 \rangle}, \tag{7.52}$$

and the denominator term of the correlation function, or the square of the average of the intensity truncated to first-order, is given by,

$$G^{(2)}(\tau \to \infty, \langle N_0 \rangle) = \left[\sum_{n=0}^{\infty} \mathrm{Poi}(n, \langle N_0 \rangle) \times \left(n \langle P(1, p(t)) \rangle \langle P(0, p(t)) \rangle^{n-1} \right) \right]^2 \tag{7.53}$$

$$= \langle N_0 \rangle^2 \langle P(1, p(t)) \rangle^2 e^{-2(1 - \langle P(0,p(t))^2 \rangle) \langle N_0 \rangle}. \tag{7.54}$$

Finally, we insert the average single-particle fluorescence probabilities derived from our earlier results and truncate to lowest order in p to arrive at the simplified low excitation flux expressions for $G^{(2)}(0, \langle N_0 \rangle)$, $G^{(2)}(T_{rep}, \langle N_0 \rangle)$, and $G^{(2)}(\tau \to \infty, \langle N_0 \rangle)$,

$$G^{(2)}(0, \langle N_0 \rangle) = \langle N_0 \rangle \langle \gamma_1 \gamma_2 \rangle \langle p(t)^2 \rangle + \langle N_0 \rangle^2 \langle \gamma_1 \rangle^2 \langle p(t) \rangle^2, \tag{7.55}$$

$$G^{(2)}(T_{rep}, \langle N_0 \rangle) = \langle N_0 \rangle \langle \gamma_1 \gamma_1 \rangle \langle p(t)^2 \rangle + \langle N_0 \rangle^2 \langle \gamma_1 \rangle^2 \langle p(t) \rangle^2, \text{ and} \tag{7.56}$$

$$G^{(2)}(\tau \to \infty, \langle N_0 \rangle) = \langle N_0 \rangle^2 \langle \gamma_1 \rangle^2 \langle p(t) \rangle^2, \tag{7.57}$$

and use these expressions to calculate the center and side peak correlation values for the solution-phase $g^{(2)}$ experiment:

$$g^{(2)}(0) = 1 + \frac{1}{\langle N_0 \rangle} \frac{\langle \gamma_1 \gamma_2 \rangle \langle p(t)^2 \rangle}{\langle \gamma_1 \rangle^2 \langle p(t) \rangle^2} \tag{7.58}$$

and,

$$g^{(2)}(T_{rep}) = 1 + \frac{1}{\langle N_0 \rangle} \frac{\langle \gamma_1^2 \rangle \langle p(t)^2 \rangle}{\langle \gamma_1 \rangle^2 \langle p(t) \rangle^2}. \tag{7.59}$$

Although these expressions are considerably simplified, they are still formed in terms of the arbitrarily defined reference volume from our derivation. To remove this dependence, we rephase our result in terms of the FCS detectivity function $\phi(t)$, which expresses the probability that if a spatial fluctuation occurs, it is reported in the experiment. [167] It is given here by the probability that a photon is produced by a given particle, i.e. the product of the exciton quantum yield of the particle and

the excitation probability. Recombining several of the averages in the second term of $g^{(2)}(T_{rep})$, and using Equation 15.5 from Webb[167]:

$$\frac{\langle\gamma_1^2\rangle\langle p(t)^2\rangle}{\langle\gamma_1\rangle^2\langle p(t)\rangle^2} = \frac{\langle\gamma_1^2 p(t)^2\rangle}{\langle\gamma_1 p(t)\rangle^2} \tag{7.60}$$

$$= \frac{\langle\phi(t)^2\rangle}{\langle\phi(t)\rangle^2} \tag{7.61}$$

$$= \frac{\frac{1}{V_0}\int_{V_0}\phi(\vec{r})^2 d\vec{r}}{\left[\frac{1}{V_0}\int_{V_0}\phi(\vec{r})d\vec{r}\right]^2} \tag{7.62}$$

$$\approx V_0\frac{\int\phi(\vec{r})^2 d\vec{r}}{\left[\int\phi(\vec{r})d\vec{r}\right]^2} \tag{7.63}$$

$$= \frac{V_0}{V}, \tag{7.64}$$

where V_0 is the reference volume from earlier and V is defined as the focal volume of the experiment. Now, we rephrase our correlation function in terms of the occupancy of the focal volume $\langle n\rangle$, which references the detectivity of the experiment, rather than the occupancy of the arbitrary reference volume. Noting that the average occupancy of the focal volume is given by the product of the average particle concentration $\frac{\langle N_0\rangle}{V_0}$ and the focal volume V,

$$g^{(2)}(T_{rep}) = 1 + \frac{1}{\langle N_0\rangle}\frac{V_0}{V} \tag{7.65}$$

$$= 1 + \frac{1}{\langle n\rangle}, \tag{7.66}$$

and,

$$g^{(2)}(0) = 1 + \frac{1}{\langle N_0\rangle}\frac{V_0}{V}\frac{\langle\gamma_1\gamma_2\rangle}{\langle\gamma_1\gamma_1\rangle} \tag{7.67}$$

$$= 1 + \frac{1}{\langle n\rangle}\frac{\langle\gamma_1\gamma_2\rangle}{\langle\gamma_1\gamma_1\rangle}. \tag{7.68}$$

If the biexciton quantum yield is set to zero, these results perfectly recover the con-

ventional FCS result that the antibunching feature should approach unity. [310] But, in the event of biexciton fluorescence, the peak area ratio is given by:

$$\frac{g^{(2)}(0)}{g^{(2)}(T_{rep})} = \frac{1 + \frac{1}{\langle n \rangle}\frac{\langle \gamma_1 \gamma_2 \rangle}{\langle \gamma_1 \gamma_1 \rangle}}{1 + \frac{1}{\langle n \rangle}} \tag{7.69}$$

$$= \frac{\langle n \rangle + \frac{\langle \gamma_1 \gamma_2 \rangle}{\langle \gamma_1 \gamma_1 \rangle}}{\langle n \rangle + 1} \tag{7.70}$$

$$= \frac{\langle n \rangle}{\langle n \rangle + 1} + \frac{1}{\langle n \rangle + 1}\frac{\langle \gamma_1 \gamma_2 \rangle}{\langle \gamma_1 \gamma_1 \rangle}, \tag{7.71}$$

which is Equation 6.4 in the previous Chapter, and the quantum yield ratio can be isolated from the correlation function values via,

$$\frac{g^{(2)}(0) - 1}{g^{(2)}(T_{rep}) - 1} = \frac{\frac{1}{\langle n \rangle}\frac{\langle \gamma_1 \gamma_2 \rangle}{\langle \gamma_1 \gamma_1 \rangle}}{\frac{1}{\langle n \rangle}} \tag{7.72}$$

$$= \frac{\langle \gamma_1 \gamma_2 \rangle}{\langle \gamma_1 \gamma_1 \rangle}, \tag{7.73}$$

which is Equation 6.3 from the previous Chapter.

The observable in Equation 7.73 can be interpreted as the ratio of the brightness-weighted average of the biexciton quantum yield to the brightness-weighted average of the exciton quantum yield because, under low excitation flux, the brightness of emitters is given by the product of their uniform absorption cross section and their exciton quantum yield. Our observable is intrinsically weighted towards brighter nanocrystals because non-emissive particles and dark blinking states will not contribute counts to either the center or side peaks of the correlation function, and simply pass through the focal volume unobserved. Pretty much all spectroscopy experiments are brightness-weighted in this fashion, but in this case, it is particularly important to keep in mind because it means that you cannot necessarily calculate the average biexciton quantum yield by multiplying the quantum yield ratio by the average exciton quantum yield of the sample.

On a side note, it is also important to recognize the helpful significance of subtracting the Poissonian background in Equation 7.72. We previously regarded the Poissonian background as only being composed of inter-particle photon pairs, and considered the existence of these inter-particle pairs as being a minor, but necessary, hassle on our way to calculating the average quantum yield ratio. However, there are other sources of Poisson background that will manifest themselves in our experiment, including dark count correlations and classical sources of background autofluorescence, which also affect single-nanocrystal measurements.[4] In the SNC-$g^{(2)}$ experiment, these sources must be accounted for and subtracted from each correlation peak area to measure an accurate quantum yield ratio, but in the solution-phase experiment, they are automatically folded into the Poisson background and do not bias our average quantum yield ratio. They simply cause a minor increase in the measured average occupancy, which may interfere with the experimenter's excitation flux estimation.

7.2 Calculating the Uncertainty in the Measured Quantum Yield Ratio

If the assumption and requirements we used for the derivation in the previous section are satisfied, then we now have the means to precisely and accurately measure the average biexciton/exciton quantum yield ratio of a sample of nanocrystals. In fact, because our measurement uses a solution-phase focal volume, we have the freedom to use arbitrarily long integration times to achieve high signal-to-noise ratio measurements, while well within the excitation flux and repetition rate requirements of the experiment. The responsible application of a solution-phase $g^{(2)}$ measurement should

[4] By classical sources of autofluorescence, we are speaking of dim, but high-concentration emitters such as glass impurities or event solvent molecules, which (due to their high concentration) will not exhibit antibunching.

have a systematic error well within the shot-noise uncertainty of the measurement, so it is worth taking a moment to derive the shot-noise uncertainty of the average quantum yield ratio.

Consider a measurement that registers N_0 correlation counts in the center peak, $N_{T_{rep}}$ counts in the first side peak, and N_∞ correlation counts in a peak beyond the diffusion time of the emitters. The simplest method of calculating the average quantum yield ratio is,

$$\frac{\langle\gamma_1\gamma_2\rangle}{\langle\gamma_1\gamma_1\rangle} = \frac{N_0 - N_\infty}{N_{T_{rep}} - N_\infty}. \tag{7.74}$$

Each of these peak area values is a Poissonian measurement with a shot noise standard deviation of $\sqrt{N}$, so, using standard error propagation, the numerator is given by,

$$N_{num} = (N_0 - N_\infty) \pm \sqrt{N_0 + N_\infty} \tag{7.75}$$

the denominator is given by,

$$N_{denom} = (N_{T_{rep}} - N_\infty) \pm \sqrt{N_{T_{rep}} + N_\infty} \tag{7.76}$$

and the average quantum yield ratio is given by,

$$\frac{\langle\gamma_1\gamma_2\rangle}{\langle\gamma_1\gamma_1\rangle} = \frac{N_0 - N_\infty}{N_{T_{rep}} - N_\infty} \pm \frac{N_0 - N_\infty}{N_{T_{rep}} - N_\infty}\sqrt{\frac{N_0 + N_\infty}{(N_0 - N_\infty)^2} + \frac{N_{T_{rep}} + N_\infty}{(N_{T_{rep}} - N_\infty)^2}}. \tag{7.77}$$

We can do better than this by noting that, even though the center peak is necessarily a single-point shot-noise measurement, we have much more information about the correct values of the side peaks because their areas should fit an FCS curve with τ. Instead of simply using their values, we can fit the side peak areas with an FCS curve and use the fit values instead of the measured values to eliminate the shot noise uncertainty for $N_{T_{rep}}$ and N_∞. Unless drift is a serious problem in the measurement (see Section 7.4), we should be able to know N_∞ with vanishing uncertainty and we

should be able to dramatically reduce our uncertainty in $N_{T_{rep}}$.[5] By fitting the side peak values, the only source of shot noise is N_0, and our shot noise uncertainty is given by,

$$\frac{\langle\gamma_1\gamma_2\rangle}{\langle\gamma_1\gamma_1\rangle} = \frac{N_0 - N_\infty}{N_{T_{rep}} - N_\infty} \pm \frac{N_0 - N_\infty}{N_{T_{rep}} - N_\infty}\sqrt{\frac{N_0}{(N_0 - N_\infty)^2}} \tag{7.78}$$

$$= \frac{N_0 - N_\infty}{N_{T_{rep}} - N_\infty} \pm \sqrt{\frac{N_0}{(N_{T_{rep}} - N_\infty)^2}} \tag{7.79}$$

$$= \frac{N_0 - N_\infty}{N_{T_{rep}} - N_\infty} \pm \sqrt{\frac{N_0}{\left(\frac{N_0}{\langle n\rangle}\right)^2}} \tag{7.80}$$

$$= \frac{N_0 - N_\infty}{N_{T_{rep}} - N_\infty} \pm \sqrt{\frac{\langle n\rangle^2}{N_0}}. \tag{7.81}$$

This expression for the uncertainty originates from the fact that the center peak is composed of two populations: the intraparticle signal we are trying to isolate and the interparticle Poisson background that we are trying to eliminate. Even though, in principle, we know the exact average magnitude of the Poisson background from the FCS curve, its actual number of correlation counts in the center peak is still dictated by shot noise. For example, a slightly larger than average number of inter-particle photon pairs would yield a slightly inflated quantum yield ratio after Poisson subtraction. The magnitude of this effect is proportional to the relative signal strength of intra-particle photon pairs compared to inter-particle photon pairs, which is dictated by the average occupancy of the focal volume.

[5] Accurately measuring the plateau value of the FCS trace (i.e. $N_{T_{rep}}$) requires a well-formed focal volume and a monodisperse sample to yield an accurate fit to the ideal FCS model. In practice, it is proper to consider the uncertainty in the FCS fit and use that as the uncertainty in $N_{T_{rep}}$. Here, for simplicity, we assume the fit is quite good and that any uncertainty in the plateau value is negligible compared to shot noise. That was the case for most of my measurements.

7.3 Balancing Average Occupation and Signal Intensity

Equation 7.81 begs the question, if the uncertainty is (explicitly) directly proportional to the average occupation, how should the experimenter design a solution-phase $g^{(2)}$ measurement in cases where the absolute signal intensity from each emitter is very weak? Should we increase the average occupancy to measure a high total signal from the focal volume, or should we decrease the average occupancy to emphasize the fraction of the signal that represents what we actually want to measure? Because N_0 represents the total number of correlation counts in the center peak, it turns out that the average occupancy does not actually (intrinsically) affect the uncertainty of the quantum yield ratio. The probability of generating a correlation count in a given peak will be proportional to the square of the total signal intensity (the probability of getting a first photon times the probability of getting a second photon) and directly proportional to the total integration time (the number of opportunities in time to make a correlation count). Since the total signal intensity is directly proportional to the number of particles in the focal volume, N_0 is proportional to the square of the average occupancy and the average occupancy of the focal volume vanishes in the uncertainty expression. Although it is generally a good idea to choose an average occupancy high enough that the total signal is much greater than the detector dark counts (or other sources of background), the parameters that truly affect the signal-to-noise ratio of the measurement are integration time, emitter brightness, and detection efficiency.

7.4 Long Measurements and How to Make Them

One of the major claims that our derivation hinges on is that the arrival of photon pairs from different particles is indeed Poissonian. This allows us to estimate their contribution to the center and side correlation peaks by measuring the area of correlation peaks well beyond the diffusion time of the emitters. Nevertheless, long timescale fluctuations in the total excitation rate, collection efficiency, or sample concentration may introduce non-Poissonian character into the arrival of otherwise uncorrelated phenomena. For instance, if there is drift in the detection arm of the setup, we may be equally likely to generate photons from uncorrelated emitters throughout the course of the experiment, but their arrival at the detector is biased towards early times in the experiment, and therefore towards shorter τ spacing. Drift in the total fluorescence signal from the focal volume over time will generally introduce a monotonically decreasing feature in the physically uncorrelated component of the correlation function, cause its contribution to the center peak to be greater than the area of correlation peaks as $\tau \to \infty$, and cause our analysis to over-estimate the quantum yield ratio.[6] This effect is exceedingly likely to occur during very long measurements. Figure 7-1 illustrates an example of such a measurement, where a monotonic decrease in fluorescence intensity over time distorts the correlation function and can lead to an erroneously high 25.8% quantum yield ratio measurement (the more carefully measured value is 13.2%).

To account for drift in the total fluorescence intensity of the signal, we can break the total measurement down into a large number of shorter measurements whose integration time is shorter than the timescale of intensity drift. Each of these measurements will be free of drift-related artifacts and yield an independent, poor signal-to-noise measurement of the quantum yield ratio. We can then use this time-series

[6] This effect can often be identified by a poor FCS fit. In general, a poor FCS fit is a bad sign for the accuracy of the measurement (at least when you believe you have a well-formed focal volume at the outset of the experiment).

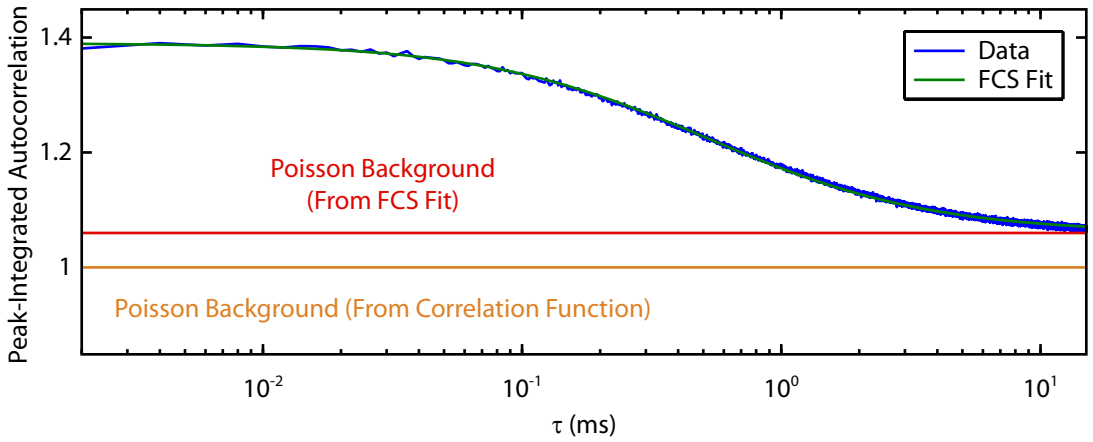

Figure 7-1: Long timescale intensity fluctuations caused by sample degradation or microscope drift can cause an offset between the Poisson-normalized baseline of the correlation function and the actual inter-particle background given by the FCS fit of the correlation function at short τ. If the Poisson background according to the correlation function is used to subtract the inter-particle contribution, it will result in an artificially high quantum yield ratio.

of correlation measurements to determine why the fluorescence intensity is decreasing over time and to calculate an overall high signal-to-noise value of the quantum yield ratio from the entire measurement that is free of correlation function distortion. Figure 7-2 show how several experimental parameters in the solution-phase $g^{(2)}$ measurement vary over the course of the experiment from Figure 7-1. By suppressing the distortion of the FCS trace from drift, we measure a much more accurate 10.9% quantum yield ratio for the sample (down from 14.0%). Furthermore, by analyzing the time-dependence of our experimental parameters, we can conclude that the intensity is slowly dropping during the course of the measurement because of corresponding decreases in the sample concentration.[7] A decrease in the sample concentration could be a cause for concern if it is accompanied by aggregation or a drift in the quantum yield ratio over time. But, since we see no corresponding trend in the quantum yield ratio over time, we can conclude that our measurement is reliable.

[7] The average occupancy of the focal volume is decreasing without a corresponding change in the diffusion time of the emitters.

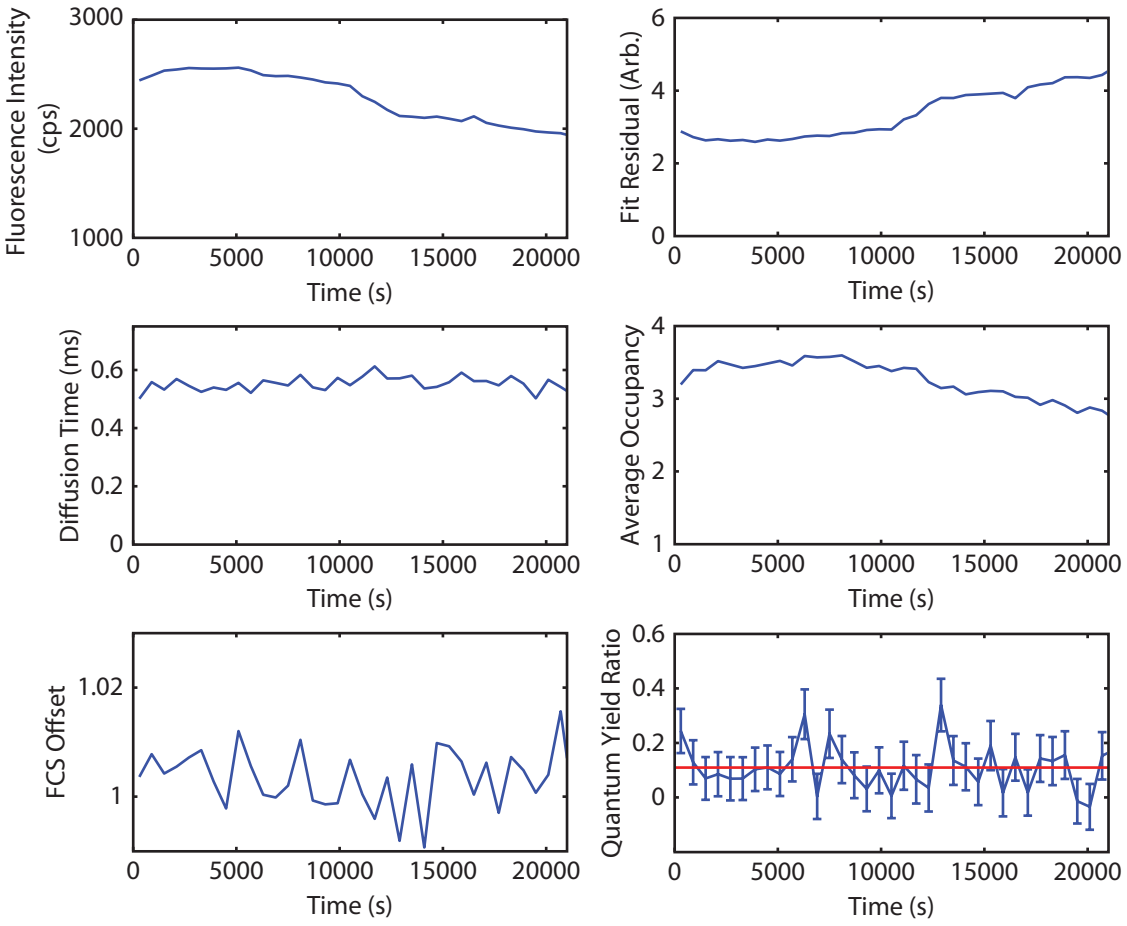

Figure 7-2: Long experiments can be analyzed without long-timescale artifacts by breaking up the integration time into several shorter integration times with low signal-to-noise, treating each sub-measurement individually, and averaging the resulting peak area ratios to improve the overall signal-to-noise. Here, we show the evolution of several experimental parameters over a long integration time. The intensity drift of the focal volume is consistent with a change in the total occupancy of the focal volume over time, suggesting some sample instability.

7.5 Coping with Long Radiative Lifetimes

Finally, the third requirement in our derivation was that the laser repetition period be much longer than the lifetime of the emitters but much shorter than their diffusion time. This is sometimes impossible to implement for particles with lifetimes of hundreds of nanoseconds but diffusion times of hundreds of milliseconds. Even though these two timescales are three orders of magnitude apart, chosing a repetition period on the order of microseconds to prevent inter-pulse excitation may still allow for some particle diffusion between subsequent pulses. This will cause the side peak to be artificially small and produce an inflated quantum yield ratio. The solution in this case is to err on the side of a long repetition period to ensure a Poisson distribution of excitations and use an FCS fit of the side peaks to determine what the amplitude of the side peak would have been if particle diffusion had not occurred (i.e. use the y-intercept of the FCS curve in lieu of the actual, diminished side peak amplitude).[8] In Figure 7-3, we show how accounting for particle diffusion can yield a more accurate quantum yield ratio.

[8] If the FCS fit is poor and clearly yields an incorrect plateau value at short τ, it could be preferable to use an empirical fit of the twenty or so data points on one side of the center peak instead of trying to capture the full FCS decay curve over many orders of magnitude in time. In the data I will show, we use both methods and they generally agree within the shot noise of the measurement.

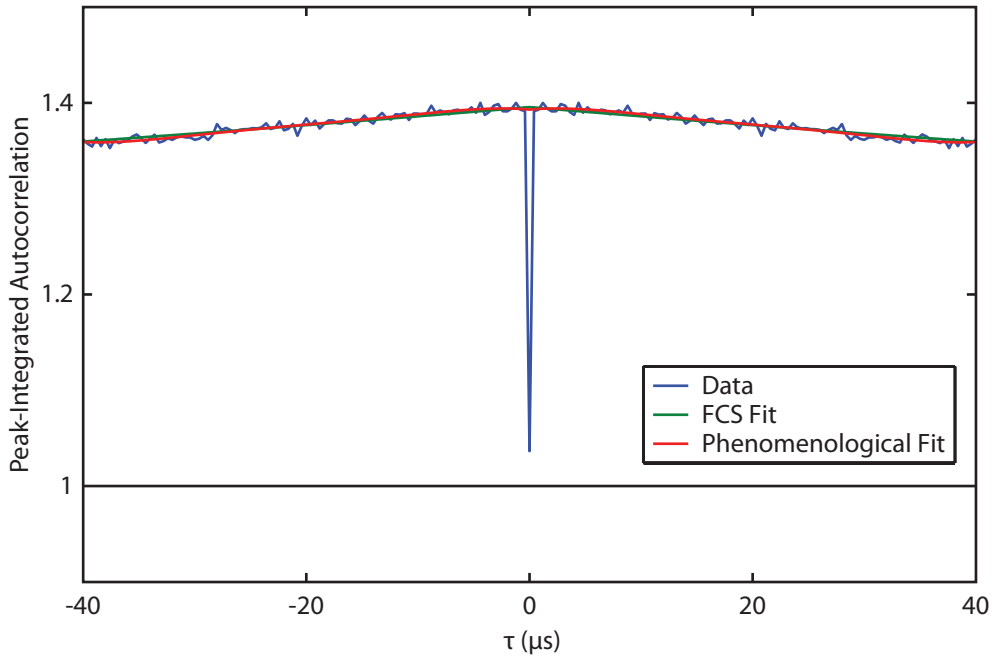

Figure 7-3: Using an FCS or phenomenological fit in long-repetition rate experiments can account for the minor curvature of the correlation function caused by diffusion between excitation pulses. This fit also removes the uncertainty in the value of the side peak due to shot noise, which can slightly improve the precision of the measurement.

Chapter 8

Measuring the Sample-Averaged Biexciton/Exciton Quantum Yield Ratio Using the Solution-Phase $g^{(2)}$ Experiment

Now that we have fleshed out the theory behind the solution-phase $g^{(2)}$ experiment, in this Chapter, we will demonstrate its implementation. We will begin by describing our experimental setup and the data analysis procedure we will follow to produce our experimental results. Second, we will show that our results are consistent with the theoretical predictions from the previous Chapter. Third, we will present two short investigations that demonstrate the flexibility, precision, and convenience of the solution-phase experiment, including a brief survey of materials that are not usually studied using single-nanocrystal spectroscopy and the characterization of a new CdSe/CdS shell growth procedure. Finally, we will summarize our results and discuss possible future directions for this technique. The results presented in this Chapter were published by Beyler et al. [244]

8.1 Experimental Setup and Data Analysis

8.1.1 Optical Setup and Data Collection

A schematic of the optical setup is shown in Figure 8-1(a).

The solution-phase sample was mounted on a fixed, inverted epifluorescence microscope equiped with a water immersion objective (Nikon, Plan Apo VC 60× WI, NA 1.2) and coupled to the excitation and emission paths via a 10:90 (R:T) visible-wavelength, non-polarizing beamsplitting cube (Thorlabs, BS025). The sample was excited using a 532 nm pulsed laser (Picoquant, LDH-P-FA-530-B) that was operated at the lasing threshold to suppress the double-pulse artifact in the temporal profile of the pulse and to achieve an optimal 50 ps pulse duration. The laser was operated at a repetition rate of 2.5 MHz for typical samples, or driven with an external sync to achieve repetition rates between 500–1000 kHz for samples with long radiative lifetimes. Once the emission from the focal volume passed through the beamsplitter into the detection arm of the setup, it was spatially filtered with a pinhole to form a well-defined focal volume (100 mm focusing lens, 50 µm pinhole, and 50 mm recollimating lens), and spectrally filtered with a 532/10 nm notch filter (Chroma, ZET532/10×) to remove laser scatter. Then, the signal was split using the interferometer setup from Chapter 5, with the path-length difference set well beyond the coherence length of the emission, and focused with two 7.5 cm focal length achromatic doublets onto two single-photon avalanche photodiodes (Excelitas, SPCM-AQRH-16). The selection of a path-length difference beyond the coherence length caused the interferometer to behave in the same fashion as the Hanbury Brown and Twiss geometry often used for photon correlation. [311] Two 700 or 800 nm shortpass filters (Thorlabs, FESH0700 or FES0800) were mounted to the front of the detector focusing optics to pass all of the signal to the detectors, but to prevent cross-detector afterpulsing artifacts (See Section 3.3).

Before the experiment was conducted, the signal was analyzed using a real time digital correlator (ALV, 7004/FAST) to confirm proper alignment (i.e. a well-formed focal volume with a good FCS fit) and to confirm sample stability (i.e. no large intensity spikes that would suggest aggregation). Then, the signal from the detectors was rerouted through an attenuator/inverter (Picoquant, SIA400) to a Hydraharp 400 time-correlated single photon counting module (Picoquant, one detection module for two input channels). To conduct the experiment, the Hydraharp was run in time-tagged time-resolved mode to record all of the photon arrival times in memory. The T3 setting was used to time all photons arrivals relative to the numbered sync pulse from the laser. It was therefore possible to directly count the number of photon arrivals after each pulse, and because we knew the repetition rate of the laser, to place each photon arrival on the absolute timeline of the experiment. Integration times varied between 1–5 h, depending on the repetition rate of the laser and quantum yield of the sample. For longer measurements, the total integration time was broken up into several sub-intervals to reconfirm alignment and to refresh the immersion water.

8.1.2 Sample Preparation

Solution-phase samples were prepared so as to avoid aggregation. Except for the serial dilution experiment, all samples were made in a single dilution step to avoid stripping ligands off of the nanocrystal surface. Furthermore, all samples were freshly prepared directly before each measurement, and they were further stabilized by the addition of several drops of a cadmium oleate/decylamine solution to passivate surface sites that were vacated by labile ligands during dilution. This solution was the same as that described in Chapter 5, synthesized by combining 1.25 mL cadmium oleate in octadecene and oleic acid (melted with a heat gun), 100 µL decylamine, and 8.75 mL toluene.

Each sample was prepared by adding between 0.5 and 20 µL of visibly colored,

concentrated nanocrystal/hexane solution to a solution composed of 0.5 mL of hexanes and several drops of the cadmium oleate solution, to produce an average occupation in the focal volume between 1 and 3 (unless otherwise specified). Then, this solution was wicked into a rectangular capillary (VitroCom, 0.10×2.00 mm i.d.) and sealed with capillary tube sealant to prevent evaporation.

8.1.3 Data Analysis

After data collection, we are left with a file essentially containing all of the photon arrivals on both of the detection channels. Our goal is to determine the autocorrelation of the overall signal. However, due to detector artifacts, namely their dead time after registering a photon arrival, it is not possible to resolve the autocorrelation of the signal as $\tau \rightarrow 0$ using only one detector. The solution, as is the standard in the literature, is to use the cross-correlation of the detection channels in lieu of the autocorrelation of either channel or the sum signal.[1] This cross correlation is functionally identical to the autocorrelation of the total signal because the two channels are unbiased and both statistically represent the behavior of the overall signal.

T3 data files were correlated in software after the measurement using the correlation software developed by T.S. Bischof and the pulse-resolved analysis described in the Supplemental of Bischof et al. [312] A typical correlation analysis was generated using the following shell command:

```
picoquant --file-in Sample_1.ht3 |
photon_gn --mode t3 --order 2 --channels 2
          --pulse -40000,80001,40000 --time -400000,1,400000
          --file-out Sample_1 &
```

The routine `picoquant` parsed the Hydraharp data file, and the routine `photon_gn`

[1] Remember that we did not have to do this in PCFS because we were interested in timescales much longer than the detector dead time.

was responsible for calculating a pulsewise correlation function out to at least $\tau = 15\,\text{ms}$.[2] The time-resolved correlation function from Figure 8-1 was calculated using the shell command:

```
picoquant --file-in Sample_1.ht3 |
photon_gn --mode t3 --order 2 --channels 2
          --pulse -100.5,201,100.5 --time -400000,800,400000
          --file-out Sample_1_HighRes &
```

which generated a hybrid pulsewise/τ-resolved correlation function that could be converted to an exclusively time-resolved correlation function in Matlab. And finally, long integration time measurements were broken up into several analysis sub-intervals using the shell command:

```
picoquant --file-in Sample_1.ht3 |
photon_gn --mode t3 --order 2 --channels 2
          --pulse -25000.5,50001,25000.5
          --time -400000,1,400000
          --window-width 3000000000 --file-out Sample_1_td &
```

After the correlation function was calculated, the output files from the correlation routine were imported into Matlab for further analysis. Each correlation measurement (i.e. for each sub-interval) was analyzed independently. They were each normalized using Equation 1.1 and the associated intensity information provided in the auxillary files of the correlation routine, fit using a 2D Gaussian focal volume FCS model, and plotted to confirm that the fit appropriately captured the plateau values of the FCS curve at long and short τ (Figure 7-3). Then, the biexciton/exciton quantum yield ratio was calculated from Equation 7.73 (with uncertainty given by Equation 7.81)

[2] A pulsewise correlation function histograms photons by their excitation pulse separation instead of their temporal separation, explicitly isolating photon pairs produced after the *same* excitation pulse in the center peak. Otherwise, photon pairs produced late in one excitation cycle and early in the next may be counted in the center peak. The rationale behind this type of analysis is provided in the Supporting Information of Bischof et al. [312]

using the center peak value from the correlation function and the y-intercept of the FCS fit. The experimental parameters from each sub-interval were graphed to confirm sample and optical setup stability (as shown in Figure 7-2). Finally, the peak area ratios for each sub-interval were averaged and the final uncertainty calculated using additive error propagation.

8.2 Results and Discussion

8.2.1 Experimental Verification of the Technique

Our first goal is to verify the theoretical results of our derivation at beginning of Chapter 7. A typical histogram of correlation counts for a solution-phase pulsed-excitation measurement (i.e. the unnormalized cross-correlation of the two detection channels) is shown in Figure 8-1(b). As in the SNC-$g^{(2)}$ experiment, the cross-correlation of the solution-phase $g^{(2)}$ is characterized by a series of peaks at the repetition period of the excitation laser. However, in solution, the integrated areas of these peaks are modulated by the diffusion physics of the sample. The center peak at $\tau = 0$ exhibits an increased area compared to a single-nanocrystal measurement due to the detection of photon pairs from different particles, and the integrated areas of the other correlation peaks decay on the time scale of particle diffusion. This point is emphasized in Figure 8-1(c), which shows that when the pulsewise autocorrelation is calculated by integrating the correlation histogram over each correlation peak and normalizing the result according to Equation 1.1, it reproduces the FCS correlation function of the solution-phase sample and informs on both the average occupation of particles in the focal volume and their average dwell time.

Furthermore, as our theory predicted, the ability for nanocrystals to sustain and emit from multiexcitonic states has caused the normalized area of the center peak to be slightly higher than the Poisson background caused by inter-particle photon

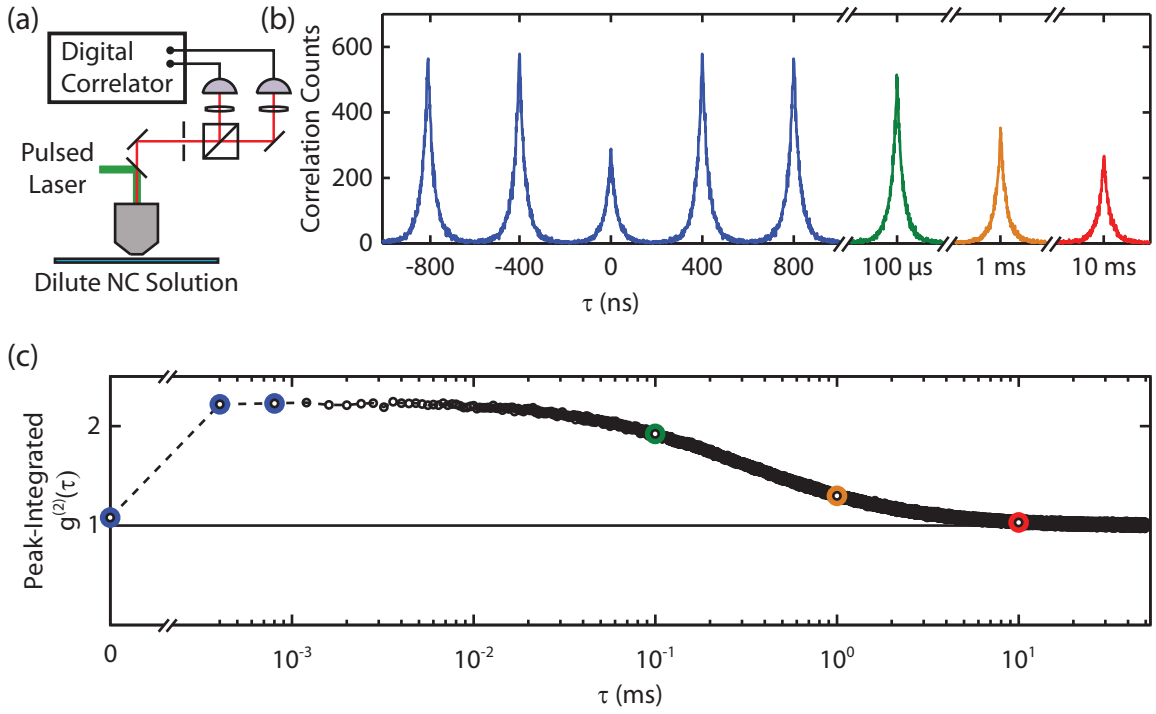

Figure 8-1: (a) Schematic representation of the solution-phase $g^{(2)}$ experiment. (b) Peak-resolved correlation function illustrating that the amplitudes of the correlation peaks are modulated by diffusion physics. (c) Peak-integrated correlation function illustrating that the side-peak areas sample the FCS trace measured by continuous-wave excitation. In both representations, the center peak at $\tau = 0$ is diminished due to antibunching, but may extend above the Poissonian inter-particle background if there is finite probability of multi-photon emission.

pairs. The pulsewise autocorrelation function does not exhibit full antibunching, and the erosion of the antibunching feature can be directly tied to the sample-averaged biexciton/exciton quantum yield ratio. To demonstrate the reproducibility of this incomplete antibunching feature and to confirm the accuracy of Equations 6.3 and 6.4, we perform the solution-phase $g^{(2)}$ experiment on a single batch of CdSe/CdS core/shell nanocrystals that has undergone serial dilution to create a series of samples with varying nanocrystal concentration. If the results of the derivation from Chapter 7 hold, the peak area ratio should increase with increasing concentration according to Equation 6.4, and the peak area ratio after Poisson background-subtraction should be constant with varying concentration, as predicted by Equation 6.3.

The peak area ratio as a function of particle concentration is shown in Figure 8-2(a) and the corresponding quantum yield ratios are shown in Figure 8-2(b). The degree of single-nanocrystal antibunching is clearly reproduced across all particle concentrations, yielding an extremely uniform measurement of the biexciton/exciton quantum yield ratio of $7.5\% \pm 1\%$. This result is consistent with our expectations from previous single-nanocrystal investigations, [187, 193] but offers precision far exceeding that of other available techniques. Moreover, this experiment demonstrates the success of our sample preparation outlined in Section 8.1.2. This sample was able to undergo five serial dilutions (with the addition of cadmium oleate solution during each dilution) without any sign of aggregation or sample degradation.

8.2.2 Measuring the Quantum Yield Ratio of Several Synthetically-Underdeveloped Materials

We now present two small investigations that highlight the primary benefits of the solution-phase $g^{(2)}$ experiment. One of the limitations of the SNC-$g^{(2)}$ experiment is that it requires samples to be optimized for single-molecule spectroscopy. Studied emitters must have high quantum yields to provide a strong single-molecule fluores-

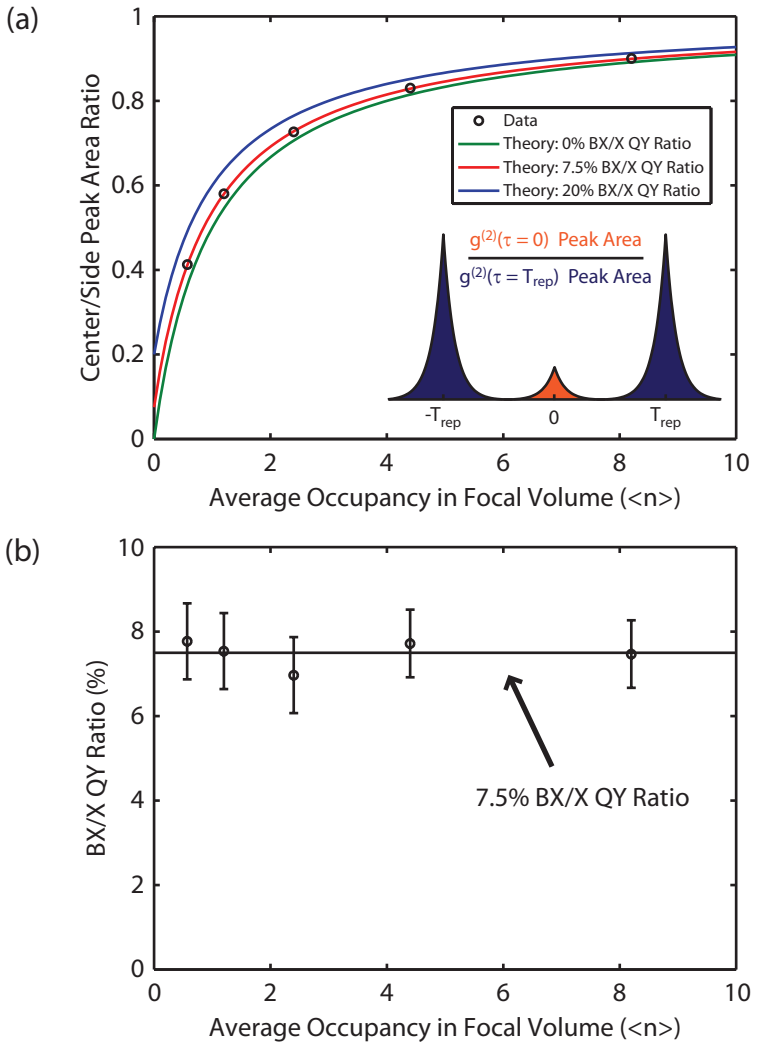

Figure 8-2: As predicted by the theory in the previous Chapter, (a) the peak area ratio increases towards unity with increasing average occupancy, and (b) the corresponding quantum yield ratio remains constant under serial dilution. This data confirms the theoretical results from the previous Chapter and demonstrates that our sample preparation does not induce aggregation.

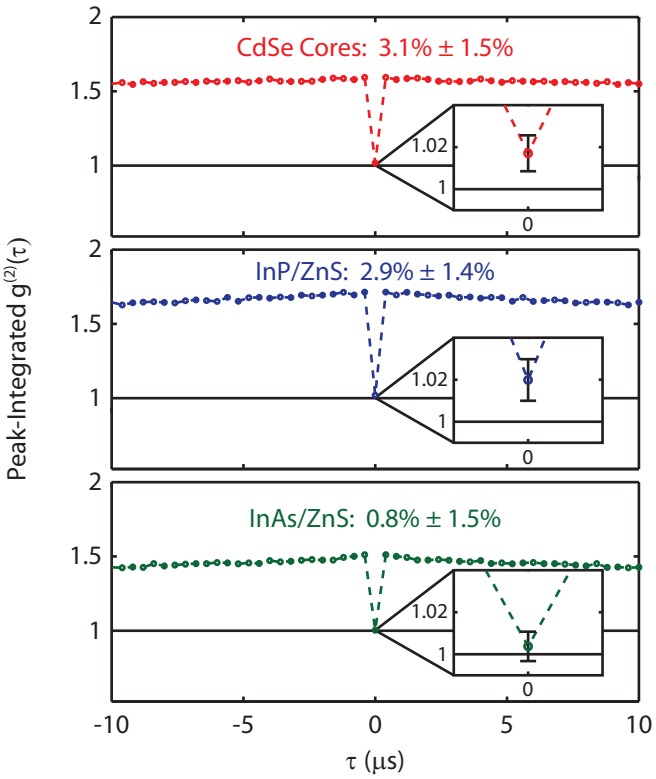

Figure 8-3: Quantum yield ratios measured for (a) CdSe cores, (b) InP/ZnS core/shell nanocrystals, and (c) small, visible-emitting InAs/ZnS core/shell nanocrystals.

cence signal under low excitation flux, and they must have fluorescence stability on the order of tens of minutes to measure the quantum yield ratio with precision near 1%. These requirements are further exacerbated when measuring samples with long fluorescence lifetimes because longer laser repetition periods further reduce photon count rate. In contrast, solution-phase $g^{(2)}$ measurements do not require fluorescence stability because of the rapid exchange of particles in the focal volume, and the duration of the experiment can be extended arbitrarily to compensate for the weak fluorescence signals produced by samples with low quantum yields or long fluorescence lifetimes.

In Figure 8-3, we show the pulsewise solution-phase autocorrelations for three types of nanocrystal samples that are not generally suitable for single-nanocrystal $g^{(2)}$ experiments: CdSe cores, which are normally overcoated for improved quantum

yield and fluorescence stability; InP/ZnS core/shell nanocrystals, which are a less synthetically-explored, cadmium-free alternative to CdSe nanocrystals; and visible-emitting InAs/ZnS NCs, which are a promising infrared-emitting material at larger core sizes. The biexciton quantum yields of all three samples are very low. The measurement of our InAs/ZnS sample sets an upper bound on the quantum yield ratio of 0.8% percent, in agreement with transient absorption measurements reporting biexciton lifetimes under 100 ps. [313] This result is also consistent with a recent SNC-$g^{(2)}$ investigation of larger, infrared-emitting InAs/CdZnS nanocrystals, which reported a wide distribution of quantum yield ratios with most particles exhibiting ratios below 5% and a few outliers exhibiting significantly larger values. [312] The biexciton/exciton quantum yield ratio of our sample was expected to be even lower than those reported by Bischof et al. [312] due to the increased quantum confinement in our visible-emitting sample.

These results also reveals that, even with an epitaxial shell to enhance their fluorescence properties, current InP samples do not appear to offer a multiexciton advantage over CdSe cores. This finding is consistent with the recent report from Mangum et al., [314] which found quantum yield ratios of less than 5% in type II InP/CdS core/shell NCs. Deliberate synthetic design with the biexciton quantum yield in mind will be required to optimize InP nanocrystals for high-flux applications.

8.2.3 Evaluating the Biexcitonic Properties Produced by a CdSe/CdS Shell Growth Procedure

The other major feature of the solution-phase $g^{(2)}$ experiment is that it is a precise method for characterizing the average biexcitonic properties of entire nanocrystal samples. In Figure 8-2, we showed how the measurement can routinely measure the quantum yield ratio of high quality samples with 1% uncertainty. With this degree of resolution in the quantum yield ratio, this technique can be used to cleanly identify

differences in the biexcitonic fluorescence properties produced by different synthetic procedures or modifications to the nanocrystal architecture.

In our second investigation, we use the solution-phase $g^{(2)}$ experiment to characterize the effect of our recent CdSe/CdS shell growth procedure. As we discussed in Chapter 1, multi-day SILAR shell growth procedures have been found to produce particles with anomalously low Auger rates [107, 301, 315] and quantum yield ratios approaching 40% in 19-monolayer samples. [187] Klimov and coworkers later hypothesized that these low Auger rates were caused by core/shell alloying due to the extended duration of the shell growth. [186, 304] They introduced a rapid shell growth procedure that was presumably resistant to core/shell alloying and found that it resulted in extremely low biexciton quantum yields unless an intentional alloy region was introduced by dual precursor injection. Although their finding conclusively demonstrates the importance of the core/shell interface in controlling biexciton fluorescence, it is still unclear whether the only difference between their intentionally alloyed and reference samples was a smoother potential boundary. Other proposed sources of Auger enhancement, including the existence of increased local electric fields via carrier trapping [316] or by trap-mediated Auger pathways, [317, 318] could also have been affected by their alloying procedure, especially given that the exciton quantum yields of both their reference and alloyed nanocrystals dipped below 50% in thicker shell samples. [304]

Our recent CdSe/CdS shell growth procedure published by Coropceanu et al. [174] is also a rapid shell growth that uses relatively nonreactive precursors and high reaction temperatures. These reaction conditions should result in nanocrystals with similar interfacial alloying as the non-intentionally alloyed reference samples measured by Park et al. [304] However, nanocrystals produced by our synthesis have higher exciton quantum yields, exceeding 85% for shells as thick as 5.0 nm (14 monolayers). In Figure 8-4, we show the biexciton/exciton quantum yield ratios measured

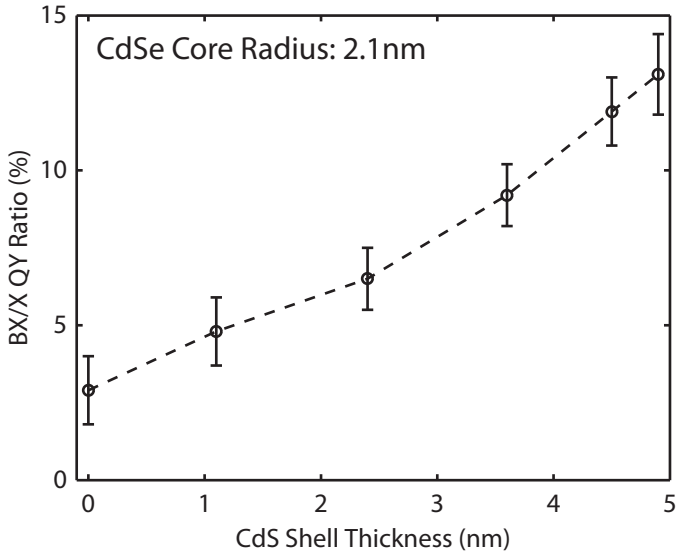

Figure 8-4: Quantum yield ratios of CdSe nanocrystals undergoing a rapid CdS shell growth. The biexciton quantum yield continues to increase with shell growth even though they have not been intentionally annealed either by dual precursor injection or extended growth period.

by solution-phase $g^{(2)}$ for a shell series of particles made by our optimized synthesis. Their quantum yield ratios, which roughly approximate the actual biexciton quantum yields due to their high exciton quantum yields, increase monotonically with shell growth in a fashion consistent with the multiday SILAR shell growth. These results show that intentional alloying is not required to increase the biexciton quantum yield of CdSe nanocrystals using a rapid CdS shell growth. Unless rapid shell growths are capable of producing the considerable core/shell alloying that has been hypothesized to occur in multiday SILAR procedures, other sources of Auger enhancement must play an active role in defining the biexciton quantum yield of CdSe/CdS core/shell samples.

8.3 Summary and Future Directions

In this Chapter, we have demonstrated that the solution-phase $g^{(2)}$ experiment is a convenient, reliable, and precise method for measuring the average biexciton/exciton

quantum yield ratio of an entire sample without user selection bias. Going forward, we have shown that it can be an ideal tool for investigating the multiexcitonic properties of materials that are not optimized for single-nanocrystal spectroscopy, a routine characterization technique for gauging the effect of a synthetic procedure on the biexciton quantum yield of samples, and a technique that should be easily extended to the investigation of short-wave infrared-emitting samples, for which single-photon sensitive detectors remain an immature technology. [159]

This technique may also find useful applications as a new addition to the growing toolbox of single-nanocrystal spectroscopic methods. Single-nanocrystal correlation experiments must remain the workhorse for the elucidation of basic nanocrystal physics because they allow the experimenter to correlate many observables from the same nanocrystal and to assemble a self-consistent physical picture for each nanocrystal. Nevertheless, as single-nanocrystal techniques have become more complicated and required longer integration times, it has become harder and harder to achieve high sample statistics using these techniques (the low temperature PCFS experiments in Part I are a textbook example). Solution-phase measurments like the one presented here can be useful complementary methods, which can easily and reliably gauge the average properties of the sample to identify selection bias in single-nanocrystal surveys. Furthermore, they may be helpful for extending the physical insight gained from in-depth single-nanocrystal investigations of highly-optimized samples to physical systems with poorer optical properties, for which in-depth single-nanocrystal investigations are not possible.

Part III

Developing Advanced Photon Correlation Experiments

Chapter 9

Three Photon-Correlation Fourier Spectroscopy-Based Techniques

Although Photon-Correlation Fourier Spectroscopy (PCFS) is one of the more complicated and conceptually difficult methods in our single-nanocrystal toolbox, its development is just as much the beginning of a new experimental paradigm as it is as a culmination of years of progress in single-photon counting analysis. The experimental parameters of the experiment can be tuned to focus on a variety of different phenomena under a spectrum of different experimental conditions and constraints. In Section 5.4, we discussed some of the ways that PCFS experiments can be tuned and modified to further elucidate the physics of single nanocrystals at low temperature, but the potential for spectrally-resolved photon-correlation methods does not stop there. In this Chapter, we will discuss three variants of the original PCFS experiment that may be useful in future investigations. For each experiment, we will discuss the motivation behind its development, how it would be (or has been) experimentally implemented, how the standard PCFS theory is modified to address their experimental modifications, and my personal outlook on their possible utility.

9.1 Raster-Scanned Photon-Correlation Fourier Spectroscopy

9.1.1 Motivation and Background

One of the biggest problems that we have had with the standard single-nanocrystal PCFS experiment is its long integration time, which limits the use of PCFS to highly-optimized samples, introduces the potential for selection bias, and makes the process of characterizing the properties of an entire sample extremely time-consuming. This issue has been addressed in room temperature investigations by the development of solution-phase PCFS. Solution-phase PCFS does everything for PCFS that the solution-phase $g^{(2)}$ experiment described in Part II does for single-nanocrystal $g^{(2)}$ experiments.[1] It can be used to measure the sample-averaged single-nanocrystal spectral correlation with high sample statistics, no user selection bias, a high signal-to-noise ratio, and using a bright and stable solution-phase sample with no inherent limitation on integration time and resistance to photodamage (because of the constant diffusion of particles into and out of the focal volume).

In fact, solution-phase PCFS has already been used in two investigations to determine that the room temperature linewidth of nanocrystals is not generally broadened by rapid spectral diffusion processes under low flux conditions, to show that the single-nanocrystal linewidth is an active parameter in defining the ensemble linewidth that can be greatly affected by nanocrystal architecture, and to easily and reliably characterize the degree of spectral polydispersity in nanocrystal samples. [176] However, its application is strictly limited to experimental conditions where a solution-phase sample is viable. At low temperatures, for example, nanocrystal solvents freeze and the only viable sample preparations are dilute films like the one we described in Section 5.1.2. Instead of using a solution-phase sample, here we consider the idea of

[1] It is actually where we got the idea for the solution-phase $g^{(2)}$ experiment in the first place.

measuring the average single-nanocrystal spectral correlation of a sample by rastering the focal volume of the microscope over a single-nanocrystal film, thereby simulating the diffusion of particles in a solution-phase sample. This experiment would not generally have sample statistics quite as high as a true solution-phase measurement and it would be more finicky to accurately implement, but it would be compatible with the low-temperature conditions where rapid spectral dynamics are manifested.

9.1.2 Experimental

Raster-scanned PCFS can be readily performed on any single-nanocrystal PCFS setup, including the one described in Section 5.1.1. In the implementation used for the preliminary measurements, the normal confocal spectroscopy program used to identify the position of nanocrystals on the substrate was used to set up a rectangular array of discrete raster positions. This vertices of this array were spaced widely enough such that there was not focal volume overlap between neighboring vertices; the total size of the array was large enough to encompass a statistically large number of vertices for sampling, but small enough such that there would not be severe focal volume distortion on the edges of the array from the angular deflection of the scanning galvomirrors; and the integration time at each raster position was set to $\sim 50\,\mathrm{ms}$, which was long enough to resolve the average single-nanocrystal spectral correlation at relevant τ (in this case, $<10\,\mathrm{ms}$) and short enough to sample the ensemble spectral correlation and to reduce nanocrystal photodamage. Then, the confocal program was set to continuously raster scan the array while the normal low temperature PCFS experiment from Chapter 5 was conducted (i.e. with the same dither conditions and stage positions[2]). No effort was made to synchronize the raster scanning with the integration time of each correlation measurement, but a large number of raster positions were required for each correlation measurement to ensure statistical equivalency

[2]Longer correlation function integration times were used, which was okay because of the small duty cycle of each raster position.

between the correlation measurements.

Particular attention should be paid to sample preparation. The film should be more concentrated than a usual single-nanocrystal film, preferably containing on the order of one nanocrystal per arbitrarily chosen focal volume. This ensures that most raster positions will have at least one nanocrystal and that the experiment will not waste time looking at places on the sample where there is no signal. However, more critical than particle concentration is to ensure that the sample preparation produces a uniform, well-dispersed film with a Poisson distribution of particles in any given focal volume. Aggregation of nanocrystals in thin films is a fairly common occurrence that will conflate the single-nanocrystal and ensemble contributions to the spectral correlation. Other sample preparations using glass matrices or other polymers than PMMA may be preferable for achieving a high quality raster-scanned PCFS film.

9.1.3 Theory

The theory behind the raster-scanned PCFS experiment is essentially identical to those of solution-phase PCFS presented elsewhere, but instead of measuring fluctuations in the behavior of the focal volume due to particle diffusion, we induce our own fluctuations by moving the focal volume itself in a well-defined, predetermined fashion. In the following section, we present a derivation to aid in the identification of possible artifacts of the measurement. The derivation will follow the notation presented in Section 3.1.1, except where new terms are introduced in-line.

Derivation. Consider the case where a PCFS experiment is conducted on a focal volume that is rastered across the surface of a dilute film, but otherwise using the same experimental procedure as was assumed in the derivation given in Section 3.1. Here, the distribution of particles in the film is assumed to exhibit no spatial correlation, such that arbitrarily chosen focal volumes have a Poisson distribution of

particles with average occupation $\langle n \rangle$, and the raster scan is assumed to regularly and instantaneously shift between uncorrelated positions on the film every T seconds. Furthermore, we require that we sample a statistically large number of raster positions per correlation measurement, and we assume that the particles we have sampled over the large number of raster positions is representative of the overall sample. This experiment no longer yields the spectral correlation of an individual nanocrystal, but its cross-correlation is still given by,

$$g^{\times}(\delta_0, \tau) = g_{fv}(\tau) \left(1 - \frac{1}{2} c(\tau) \mathcal{F}_{\mathbf{cos}}[\tilde{P}_{fv}(\zeta, \tau)]_{\delta_0} - \frac{1}{2} d(\tau) \mathcal{F}_{\mathbf{sin}}[\tilde{P}_{fv}(\zeta, \tau)]_{\delta_0} \right), \qquad (9.1)$$

where we have used the correlated spectral and intensity fluctuation formulation from Section 3.5, because each change in raster position will induce a change in both the spectrum and intensity from the focal volume, and where $g_{fv}(\tau)$ and $\tilde{P}_{fv}(\zeta, \tau)$ are now defined as the autocorrelation and spectral correlation of the entire focal volume over the course of the measurement. Our goal is to relate these two focal volume quantities to the ensemble and average single-nanocrystal properties of the sample at large.

To accomplish this goal, we will consider the contribution to the focal volume correlation functions from photon pairs whose first photon arrives during an average raster position whose focal volume contains n particles, and then we will average this contribution over a Poisson distribution of particle occupancies. In general, raster positions are defined by their time-dependent intensity,

$$I_{fv}(t) = \sum_{i=1}^{n} I_i(t), \qquad (9.2)$$

where $I_i(t)$ is the intensity of the ith particle in the focal volume, and their time-dependent spectrum,

$$S_{fv}(\omega, t) = \sum_{i=1}^{n} I_i(t) s_i(\omega, t), \tag{9.3}$$

where $s_i(\omega, t)$ is the normalized spectrum of the ith particle in the focal volume.

To compose the contribution from a single raster position, it is helpful to note that both correlation functions exhibit two distinct temporal regimes: where $\tau < T$ and where $\tau > T$. For $\tau > T$, the second photon must necessarily come from a different, uncorrelated raster position with m particles. Thus, the average contribution that a pair of frames with occupancies n and m, respectively, will make to the numerator of the focal volume autocorrelation is,[3]

$$\begin{aligned}
\big\langle I_{fv}^n(t) I_{fv}^m(t+\tau) \big\rangle &= \big\langle \sum_{i=1}^{n} I_i(t) \sum_{j=1}^{m} I_j(t+\tau) \big\rangle && (9.4)\\
&= \big\langle \sum_{i=1}^{n} I_i(t) \big\rangle \big\langle \sum_{j=1}^{m} I_j(t+\tau) \big\rangle && (9.5)\\
&= nm \big\langle I(t) \big\rangle^2, && (9.6)
\end{aligned}$$

where $\big\langle I(t) \big\rangle$ is the average intensity of a single particle. Similarly, the average contributions to the denominator time averages in the focal volume autocorrelation are given by,

$$\begin{aligned}
\big\langle I_{fv}^n(t) \big\rangle &= \big\langle \sum_{i=1}^{n} I_i(t) \big\rangle && (9.7)\\
&= n \big\langle I(t) \big\rangle, && (9.8)
\end{aligned}$$

and,

$$\big\langle I_{fv}^m(t+\tau) \big\rangle = \big\langle \sum_{i=1}^{m} I_i(t+\tau) \big\rangle = m \big\langle I(t) \big\rangle. \tag{9.9}$$

[3]The notation is a little sloppy here. In the inter-raster-position case, i and j index different particles whose behavior is uncorrelated.

Independently calculating the Poisson average of these time averages over n and m,[4] and assembling the final focal volume autocorrelation yields, for $\tau > T$,

$$g_{fv}(\tau) = \frac{\langle n \rangle^2 \langle I(t) \rangle^2}{\left(\langle n \rangle \langle I(t) \rangle\right)\left(\langle n \rangle \langle I(t) \rangle\right)} \tag{9.10}$$

$$= 1. \tag{9.11}$$

We calculate the average contribution that these frames make to the focal volume spectral correlation $\tilde{P}_{fv}^{n,m}(\zeta, \tau)$ using a slightly different method. Using a slightly modified version of Equation 3.98,

$$\tilde{P}_{fv}^{n,m}(\zeta, \tau) = \frac{\left\langle S_{fv}(\omega, t) \circ S_{fv}(\omega + \zeta, t + \tau) \right\rangle}{\left\langle \left[I_{fv}(t) I_{fv}(t + \tau) \right] \right\rangle} \tag{9.12}$$

$$= \frac{\left\langle \sum_{i=1}^{n} \sum_{j=1}^{m} I_i(t) I_j(t + \tau) \left[s_i(\omega, t) \circ s_j(\omega, t + \tau) \right] \right\rangle}{\left\langle \sum_{i=1}^{n} \sum_{j=1}^{m} I_i(t) I_j(t + \tau) \right\rangle} \tag{9.13}$$

$$= p_{ens}(\zeta), \tag{9.14}$$

where $p_{ens}(\zeta)$ is the spectral autocorrelation of the ensemble spectrum.[5] This expression is trivially averaged over a Poisson distribution of occupancies to yield, for $\tau > T$,

$$\tilde{P}_{fv}(\zeta, \tau) = p_{ens}(\zeta). \tag{9.15}$$

Neither of these are surprising results because we asserted at the beginning that there should be no correlation in the behaviors between different raster positions. Things get much more interesting when we begin to consider the values of the focal volume correlation functions for $\tau < T$. There is still a region of time in this regime when the first photon is in the raster position of interest and the second photon spills into the next raster position (namely, when $t > T - \tau$) and the average contribution is

[4] Both variables have an average value of $\langle n \rangle$.

[5] Remember that the spectral autocorrelation is, by its nature, an intensity-weighted quantity because the ensemble spectrum is an intensity-weighted quantity.

still given by the previous, uncorrelated result, but now there is also a region of time where both photons originate from the the same raster position (when $t < T - \tau$). This is where we may detect photon pairs from the same particle.

The average intra-raster-frame contribution from a raster position with n particles to the numerator of the focal volume autocorrelation is given by,[6]

$$\begin{aligned}\big\langle I^n_{fv}(t) I^n_{fv}(t+\tau)\big\rangle =& \Big\langle \sum_{i=1}^{n} I_i(t) \sum_{j=1}^{n} I_j(t+\tau)\Big\rangle && (9.16)\\ =& (n^2 - n)\big\langle I(t)\big\rangle^2 + n\big\langle I(t) I(t+\tau)\big\rangle. && (9.17)\end{aligned}$$

This can be combined with the inter-raster position contribution from Equation 9.6 to yield a total position average of,

$$\begin{aligned}\big\langle I^n_{fv}(t) I^{n/m}_{fv}(t+\tau)\big\rangle = &\left(1 - \frac{\tau}{T}\right)\left[(n^2 - n)\big\langle I(t)\big\rangle^2 + n\big\langle I(t) I(t+\tau)\big\rangle\right]\\ &+ \frac{\tau}{T}\left[nm\big\langle I(t)\big\rangle^2\right], \qquad (9.18)\end{aligned}$$

and a resulting Poisson-average for the numerator of,

$$\big\langle I_{fv}(t) I_{fv}(t+\tau)\big\rangle = \big\langle n\big\rangle^2\big\langle I(t)\big\rangle^2 + \left(1 - \frac{\tau}{T}\right)\big\langle n\big\rangle\big\langle I(t) I(t+\tau)\big\rangle. \qquad (9.19)$$

The denominator terms are treated exactly in the same fashion as in the purely inter-raster position case, yielding a final focal volume autocorrelation for $\tau < T$

$$\begin{aligned} g_{fv}(\tau) =& \frac{\big\langle n\big\rangle^2\big\langle I(t)\big\rangle^2 + \left(1 - \frac{\tau}{T}\right)\big\langle n\big\rangle\big\langle I(t) I(t+\tau)\big\rangle}{\big\langle n\big\rangle^2\big\langle I(t)\big\rangle^2} && (9.20)\\ =& 1 + \left(1 - \frac{\tau}{T}\right)\frac{1}{\big\langle n\big\rangle}\big\langle g(\tau)\big\rangle, && (9.21)\end{aligned}$$

where $\big\langle g(\tau)\big\rangle$ is the average intensity autocorrelation of single particles within the

[6]Now, we are in the intra-raster-frame case, where i and j index the same particle when $i = j$.

sample. In the case where blinking effects are minimal, $\langle g(\tau) \rangle \approx 1$ and the focal volume autocorrelation takes a simple, known functional form. This can be used as a control to evaluate whether or not the experiment is conforming to the assumptions used in this derivation. Deviation from a triangular intensity autocorrelation may suggest severe blinking dynamics (especially deviations for $\tau < T$), poor particle dispersion (especially deviations for $\tau > T$), or other experimental effects such as drift or focal volume distortion over the raster grid.

The same general procedure is used to calculate the focal volume spectral correlation for $\tau < T$. The average intra-raster-position contribution from a raster position with n particles to the numerator of Equation 9.12 is given by,

$$P_{fv}^{n}(\zeta,\tau) = \Big\langle \sum_{i=1}^{n}\sum_{j=1}^{m} I_i(t) I_j(t+\tau)\left[s_i(\omega,t) \circ s_j(\omega,t+\tau)\right] \Big\rangle \tag{9.22}$$

$$= (n^2-n)\big\langle I(t)\big\rangle^2 p_{ens}(\zeta) + n\big\langle I(t)I(t+\tau)\big\rangle\big\langle p(\zeta,\tau)\big\rangle, \tag{9.23}$$

where $\big\langle p(\zeta,\tau)\big\rangle$ is the average single-emitter spectral correlation of the sample. This leads to a whole-position contribution to the numerator of,

$$P_{fv}^{n,n/m}(\zeta,\tau) = \left(1-\frac{\tau}{T}\right)\Big[(n^2-n)\big\langle I(t)\big\rangle^2 p_{ens}(\zeta) + n\big\langle I(t)I(t+\tau)\big\rangle\big\langle p(\zeta,\tau)\big\rangle\Big] + \frac{\tau}{T}\Big[nm\big\langle I(t)\big\rangle^2 p_{ens}(\zeta)\Big], \tag{9.24}$$

and a resulting Poisson-average for the numerator of,

$$P_{fv}(\zeta,\tau) = \big\langle n\big\rangle^2\big\langle I(t)\big\rangle^2 p_{ens}(\zeta) + \left(1-\frac{\tau}{T}\right)\big\langle n\big\rangle\big\langle I(t)I(t+\tau)\big\rangle\big\langle p(\zeta,\tau)\big\rangle. \tag{9.25}$$

The denominator of the focal volume spectral correlation for $\tau < T$ is given by Equation 9.19. Thus,

$$\tilde{P}_{fv}(\zeta,\tau) = \frac{\langle n\rangle^2\langle I(t)\rangle^2 p_{ens}(\zeta) + \left(1-\frac{\tau}{T}\right)\langle n\rangle\langle I(t)I(t+\tau)\rangle\langle p(\zeta,\tau)\rangle}{\langle n\rangle^2\langle I(t)\rangle^2 + \left(1-\frac{\tau}{T}\right)\langle n\rangle\langle I(t)I(t+\tau)\rangle} \tag{9.26}$$

$$= \frac{p_{ens}(\zeta) + (g_{fv}(\tau)-1)\langle p(\zeta,\tau)\rangle}{g_{fv}(\tau)}, \tag{9.27}$$

and Equation 9.1 can be rewritten to yield the dithered PCFS analog of Equation 9 of Brokmann et al., [285]

$$g^{\times}(\delta_0,\tau) = g_{fv}(\tau) - \frac{1}{2}c(\tau)\mathcal{F}_{\mathbf{cos}}[p_{ens}(\zeta) + (g_{fv}(\tau)-1)\langle p(\zeta,\tau)\rangle]_{\delta_0} - \frac{1}{2}d(\tau)\mathcal{F}_{\mathbf{sin}}[p_{ens}(\zeta) + (g_{fv}(\tau)-1)\langle p(\zeta,\tau)\rangle]_{\delta_0}, \tag{9.28}$$

which is their final result for the interpretation of the solution-phase PCFS experiment. However, in this case, the overall intensity autocorrelation of the signal is not given by the FCS curve of a solution-phase focal volume, but instead is given by,

$$g_{fv}(\tau) = 1 + \left(1-\frac{\tau}{T}\right)\frac{1}{\langle n\rangle}\langle g(\tau)\rangle. \tag{9.29}$$

9.1.4 Outlook

My preliminary work shows that it is fairly straightforward to implement raster-scanned PCFS in practice and to use it to measure the average single-emitter spectral correlation of a sample of nanocrystals deposited on a substrate. However, there are two critical drawbacks of the experiment that dissuaded me from further developing the technique. First, because we are responsible for manually inducing the fluctuations in focal volume occupancy, the results of the scanning measurement will be inherently less accurate and precise than its solution-phase analogue. Not only will it have lower sample statistics and be more prone to drift and other focal volume artifacts due to the active sampling process, but the focal volume occupancy will also be more

susceptible to breakdowns in the Poisson distribution. If this occurs, it is no longer possible to make the essential Poisson simplication that $\langle n^2 \rangle - \langle n \rangle = \langle n \rangle^2$, and we can no longer accurately parse the single and ensemble contributions to the spectral correlation when $\tau < T$. With a sample preparation, the latter concern can be minimized, but small-number fluctuations will still introduce noise into the spectral correlation. Raster-scanned PCFS gives us the ability to extend room-temperature measurements of the single-nanocrystal linewidth to lower temperatures, but we should not expect as clean and precise a result.

Second, although raster-scanned PCFS will not be affected by the same severly-limiting fluorescence stability considerations as single-nanocrystal PCFS, its sample-averaged observable is less useful for measuring highly variable phenomena such as rapid spectral diffusion. By averaging over the spectral correlations of many particles with very different spectral diffusion kinetics, jump distributions, and quasi-continuous broadening exponents, the qualitative features of the discrete spectral correlation profile are obfuscated and it is impossible to tease out the average diffusion parameters of the sample. It may still be possible to compare the overall magnitudes of the spectral dynamics between samples, but the significance of such a comparions would not necessarily be immediately obvious. One area where the raster-scanned PCFS experiment may be useful is in determining the physics behind the linewidth of the zero-phonon line (ZPL) of nanocrystals at low temperatures. This observable is not expected to vary widely within samples, but long integration times are generally required to resolve the spectral correlation of the ZPL on timescales faster than rapid spectral dynamics. Raster-scanned PCFS may provide a means for reliably measuring the effect of nanocrystal architecture on the nanocrystal ZPL linewidth, even in poorly optimized (but physically interesting) samples that could not be investigated using single-nanocrystal PCFS.

9.2 Pulsed-Excitation Photon-Correlation Fourier Spectroscopy

9.2.1 Motivation and Background

Another PCFS experiment we have considered is combining PCFS with the solution-phase $g^{(2)}$ experiment to measure the sample-averaged biexciton binding energy of nanocrystal samples. The biexciton binding energy is an important nanocrystal parameter because it is related to the strength of the Coulomb interaction between multiexcitonic states that mediates their many-body interactions, it plays a major role in mediating absorption and stimulated emission in nanocrystal lasers, and it is a factor that controls the spectral purity of nanocrystal fluorescence under high excitation flux. [319] Nevertheless, it can be a tricky parameter to measure experimentally. Several investigations have reported biexciton binding energies on the order of 15 meV at low temperatures, where the nanocrystal spectrum becomes very narrow, but such a small binding energy can be very difficult to resolve compared to the ∼60 meV excitonic spectrum of nanocrystals at room temperature. [320, 321] Because of the low biexciton quantum yields of nanocrystals, extremely high excitation flux is required to generate a high enough biexciton fluorescence signal that it can be detected next to the nearly saturated exciton fluorescence using traditional spectroscopies. Under these conditions, the excitonic spectrum may also undergo charging and spectral diffusion processes that broaden the single-exciton spectrum and obfuscate the biexcitonic spectral feature.

Pulsed-excitation photon-correlation Fourier spectroscopy is an interesting alternative for measuring the biexciton binding energy because it both temporally and spectrally resolves biexcitonic emission. It can be conducted at lower excitation fluxes to prevent photodamage and it resolves the relative energies of the biexciton and exciton on timescales faster than charging and spectral diffusion effects.

9.2.2 Experimental

Pulsed-excitation PCFS can be readily implemented using the solution-phase $g^{(2)}$ setup described in Section 8.1.1. But now, instead of measuring photon arrivals on the two detection channels at an interferometer path-length difference well beyond the coherence length of the emission, the goal is to record the photon arrivals on both detectors during a series of integration times at a set of evenly-spaced of path-length differences, as we would in PCFS. Once this data has been collected, it can be used to generate pulsewise correlation functions of the cross-correlation and autocorrelation of the sum signals,[7] which are discrete samples of their analogous continuous-wave correlation functions (see Figure 8-1). These pulsewise correlation functions can be immediately analyzed without adulteration using the solution-phase PCFS equation (Equation 9.28) to calculate the ensemble spectral autocorrelation and the average single-molecule spectral correlation.

9.2.3 Theory

As with the solution-phase $g^{(2)}$ measurement, pulsed-excitation PCFS provides the exact same information as its continuous-wave analogue, except with one important caveat: the correlation counts in the center peak correspond to a distinct physical process from the correlation counts in the side peaks. Whereas the single-nanocrystal contributions to the side peaks are dominated by fluorescence from single-exciton emission, the single-nanocrystal contribution to the center peak is exclusively composed of one biexciton photon and one exciton photon. Therefore, we can use the difference between the single-nanocrystal spectral correlations calculated from the

[7] Because of dead time and afterpulsing, it will not be possible to calculate the autocorrelation of the sum signal at timescales faster than $\sim$1 µs. If there is no drift in the FCS curve as a function of time, the baseline cross-correlation measurements beyond the coherence length of the emission can be used in lieu of the intensity autocorrelation (just as we do in the solution-phase $g^{(2)}$). Otherwise, we can use an FCS fit of the autocorrelation of the sum signal to extrapolate the intensity autocorrelation to $\tau = 0$ in order to actively correct for changes in average occupancy over the course of the measurement.

center and side peaks to extract the average biexciton binding energy of the sample.

In fact, as we will now show, it may be possible to extract the biexciton binding energy from the pulsed-excitation single-nanocrystal spectral correlation without the need for quantitative modeling of the homogeneous fluorescence lineshape by using a couple of well-defined assumptions and approximations. The concern that we have at the outset of our analysis is that, although we have an experimental handle on the homogeneous lineshape of exciton fluorescence via its spectral autocorrelation (i.e. the spectral correlation of the first side peak), we do not have a very good theoretical handle on what the homogeneous lineshape of biexciton fluorescence should be. Specifically, we (or at least, I) do not know how the extent of exciton-phonon coupling should be affected by the presence of a second exciton. In the uninteresting case where the second exciton does not affect the homogeneous lineshape of biexciton fluorescence, the math linking the center peak autocorrelation to the biexciton binding energy is very straightforward (and reminiscent of that in Section 3.6).

Consider a sample that may be very polydisperse, but that exhibits a relatively consistent single-nanocrystal lineshape $\tilde{s}(\omega')$ and biexciton binding energy Δ. If the biexciton lineshape is identical to the exciton lineshape, then a single particle in the ensemble is characterized by its (potentially time-dependent) average exciton emission energy $\omega_0(t)$, its homogeneous exciton spectrum $s_x(\omega, t) = \delta(\omega - \omega_0(t)) \otimes \tilde{s}(\omega)$ and its homogeneous biexciton spectrum $s_{bx}(\omega, t) = \delta(\omega - \omega_0(t) - \Delta) \otimes \tilde{s}(\omega)$. In the average single-nanocrystal spectral correlation derived from the first side peak $p(\zeta, T_{rep})$, both photons are drawn from the excitonic spectrum of the same nanocrystal before and spectral dynamics can occur, and its value is given by,

$$p(\zeta, T_{rep}) = [\delta(\omega - \omega_0(t)) \otimes \tilde{s}(\omega)] \circ [\delta(\omega - \omega_0(t)) \otimes \tilde{s}(\omega)] \tag{9.30}$$

$$= \tilde{s}(\omega) \circ \tilde{s}(\omega). \tag{9.31}$$

In contrast, the average single-nanocrystal spectral correlation derived from the center peak $p(\zeta, 0)$ is still composed of photons pairs drawn from the same nanocrystal before spectral dynamics can occur, but now one of the photons is drawn from the biexcitonic spectrum and the other is drawn from the excitonic spectrum. The photon arrivals are time-ordered such that the biexciton photon arrives first, but there is no bias in which detector they arrive at and we integrate the value of the cross-correlation over both the positive and negative τ sides of the center peak. Therefore, the value of the center peak spectral correlation is given by,

$$
\begin{aligned}
p(\zeta, 0) =& \frac{1}{2}\left(s_x(\omega, t) \circ s_{bx}(\omega, t) + s_{bx}(\omega, t) \circ s_x(\omega, t)\right) && (9.32)\\
=& \frac{1}{2}\left[\delta(\omega - \omega_0(t)) \otimes \tilde{s}(\omega)\right] \circ \left[\delta(\omega - \omega_0(t) - \Delta) \otimes \tilde{s}(\omega)\right] \\
&+ \frac{1}{2}\left[\delta(\omega - \omega_0(t) - \Delta) \otimes \tilde{s}(\omega)\right] \circ \left[\delta(\omega - \omega_0(t)) \otimes \tilde{s}(\omega)\right] && (9.33)\\
=& \frac{1}{2}\left[\delta\left(\omega - \frac{\Delta}{2}\right) + \delta\left(\omega + \frac{\Delta}{2}\right)\right] \circ \left[\tilde{s}(\omega) \circ \tilde{s}(\omega)\right] && (9.34)\\
=& \frac{1}{2}\left[\delta\left(\omega - \frac{\Delta}{2}\right) + \delta\left(\omega + \frac{\Delta}{2}\right)\right] \circ p(\zeta, T_{rep}). && (9.35)
\end{aligned}
$$

In the case where the fluorescence lineshape is unaffected by biexciton formation, the spectral correlations of the center and side peaks are related by a single free parameter, which is the average biexciton binding energy we desire. And, because this parameter is closely linked to the difference in spectral correlation linewidth, it can be suprisingly easy to pick out the influence of the binding energy. In Figure 9-1, we show the center and side peak spectral correlations of a hypothetical sample with a 60 meV FWHM Gaussian linewidth and a 15 meV biexcitonic binding energy. Although harsh experimental conditions may make it difficult to pick out the shoulder of the spectrum at high flux caused by biexciton emission, the effect of the binding energy on the center peak spectral correlation is clear.

This model also gives us a starting point in the search for novel physics because

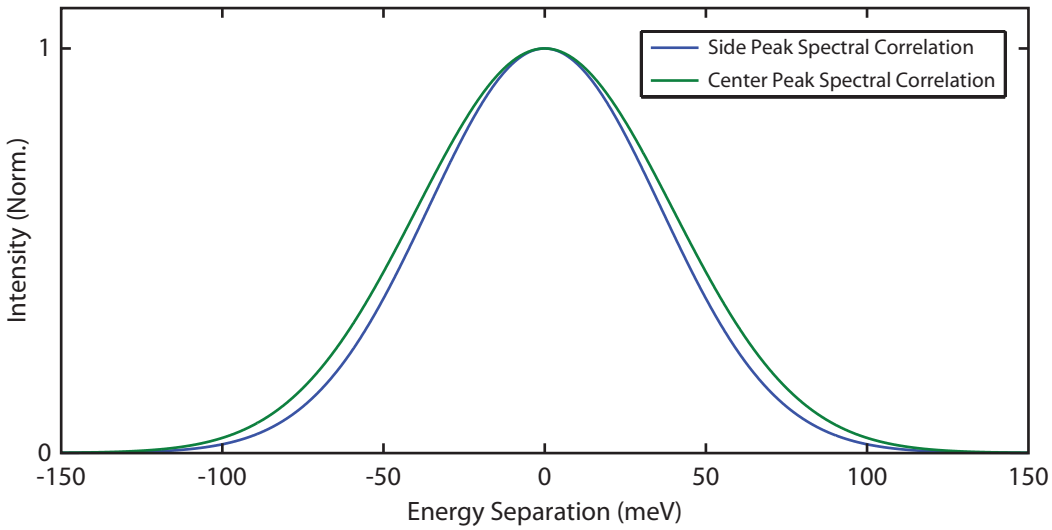

Figure 9-1: Spectral correlations corresponding to biexciton-exciton emission (center peak) and purely exciton emission (side peak) for a nanocrystal with a 60 meV FWHM Gaussian lineshape and a 15 meV biexcitonic binding energy. The biexciton binding energy causes the center peak spectral correlation to be 10% broader than the side-peak spectral correlation.

it has a clear failure condition. If this single free parameter is not enough to link the two spectral correlations (or if the binding energy is decidedly unphysical), something more complicated must be going on. For example if the one-parameter fit cannot capture the shape, it may suggest that there is variability in the biexciton binding energy between particles in the sample, and if center peak spectral correlation is narrower than the side peak spectral correlation (or it yields a suspiciously large binding energy), it may suggest that the lineshape of the biexciton is not the same as the exciton. By correlating the results of pulsed-excitation PCFS with temperature-dependent single-nanocrystal measurements of the biexciton binding energy, it should be possible to accurately determine the average biexciton binding energy of a sample at room temperature and to gain new insight into the subtle physics of biexciton fluorescence.

9.2.4 Outlook

The major drawback of this method is that it takes a very long time to measure the center and side peak spectral correlations with high signal-to-noise ratios. The basis experiment for the pulsed-excitation PCFS technique is the solution-phase $g^{(2)}$. In Figure 8-2, an hour-long solution-phase $g^{(2)}$ measurement on a well-behaved sample was used to measure a quantum yield ratio of $7.5\% \pm 1\%$. On an absolute scale, an uncertainty of 1% is fantastic, and exactly what we need to carefully evaluate small differences in the quantum yield ratio between samples. However, the goal of the pulsed-excitation PCFS experiment is to resolve the lineshape of the spectral correlation from the center peak, whose total signal magnitude is proportional to the quantum yield ratio of the sample. We are therefore more concerned with the relative uncertainty in the center peak value, which in these measurments, is over 10% and just barely enough to resolve the shape of the center peak spectral correlation. Not only will we require many of these hour-long integration times to sketch out the PCFS interferogram, but its value manifests as an anticorrelation feature within the coherence length of the emission. This means that our signal is actually a decrease in the number of correlation counts in the center peak, which in turn, means that we require *even longer* integration times to achieve high signal-to-noise ratios.

Certain provisions may be made to practically implement this technique. First, we could mainly focus on samples with relatively high biexciton quantum yields. Whereas the signal amplitude of solution-phase PCFS is only limited by the average occupancy of the focal volume and the quality of the interferometer alignment, the signal amplitude of the center peak spectral correlation (i.e. the piece of information we are particularly interested in) in pulsed-excitation PCFS is further modulated by the quantum yield. Samples with inherently high quantum yield rations like semiconductor nanoplatelets or CdSe/CdS heterostructures will be significantly easier to investigate. Second, we could use higher excitation flux. In pulsed-excitation PCFS,

we are no longer concerned about the absolute magnitude of the peak area ratio, so increased excitation flux may be used to violate our low-flux approximations and generate more biexciton photons. The main concerns are that we are no longer operating in the asymptotic regime, so our result will vary with excitation flux and we must maintain a very uniform excitation flux over the measurement, and the increased excitation flux may also generate signficant numbers of triexciton photons and cause significant biexciton bleed-through in the side peaks spectral correlations.[8] Ultimately, other techniques such as conventional single-nanocrystal spectroscopy (or even conventional spectroscopy in monodisperse samples), the spectrally-resolved transient approach of Cihan et al., [322] or the amplified spontaneous emission approach of Kelestemur et al. [323] may be more convenient techniques for measuring the average biexciton quantum yield.

9.3 Heterodyne-Detection Photon-Correlation Fourier Spectroscopy

9.3.1 Motivation and Background

In Section 3.7, we discussed that even though the spectral correlation may be the ideal and natural observable for studying spectral diffusion processes, it is a sub-optimal observable for measuring the underlying intrinsic spectrum of the emitter (or dilute solution of emitters). This is because critical phase information is lost when calculating the autocorrelation of the spectrum that would normally inform on the symmetry of the spectrum. There are an infinite set of spectra with roughly similar

[8] This will occur when the biexciton contribution to the total fluorescence spectrum becomes significant. If these conditions are required, conventional spectroscopy should be able to resolve the biexciton contribution, but pulsed-PCFS may still be a superior approach because its higher temporal resolution should suppress spectral diffusion effects. Modeling will be required to account for the influence of biexciton-exciton photon pairs in the side peak spectral correlation.

linewidths but varying lineshape asymmetry that are fully consistent with any given measured spectral autocorrelation, and it is mathematically impossible to determine a priori which of them is correct. Fundamentally, the problem is that PCFS is a homodyne measurement that compares the relative energy spacing between pairs of signal photons. PCFS can tell us that two signal photons are 15 meV apart, but it cannot tell us which one is higher energy nor can it tell us whether the pair of photons is more red or blue than usual. The solution is to design a PCFS experiment that relies on a heterodyne detection scheme, where the energies of photon pairs are not only measured with respect to each other, but also with respect to some external reference source with an arbitrarily narrow and constant spectrum.

9.3.2 Experimental

The observable of a heterodyne-detection PCFS experiment will have five independent variables: the energy separation between a reference photon and the first signal photon, the energy separation between the reference photon and the second signal photon, the temporal separation between the two signal photons, and the temporal separation between the two signal photons and their corresponding reference photons (which should be uninteresting on short timescales where there are no dither effects). The need for two independent spectral variables and three independent temporal variables requires that our measured quantity be a fourth-order correlation function of output channels from two interferometers. This will therefore be a much more complicated optical setup than that used for a standard PCFS experiment.

A schematic representation of a possible experimental setup (and the setup assumed for the derivation below) is shown in Figure 9-2. The signal is created using the same type of microscope as is used for the typical single-nanocrystal or solution-phase PCFS experiment. Then, the signal is split, fed through two different two-output interferometers, and incident on four detectors. Two of these channels are spectrally

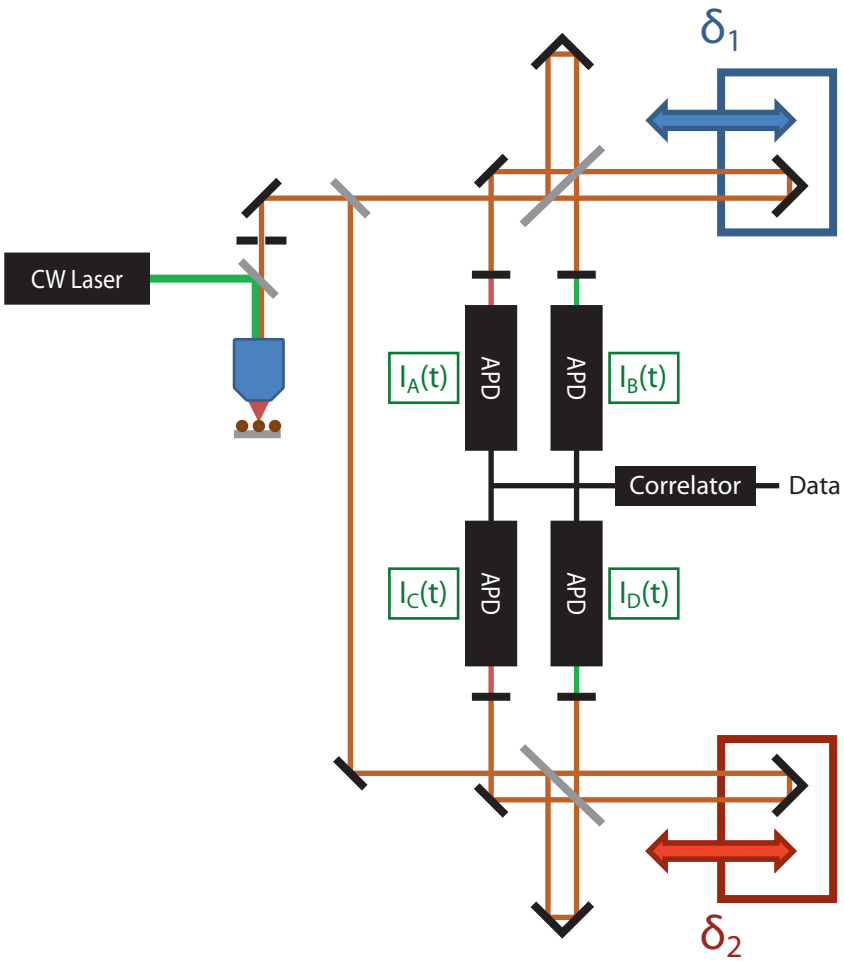

Figure 9-2: Schematic representation of the homodyne-PCFS experimental setup. Two nested interferometers are used to spectrally-resolve the energy shifts between the first and second, and second and third photons of three-photon arrival events in the third-order cross-correlation function.

filtered to accept only signal photons, while the other two channels are spectrally filtered to accept only reference photons (for convenience, in this case, we use the excitation source as the heterodyne reference). The experiment is carried out much in the same fashion as a standard PCFS experiment. The path-length differences of the interferometers are dithered over several fringes of both the reference and signal spectra to average over terms that are odd-order in the Fourier transform of their respective spectra. In order to maintain the phase relationship between the signal channels on the different interferometers, the dithers are synchronized such that the cross-correlation of any two channels can be accurately interpreted as a standard PCFS experiment. Then, the photon arrival times on all four channels are measured during a series of integration times that sample a discrete, evenly spaced two-dimensional array of the two interferometer path-length differences. This array is centered on the white fringes of the two interferometers with a path-length difference spacing small enough to resolve the beat frequency between the reference and signal, and an overall path-length difference range long enought to achieve the desired resolution after discrete Fourier transform. These photon arrivals are then used to calculate the corresponding fourth-order cross correlations and total signal autocorrelations in software.[9]

9.3.3 Theory

In this Section, we will present a prospective derivation of the heterodyne PCFS experiment for the setup described in Figure 9-2. This derivation will not address many of the finer details of implementing and interpreting such an experiment, but it will attempt to convey the broader picture of how such an experiment would theoretically work.

We begin by constructing expressions for the output intensity for the four outputs

[9]Some ingenuity will be required to measure the autocorrelations because we can no longer get an unbiased signal by adding the intensities on multiple channels.

of the pair of interferometers. If channels A and C are filtered to accept the signal and channels B and D are filtered to accept the laser for heterodyne detection, according to established interferometer theory,

$$I_A(\delta_1(t),t) = I(t)\left(1+\mathcal{F}_{\mathbf{cos}}[s(\omega,t)]_{\delta_1(t)}\right) \tag{9.36}$$

$$I_B(\delta_1(t),t) = I_L(t)\left(1-\cos(\omega_L\delta_1(t))\right) \tag{9.37}$$

$$I_C(\delta_2(t),t) = I(t)\left(1+\mathcal{F}_{\mathbf{cos}}[s(\omega,t)]_{\delta_2(t)}\right) \tag{9.38}$$

$$I_D(\delta_2(t),t) = I_L(t)\left(1-\cos(\omega_L\delta_2(t))\right), \tag{9.39}$$

where the signal is given by the intensity $I(t)$ and normalized spectrum $s(\omega,t)$ and the laser is given by the hopefully constant intensity $I_L(t)$ and the laser energy ω_L.

Using these intensity expressions, we can assemble a fourth-order cross-correlation function that will relate the energies of pairs of photons, each with respect to the constant laser energy. The ABCD cross-correlation is given by,

$$g^{(4)}_{ABCD}(\delta_{01},\delta_{02},\tau_1,\tau_2,\tau_3) = \frac{\left\langle I_A(\delta_1(t),t)I_B(\delta_1(t+\tau_1),t+\tau_1)I_C(\delta_2(t+\tau_2),t+\tau_2)I_D(\delta_2(t+\tau_3),t+\tau_3)\right\rangle}{\left\langle I_A(\delta_1(t),t)\right\rangle\left\langle I_B(\delta_1(t+\tau_1),t+\tau_1)\right\rangle\left\langle I_C(\delta_2(t+\tau_2),t+\tau_2)\right\rangle\left\langle I_D(\delta_2(t+\tau_3),t+\tau_3)\right\rangle} \tag{9.40}$$

This will clearly turn into a huge mess very quickly as we begin to insert the expressions from Equations 9.36-9.39 into Equation 9.40. Nevertheless, the mathematical steps we will follow are directly analogous to those used in the standard PCFS derivation in Chapter 3. First, we note that under the standard PCFS dither conditions, the denominator terms reduce to their respective average signal intensities, and because the spectral and intensity dynamics of the signal are presumed to be independent, we can separate the intensity component of the numerator average to isolate the effect of intensity fluctuations. This total intensity contribution is given

by,

$$= \frac{\big\langle I(t)I_L(t+\tau_1)I(t+\tau_2)I_L(t+\tau_3)\big\rangle}{\big\langle I(t)\big\rangle\big\langle I_L(t+\tau_1)\big\rangle\big\langle I(t+\tau_2)\big\rangle\big\langle I_L(t+\tau_3)\big\rangle}, \tag{9.41}$$

which can be simplified if the laser signal is Poissonian and does not drift over time to,

$$= \frac{\big\langle I(t)I(t+\tau_2)\big\rangle\big\langle I_L(t+\tau_1)\big\rangle\big\langle I_L(t+\tau_3)\big\rangle}{\big\langle I(t)\big\rangle\big\langle I_L(t+\tau_1)\big\rangle\big\langle I(t+\tau_2)\big\rangle\big\langle I_L(t+\tau_3)\big\rangle} \tag{9.42}$$

$$= g^{(2)}(\tau_2), \tag{9.43}$$

where $g^{(2)}(\tau)$ is the second-order correlation function of the signal intensity from the sample. As in the derivation of standard PCFS, after the intensity-component is removed, the remainder is a product of purely-spectral terms from each of the output channels with the form $1 + \mathcal{F}_{\mathbf{cos}}[s(\omega, t+\tau)]_{\delta(t)}$. When the product is expanded, all terms with odd numbers of spectral products average to zero due to the dither, leaving a constant term, six second-order terms, and one fourth-order term. That is,

$$\begin{aligned}
&g^{(4)}_{ABCD}(\delta_{01}, \delta_{02}, \tau_1, \tau_2, \tau_3) = \\
&g^{(2)}(\tau_2)\Big\langle 1 - \cos(\omega_L\delta_1(t+\tau_1))\mathcal{F}_{\mathbf{cos}}[s(\omega,t)]_{\delta_1(t)} + \mathcal{F}_{\mathbf{cos}}[s(\omega,t)]_{\delta_1(t)}\mathcal{F}_{\mathbf{cos}}[s(\omega,t+\tau_2)]_{\delta_2(t+\tau_2)} \\
&- \cos(\omega_L\delta_2(t+\tau_3))\mathcal{F}_{\mathbf{cos}}[s(\omega,t)]_{\delta_1(t)} - \cos(\omega_L\delta_1(t+\tau_1))\mathcal{F}_{\mathbf{cos}}[s(\omega,t+\tau_2)]_{\delta_2(t+\tau_2)} \\
&+ \cos(\omega_L\delta_1(t+\tau_1))\cos(\omega_L\delta_2(t+\tau_3)) - \cos(\omega_L\delta_2(t+\tau_3))\mathcal{F}_{\mathbf{cos}}[s(\omega,t)]_{\delta_2(t+\tau_2)} \\
&+ \cos(\omega_L\delta_1(t+\tau_1))\cos(\omega_L\delta_2(t+\tau_3))\mathcal{F}_{\mathbf{cos}}[s(\omega,t)]_{\delta_1(t)}\mathcal{F}_{\mathbf{cos}}[s(\omega,t+\tau_2)]_{\delta_2(t+\tau_2)}\Big\rangle.
\end{aligned} \tag{9.44}$$

We are interested in isolating and interpreting the fourth-order term, which contains the heterodyned spectral correlation we desire. The second-order terms can be accounted for by noting that because of the synchronized dither, cross-correlating any pair of channels on either interferometer should be equivalent to conducting a standard PCFS experiment. Each product of two spectral terms can be recast in

terms of the cross-correlation of their respective channels according to Equation 3.13 (noting that when both channels are sample signal, the autocorrelation of the sum signal may not be non-unity and must be accounted for). This process yields,

$$
\begin{aligned}
&g^{(4)}_{ABCD}(\delta_{01},\delta_{02},\tau_1,\tau_2,\tau_3) = \\
&g^{(2)}(\tau_2)\Big(-1 + g^{(2)}_{AB}(\delta_{01},\delta_{02},\tau_1) - \frac{g^{(2)}_{AC}(\delta_{01},\delta_{02},\tau_2)}{g^{(2)}(\tau_2)} + g^{(2)}_{AD}(\delta_{01},\delta_{02},\tau_3) \\
&+ g^{(2)}_{BC}(\delta_{01},\delta_{02},\tau_2-\tau_1) - g^{(2)}_{BD}(\delta_{01},\delta_{02},\tau_3-\tau_1) + g^{(2)}_{CD}(\delta_{01},\delta_{02},\tau_3-\tau_2) \\
&+ \Big\langle \cos(\omega_L\delta_1(t+\tau_1))\cos(\omega_L\delta_2(t+\tau_3))\mathcal{F}_{\mathbf{cos}}[s(\omega,t)]_{\delta_1(t)}\mathcal{F}_{\mathbf{cos}}[s(\omega,t+\tau_2)]_{\delta_2(t+\tau_2)}\Big\rangle\Big),
\end{aligned}
\tag{9.45}
$$

and gives us a way of calculating the value of the fourth-order term from the fourth-order intensity cross-cross-correlation, the second-order autocorrelation of the sample signal, and several output cross-correlations that can be simultaneously calculated alongside the fourth-order cross-correlation.

Our final order of buisiness is to unpack the fourth-order term. If we try to keep track of the dither as we did in the formal derivation of the standard PCFS experiment, this will become very complicated very fast. To keep this treatment on a higher level, we will take cues from the derivation in Chapter 3 and rephrase the cosine terms as cosine transforms of Dirac delta functions (notated by $L(\omega_L-\omega)$ because we already have too many δ floating around). This yields the following expression,

$$
\begin{aligned}
(4^{th}) = &\Big\langle \mathcal{F}_{\mathbf{cos}}[L(\omega_L-\omega)]_{\delta_1(t+\tau_1)}\mathcal{F}_{\mathbf{cos}}[L(\omega_L-\omega)]_{\delta_2(t+\tau_3)} \\
&\times \mathcal{F}_{\mathbf{cos}}[s(\omega,t)]_{\delta_1(t)}\mathcal{F}_{\mathbf{cos}}[s(\omega,t+\tau_2)]_{\delta_2(t+\tau_2)}\Big\rangle,
\end{aligned}
\tag{9.46}
$$

which is a product of two products of Fourier transforms, where each product is analogous to the right side of Equation 3.13 for its respective path-length difference variable (either $\delta_1(t)$ or $\delta_2(t)$). The two products are not independent because the

dithers of the two interferometers are synchronized,[10] but as long as we do not evaluate the time-average, we are still free to manipulate each product independently in the fashion of the derivation in Chapter 3. This time without involving the time average, we shift the dither into the integrand of the cosine transforms, rephrase each transform as sums or differences of the real and imaginary parts of Fourier transforms, combine the products with the convolution or cross-correlation theorems, merge terms by reforming the (co)sine transforms, and discard the spectral convolution terms as dithered away, yielding,

$$
\begin{aligned}
=\Big\langle \Big(& \mathcal{F}_{\mathbf{cos}}[\int_{-\infty}^{\infty} L(\omega_L-\omega)s(\omega+\zeta,t)\cos(\omega x(t)-(\omega+\zeta)x(t+\tau_1))\,\mathrm{d}\omega]_{\delta_{01}} \\
& + \mathcal{F}_{\mathbf{sin}}[\int_{-\infty}^{\infty} L(\omega_L-\omega)s(\omega+\zeta,t)\sin(\omega x(t)-(\omega+\zeta)x(t+\tau_1))\,\mathrm{d}\omega]_{\delta_{01}}\Big) \\
& \times \Big(\mathcal{F}_{\mathbf{cos}}[\int_{-\infty}^{\infty} L(\omega_L-\omega)s(\omega+\zeta,t+\tau_2)\cos(\omega x(t+\tau_2)-(\omega+\zeta)x(t+\tau_3))\,\mathrm{d}\omega]_{\delta_{02}} \\
& + \mathcal{F}_{\mathbf{sin}}[\int_{-\infty}^{\infty} L(\omega_L-\omega)s(\omega+\zeta,t+\tau_2)\sin(\omega x(t+\tau_2)-(\omega+\zeta)x(t+\tau_3))\,\mathrm{d}\omega]_{\delta_{02}}\Big)\Big\rangle.
\end{aligned}
\tag{9.47}
$$

If we paid careful attention to the dither component of the integrand, it would be possible to determine the values for $c(\tau)$ and $d(\tau)$ like we did in Chapter 3. However, guided by our discussion of the ideal dither in Section 3.2.2, we will simply assume that the relevant τ of interest are much faster than the dither and let $\delta(t+\tau) \approx \delta(t)$. As long as the average energies of the laser and signal are much greater than the linewidth of the spectral correlation of the laser and the signal (i.e. the laser and signal are relatively close together in energy), the cosine terms will reduce to unity and the sine terms will vanish (as they did in Section 3.2.2), leaving,

[10] This is important, because otherwise the time average could be distributed, yielding ensemble (or time-averaged) spectra.

$$
\begin{aligned}
(4^{th}) =& \Big\langle \mathcal{F}_{\mathbf{cos}}[\int_{-\infty}^{\infty} L(\omega_L - \omega) s(\omega + \zeta, t)\, \mathrm{d}\omega]_{\delta_{01}} \\
& \times \mathcal{F}_{\mathbf{cos}}[\int_{-\infty}^{\infty} L(\omega_L - \omega) s(\omega + \zeta, t + \tau_2)\, \mathrm{d}\omega]_{\delta_{02}} \Big\rangle && (9.48) \\
=& \Big\langle \mathcal{F}_{\mathbf{cos}}[L(\omega_L - \omega) \circ s(\omega, t)]_{\delta_{01}} \mathcal{F}_{\mathbf{cos}}[L(\omega_L - \omega) \circ s(\omega, t + \tau_2)]_{\delta_{02}} \Big\rangle && (9.49) \\
=& \int_{-\infty}^{\infty} \int_{-\infty}^{\infty} \Big\langle p_L(\zeta_1, t) p_L(\zeta_2, t + \tau_2) \Big\rangle \cos(\zeta_1 \delta_{01}) \cos(\zeta_2 \delta_{02})\, \mathrm{d}\zeta_1\, \mathrm{d}\zeta_2, && (9.50)
\end{aligned}
$$

where $p_L(\zeta_1, \tau)$ represents the spectral correlation of each signal photon on channel A with the laser reference (integrated over all laser-signal photon pair τ much less than the dither because the laser reference is static) and where $p_L(\zeta_2, \tau)$ represents the heterodyned spectral correlation of each signal photon on channel C with the laser reference (integrated over all laser-signal photon pair τ much less than the dither because the laser reference is static), for all signal photons that arrived τ_2 *after* the corresponding count on channel A.

Equation 9.50 represents the double cosine transform of the heterodyned spectral correlation,

$$
p_H(\zeta_1, \zeta_2, \tau_2) = p_L(\zeta_1, t) p_L(\zeta_2, t + \tau_2), \tag{9.51}
$$

which represents the probability distribution function that if a pair of signal photons arrive with temporal spacing τ_2, then the first photon has energy ζ_1 with respect to the laser reference and the second photon has energy ζ_2 with respect to the laser reference. Because we know the absolute energy of the laser reference, this two dimensional probability distribution gives us an absolute energy mapping for the spectrum before and after a given waiting τ_2 that can be interpreted in a fashion very similar to data produced by 2D ultrafast spectroscopies. Broadening along the diagonal is related to the degree of inhomogeneous broadening (or the width of the time-averaged spectrum), broadening along the antidiagonal is related to homogeneous broadening,

and the evolution of the contour map with waiting time is related to spectral diffusion on that timescale.

There are a couple of details that we have skimmed over, which are particularly worth emphasizing. First, note that although the fourth-order correlation function has three temporal variables corresponding to the temporal separations between the four photon arrival events in a coincidence count, the physical observable only has one temporal variable corresponding to the temporal separation between the two signal photons. This is a critical point because as T.S. Bischof has noted in his higher-order correlation work, even with relatively healthy signal intensities, four-photon coincidence events are quite rare and difficult to collect with good signal-to-noise. We benefit in this experiment from the fact that because the laser reference is static, the correlation function should be constant over temporal variables relating the signal and reference photon arrivals. Without loss of information, we can integrate over a wide range of those τ to improve our signal-to-noise and to effectively reduce the dimensionality of the measured correlation function. Second, as long as we have arbitrarily large electronic storage space, we are free to improve the signal-to-noise ratio of the experiment by increasing the count rate on the reference channels. In fact, it is worth pointing out that the main role of the reference channels in the mathemetics of the derivation is to report on the absolute path-length-difference at any given signal photon arrival. With some experimental and mathematical cleverness, it may be possible to replace the reference channels with absolute stage-positioning information, thereby reducing the observable to a manageable second-order correlation function. Third, it is important to keep in mind that the heterodyne PCFS experiment is subject to the same instrument function concerns as the standard PCFS experiment. The bandwidth of the heterodyned spectral correlation is defined by the dither, and if the reference wavelength is too far from the signal wavelength, it will be distorted or averaged away by the dither. And finally, this heterodyne experiment is entirely

compatible with the ensemble-averaged, solution-phase treatment we have required in order to implement long integration time experiments.

9.3.4 Outlook

The heterodyne PCFS experiment is a remarkably more complicated and difficult experiment than we are currently implementing in our group right now, both from a conceptual and experimental standpoint. However, there are two major reasons why it might be worth pursuing in future work. It addresses the major drawback of the standard PCFS experiment, namely that the PCFS spectral correlation does not contain the phase information necessary to extract the lineshape or asymmetry of the intrinsic spectrum or probability distribution function of spectral dynamics. And, it provides a useful conceptual bridge between the the current state of photon correlation experiments and the ongoing development and application of multi-dimensional ultrafast spectroscopies. If there is a system with particularly asymmetric spectral dynamics or for which an absolute measurement of the underlying spectrum is essential, heterodyne PCFS may very well be the ideal tool.

Bibliography

[1] StatNano.com. Top 20 countries in production of nanoscience. `http://statnano.com/news/48147`, Jan 2015. Accessed 01/06/2015.

[2] Jamie Ford, Seth R. Marder, and Shu Yang. Growing "nanofruit" textures on photo-crosslinked SU-8 surfaces through layer-by-layer grafting of hyperbranched poly(ethyleneimine). *Chem. Mater.*, 21:476–483, 2009.

[3] Masih Darbandi, Tesfaye Gebre, Lucas Mitchell, William Erwin, Rizia Bardhan, M. Douglas Levan, Mogus D. Mochena, and James H. Dickerson. Nanoporous TiO_2 nanoparticle assemblies with mesoscale morphologies: nano-cabbage versus sea-anemone. *Nanoscale*, 6:5652–5656, 2014.

[4] Peter Chhour, Nicolas Gallo, Rabee Cheheltani, Dewight Williams, Ajlan Al-Zaki, Taejong Paik, Jessica L. Nichol, Zhicheng Tian, Pratap C. Naha, Walter R. Witschey, Harry R. Allcock, Christopher B. Murray, Andrew Tsourkas, and David P. Cormode. Nanodisco balls: Control over surface versus core loading of diagnostically active nanocrystals into polymer nanoparticles. *ACS Nano*, 8:9143–9153, 2014.

[5] Gabor A. Somerjai and Yimin Li. *Introduction to Surface Chemistry and Catalysis*. John Wiley & Sons, 2nd edition edition, 2010.

[6] Harald Hoppe and Niyazi Serdar Sariciftci. Morphology of polymer/fullerene bulk heterojunction solar cells. *J. Mater. Chem.*, 16:45–61, 2006.

[7] Michael Gratzel. Perspectives for dye-sensitized nanocrystalline solar cells. *Prog. Photovolt.*, 8:171–185, 2000.

[8] Neil W. Ashcroft and N. David Mermin. *Solid State Physics*. Brooks/Cole, Cengage Learning, 1976.

[9] Alexander L. Efros and M. Rosen. The electronic structure of semiconductor nanocrystals. *Annu. Rev. Mater. Sci.*, 30:475–521, 2000.

[10] Miguel A. García. Surface plasmons in metallic nanoparticles: fundamentals and applications. *J. Phys. D: Appl. Phys.*, 44:283001, 2011.

[11] Hans-Joachim Böhm, David Banner, Stefanie Bendels, Manfred Kansy, Bernd Kuhn, Klaus Müller, Ulrike Obst-Sander, and Martin Stahl. Fluorine in medicinal chemistry. *ChemBioChem*, 5:637–643, 2004.

[12] Younan Xia, Hong Yang, and Charles T. Campbell. Nanoparticles for catalysis. *Acc. Chem. Res.*, 46:1671–1672, 2013.

[13] Abe D. Yoffe. Low-dimensional systems: quantum size effects and electronic properties of semiconductor microcrystallites (zero-dimensional systems) and some quasi-two-dimensional systems. *Adv. Phys.*, 42:173–262, 1993.

[14] Juh-Tzeng Lue. A review of characterization and physical property studies of metallic nanoparticles. *J. Phys. Chem. Solids*, 62:1599–1612, 2001.

[15] Timothy E. Barder, Shawn D. Walker, Joseph R. Martinelli, and Stephen L. Buchwald. Catalysts for Suzuki–Miyaura coupling processes: Scope and studies of the effect of ligand structure. *J. Am. Chem. Soc.*, 127:4685–4696, 2005.

[16] Didier Astruc, Feng Lu, and Jaime Ruiz Aranzaes. Nanoparticles as recyclable catalysts: The frontier between homogeneous and heterogeneous catalysis. *Angew. Chem. Int. Ed.*, 44:7852–7872, 2005.

[17] Jeff Grunes, Ji Zhu, and Gabor A. Somorjai. Catalysis and nanoscience. *Chem. Commun.*, (18):2257–2260, 2003.

[18] Wenhao Liu, Andrew B. Greytak, Jungmin Lee, Cliff R. Wong, Jongnam Park, Lisa F. Marshall, Wen Jiang, Peter N. Curtin, Alice Y. Ting, Daniel G. Nocera, Dai Fukumura, Rakesh K. Jain, and Moungi G. Bawendi. Compact biocompatible quantum dots via RAFT-mediated synthesis of imidazole-based random copolymer ligand. *J. Am. Chem. Soc.*, 132:472–483, 2010.

[19] Ou Chen, Lars Riedemann, Fred Etoc, Hendrik Herrmann, Mathieu Coppey, Mariya Barch, Christian T. Farrar, Jing Zhao, Oliver T. Bruns, He Wei, Peng Guo, Jian Cui, Russ Jensen, Yue Chen, Daniel K. Harris, Jose M. Cordero, Zhongwu Wang, Alan Jasanoff, Dai Fukumura, Rudolph Reimer, Maxime Dahan, Rakesh K. Jain, and Moungi G. Bawendi. Magneto-fluorescent core-shell supernanoparticles. *Nat. Commun.*, 5:5093, 2014.

[20] Cliff Wong, Triantafyllos Stylianopoulos, Jian Cui, John Martin, Vikash P. Chauhan, Wen Jiang, Zoran Popović, Rakesh K. Jain, Moungi G. Bawendi, and Dai Fukumura. Multistage nanoparticle delivery system for deep penetration into tumor tissue. *Proc. Nat. Acad. Sci. U.S.A.*, 108:2426–2431, 2011.

[21] Triantafyllos Stylianopoulos, Cliff Wong, Moungi G. Bawendi, Rakesh K. Jain, and Dai Fukumura. Chapter six – multistage nanoparticles for improved delivery into tumor tissue. In *Nanomedicine Cancer, Diabetes, and Cardiovascular, Central Nervous System, Pulmonary and Inflammatory Diseases*, volume 508 of *Methods in Enzymology*, pages 109 – 130. Academic Press, 2012.

[22] Galen D. Stucky and James E. Mac Dougall. Quantum confinement and host/guest chemistry: Probing a new dimension. *Science*, 247:669–678, 1990.

[23] Gordon E. Moore. Cramming more components onto integrated circuits. *Electronics*, 38:114–117, 1965.

[24] Raymond Dingle, William Wiegmann, and Charles H. Henry. Quantum states of confined carriers in very thin $Al_xGa_{1-x}As-GaAs-Al_xGa_{1-x}As$ heterostructures. *Phys. Rev. Lett.*, 33:827–830, 1974.

[25] John C. Slater. Electrons in perturbed periodic lattices. *Phys. Rev.*, 76:1592–1601, 1949.

[26] Mark Lundstrom. *Fundamentals of Carrier Transport*. Cambridge University Press, second edition, 2000.

[27] Zhores I. Alferov. The history and future of semiconductor heterostructures. *Semiconductors*, 32:1–14, 1998.

[28] David A. B. Miller. Optoelectronic applications of quantum wells. *Opt. Photon. News*, 1:7–15, 1990.

[29] M. A. Reed, J. N. Randall, R. J. Aggarwal, R. J. Matyi, T. M. Moore, and A. E. Wetsel. Observation of discrete electronic states in a zero-dimensional semiconductor nanostructure. *Phys. Rev. Lett.*, 60:535–537, Feb 1988.

[30] D. Leonard, M. Krishnamurthy, C. M. Reaves, Steven P. DenBaars, and Pierre M. Petroff. Direct formation of quantum-sized dots from uniform coherent islands of InGaAs on GaAs surfaces. *Appl. Phys. Lett.*, 63:3203–3205, 1993.

[31] Alexey I. Ekimov and Alexei A. Onushchenko. Quantum size effect in three-dimensional microscopic semiconductor crystals. *JETP Lett.*, 34:345, 1982.

[32] Horst Weller, U. Koch, M. Gutiérrez, and Arnim Henglein. Photochemistry of colloidal metal sulfides. 7. absorption and fluorescence of extremely small ZnS particles (the world of the neglected dimensions). *Ber. Bunsenges. Phys. Chem.*, 88:649–656, 1984.

[33] Anton Fojtík, Horst Weller, U Koch, and Arnim Henglein. Photo-chemistry of colloidal metal sulfides 8. photo-physics of extremely small CdS particles: Q-state CdS and magic agglomeration numbers. *Ber. Bunsenges. Phys. Chem.*, 88:969–977, 1984.

[34] Horst Weller, Anton Fojtik, and Arnim Henglein. Photochemistry of semiconductor colloids: Properties of extremely small particles of Cd_3P_2 and Zn_3P_2. *Chem. Phys. Lett.*, 117:485–488, 1985.

[35] Anton Fojtík, Horst Weller, and Arnim Henglein. Photochemistry of semiconductor colloids. size quantization effects in Q-cadmium arsenide. *Chem. Phys. Lett.*, 120:552–554, 1985.

[36] R. Rossetti, S. Nakahara, and Louis E. Brus. Quantum size effects in the redox potentials, resonance Raman spectra, and electronic spectra of CdS crystallites in aqueous solution. *J. Chem. Phys.*, 79:1086–1088, 1983.

[37] R. Rossetti, J. L. Ellison, J. M. Gibson, and Louis E. Brus. Size effects in the excited electronic states of small colloidal CdS crystallites. *J. Chem. Phys.*, 80:4464–4469, 1984.

[38] R. Rossetti, R. Hull, J. M. Gibson, and Louis E. Brus. Excited electronic states and optical spectra of ZnS and CdS crystallites in the 15åto 50åsize range: Evolution from molecular to bulk semiconducting properties. *J. Chem. Phys.*, 82:552–559, 1985.

[39] Panagiotis Lianos and J. Kerry Thomas. Cadmium sulfide of small dimensions produced in inverted micelles. *Chem. Phys. Lett.*, 125:299–302, 1986.

[40] Ying Wang and Norman Herron. Optical properties of cadmium sulfide and lead(II) sulfide clusters encapsulated in zeolites. *J. Phys. Chem.*, 91:257–260, 1987.

[41] Janos H. Fendler. Atomic and molecular clusters in membrane mimetic chemistry. *Chem. Rev.*, 87:877–899, 1987.

[42] Michael L. Steigerwald, A. Paul Alivisatos, J. M. Gibson, T. D. Harris, R. Kortan, A. J. Muller, A. M. Thayer, T. M. Duncan, D. C. Douglass, and Louis E. Brus. Surface derivatization and isolation of semiconductor cluster molecules. *J. Am. Chem. Soc.*, 110:3046–3050, 1988.

[43] Christopher B. Murray, David J. Norris, and Moungi G. Bawendi. Synthesis and characterization of nearly monodisperse CdE (E = sulfur, selenium, tellurium) semiconductor nanocrystallites. *J. Am. Chem. Soc.*, 115:8706–8715, 1993.

[44] Joaquin M. Luttinger and Walter Kohn. Motion of electrons and holes in perturbed periodic fields. *Phys. Rev.*, 97:869–883, 1955.

[45] Carl R. Pidgeon and R. N. Brown. Interband magneto-absorption and faraday rotation in InSb. *Phys. Rev.*, 146:575–583, 1966.

[46] Alexey I. Ekimov, Alexander L. Efros, and Alexei A. Onushchenko. Quantum size effect in semiconductor microcrystals. *Solid State Commun.*, 56:921–924, 1985.

[47] Alexey I. Ekimov, I. A. Kudryavtsev, Alexander L. Efros, T. V. Yazeva, F. Hache, M. C. Schanne-Klein, Anna V. Rodina, D. Ricard, and C. Flytzanis. Absorption and intensity-dependent photoluminescence measurements on CdSe

quantum dots: assignment of the first electronic transitions. *J. Opt. Soc. Am. B*, 10:100–107, 1993.

[48] Alexander L. Efros and Anna V. Rodina. Band-edge absorption and luminescence of nonspherical nanometer-size crystals. *Phys. Rev. B*, 47:10005–10007, 1993.

[49] Alexander L. Efros. Luminescence polarization of CdSe microcrystals. *Phys. Rev. B*, 46:7448–7458, 1992.

[50] Manoj Nirmal, David J. Norris, Masaru Kuno, Moungi G. Bawendi, Alexander L. Efros, and M. Rosen. Observation of the "dark exciton" in CdSe quantum dots. *Phys. Rev. Lett.*, 75:3728–3731, 1995.

[51] Alexander L. Efros, M. Rosen, Masaru Kuno, Manoj Nirmal, David J. Norris, and Moungi G. Bawendi. Band-edge exciton in quantum dots of semiconductors with a degenerate valence band: Dark and bright exciton states. *Phys. Rev. B*, 54:4843–4856, 1996.

[52] David J. Norris, Alexander L. Efros, M. Rosen, and Moungi G. Bawendi. Size dependence of exciton fine structure in CdSe quantum dots. *Phys. Rev. B*, 53:16347–16354, 1996.

[53] Mark J. Fernée, Philippe Tamarat, and Brahim Lounis. Spectroscopy of single nanocrystals. *Chem. Soc. Rev.*, 43:1311–1337, 2014.

[54] Chiara Sinito, Mark J. Fernée, Serguei V. Goupalov, Paul Mulvaney, Philippe Tamarat, and Brahim Lounis. Tailoring the exciton fine structure of cadmium selenide nanocrystals with shape anisotropy and magnetic field. *ACS Nano*, 8:11651–11656, 2014.

[55] T. Dannhauser, M. O'Neil, K. Johansson, D. Whitten, and G. McLendon. Photophysics of quantized colloidal semiconductors. dramatic luminescence enhancement by binding of simple amines. *J. Phys. Chem.*, 90:6074–6076, 1986.

[56] Arnim Henglein. Mechanism of reactions on colloidal microelectrodes and size quantization effects. In E. Steckhan, editor, *Electrochemistry II*, volume 143 of *Topics in Current Chemistry*, pages 113–180. Springer Berlin Heidelberg, 1988.

[57] N. Chestnoy, T. David Harris, Robert Hull, and Louis E. Brus. Luminescence and photophysics of cadmium sulfide semiconductor clusters: the nature of the emitting electronic state. *J. Phys. Chem.*, 90:3393–3399, 1986.

[58] Louis E. Brus. Electronic wave functions in semiconductor clusters: experiment and theory. *J. Phys. Chem.*, 90:2555–2560, 1986.

[59] Peter C. Sercel, Alexander L Efros, and M. Rosen. Intrinsic gap states in semiconductor nanocrystals. *Phys. Rev. Lett.*, 83:2394–2397, 1999.

[60] Moungi G. Bawendi, Michael L. Steigerwald, and Louis E. Brus. The quantum mechanics of larger semiconductor clusters ("quantum dot"). *Annu. Rev. Phys. Chem.*, 41:477–496, 1990.

[61] Manoj Nirmal, Bashir O. Dabbousi, Moungi G. Bawendi, J. J. Macklin, J. K. Trautman, T. D. Harris, and Louis E. Brus. Fluorescence intermittency in single cadmium selenide nanocrystals. *Nature*, 383:802–804, 1996.

[62] Masaru Kuno, David P. Fromm, Hendrik F. Hamann, Allan C. Gallagher, and David J. Nesbitt. Nonexponential blinking kinetics of single CdSe quantum dots: A universal power law behavior. *J. Chem. Phys.*, 112:3117–3120, 2000.

[63] Stephen A. Empedocles and Moungi G. Bawendi. Quantum-confined stark effect in single CdSe nanocrystallite quantum dots. *Science*, 278:2114–2117, 1997.

[64] Stephen A. Empedocles and Moungi G. Bawendi. Influence of spectral diffusion on the line shapes of single CdSe nanocrystallite quantum dots. *J. Phys. Chem. B*, 103:1826–1830, 1999.

[65] Ken T. Shimizu, Robert G. Neuhauser, Catherine A. Leatherdale, Stephen A. Empedocles, W. K. Woo, and Moungi G. Bawendi. Blinking statistics in single semiconductor nanocrystal quantum dots. *Phys. Rev. B*, 63:205316, 2001.

[66] Alexander L. Efros and M. Rosen. Random telegraph signal in the photoluminescence intensity of a single quantum dot. *Phys. Rev. Lett.*, 78:1110–1113, 1997.

[67] Rogier Verberk, Antoine M. van Oijen, and Michel Orrit. Simple model for the power-law blinking of single semiconductor nanocrystals. *Phys. Rev. B*, 66:233202, 2002.

[68] Jau Tang and Rudolph A. Marcus. Diffusion-controlled electron transfer processes and power-law statistics of fluorescence intermittency of nanoparticles. *Phys. Rev. Lett.*, 95:107401, 2005.

[69] Pavel A. Frantsuzov and Rudolph A. Marcus. Explanation of quantum dot blinking without the long-lived trap hypothesis. *Phys. Rev. B*, 72:155321, 2005.

[70] Pavel Frantsuzov, Masaru Kuno, Boldizsár Jankó, and Rudolph A. Marcus. Universal emission intermittency in quantum dots, nanorods and nanowires. *Nature Phys.*, 4:519–522, 2008.

[71] Daniel E. Gómez, Marco Califano, and Paul Mulvaney. Optical properties of single semiconductor nanocrystals. *Phys. Chem. Chem. Phys.*, 8:4989–5011, 2006.

[72] Simone Pokrant and K. Birgitta Whaley. Tight-binding studies of surface effects on electronic structure of CdSe nanocrystals: the role of organic ligands, surface reconstruction, and inorganic capping shells. *Eur. Phys. J. D*, 6:255–267, 1999.

[73] Garnett W. Bryant and W. Jaskolski. Surface effects on capped and uncapped nanocrystals. *J. Phys. Chem. B*, 109:19650–19656, 2005.

[74] José G. Díaz, Michał Zieliński, Wlodzimierz Jaskólski, and Garnett W. Bryant. Tight-binding theory of ZnS/CdS nanoscale heterostructures: Role of strain and *d* orbitals. *Phys. Rev. B*, 74:205309, 2006.

[75] José G. Díaz, Garnett W. Bryant, and Wlodzimierz Jaskólski. Optical fine structure of II-VI and III-V nanocrystals: the role of d orbitals in a tight-binding approach. *Phys. Status Solidi C*, 3:3823–3826, 2006.

[76] Lin-Wang Wang and Alex Zunger. Pseudopotential calculations of nanoscale CdSe quantum dots. *Phys. Rev. B*, 53:9579–9582, 1996.

[77] James C. Phillips and Leonard Kleinman. New method for calculating wave functions in crystals and molecules. *Phys. Rev.*, 116:287–294, 1959.

[78] Alex Zunger. Pseudopotential theory of semiconductor quantum dots. *Phys. Status Solidi B*, 224:727–734, 2001.

[79] Oleksandr Voznyy. Mobile surface traps in CdSe nanocrystals with carboxylic acid ligands. *J. Phys. Chem. C*, 115:15927–15932, 2011.

[80] Jingbo Li and Lin-Wang Wang. First principle study of core/shell structure quantum dots. *Appl. Phys. Lett.*, 84:3648–3650, 2004.

[81] Johannes Frenzel, Jan-Ole Joswig, Pranab Sarkar, Gotthard Seifert, and Michael Springborg. The effects of organisation, embedding and surfactants on the properties of cadmium chalcogenide (CdS, CdSe and CdS/CdSe) semiconductor nanoparticles. *Eur. J. Inorg. Chem.*, 2005:3585–3596, 2005.

[82] Sean A. Fischer, Angela M. Crotty, Svetlana V. Kilina, Sergei A. Ivanov, and Sergei Tretiak. Passivating ligand and solvent contributions to the electronic properties of semiconductor nanocrystals. *Nanoscale*, 4:904–914, 2012.

[83] Ahmed M. Abuelela, Tarek A. Mohamed, and Oleg V. Prezhdo. DFT simulation and vibrational analysis of the IR and Raman spectra of a CdSe quantum dot capped by methylamine and trimethylphosphine oxide ligands. *J. Phys. Chem. C*, 116:14674–14681, 2012.

[84] Oleksandr Voznyy and Edward H. Sargent. Atomistic model of fluorescence intermittency of colloidal quantum dots. *Phys. Rev. Lett.*, 112:157401, 2014.

[85] Amanda J. Neukirch, Kim Hyeon-Deuk, and Oleg V. Prezhdo. Time-domain ab initio modeling of excitation dynamics in quantum dots. *Coord. Chem. Rev.*, 263–264:161–181, 2014.

[86] Ou Chen, Xian Chen, Yongan Yang, Jared Lynch, Huimeng Wu, Jiaqi Zhuang, and Y. Charles Cao. Synthesis of metal selenide nanocrystals using selenium dioxide as the selenium precursor. *Angew. Chem. Int. Ed.*, 47:8638, 2008.

[87] Y. Charles Cao and Jianhui Wang. One-pot synthesis of high-quality zinc-blende CdS nanocrystals. *J. Am. Chem. Soc.*, 126:14336–14337, 2004.

[88] Yongan Andrew Yang, Huimeng Wu, Kathryn R. Williams, and Y. Charles Cao. Synthesis of CdSe and CdTe nanocrystals without precursor injection. *Angew. Chem. Int. Ed.*, 44:6712–6715, 2005.

[89] Jonathan S. Owen, Emory M. Chan, Haitao Liu, and A. Paul Alivisatos. Precursor conversion kinetics and the nucleation of cadmium selenide nanocrystals. *J. Am. Chem. Soc.*, 132:18206–18213, 2010.

[90] Mark P. Hendricks, Michael P. Campos, Gregory T. Cleveland, Ilan Jen-La Plante, and Jonathan S. Owen. A tunable library of substituted thiourea precursors to metal sulfide nanocrystals. *Science*, 348:1226–1230, 2015.

[91] Dingan Chen, Fei Zhao, Hang Qi, Michael Rutherford, and Xiaogang Peng. Bright and stable purple/blue emitting CdS/ZnS core/shell nanocrystals grown by thermal cycling using a single-source precursor. *Chem. Mater.*, 22:1437–1444, 2010.

[92] Hongbo Li, Rosaria Brescia, Roman Krahne, Giovanni Bertoni, Marcelo J. P. Alcocer, Cosimo D'Andrea, Francesco Scotognella, Francesco Tassone, Marco Zanella, Milena De Giorgi, and Liberato Manna. Blue-uv-emitting ZnSe(dot)/ZnS(rod) core/shell nanocrystals prepared from CdSe/CdS nanocrystals by sequential cation exchange. *ACS Nano*, 6:1637–1647, 2012.

[93] Renguo Xie, David Battaglia, and Xiaogang Peng. Colloidal InP nanocrystals as efficient emitters covering blue to near-infrared. *J. Am. Chem. Soc.*, 129:15432–15433, 2007.

[94] Benjamin F. P. McVey and Richard D. Tilley. Solution synthesis, optical properties, and bioimaging applications of silicon nanocrystals. *Acc. Chem. Res.*, 47:3045–3051, 2014.

[95] Huiying Fu and Sai-Wing Tsang. Infrared colloidal lead chalcogenide nanocrystals: Synthesis, properties, and photovoltaic applications. *Nanoscale*, 4:2187–2201, 2012.

[96] Daniel K. Harris and Moungi G. Bawendi. Improved precursor chemistry for the synthesis of III-V quantum dots. *J. Am. Chem. Soc.*, 134:20211–20213, 2012.

[97] Daniel K. Harris, Peter M. Allen, Hee-Sun Han, Brian J. Walker, Jungmin Lee, and Moungi G. Bawendi. Synthesis of cadmium arsenide quantum dots luminescent in the infrared. *J. Am. Chem. Soc.*, 133:4676–4679, 2011.

[98] Emmanuel Lhuillier, Sean Keuleyan, Heng Liu, and Philippe Guyot-Sionnest. Mid-IR colloidal nanocrystals. *Chem. Mater.*, 25:1272–1282, 2013.

[99] Dylan C. Gary, Benjamin A. Glassy, and Brandi M. Cossairt. Investigation of indium phosphide quantum dot nucleation and growth utilizing triarylsilylphosphine precursors. *Chem. Mater.*, 26:1734–1744, 2014.

[100] A. R. Kortan, R. Hull, Robert L. Opila, Moungi G. Bawendi, Michael L. Steigerwald, P. J. Carroll, and Louis E. Brus. Nucleation and growth of cadmium selendie on zinc sulfide quantum crystallite seeds, and vice versa, in inverse micelle media. *J. Am. Chem. Soc.*, 112:1327–1332, 1990.

[101] Michal Danek, Klavs F. Jensen, Chris B. Murray, and Moungi G. Bawendi. Synthesis of luminescent thin-film CdSe/ZnSe quantum dot composites using CdSe quantum dots passivated with an overlayer of ZnSe. *Chem. Mater.*, 8:173–180, 1996.

[102] Margaret A. Hines and Philippe Guyot-Sionnest. Synthesis and characterization of strongly luminescing ZnS-capped CdSe nanocrystals. *J. Phys. Chem.*, 100:468–471, 1996.

[103] Bashir O. Dabbousi, Javier Rodriguez-Viejo, Frederic V. Mikulec, Jason R. Heine, Hedi Mattoussi, Raymond Ober, Klavs F. Jensen, and Moungi G. Bawendi. (CdSe)ZnS core–shell quantum dots: Synthesis and characterization of a size series of highly luminescent nanocrystallites. *J. Phys. Chem. B*, 101:9463–9475, 1997.

[104] Wilfried G. J. H. M. van Sark, Patrick L. T. M. Frederix, Ageeth A. Bol, Hans C. Gerritsen, and Andries Meijerink. Blueing, bleaching, and blinking of single CdSe/ZnS quantum dots. *ChemPhysChem*, 3:871–879, 2002.

[105] Xiaogang Peng, Michael C. Schlamp, Andreas V. Kadavanich, and A. Paul Alivisatos. Epitaxial growth of highly luminescent CdSe/CdS core/shell nanocrystals with photostability and electronic accessibility. *J. Am. Chem. Soc.*, 119:7019–7029, 1997.

[106] Ou Chen, Jing Zhao, Vikash P. Chauhan, Jian Cui, Cliff Wong, Daniel K. Harris, He Wei, Hee-Sun Han, Dai Fukumura, Rakesh K. Jain, and Moungi Bawendi. Compact high-quality CdSe-CdS core-shell nanocrystals with narrow emission linewidths and suppressed blinking. *Nature Mater.*, 12:445–451, 2013.

[107] Yongfen Chen, Javier Vela, Han Htoon, Joanna L. Casson, Donald J. Werder, David A. Bussian, Victor I. Klimov, and Jennifer A. Hollingsworth. "giant" multishell CdSe nanocrystal quantum dots with suppressed blinking. *J. Am. Chem. Soc.*, 130:5026–5027, 2008.

[108] Christophe Galland, Yagnaseni Ghosh, Andrea Steinbruck, Jennifer A. Hollingsworth, Han Htoon, and Victor I. Klimov. Lifetime blinking in non-blinking nanocrystal quantum dots. *Nat. Commun.*, 3:908, 2012.

[109] Michel Nasilowski, Piernicola Spinicelli, Gilles Patriarche, and Benoit Dubertret. Gradient CdSe/CdS quantum dots with room temperature biexciton unity quantum yield. *Nano Lett.*, 15:3953–3958, 2015.

[110] Dmitri V. Talapin, Ivo Mekis, Stephan Gotzinger, Andreas Kornowski, Oliver Benson, and Horst Weller. CdSe/CdS/ZnS and CdSe/ZnSe/ZnS core–shell–shell nanocrystals. *J. Phys. Chem. B*, 108:18826–18831, 2004.

[111] Klaus Boldt, Nicholas Kirkwood, Gary A. Beane, and Paul Mulvaney. Synthesis of highly luminescent and photo-stable, graded shell $CdSe_/Cd_xZn_{1-x}S$ nanoparticles by in situ alloying. *Chem. Mater.*, 25:4731–4738, 2013.

[112] Yun-Wei Cao and Uri Banin. Synthesis and characterization of InAs/InP and InAs/CdSe core/shell nanocrystals. *Angew. Chem. Int. Ed.*, 38:3692–3694, 1999.

[113] Peter M. Allen, Wenhao Liu, Vikash P. Chauhan, Jungmin Lee, Alice Y. Ting, Dai Fukumura, Rakesh K. Jain, and Moungi G. Bawendi. InAs(ZnCdS) quantum dots optimized for biological imaging in the near-infrared. *J. Am. Chem. Soc.*, 132:470–471, 2010.

[114] Jothirmayanantham Pichaandi and Frank C.J.M. van Veggel. Near-infrared emitting quantum dots: Recent progress on their synthesis and characterization. *Coord. Chem. Rev.*, 263–264:138–150, 2014.

[115] Lino R. Becerra, Christopher B. Murray, Robert G. Griffin, and Moungi G. Bawendi. Investigation of the surface morphology of capped CdSe nanocrystallites by ^{31}p nuclear magnetic resonance. *J. Chem. Phys.*, 100:3297–3300, 1994.

[116] Masaru Kuno, Jong-Keuk Lee, Bashir O. Dabbousi, Frederic V. Mikulec, and Moungi G. Bawendi. The band edge luminescence of surface modified CdSe nanocrystallites: Probing the luminescing state. *J. Chem. Phys.*, 106:9869–9882, 1997.

[117] Fudong Wang, Rui Tang, and William E. Buhro. The trouble with TOPO; identification of adventitious impurities beneficial to the growth of cadmium selenide quantum dots, rods, and wires. *Nano Lett.*, 8:3521–3524, 2008.

[118] Jonathan S. Owen, Jungwon Park, Paul-Emile Trudeau, and A. Paul Alivisatos. Reaction chemistry and ligand exchange at cadmium–selenide nanocrystal surfaces. *J. Am. Chem. Soc.*, 130:12279–12281, 2008.

[119] Jordan T. Kopping and Timothy E. Patten. Identification of acidic phosphorus-containing ligands involved in the surface chemistry of CdSe nanoparticles prepared in tri-N-octylphosphine oxide solvents. *J. Am. Chem. Soc.*, 130:5689–5698, 2008.

[120] Fudong Wang, Rui Tang, Jeff L.-F. Kao, Sean D. Dingman, and William E. Buhro. Spectroscopic identification of tri-n-octylphosphine oxide (TOPO) impurities and elucidation of their roles in cadmium selenide quantum-wire growth. *J. Am. Chem. Soc.*, 131:4983–4994, 2009.

[121] Raquel Gomes, Antti Hassinen, Agnieszka Szczygiel, Qiang Zhao, André Vantomme, José C. Martins, and Zeger Hens. Binding of phosphonic acids to CdSe quantum dots: A solution NMR study. *J. Phys. Chem. Lett.*, 2:145–152, 2011.

[122] Jonathan S. Owen. The coordination chemistry of nanocrystal surfaces. *Science*, 347:615–616, 2015.

[123] Danylo Zherebetskyy, Marcus Scheele, Yingjie Zhang, Noah Bronstein, Christopher Thompson, David Britt, Miquel Salmeron, A. Paul Alivisatos, and Lin-Wang Wang. Hydroxylation of the surface of PbS nanocrystals passivated with oleic acid. *Science*, 344:1380–1384, 2014.

[124] Dmitri V. Talapin, Andrey L. Rogach, Ivo Mekis, Stephan Haubold, Andreas Kornowski, Markus Haase, and Horst Weller. Synthesis and surface modification of amino-stabilized CdSe, CdTe and InP nanocrystals. *Colloids and Surfaces A: Physicochemical and Engineering Aspects*, 202:145–154, 2002.

[125] Xiaogang Peng, Liberato Manna, Weidong Yang, Juanita Wickham, Erik Scher, Andreas Kadavanich, and A. Paul Alivisatos. Shape control of cdse nanocrystals. *Nature*, 404:59–61, 2000.

[126] Joseph M. Luther, Matt Law, Qing Song, Craig L. Perkins, Matthew C. Beard, and Arthur J. Nozik. Structural, optical, and electrical properties of self-assembled films of PbSe nanocrystals treated with 1,2-ethanedithiol. *ACS Nano*, 2:271–280, 2008.

[127] Maksym V. Kovalenko, Marcus Scheele, and Dmitri V. Talapin. Colloidal nanocrystals with molecular metal chalcogenide surface ligands. *Science*, 324:1417–1420, 2009.

[128] Jiang Tang, Kyle W. Kemp, Sjoerd Hoogland, Kwang S. Jeong, Huan Liu, Larissa Levina, Melissa Furukawa, Xihua Wang, Ratan Debnath, Dongkyu Cha, Kang Wei Chou, Armin Fischer, Aram Amassian, John B. Asbury, and Edward H. Sargent. Colloidal-quantum-dot photovoltaics using atomic-ligand passivation. *Nature Mater.*, 10:765–771, 2011.

[129] H. Tetsuo Uyeda, Igor L. Medintz, Jyoti K. Jaiswal, Sanford M. Simon, and Hedi Mattoussi. Synthesis of compact multidentate ligands to prepare stable hydrophilic quantum dot fluorophores. *J. Am. Chem. Soc.*, 127:3870–3878, 2005.

[130] Nicholas C. Anderson and Jonathan S. Owen. Soluble, chloride-terminated CdSe nanocrystals: Ligand exchange monitored by 1H and 31P NMR spectroscopy. *Chem. Mater.*, 25:69–76, 2013.

[131] Di Liu and Preston T. Snee. Water-soluble semiconductor nanocrystals cap exchanged with metalated ligands. *ACS Nano*, 5:546–550, 2011.

[132] Preston T. Snee, Rebecca C. Somers, Gautham Nair, John P. Zimmer, Moungi G. Bawendi, and Daniel G. Nocera. A ratiometric CdSe/ZnS nanocrystal pH sensor. *J. Am. Chem. Soc.*, 128:13320–13321, 2006.

[133] Hee-Sun Han, Elisabeth Niemeyer, Yuhui Huang, Walid S. Kamoun, John D. Martin, Jayeeta Bhaumik, Yunching Chen, Sylvie Roberge, Jian Cui, Margaret R. Martin, Dai Fukumura, Rakesh K. Jain, Moungi G. Bawendi, and Dan G. Duda. Quantum dot/antibody conjugates for in vivo cytometric imaging in mice. *Proc. Nat. Acad. Sci. U.S.A.*, 112:1350–1355, 2015.

[134] Hee-Sun Han, Neal K. Devaraj, Jungmin Lee, Scott A. Hilderbrand, Ralph Weissleder, and Moungi G. Bawendi. Development of a bioorthogonal and highly efficient conjugation method for quantum dots using tetrazine–norbornene cycloaddition. *J. Am. Chem. Soc.*, 132:7838–7839, 2010.

[135] Dmitri V. Talapin, Jong-Soo Lee, Maksym V. Kovalenko, and Elena V. Shevchenko. Prospects of colloidal nanocrystals for electronic and optoelectronic applications. *Chem. Rev.*, 110:389–458, 2010.

[136] Sean E. Keuleyan, Emmanuel Lhuillier, Vuk Brajuskovic, and Philippe Guyot-Sionnest. Mid-infrared HgTe colloidal quantum dot photodetectors. *Nat. Photon.*, 5:489–493, 2011.

[137] Emmanuel Lhuillier, Sean Keuleyan, Pavlo Zolotavin, and Philippe Guyot-Sionnest. Mid-infrared HgTe/As_2S_3 field effect transistors and photodetectors. *Adv. Mater.*, 25:137–141, 2013.

[138] Sean E. Keuleyan, Philippe Guyot-Sionnest, Christophe Delerue, and Guy Allan. Mercury telluride colloidal quantum dots: Electronic structure, size-dependent spectra, and photocurrent detection up to 12µm. *ACS Nano*, 8:8676–8682, 2014.

[139] Graham H. Carey, Larissa Levina, Riccardo Comin, Oleksandr Voznyy, and Edward H. Sargent. Record charge carrier diffusion length in colloidal quantum dot solids via mutual dot-to-dot surface passivation. *Adv. Mater.*, 27:3325–3330, 2015.

[140] Benjamin S. Mashford, Matthew Stevenson, Zoran Popović, Charles Hamilton, Zhaoqun Zhou, Craig Breen, Jonathan Steckel, Vladimir Bulović, Moungi G. Bawendi, Seth Coe-Sullivan, and Peter T. Kazlas. High-efficiency quantum-dot light-emitting devices with enhanced charge injection. *Nat. Photon.*, 7:407–412, 2013.

[141] Geoffrey J. Supran, Katherine W. Song, Gyu Weon Hwang, Raoul E. Correa, Jennifer Scherer, Eric A. Dauler, Yasuhiro Shirasaki, Moungi G. Bawendi, and

Vladimir Bulović. High-performance shortwave-infrared light-emitting devices using core–shell (PbS–CdS) colloidal quantum dots. *Adv. Mater.*, 27(8):1437–1442, 2015.

[142] Ken Marrin. Quantum dot technology progresses, ships in LED-backlit LCD TVs. *LEDs Magazine*, page 41, 2013.

[143] Isamu Akasaki and Hiroshi Amano. Breakthroughs in improving crystal quality of GaN and invention of the p–n junction blue-light-emitting diode. *Jpn. J. Appl. Phys.*, 45:9001, 2006.

[144] Scott M. Geyer, Jennifer M. Scherer, Nosipho Moloto, Frank B. Jaworski, and Moungi G. Bawendi. Efficient luminescent down-shifting detectors based on colloidal quantum dots for dual-band detection applications. *ACS Nano*, 5:5566–5571, 2011.

[145] Scott M. Geyer, Jennifer M. Scherer, Frank B. Jaworski, and Moungi G. Bawendi. Multispectral imaging via luminescent down-shifting with colloidal quantum dots. *Opt. Mater. Express*, 3:1167–1175, 2013.

[146] Scott M. Geyer, Jennifer M. Scherer, Michael D. Jack, Moungi G. Bawendi, and Frank B. Jaworski. Dual-band ultraviolet-short-wavelength infrared imaging via luminescent downshifting with colloidal quantum dots. *J. Nanophotonics*, 7:073083–073083, 2013.

[147] Armen Kherlopian, Ting Song, Qi Duan, Mathew Neimark, Ming Po, John Gohagan, and Andrew Laine. A review of imaging techniques for systems biology. *BMC Syst. Biol.*, 2:74, 2008.

[148] Laurent Cognet, Cécile Leduc, and Brahim Lounis. Advances in live-cell single-particle tracking and dynamic super-resolution imaging. *Current Opinion in Chemical Biology*, 20:78–85, 2014.

[149] Yong Taik Lim, Sungjee Kim, Akira Nakayama, Nathan E. Stott, Moungi G. Bawendi, and John V. Frangioni. Selection of quantum dot wavelengths for biomedical assays and imaging. *Mol. Imaging*, 2:50–64, 2003.

[150] Octavi E. Semonin, Justin C. Johnson, Joseph M. Luther, Aaron G. Midgett, Arthur J. Nozik, and Matthew C. Beard. Absolute photoluminescence quantum yields of IR-26 dye, PbS, and PbSe quantum dots. *J. Phys. Chem. Lett.*, 1:2445–2450, 2010.

[151] Guosong Hong, Jerry C. Lee, Joshua T. Robinson, Uwe Raaz, Liming Xie, Ngan F. Huang, John P. Cooke, and Hongjie Dai. Multifunctional in vivo vascular imaging using near-infrared II fluorescence. *Nat. Med.*, 18:1841–1846, 2012.

[152] Soheil Hatami, Christian Wurth, Martin Kaiser, Susanne Leubner, Stefanie Gabriel, Lydia Bahrig, Vladimir Lesnyak, Jutta Pauli, Nikolai Gaponik, Alexander Eychmuller, and Ute Resch-Genger. Absolute photoluminescence quantum yields of IR26 and IR-emissive $Cd_{1-x}Hg_xTe$ and PbS quantum dots – method- and material-inherent challenges. *Nanoscale*, 7:133–143, 2015.

[153] Rui Tang, Jianpeng Xue, Baogang Xu, Duanwen Shen, Gail P. Sudlow, and Samuel Achilefu. Tunable ultrasmall visible-to-extended near-infrared emitting silver sulfide quantum dots for integrin-targeted cancer imaging. *ACS Nano*, 9:220–230, 2015.

[154] Yan Zhang, Guosong Hong, Yejun Zhang, Guangcun Chen, Feng Li, Hongjie Dai, and Qiangbin Wang. Ag_2S quantum dot: A bright and biocompatible fluorescent nanoprobe in the second near-infrared window. *ACS Nano*, 6:3695–3702, 2012.

[155] Oliver T. Bruns, Thomas S. Bischof, Daniel K. Harris, Yanxiang Shi, Lars Riedemann, Thomas Reiberger, Alexander Bartelt, Frank B. Jaworski, Daniel Franke, Mark WB Wilson, Ou Chen, He Wei, Gyu Weon Hwang, Daniel Montana, Igor Coropceanu, Jonas Kloepper, Joerg Heeren, Dai Fukumura, Klavs F. Jensen, Rakesh K. Jain, and Moungi G. Bawendi. Next generation in vivo optical imaging with short-wave infrared quantum dots. *Submitted.*

[156] Brent R. Fisher, Hans-Jurgen Eisler, Nathan E. Stott, and Moungi G. Bawendi. Emission intensity dependence and single-exponential behavior in single colloidal quantum dot fluorescence lifetimes. *J. Phys. Chem. B*, 108:143–148, 2004.

[157] Jian Cui, Andrew P. Beyler, Thomas S. Bischof, Mark W. B. Wilson, and Moungi G. Bawendi. Deconstructing the photon stream from single nanocrystals: from binning to correlation. *Chem. Soc. Rev.*, 43:1287–1310, 2014.

[158] Russell A. Jensen, I-C Huang, Ou Chen, Jennifer Choy, Thomas S. Bischof, Marko Lončar, and Moungi G. Bawendi. Optical trapping and two-photon excitation of colloidal quantum dots using bowtie apertures. *Submitted.*

[159] Raoul E. Correa, Eric A. Dauler, Gautham Nair, Si H. Pan, Danna Rosenberg, Andrew J. Kerman, Richard J. Molnar, Xiaolong Hu, Francesco Marsili, Vikas Anant, Karl K. Berggren, and Moungi G. Bawendi. Single photon counting from individual nanocrystals in the infrared. *Nano Lett.*, 12:2953–2958, 2012.

[160] Aaron L. Routzahn and Prashant K. Jain. Single-nanocrystal reaction trajectories reveal sharp cooperative transitions. *Nano Lett.*, 14:987–992, 2014.

[161] Stephen A. Empedocles, Robert G. Neuhauser, and Moungi G. Bawendi. Three-dimensional orientation measurements of symmetric single chromophores using polarization microscopy. *Nature*, 399:126–130, 1999.

[162] Stephen A. Empedocles, Robert G. Neuhauser, Ken D. Shimizu, and Moungi G. Bawendi. Photoluminescence from single semiconductor nanostructures. *Adv. Mater.*, 11:1243–1256, 1999.

[163] Eric A. Dauler, Andrew J. Kerman, Bryan S. Robinson, Joel K.W. Yang, Boris Voronov, Gregory Goltsman, Scott A. Hamilton, and Karl K. Berggren. Photon-number-resolution with sub-30-ps timing using multi-element superconducting nanowire single photon detectors. *J. Mod. Opt.*, 56:364–373, 2009.

[164] Catherine H. Crouch, Orion Sauter, Xiaohua Wu, Robert Purcell, Claudia Querner, Marija Drndic, and Matthew Pelton. Facts and artifacts in the blinking statistics of semiconductor nanocrystals. *Nano Lett.*, 10:1692–1698, 2010.

[165] Germar Schlegel, Jolanta Bohnenberger, Inga Potapova, and Alf Mews. Fluorescence decay time of single semiconductor nanocrystals. *Phys. Rev. Lett.*, 88:137401, 2002.

[166] Gautham Nair, Jing Zhao, and Moungi G. Bawendi. Biexciton quantum yield of single semiconductor nanocrystals from photon statistics. *Nano Lett.*, 11:1136–1140, 2011.

[167] Watt W. Webb. Fluorescence correlation spectroscopy: Genesis, maturation and prognosis. In R. Rigler and E. L. Elson, editors, *Fluorescence Correlation Spectroscopy: Theory and Applications*, pages 305–330. Springer, Berlin, 2001.

[168] Yan Chen, Joachim D. Müller, Peter T. C. So, and Enrico Gratton. The photon counting histogram in fluorescence fluctuation spectroscopy. *Biophys. J.*, 77:553–567, 1999.

[169] Bo Huang, Thomas D. Perroud, and Richard N. Zare. Photon counting histogram: one-photon excitation. *ChemPhysChem*, 5:1523–1531, 2004.

[170] Gaetan Messin, Jean-Pierre Hermier, Élisabeth Giacobino, P. Desbiolles, and Maxime Dahan. Bunching and antibunching in the fluorescence of semiconductor nanocrystals. *Opt. Lett.*, 26:1891–1893, 2001.

[171] Christophe Galland, Yagnaseni Ghosh, Andrea Steinbruck, Milan Sykora, Jennifer A. Hollingsworth, Victor I. Klimov, and Han Htoon. Two types of luminescence blinking revealed by spectroelectrochemistry of single quantum dots. *Nature*, 479:203–207, 2011.

[172] Tom J. Liptay, Lisa F. Marshall, P. S. Rao, Rajeev J. Ram, and M. G. Bawendi. Anomalous stokes shift in CdSe nanocrystals. *Phys. Rev. B*, 76:155314, 2007.

[173] Catherine A. Leatherdale, Won Woo, Frederic V. Mikulec, and Moungi G. Bawendi. On the absorption cross section of CdSe nanocrystal quantum dots. *J. Phys. Chem. B*, 106:7619–7622, 2002.

[174] Igor Coropceanu and Moungi G. Bawendi. Core/shell quantum dot based luminescent solar concentrators with reduced reabsorption and enhanced efficiency. *Nano Lett.*, 14:4097–4101, 2014.

[175] Peter Reiss, Myriam Protiere, and Liang Li. Core/shell semiconductor nanocrystals. *Small*, 5(2):154–168, 2009.

[176] Jian Cui, Andrew P. Beyler, Lisa F. Marshall, Ou Chen, Daniel K. Harris, Darcy D. Wanger, Xavier Brokmann, and Moungi G. Bawendi. Direct probe of spectral inhomogeneity reveals synthetic tunability of single-nanocrystal spectral linewidths. *Nat. Chem.*, 5:602–606, 2013.

[177] Lisa F. Marshall, Jian Cui, Xavier Brokmann, and Moungi G. Bawendi. Extracting spectral dynamics from single chromophores in solution. *Phys. Rev. Lett.*, 105:053005, 2010.

[178] Anne Myers Kelley. Electron–phonon coupling in CdSe nanocrystals. *J. Phys. Chem. Lett.*, 1:1296–1300, 2010.

[179] Dan Oron, Miri Kazes, Itzik Shweky, and Uri Banin. Multiexciton spectroscopy of semiconductor nanocrystals under quasi-continuous-wave optical pumping. *Phys. Rev. B*, 74:115333, 2006.

[180] Daniel E. Gómez, Joel van Embden, Paul Mulvaney, Mark J. Fernée, and Halina Rubinsztein-Dunlop. Exciton–trion transitions in single CdSe–CdS core–shell nanocrystals. *ACS Nano*, 3:2281–2287, 2009.

[181] Mark J. Fernée, Bradley N. Littleton, and Halina Rubinsztein-Dunlop. Detection of bright trion states using the fine structure emission of single CdSe/ZnS colloidal quantum dots. *ACS Nano*, 3:3762–3768, 2009.

[182] Yann Louyer, Louis Biadala, Philippe Tamarat, and Brahim Lounis. Spectroscopy of neutral and charged exciton states in single CdSe/ZnS nanocrystals. *Appl. Phys. Lett.*, 96:203111, 2010.

[183] Mark. J. Fernée, Chiara Sinito, Yann Louyer, Christian Potzner, Tich-Lam Nguyen, Paul Mulvaney, Philippe Tamarat, and Brahim Lounis. Magneto-optical properties of trions in non-blinking charged nanocrystals reveal an acoustic phonon bottleneck. *Nature Commun.*, 3:1287, 2012.

[184] Xavier Brokmann, Jean-Pierre Hermier, Gaétan Messin, P. Desbiolles, Jean-Phillipe Bouchaud, and Maxime Dahan. Statistical aging and nonergodicity in the fluorescence of single nanocrystals. *Phys. Rev. Lett.*, 90:120601, 2003.

[185] Inhee Chung and Moungi G. Bawendi. Relationship between single quantum-dot intermittency and fluorescence intensity decays from collections of dots. *Phys. Rev. B*, 70:165304, 2004.

[186] Wan Ki Bae, Lazaro A. Padilha, Young-Shin Park, Hunter McDaniel, Istvan Robel, Jeffrey M. Pietryga, and Victor I. Klimov. Controlled alloying of the core-shell interface in CdSe/CdS quantum dots for suppression of Auger recombination. *ACS Nano*, 7:3411–3419, 2013.

[187] Young-Shin Park, Anton V. Malko, Javier Vela, Yongfen Chen, Yagnaseni Ghosh, Florencio García-Santamaría, Jennifer A. Hollingsworth, Victor I. Klimov, and Han Htoon. Near-unity quantum yields of biexciton emission from CdSe/CdS nanocrystals measured using single-particle spectroscopy. *Phys. Rev. Lett.*, 106:187401, 2011.

[188] Brian L. Wehrenberg, Conjung Wang, and Philippe Guyot-Sionnest. Interband and intraband optical studies of PbSe colloidal quantum dots. *J. Phys. Chem. B*, 106:10634–10640, 2002.

[189] Jamie H. Warner, Elizabeth Thomsen, Andrew R. Watt, Norman R. Heckenberg, and Halina Rubinsztein-Dunlop. Time-resolved photoluminescence spectroscopy of ligand-capped PbS nanocrystals. *Nanotechnology*, 16:175–179, 2005.

[190] Sungjee Kim, Brent R. Fisher, Hans-Jurgen Eisler, and Moungi G. Bawendi. Type-II quantum dots: CdTe/CdSe(core/shell) and CdSe/ZnTe(core/shell) heterostructures. *J. Am. Chem. Soc.*, 125:11466–11467, 2003.

[191] Benjamin Bruhn, Fatjon Qejvanaj, Ilya Sychugov, and Jan Linnros. Blinking statistics and excitation-dependent luminescence yield in Si and CdSe nanocrystals. *J. Phys. Chem. C*, 118:2202–2208, 2014.

[192] Roger Y. Tsien, Lauren Ernst, and Alan Waggoner. Fluorophores for confocal microscopy: Photophysics and photochemistry. In J. B. Pawley, editor, *Handbook Of Biological Confocal Microscopy*, pages 338–352. Springer (US), 2006.

[193] Jing Zhao, Ou Chen, David B. Strasfeld, and Moungi G. Bawendi. Biexciton quantum yield heterogeneities in single CdSe(CdS) core(shell) nanocrystals and its correlation to exciton blinking. *Nano Lett.*, 12:4477–4483, 2012.

[194] Yao Liu, Markelle Gibbs, James Puthussery, Steven Gaik, Rachelle Ihly, Hugh W. Hillhouse, and Matt Law. Dependence of carrier mobility on nanocrystal size and ligand length in PbSe nanocrystal solids. *Nano Lett.*, 10:1960–1969, 2010.

[195] Nuri Yazdani, Deniz Bozyigit, Olesya Yarema, Maksym Yarema, and Vanessa Wood. Hole mobility in nanocrystal solids as a function of constituent nanocrystal size. *J. Phys. Chem. Lett.*, 5:3522–3527, 2014.

[196] Maksym V. Kovalenko, Maryna I. Bodnarchuk, Jana Zaumseil, Jong-Soo Lee, and Dmitri V. Talapin. Expanding the chemical versatility of colloidal nanocrystals capped with molecular metal chalcogenide ligands. *J. Am. Chem. Soc.*, 132:10085–10092, 2010.

[197] Jong-Soo Lee, Maksym V. Kovalenko, Jing Huang, Dae Sung Chung, and Dmitri V. Talapin. Band-like transport, high electron mobility and high photoconductivity in all-inorganic nanocrystal arrays. *Nat. Nano*, 6:348–352, 2011.

[198] Philippe Guyot-Sionnest. Electrical transport in colloidal quantum dot films. *J. Phys. Chem. Lett.*, 3:1169–1175, 2012.

[199] Patrick R. Brown, Donghun Kim, Richard R. Lunt, Ni Zhao, Moungi G. Bawendi, Jeffrey C. Grossman, and Vladimir Bulović. Energy level modification in lead sulfide quantum dot thin films through ligand exchange. *ACS Nano*, 8:5863–5872, 2014.

[200] Jacek Jasieniak, Marco Califano, and Scott E. Watkins. Size-dependent valence and conduction band-edge energies of semiconductor nanocrystals. *ACS Nano*, 5:5888–5902, 2011.

[201] Michal Soreni-Harari, Nir Yaacobi-Gross, Dov Steiner, Assaf Aharoni, Uri Banin, Oded Millo, and Nir Tessler. Tuning energetic levels in nanocrystal quantum dots through surface manipulations. *Nano Lett.*, 8:678–684, 2008.

[202] Chia-Hao M. Chuang, Patrick R. Brown, Vladimir Bulović, and Moungi G. Bawendi. Improved performance and stability in quantumÊdot solar cells through band alignmentÊengineering. *Nature Mater.*, 13:796–801, 2014.

[203] Dong-Kyun Ko, Patrick R. Brown, Moungi G. Bawendi, and Vladimir Bulović. p-i-n heterojunction solar cells with a colloidal quantum-dot absorber layer. *Adv. Mater.*, 26:4845–4850, 2014.

[204] Kurtis S. Leschkies, Moon Sung Kang, Eray S. Aydil, and David J. Norris. Influence of atmospheric gases on the electrical properties of PbSe quantum-dot films. *J. Phys. Chem. C*, 114:9988–9996, 2010.

[205] Joseph M. Luther and Jeffrey M. Pietryga. Stoichiometry control in quantum dots: A viable analog to impurity doping of bulk materials. *ACS Nano*, 7:1845–1849, 2013.

[206] Soong Ju Oh, Nathaniel E. Berry, Ji-Hyuk Choi, E. Ashley Gaulding, Taejong Paik, Sung-Hoon Hong, Christopher B. Murray, and Cherie R. Kagan. Stoichiometric control of lead chalcogenide nanocrystal solids to enhance their electronic and optoelectronic device performance. *ACS Nano*, 7:2413–2421, 2013.

[207] Soong Ju Oh, Nathaniel E. Berry, Ji-Hyuk Choi, E. Ashley Gaulding, Hangfei Lin, Taejong Paik, Benjamin. T. Diroll, Shin Muramoto, Christopher B. Murray, and Cherie R. Kagan. Designing high-performance PbS and PbSe nanocrystal electronic devices through stepwise, post-synthesis, colloidal atomic layer deposition. *Nano Lett.*, 14:1559–1566, 2014.

[208] Raffaella Buonsanti and Delia J. Milliron. Chemistry of doped colloidal nanocrystals. *Chem. Mater.*, 25:1305–1317, 2013.

[209] Pralay K. Santra and Prashant V. Kamat. Mn-doped quantum dot sensitized solar cells: A strategy to boost efficiency over 5%. *J. Am. Chem. Soc.*, 134:2508–2511, 2012.

[210] Abhijit Hazarika, Anshu Pandey, and Dipankar D. Sarma. Rainbow emission from an atomic transition in doped quantum dots. *J. Phys. Chem. Lett.*, 5:2208–2213, 2014.

[211] Steven C. Erwin, Lijun Zu, Michael I. Haftel, Alexander L. Efros, Thomas A. Kennedy, and David J. Norris. Doping semiconductor nanocrystals. *Nature*, 436:91–94, 2005.

[212] Heng Liu and Philippe Guyot-Sionnest. Magnetoresistance of manganese-doped colloidal quantum dot films. *J. Phys. Chem. C*, 119:14797–14804, 2015.

[213] Darcy D. Wanger, Raoul E. Correa, Eric A. Dauler, and Moungi G. Bawendi. The dominant role of exciton quenching in PbS quantum-dot-based photovoltaic devices. *Nano Lett.*, 13:5907–5912, 2013.

[214] Mirna V. Jarosz, Nathan E. Stott, Marija Drndic, N. Y. Morgan, Marc A. Kastner, and Moungi G. Bawendi. Observation of bimolecular carrier recombination dynamics in close-packed films of colloidal CdSe nanocrystals. *J. Phys. Chem. B*, 107:12585–12588, 2003.

[215] Jian Zhang and Xiaomei Jiang. Confinement-dependent below-gap state in PbS quantum dot films probed by continuous-wave photoinduced absorption. *J. Phys. Chem. B*, 112:9557–9560, 2008.

[216] Chia-Hao Marcus Chuang, Andrea Maurano, Riley E. Brandt, Gyu Weon Hwang, Joel Jean, Tonio Buonassisi, Vladimir Bulović, and Moungi G. Bawendi. Open-circuit voltage deficit, radiative sub-bandgap states, and prospects in quantum dot solar cells. *Nano Lett.*, 15:3286–3294, 2015.

[217] Matthew J. Greaney, Elsa Couderc, Jing Zhao, Benjamin A. Nail, Matthew Mecklenburg, William Thornbury, Frank E. Osterloh, Stephen E. Bradforth, and Richard L. Brutchey. Controlling the trap state landscape of colloidal CdSe nanocrystals with cadmium halide ligands. *Chem. Mater.*, 27:744–756, 2015.

[218] Gyu Weon Hwang, D. Kim, Jose M. Cordero, Mark W. B. Wilson, Chia-Hao M. Chuang, Jeffrey C. Grossman, and Moungi G. Bawendi. Identifying and eliminating emissive subbandgap states in thin films of PbS nanocrystals. *Adv. Mater.*, 2015 (Accepted).

[219] Deniz Bozyigit, Weyde M. M. Lin, Nuri Yazdani, Olesya Yarema, and Vanessa Wood. A quantitative model for charge carrier transport, trapping and recombination in nanocrystal-based solar cells. *Nat. Commun.*, 6:6180, 2015.

[220] William Shockley and Hans J. Queisser. Detailed balance limit of efficiency of *p-n* junction solar cells. *J. Appl. Phys.*, 32:510–519, 1961.

[221] Gautham Nair, Liang-Yi Chang, Scott M. Geyer, and Moungi G. Bawendi. Perspective on the prospects of a carrier multiplication nanocrystal solar cell. *Nano Lett.*, 11:2145–2151, 2011.

[222] Anshu Pandey and Philippe Guyot-Sionnest. Slow electron cooling in colloidal quantum dots. *Science*, 322:929–932, 2008.

[223] Alexander L. Efros, V.A. Kharchenko, and M. Rosen. Breaking the phonon bottleneck in nanometer quantum dots: Role of Auger-like processes. *Solid State Commun.*, 93(4):281 – 284, 1995.

[224] Patanjali Kambhampati. Hot exciton relaxation dynamics in semiconductor quantum dots: Radiationless transitions on the nanoscale. *J. Phys. Chem. C*, 115:22089–22109, 2011.

[225] Gautham Nair, Scott M. Geyer, Liang-Yi Chang, and Moungi G. Bawendi. Carrier multiplication yields in PbS and PbSe nanocrystals measured by transient photoluminescence. *Phys. Rev. B*, 78:125325, 2008.

[226] Christophe Delerue, Guy Allan, J. J. H. Pijpers, and Mischa Bonn. Carrier multiplication in bulk and nanocrystalline semiconductors: Mechanism, efficiency, and interest for solar cells. *Phys. Rev. B*, 81:125306, 2010.

[227] Octavi E. Semonin, Joseph M. Luther, Sukgeun Choi, Hsiang-Yu Chen, Jianbo Gao, Arthur J. Nozik, and Matthew C. Beard. Peak external photocurrent quantum efficiency exceeding 100% via MEG in a quantum dot solar cell. *Science*, 334:1530–1533, 2011.

[228] Matthew C. Beard, Joseph M. Luther, Octavi E. Semonin, and Arthur J. Nozik. Third generation photovoltaics based on multiple exciton generation in quantum confined semiconductors. *Acc. Chem. Res.*, 46:1252–1260, 2013.

[229] Zoran Popović, Wenhao Liu, Vikash P. Chauhan, Jungmin Lee, Cliff Wong, Andrew B. Greytak, Numpon Insin, Daniel G. Nocera, Dai Fukumura, Rakesh K. Jain, and Moungi G. Bawendi. A nanoparticle size series for in vivo fluorescence imaging. *Angew. Chem. Int. Ed.*, 49:8649–8652, 2010.

[230] Hak Soo Choi, Wenhao Liu, Preeti Misra, Eiichi Tanaka, John P. Zimmer, Binil Itty Ipe, Moungi G. Bawendi, and John V. Frangioni. Renal clearance of quantum dots. *Nat. Biotech.*, 25:1165–1170, 2007.

[231] Michelle Longmire, Peter L. Choyke, and Hisataka Kobayashi. Clearance properties of nano-sized particles and molecules as imaging agents: Considerations and caveats. *Nanomedicine-UK*, 3:703–717, 2008.

[232] Vikash P. Chauhan, Zoran Popović, Z., Ou Chen, Jian Cui, Dai Fukumura, Moungi G. Bawendi, and Rakesh K. Jain. Fluorescent nanorods and nanospheres for real-time in vivo probing of nanoparticle shape-dependent tumor penetration. *Angew. Chem. Int. Ed.*, 50:11417–11420, 2011.

[233] He Wei, Numpon Insin, Jungmin Lee, Hee-Sun Han, Jose M. Cordero, Wenhao Liu, and Moungi G. Bawendi. Compact zwitterion-coated iron oxide nanoparticles for biological applications. *Nano Lett.*, 12:22–25, 2012.

[234] Wenhao Liu, Hak Soo Choi, John P. Zimmer, Eiichi Tanaka, John V. Frangioni, and Moungi G. Bawendi. Compact cysteine-coated CdSe(ZnCdS) quantum dots for in vivo applications. *J. Am. Chem. Soc.*, 129:14530–14531, 2007.

[235] Kimihiro Susumu, H. Tetsuo Uyeda, Igor L. Medintz, Thomas Pons, James B. Delehanty, and Hedi Mattoussi. Enhancing the stability and biological functionalities of quantum dots via compact multifunctional ligands. *J. Am. Chem. Soc.*, 129:13987–13996, 2007.

[236] Vladimir V. Breus, Colin D. Heyes, Kyrylo Tron, and G. Ulrich Nienhaus. Zwitterionic biocompatible quantum dots for wide pH stability and weak nonspecific binding to cells. *ACS Nano*, 3:2573–2580, 2009.

[237] Igor L. Medintz, H. Tetsuo Uyeda, Ellen R. Goldman, and Hedi Mattoussi. Quantum dot bioconjugates for imaging, labelling and sensing. *Nature Mater.*, 4:435–446, 2005.

[238] Shahriar Sharifi, Shahed Behzadi, Sophie Laurent, M. Laird Forrest, Pieter Stroeve, and Morteza Mahmoudi. Toxicity of nanomaterials. *Chem. Soc. Rev.*, 41:2323–2343, 2012.

[239] Anna O. W. Leung, Nurdan S. Duzgoren-Aydin, K. C. Cheung, and Ming H. Wong. Heavy metals concentrations of surface dust from e-waste recycling and its human health implications in southeast china. *Environ. Sci. Technol.*, 42:2674–2680, 2008.

[240] Dustin Mulvaney and Paul Robbins, editors. *The SAGE Reference Series on Green Society toward a Sustainable Future: Green technology: An A-to-Z guide.* Thousand Oaks, CA: SAGE Publications, Inc., 2011.

[241] Akiyoshi Hoshino, Kouki Fujioka, Taisuke Oku, Masakazu Suga, Yu F. Sasaki, Toshihiro Ohta, Masato Yasuhara, Kazuo Suzuki, and Kenji Yamamoto. Physicochemical properties and cellular toxicity of nanocrystal quantum dots depend on their surface modification. *Nano Lett.*, 4:2163–2169, 2004.

[242] Justin N. Weilnau, Sarah E. Black, Veronica J. Chehata, Michael P. Schmidt, Kimberly L. Holt, Lindsay M. Carl, Collin J. Straka, Anderson L. Marsh, Walter A. Patton, and Courtney M. Lappas. ZnS nanocrystal cytotoxicity is influenced by capping agent chemical structure and duration of time in suspension. *J. Appl. Toxicol.*, 33:227–237, 2013.

[243] Andrew P. Beyler, Lisa F. Marshall, Jian Cui, Xavier Brokmann, and Moungi G. Bawendi. Direct observation of rapid discrete spectral dynamics in single colloidal CdSe-CdS core-shell quantum dots. *Phys. Rev. Lett.*, 111:177401, 2013.

[244] Andrew P. Beyler, Thomas S. Bischof, Jian Cui, Igor Coropceanu, Daniel K. Harris, and Moungi G. Bawendi. Sample-averaged biexciton quantum yield measured by solution-phase photon correlation. *Nano Lett.*, 14:6792–6798, 2014.

[245] Huiyoun Shin, Dongseon Jang, Jaesung Hwang, Youngil Jang, Myungju Cho, and Kyuho Park. Structural characterization of CdSe/ZnS core–shell quantum dots (QDs) using TEM/STEM observation. *J. Mater. Sci.: Mater. Electron.*, 25:2047–2052, 2014.

[246] Sara Bals, Marianna Casavola, Marijn A. van Huis, Sandra Van Aert, K. Joost Batenburg, Gustaaf Van Tendeloo, and DaniÌÇl Vanmaekelbergh. Three-dimensional atomic imaging of colloidal core–shell nanocrystals. *Nano Lett.*, 11:3420–3424, 2011.

[247] Keith A. Abel, Paul A. Fitzgerald, Ting-Yu Wang, Tom Z. Regier, Mati Raudsepp, Simon P. Ringer, Gregory G. Warr, and Frank C. J. M. van Veggel. Probing the structure of colloidal core/shell quantum dots formed by cation exchange. *J. Phys. Chem. C*, 116:3968–3978, 2012.

[248] Mark P. Boneschanscher, Wiel H. Evers, Jaco J. Geuchies, Thomas Altantzis, Bart Goris, Freddy T. Rabouw, S. A. P. van Rossum, Herre S. J. van der Zant, Laurent D. A. Siebbeles, Gustaaf Van Tendeloo, Ingmar Swart, Jan Hilhorst, Andrei V. Petukhov, S. Bals, and Daniël Vanmaekelbergh. Long-range orientation and atomic attachment of nanocrystals in 2D honeycomb superlattices. *Science*, 344:1377–1380, 2014.

[249] Sandrine Ithurria, G. Bousquet, and Benoit Dubertret. Continuous transition from 3D to 1D confinement observed during the formation of CdSe nanoplatelets. *J. Am. Chem. Soc.*, 133:3070–3077, 2011.

[250] Eline M. Hutter, Eva Bladt, Bart Goris, Francesca Pietra, Johanna C. van der Bok, Mark P. Boneschanscher, Celso de Mello Donegá, Sara Bals, and Daniël Vanmaekelbergh. Conformal and atomic characterization of ultrathin CdSe platelets with a helical shape. *Nano Lett.*, 14:6257–6262, 2014.

[251] Timothy J. Pennycook, James R. McBride, Sandra J. Rosenthal, Stephen J. Pennycook, and Sokrates T. Pantelides. Dynamic fluctuations in ultrasmall nanocrystals induce white light emission. *Nano Lett.*, 12:3038–3042, 2012.

[252] Jong Min Yuk, Jungwon Park, Peter Ercius, Kwanpyo Kim, Daniel J. Hellebusch, Michael F. Crommie, Jeong Yong Lee, A. Zettl, and A. Paul Alivisatos. High-resolution EM of colloidal nanocrystal growth using graphene liquid cells. *Science*, 336:61–64, 2012.

[253] Zeger Hens and José C. Martins. A solution NMR toolbox for characterizing the surface chemistry of colloidal nanocrystals. *Chem. Mater.*, 25:1211–1221, 2013.

[254] Arun Lobo, Thomas Möller, Matthias Nagel, Holger Borchert, Stephen G. Hickey, and Horst Weller. Photoelectron spectroscopic investigations of chemical bonding in organically stabilized PbS nanocrystals. *J. Phys. Chem. B*, 109:17422–17428, 2005.

[255] Sameer Sapra, J. Nanda, Jeffrey M. Pietryga, Jennifer A. Hollingsworth, and Dipankar D. Sarma. Unraveling internal structures of highly luminescent PbSe nanocrystallites using variable-energy synchrotron radiation photoelectron spectroscopy. *J. Phys. Chem. B*, 110:15244–15250, 2006.

[256] Adam J. Morris-Cohen, Michałâ Malicki, Mark D. Peterson, John W. J. Slavin, and Emily A. Weiss. Chemical, structural, and quantitative analysis of the ligand shells of colloidal quantum dots. *Chem. Mater.*, 25:1155–1165, 2013.

[257] Mark D. Peterson, Laura C. Cass, Rachel D. Harris, Kedy Edme, Kimberly Sung, and Emily A. Weiss. The role of ligands in determining the exciton relaxation dynamics in semiconductor quantum dots. *Annu. Rev. Phys. Chem.*, 65:317–339, 2014.

[258] Jonathan I. Saari, Eva A. Dias, Danielle Reifsnyder, Michael M. Krause, Brenna R. Walsh, Christopher B. Murray, and Patanjali Kambhampati. Ultrafast electron trapping at the surface of semiconductor nanocrystals: Excitonic and biexcitonic processes. *J. Phys. Chem. B*, 117:4412–4421, 2013.

[259] Noah J. Orfield, James R. McBride, Joseph D. Keene, Lloyd M. Davis, and Sandra J. Rosenthal. Correlation of atomic structure and photoluminescence of the same quantum dot: Pinpointing surface and internal defects that inhibit photoluminescence. *ACS Nano*, 9:831–839, 2015.

[260] Robert G. Neuhauser, Ken. T. Shimizu, W. K. Woo, Stephen A. Empedocles, and Moungi G. Bawendi. Correlation between fluorescence intermittency and spectral diffusion in single semiconductor quantum dots. *Phys. Rev. Lett.*, 85:3301, 2000.

[261] Daniel E. Gómez, Joel van Embden, and Paul Mulvaney. Spectral diffusion of single semiconductor nanocrystals: The influence of the dielectric environment. *Appl. Phys. Lett.*, 88:154106, 2006.

[262] Mark. J. Fernée, Bradley N. Littleton, Taras Plakhotnik, Halina Rubinsztein-Dunlop, Daniel E. Gómez, and Paul Mulvaney. Charge hopping revealed by jitter correlations in the photoluminescence spectra of single CdSe nanocrystals. *Phys. Rev. B*, 81:155307, 2010.

[263] Mark. J. Fernée, Taras Plakhotnik, Yann Louyer, Bradley N. Littleton, Christian Potzner, Philippe Tamarat, Paul Mulvaney, and Brahim Lounis. Spontaneous spectral diffusion in CdSe quantum dots. *J. Phys. Chem. Lett.*, 3:1716, 2012.

[264] Taras Plakhotnik, Mark J. Fernée, Bradley N. Littleton, Halina Rubinsztein-Dunlop, Christian Potzner, and Paul Mulvaney. Anomalous power laws of spectral diffusion in quantum dots: A connection to luminescence intermittency. *Phys. Rev. Lett.*, 105:167402, 2010.

[265] Josef Müller, John M. Lupton, Andrey L. Rogach, Jochen Feldmann, Dmitri V. Talapin, and Horst Weller. Monitoring surface charge movement in single elongated semiconductor nanocrystals. *Phys. Rev. Lett.*, 93:167402, 2004.

[266] Josef Müller, John M. Lupton, Andrey L. Rogach, Jochen Feldmann, Dmitri V. Talapin, and Horst Weller. Monitoring surface charge migration in the spectral dynamics of single CdSe/CdS nanodot/nanorod heterostructures. *Phys. Rev. B*, 72:205339, 2005.

[267] Phedon Palinginis, Sasha Tavenner, Mark Lonergan, and Hailin Wang. Spectral hole burning and zero phonon linewidth in semiconductor nanocrystals. *Phys. Rev. B*, 67:201307, 2003.

[268] Phedon Palinginis and Hailin Wang. High-resolution spectral hole burning in CdSe/ZnS core/shell nanocrystals. *Appl. Phys. Lett.*, 78:1541, 2001.

[269] Francesco Masia, Nicolò Accanto, Wolfgang Langbein, and Paola Borri. Spin-flip limited exciton dephasing in CdSe/ZnS colloidal quantum dots. *Phys. Rev. Lett.*, 108:087401, 2012.

[270] Nicolò Accanto, Francesco Masia, Iwan Moreels, Zeger Hens, Wolfgang Langbein, and Paola Borri. Engineering the spin-flip limited exciton dephasing in colloidal CdSe/CdS quantum dots. *ACS Nano*, 6(6):5227, 2012.

[271] Louis Biadala, Yann Louyer, Philippe Tamarat, and Brahim Lounis. Direct observation of the two lowest exciton zero-phonon lines in single CdSe/ZnS nanocrystals. *Phys. Rev. Lett.*, 103:037404, 2009.

[272] Mark J. Fernée, Chiara Sinito, Yann Louyer, Philippe Tamarat, and Brahim Lounis. The ultimate limit to the emission linewidth of single nanocrystals. *Nanotechnology*, 24:465703, 2013.

[273] Laurent Coolen, Piernicola Spinicelli, and Jean-Pierre Hermier. Emission spectrum and spectral diffusion of a single CdSe/ZnS nanocrystal measured by photon-correlation Fourier spectroscopy. *J. Opt. Soc. Am. B*, 26:1463, 2009.

[274] Bradley N. Littleton, Mark J. Fernée, Daniel E. Gómez, Paul Mulvaney, and Halina Rubinsztein-Dunlop. High-resolution line width measurement of single CdSe nanocrystals at long time scales. *J. Phys. Chem. C*, 113:5345, 2009.

[275] Louis Biadala, Hugo Frederich, Laurent Coolen, Stéphanie Buil, Xavier Quélin, Clémentine Javaux, Michel Nasilowski, Benoit Dubertret, and Jean-Pierre Hermier. Photon-correlation Fourier spectroscopy of the trion fluorescence in thick-shell CdSe/CdS nanocrystals. *Phys. Rev. B*, 91:085416, 2015.

[276] Brent R. Fisher, Jean-Michel Caruge, Don Zehnder, and Moungi G. Bawendi. Room-temperature ordered photon emission from multiexciton states in single CdSe core-shell nanocrystals. *Phys. Rev. Lett.*, 94:087403, 2005.

[277] Christophe Galland, Sergio Brovelli, Wan Ki Bae, Lazaro A. Padilha, Francesco Meinardi, and Victor I. Klimov. Dynamic hole blockade yields two-color quantum and classical light from dot-in-bulk nanocrystals. *Nano Lett.*, 13:321–328, 2013.

[278] Xavier Brokmann, Moungi Bawendi, Laurent Coolen, and Jean-Pierre Hermier. Photon-correlation Fourier spectroscopy. *Opt. Express*, 14:6333–6341, 2006.

[279] Laurent Coolen, Xavier Brokmann, Piernicola Spinicelli, and Jean-Pierre Hermier. Emission characterization of a single CdSe-ZnS nanocrystal with high temporal and spectral resolution by photon-correlation Fourier spectroscopy. *Phys. Rev. Lett.*, 100:027403, 2008.

[280] Gregory Sallen, Adrian Tribu, Thomas Aichele, Régis André, Lucien Besombes, Catherine Bougerol, Maxime Richard, Serge Tatarenko, Kuntheak Kheng, and Jean-Philippe Poizat. Subnanosecond spectral diffusion measurement using photon correlation. *Nat. Photon.*, 4:696–699, 2010.

[281] Gregory Sallen, Adrian Tribu, Thomas Aichele, Régis André, Lucien Besombes, Catherine Bougerol, Maxime Richard, Serge Tatarenko, Kuntheak Kheng, and Jean-Philippe Poizat. Subnanosecond spectral diffusion of a single quantum dot in a nanowire. *Phys. Rev. B*, 84:041405, 2011.

[282] Samir Bounouar, Aurélien Trichet, Miryam Elouneg-Jamroz, Régis André, E. Bellet-Amalric, Catherine Bougerol, Martin Den Hertog, Kuntheak Kheng, Serge Tatarenko, and Jean-Philippe Poizat. Extraction of the homogeneous linewidth of the spectrally diffusing line of a CdSe/ZnSe quantum dot embedded in a nanowire. *Phys. Rev. B*, 86:085325, 2012.

[283] Janik Wolters, Nikola Sadzak, Andreas W. Schell, Tim Schröder, and Oliver Benson. Measurement of the ultrafast spectral diffusion of the optical transition of nitrogen vacancy centers in nano-size diamond using correlation interferometry. *Phys. Rev. Lett.*, 110:027401, 2013.

[284] Marco Abbarchi, Takashi Kuroda, Takaaki Mano, Massimo Gurioli, and Kazuaki Sakoda. Bunched photon statistics of the spectrally diffusive photoluminescence of single self-assembled GaAs quantum dots. *Phys. Rev. B*, 86:115330, 2012.

[285] Xavier Brokmann, Lisa F. Marshall, and Moungi G. Bawendi. Revealing single emitter spectral dynamics from intensity correlations in an ensemble fluorescence spectrum. *Opt. Express*, 17:4509–4517, 2009.

[286] Jian Cui. *Deconstructing the Room-Temperature Emission Spectra of Nancrystals Using Photon-Correlation Fourier Spectroscopy.* PhD thesis, Massachusetts Institute of Technology, 2014.

[287] Lisa F. Marshall. *Spectral dynamics of single quantum dots: A study using photon-correlation Fourier spectroscopy for submillisecond time resolution at low temperature and in solution.* PhD thesis, Massachusetts Institute of Technology, 2011.

[288] Ming Zhao, Lei Jin, Bo Chen, Yao Ding, Hui Ma, and Dieyan Chen. Afterpulsing and its correction in fluorescence correlation spectroscopy experiments. *Appl. Opt.*, 42:4031, 2003.

[289] Robert M. Mazo. *Brownian Motion: Fluctuations, Dynamics, and Applications.* International Series of Monographs on Physics. Clarendon Press, Oxford, 2002.

[290] Taras Plakhotnik and Daniel Walser. Time resolved single molecule spectroscopy. *Phys. Rev. Lett.*, 80:4064–4067, 1998.

[291] Victor I. Klimov. Spectral and dynamical properties of multiexcitons in semiconductor nanocrystals. *Annu. Rev. Phys. Chem.*, 58:635–673, 2007.

[292] Anshu Pandey and Philippe Guyot-Sionnest. Multicarrier recombination in colloidal quantum dots. *J. Chem. Phys.*, 127:111104, 2007.

[293] Jing Zhao, Gautham Nair, Brent R. Fisher, and Moungi G. Bawendi. Challenge to the charging model of semiconductor-nanocrystal fluorescence intermittency from off-state quantum yields and multiexciton blinking. *Phys. Rev. Lett.*, 104:157403, 2010.

[294] Shamir Rosen, Osip Schwartz, and Dan Oron. Transient fluorescence of the off state in blinking CdSe/CdS/ZnS semiconductor nanocrystals is not governed by Auger recombination. *Phys. Rev. Lett.*, 104:157404, 2010.

[295] Vitaly A. Kharchenko and M. Rosen. Auger relaxation processes in semiconductor nanocrystals and quantum wells. *J. Lumin.*, 70:158–169, 1996.

[296] Victor I. Klimov, Alexander A. Mikhailovsky, D. W. McBranch, Catherine A. Leatherdale, and Moungi G. Bawendi. Quantization of multiparticle Auger rates in semiconductor quantum dots. *Science*, 287:1011–1013, 2000.

[297] István Robel, Ryan Gresback, Uwe Kortshagen, Richard D. Schaller, and Victor I. Klimov. Universal size-dependent trend in Auger recombination in direct-gap and indirect-gap semiconductor nanocrystals. *Phys. Rev. Lett.*, 102:177404, 2009.

[298] Allison M. Dennis, Benjamin D. Mangum, Andrei Piryatinski, Young-Shin Park, Daniel C. Hannah, Joanna L. Casson, Darrick J. Williams, Richard D. Schaller, Han Htoon, and Jennifer A. Hollingsworth. Suppressed blinking and auger recombination in near-infrared type-II InP/CdS nanocrystal quantum dots. *Nano Lett.*, 12:5545–5551, 2012.

[299] Sergio Brovelli, Richard D. Schaller, Scott Crooker, Florencio García-Santamaría, Yongfen Chen, Ranjani Viswanatha, Jennifer A. Hollingsworth, Han Htoon, and Victor I. Klimov. Nano-engineered electron–hole exchange interaction controls exciton dynamics in core–shell semiconductor nanocrystals. *Nat. Commun.*, 2:280, 2011.

[300] George E. Cragg and Alexander L. Efros. Suppression of auger processes in confined structures. *Nano Lett.*, 10:313–317, 2010.

[301] F. García-Santamaría, S. Brovelli, R. Viswanatha, J. A. Hollingsworth, H. Htoon, S. A. Crooker, and V. I. Klimov. Breakdown of volume scaling in auger recombination in CdSe/CdS heteronanocrystals: the role of the core-shell interface. *Nano Lett.*, 11:687–693, 2011.

[302] Wei Qin, Heng Liu, and Ph Guyot-Sionnest. Small bright charged colloidal quantum dots. *ACS Nano*, 8:283–291, 2014.

[303] Pooja Tyagi and Patanjali Kambhampati. False multiple exciton recombination and multiple exciton generation signals in semiconductor quantum dots arise from surface charge trapping. *J. Chem. Phys.*, 134:094706, 2011.

[304] Young-Shin Park, Wan Ki Bae, Lazaro A. Padilha, Jeffrey M. Pietryga, and Victor I. Klimov. Effect of the core/shell interface on Auger recombination evaluated by single-quantum-dot spectroscopy. *Nano Lett.*, 14:396–402, 2014.

[305] H. Jeff Kimble, Mario Dagenais, and Leonard Mandel. Photon antibunching in resonance fluorescence. *Phys. Rev. Lett.*, 39:691–695, 1977.

[306] Xavier Brokmann, Élisabeth Giacobino, Maxime Dahan, and Jean-Pierre Hermier. Highly efficient triggered emission of single photons by colloidal CdSe/ZnS nanocrystals. *Appl. Phys. Lett.*, 85:712, 2004.

[307] Brahim Lounis and William E. Moerner. Single photons on demand from a single molecule at room temperature. *Nature*, 407:491–493, 2000.

[308] David A. Bussian, Anton V. Malko, Han Htoon, Yongfen Chen, Jennifer A. Hollingsworth, and Victor I. Klimov. Quantum optics with nanocrystal quantum dots in solution: Quantitative study of clustering. *J. Phys. Chem. C*, 113:2241–2246, 2009.

[309] Jan Sýkora, Karin Kaiser, Ingo Gregor, Wolfgang Bönigk, Günther Schmalzing, and Jörg Enderlein. Exploring fluorescence antibunching in solution to determine the stoichiometry of molecular complexes. *Anal. Chem.*, 79(11):4040–4049, June 2007.

[310] Ülo Mets. Antibunching and rotational diffusion in fcs. In R. Rigler and E. L. Elson, editors, *Fluorescence Correlation Spectroscopy: Theory and Applications*, pages 346–359. Springer, Berlin, 2001.

[311] Robert Hanbury Brown and Richard Q. Twiss. Correlation between photons in two coherent beams of light. *Nature*, 177:27–29, 1956.

[312] Thomas S. Bischof, Raoul E. Correa, Danna Rosenberg, Eric A. Dauler, and Moungi G. Bawendi. Measurement of emission lifetime dynamics and biexciton emission quantum yield of individual InAs colloidal nanocrystals. *Nano Lett.*, 14:6787–6791, 2014.

[313] Meirav Ben-Lulu, David Mocatta, Mischa Bonn, Uri Banin, and Sanford Ruhman. On the absence of detectable carrier multiplication in a transient absorption study of InAs/CdSe/ZnSe core/shell1/shell2 quantum dots. *Nano Lett.*, 8:1207–1211, 2008.

[314] Benjamin D. Mangum, Feng Wang, Allison M. Dennis, Yongqian Gao, Xuedan Ma, Jennifer A. Hollingsworth, and Han Htoon. Competition between Auger recombination and hot-carrier trapping in PL intensity fluctuations of type II nanocrystals. *Small*, 10:2892–2901, 2014.

[315] Han Htoon, Anton V. Malko, David A. Bussian, Javier Vela, Yongfen Chen, Jennifer A. Hollingsworth, and Victor I. Klimov. Highly emissive multiexcitons in steady-state photoluminescence of individual "giant" CdSe/CdS core/shell nanocrystals. *Nano Lett.*, 10:2401–2407, 2010.

[316] Zhong-Jie Jiang and David F. Kelley. Surface charge and piezoelectric fields control auger recombination in semiconductor nanocrystals. *Nano Lett.*, 11:4067–4073, 2011.

[317] Alicia W. Cohn, Alina M. Schimpf, Carolyn E. Gunthardt, and Daniel R. Gamelin. Size-dependent trap-assisted auger recombination in semiconductor nanocrystals. *Nano Lett.*, 13:1810–1815, 2013.

[318] Benjamin D. Mangum, Siddharth Sampat, Yagnaseni Ghosh, Jennifer A. Hollingsworth, Han Htoon, and Anton V. Malko. Influence of the core size on biexciton quantum yield of giant CdSe/CdS nanocrystals. *Nanoscale*, 6:3712–3720, 2014.

[319] Yann Louyer, Louis Biadala, J.-B. Trebbia, Mark J. Fernée, Philippe Tamarat, and Brahim Lounis. Efficient biexciton emission in elongated CdSe/ZnS nanocrystals. *Nano Lett.*, 11:4370–4375, 2011.

[320] Marc Achermann, Jennifer A. Hollingsworth, and Victor I. Klimov. Multiexcitons confined within a subexcitonic volume: Spectroscopic and dynamical signatures of neutral and charged biexcitons in ultrasmall semiconductor nanocrystals. *Phys. Rev. B*, 68:245302, Dec 2003.

[321] Brent R. Fisher, Jean-Michel Caruge, Yin-Thai Chan, Jonathan Halpert, and Moungi G. Bawendi. Multiexciton fluorescence from semiconductor nanocrystals. *Chem. Phys.*, 318:71–81, 2005.

[322] Ahmet Fatih Cihan, Pedro Ludwig Hernandez Martinez, Yusuf Kelestemur, Evren Mutlugun, and Hilmi Volkan Demir. Observation of biexcitons in nanocrystal solids in the presence of photocharging. *ACS Nano*, 7:4799–4809, 2013.

[323] Yusuf Kelestemur, Ahmet Fatih Cihan, Burak Guzelturk, and Hilmi Volkan Demir. Type-tunable amplified spontaneous emission from core-seeded cdse/cds nanorods controlled by exciton-exciton interaction. *Nanoscale*, 6:8509–8514, 2014.